Characterizing the extended Lyman-α emission around high-redshift massive galaxies

Jay González Lobos

München 2024

Characterizing the extended Lyman-α emission around high-redshift massive galaxies

Jay González Lobos

Dissertation
an der Fakultät für Physik
der Ludwig–Maximilians–Universität
München

vorgelegt von
Jay González Lobos
aus Providencia, Chile

München, den 01.10.2024

A mi madre,
quien su lucha llevo conmigo.

Contents

List of Figures

List of Tables

Zusammenfassung

Das circumgalaktische Medium (CGM) enthält wertvolle Informationen über die Gaswechsel, die zwischen einer Galaxie und ihrer Umgebung stattfinden (z. B. Ein- und Ausflüsse), und bietet somit Einblicke in die physikalischen Prozesse, die das Wachstum und die Entwicklung von Galaxien regulieren. Diese Arbeit konzentriert sich auf die direkte Charakterisierung der kühlen Gasreservoire des CGM mit Temperaturen von $T \sim 10^4$ K um massive Galaxien bei $z \sim 3$ mit unterschiedlichen Graden der Strahlung aktiver Galaxienkerne (AGN), basierend auf über 100 Stunden VLT/MUSE-Beobachtungen, die nach ausgedehnter Linienemission suchen. Diese Emission stammt überwiegend von Gas, das in den Halo einfällt, während sich eine Galaxie bildet, und kann in Anwesenheit von ionisierender Strahlung sichtbar gemacht werden, die diffuse Lyα-Emission erzeugt. Ziel dieser Arbeit war es, diese ausgedehnte Lyα-Emission zu charakterisieren und mit den physikalischen Mechanismen zu verknüpfen, die an der Galaxienentwicklung beteiligt sind (Akkretion, Sternentstehung, Rückkopplung), sowie mit den physikalischen Eigenschaften ihres zentralen AGN und der Wirtsgalaxie (Quasarstrahlung, Schwarzes-Loch-Masse, Halomasse, Sternentstehungsrate, Staubgehalt).

Ich liefere einen Überblick über die Leuchtkraft, Morphologie und Kinematik von Lyα-Nebel und finde wichtige Korrelationen mit den Eigenschaften der Wirtsgalaxie und des AGN. Hellere und größere Nebel werden normalerweise mit helleren Quasaren in Verbindung gebracht, während die Lyα-Emission möglicherweise durch den Staubgehalt der Wirtsgalaxie oder den Öffnungswinkel des Quasars moduliert wird. Zusätzlich ist es möglich, dass AGN-Feedback kinematische Spuren in der beobachteten Lyα-Emission hinterlässt, da in den zentralen Regionen des CGM um AGN mit stärkerer Strahlung breitere Linienbreiten gemessen werden. Diese Ergebnisse zeigen eine wichtige Verbindung zwischen den Eigenschaften des CGM und ihrer Wirtsgalaxie, was zusätzliche Einblicke in den Prozess der Galaxienentwicklung bietet. Zukünftige Beobachtungen, die auf zusätzliche Linienemissionen wie C IV, He II und Hα abzielen, sowie detaillierte Strahlungstransfer-Simulationen könnten dazu beitragen, diese Zusammenhänge besser zu interpretieren. Durch das Erforschen dieser Emissionslinien können wir theoretische Modelle verfeinern und letztendlich die Mechanismen aufdecken, die das Wachstum von Galaxien regulieren.

Summary

The circumgalactic medium (CGM) carries valuable information on the gas exchanges that occur between a galaxy and its surroundings (e.g., inflows and outflows), offering a perspective into the physical processes that regulate galaxy growth and evolution. This thesis focuses on the direct characterization of the cool $T \sim 10^4$ K gas reservoirs of the CGM around $z \sim 3$ massive galaxies with different degrees of active galactic nucleus (AGN) radiation, through more than 100 hrs of VLT/MUSE observations searching for extended line emission. This emission originates predominantly from gas infalling into the halo as a galaxy forms and can be illuminated in the presence of ionizing radiation producing diffuse Lyα emission. The goal of this thesis has been to characterize this extended Lyα emission and link it to the physical mechanisms involved in galaxy evolution (accretion, star formation, feedback) and the physical properties of their central AGN and host galaxy (quasar radiation, black hole mass, halo mass, star formation rate, dust content).

I provide an overview of the luminosity, morphology and kinematics of Lyα nebulae and find important correlations with the host galaxy and AGN properties. Brighter and larger nebulae are usually associated to brighter quasars, while the Lyα emission could be modulated by the dust content of the host galaxy or opening angle of the quasar. Additionally, it is possible that AGN feedback has kinematic imprints in the observed Lyα emission, due to larger linewidths measured in the central regions of the CGM around AGN with stronger radiation. These results revealed an important link between the properties of the CGM and their hosts, which provide additional insights into the process of galaxy evolution. Future observations targeting additional line emissions (C IV, He II and Hα) and detailed radiative transfer simulations could further aid in the interpretation of these relationships. By probing these emission lines we can refine theoretical models, ultimately uncovering the mechanisms regulating galaxy growth.

Chapter 1

Introduction

1.1 How do galaxies form?

Describing the observed variety and origin of galaxies in the present universe requires understanding of the physical processes shaping galaxy formation and evolution in a cosmological context. In the current Λ Cold Dark Matter (CDM) paradigm (Blumenthal et al., 1982), the density field of the universe is composed of 4.8% baryons corresponding to all visible matter in the universe, 26.6% CDM collisionless particles that only interact through gravity (Peebles, 1982) and 68.6% dark energy which causes the accelerated expansion of the universe (Planck Collaboration et al., 2020). The cosmic density field after the Big Bang is thought to be initially nearly homogeneous, however small perturbations are originated by quantum fluctuations during an inflationary[1] period. These perturbations grow as the universe expands until they are able to become gravitationally unstable and collapse forming virialized structures[2] (Jeans, 1902). Depending on the initial perturbations, this process can distribute baryons and dark matter into a large-scale filamentary cosmic web (Bond et al., 1996).

Large scale spectroscopic surveys, such as the 2dF survey (Colless, 1999; Colless et al., 2001) and the Sloan Digital Sky Survey (SDSS; Stoughton et al. 2002; Almeida et al. 2023), have been carried out to map the distribution of galaxies in the sky as a function of their redshift[3]. The left panel of Figure 1.1 shows the distribution of SDSS galaxies out to

---

[1]The theory of cosmic inflation (Guth and Steinhardt, 1984) refers to a period of exponential expansion of the universe shortly after the Big Bang. This theory can explain the isotropy and flatness of the universe.

[2]A virialized structure is in hydrostatic equilibrium, i.e., gravity is balanced by the internal pressure of its particles (due to thermal or kinetic energy). Virialized structures are gravitationally bound and obey the virial theorem $2\langle K \rangle + \langle U \rangle = 0$, where $\langle K \rangle$ and $\langle U \rangle$ are the kinetic energy and potential energy averaged over time, respectively.

[3]The redshift is a measurement of the observed change in wavelength of electromagnetic radiation due to the relative velocities between the source and the observer. The redshift is defined in terms of the observed wavelength λ_{obs} and the emitted wavelength λ_0 as:

$$z = \frac{\lambda_{\mathrm{obs=}} - \lambda_0}{\lambda_0}. \tag{1.1}$$
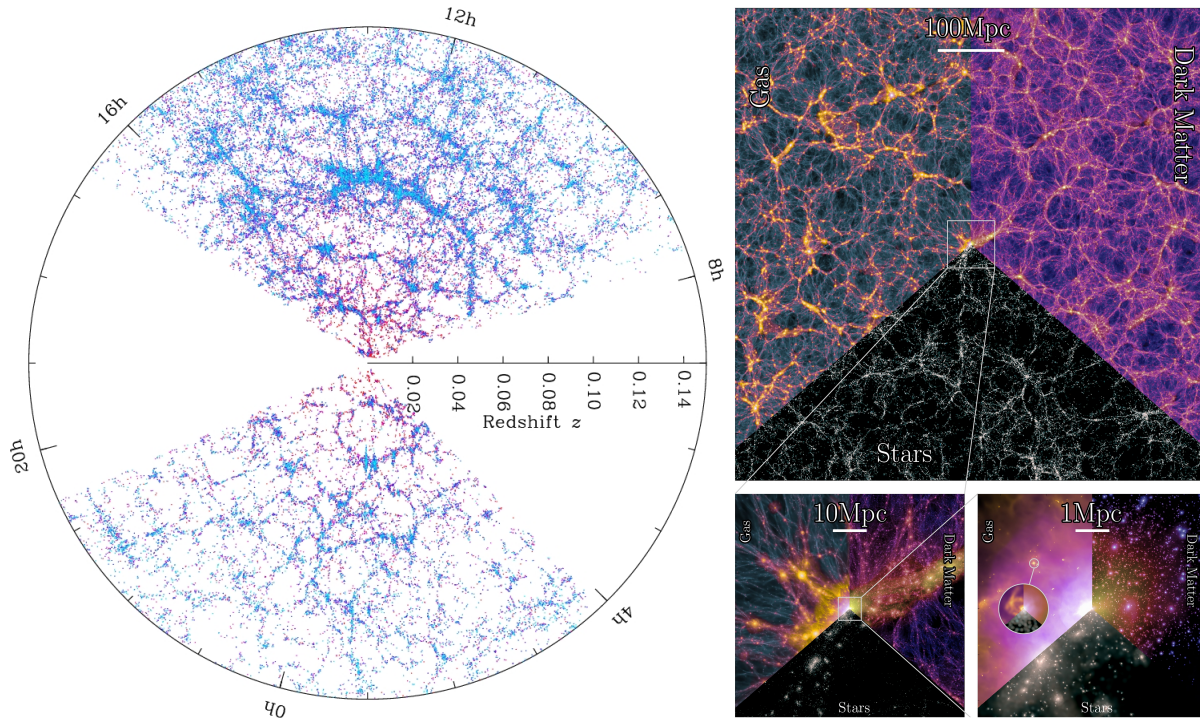
Figure 1.1: Large-scale distribution of matter. *Left:* Diagram of the distribution of galaxies across the plane of the sky as a function of redshift observed with SDSS (Stoughton et al., 2002; Almeida et al., 2023), the redshift of $z = 0.14$ corresponds to a distance of roughly 500 Mpc. Image credit: SDSS science results website (https://www.sdss4.org/science/). *Right:* Distribution of gas (top left), dark matter (top right) and starlight (bottom center) projected within 10 Mpc of the full 740 Mpc box of the MilleniumTNG project cosmological simulations. The panels show zooms of different physical scales such as filaments (top), galaxy super cluster (bottom left) and galaxy cluster (bottom right). The bottom right panel additionally shows a zoom within a radius of 50 kpc of an individual spiral galaxy. Figure obtained from Pakmor et al. (2023).

$z = 0.14$, each dot is a galaxy and the color-scale represents the local density (increasing from red to blue). It is possible to see that galaxies are distributed in a filamentary pattern, which is similar to the one arising from initial perturbations in the density field predicted in large cosmological simulations, such as the MilleniumTNG project (right panel of Figure 1.1; Hernández-Aguayo et al. 2023; Pakmor et al. 2023). These studies show that dark matter and baryons are distributed in a pattern set by the initial perturbations, known as the cosmic web.

Additionally, the observed properties of galaxies reveal a variety of morphologies and luminosities, which fall into a spectrum ranging from low mass faint galaxies (e.g., dwarf galaxies) to massive bright galaxies (e.g., elliptical galaxies). The number density of galax-

---

In a cosmological context, objects can appear redshifted due to the Doppler shift caused in an accelerating expanding universe (Riess et al., 1998).

ies within a range of luminosities is described by the luminosity function $\phi(L)\mathrm{d}L$, which can be modeled with a Schechter function (Schechter, 1976) and is given by:

$$\phi(L)\mathrm{d}L = \phi^* \left(\frac{L}{L^*} \right)^\alpha \exp \left(-\frac{L}{L^*} \right) \frac{\mathrm{d}L}{L^*}. \tag{1.2}$$

Where, ϕ^* is the volume density scale factor, L^* is the characteristic luminosity and α is the faint end slope of the distribution. This function is an analytical approximation to the observed luminosity distribution of galaxies and can be traced to the mass distribution of baryons. In order to measure the luminosity function, large surveys covering the faint end of magnitudes are required. For example, Blanton et al. (2003) used SDSS data to determine that the luminosity function at $z = 0.1$ can be fitted using a Schechter function, in units of magnitude, with parameters $\phi^* = 1.49 \times 10^{-2}\,\mathrm{Mpc}^{-3}$, $M^* = -20.44$ and $\alpha = -1.05$. This value for the characteristic magnitude translates into a luminosity of $L^* \sim 10^{10}\,\mathrm{L}_\odot$, which is roughly the luminosity of the Milky Way. The fitted Schechter function implies that most of the observed light is contributed by galaxies with L^*, while the number of brighter galaxies declines exponentially. On the other hand, the observed value for the faint end slope of the luminosity function implies that faint dwarf galaxies dominate the population. These observations can be translated into mass using the mass-luminosity relation (Eddington and Vogt, 1924) and be used to constrain the density of baryons within galaxies and test cosmological models. Figure 1.2 shows the luminosity (left) and mass (right) function for SDSS galaxies shown in Blanton and Moustakas (2009).

If baryons co-evolve with dark matter due to the influence of the same initial density perturbations, then the observed properties of the galaxies (such as the luminosity function) should be correlated to the evolution of the underlying dark matter distribution. Rees and Ostriker (1977) explored this scenario and predicted that the early stages of collapse arranges the baryons into a multi-phase medium: ionized gas at virial temperatures $T \geq 10^6\,\mathrm{K}$ can be cooled down to neutral $T \geq 10^4\,\mathrm{K}$ through collisions, the condensed neutral gas can continue cooling down and reach temperatures of $T \sim 100\,\mathrm{K}$ where is suitable to form molecular gas and allow star formation. Moreover, the formalism presented in Press and Schechter (1974) uses linear perturbation theory to describe the mass distribution of virialized objects that arise from a set of initial density perturbations. Similar to the Schechter function, the Press-Schechter formalism provides a characteristic halo mass that increases with time for which only halos with $M \leq M^*$ can form at a given moment. Following these works, White and Rees (1978) proposed a model for galaxy formation, in which dark matter halos grow through clustering with other halos and that baryons condense into the potential well of these halos. In this cosmological framework, galaxies grow embedded in dark matter halos, which are located at the peaks of the initial density perturbations, and build their stellar mass through gas accretion from the surrounding filamentary cosmic web and through merging with other halos.

White and Rees (1978) also highlighted the importance that baryonic effects have in regulating the growth of structures. They discuss effects such as gas cooling, which occurs as baryons set into the gravitational potential well and emit radiation due to collisional excitation. Additionally, gas falling into the potential well can be shock heated from
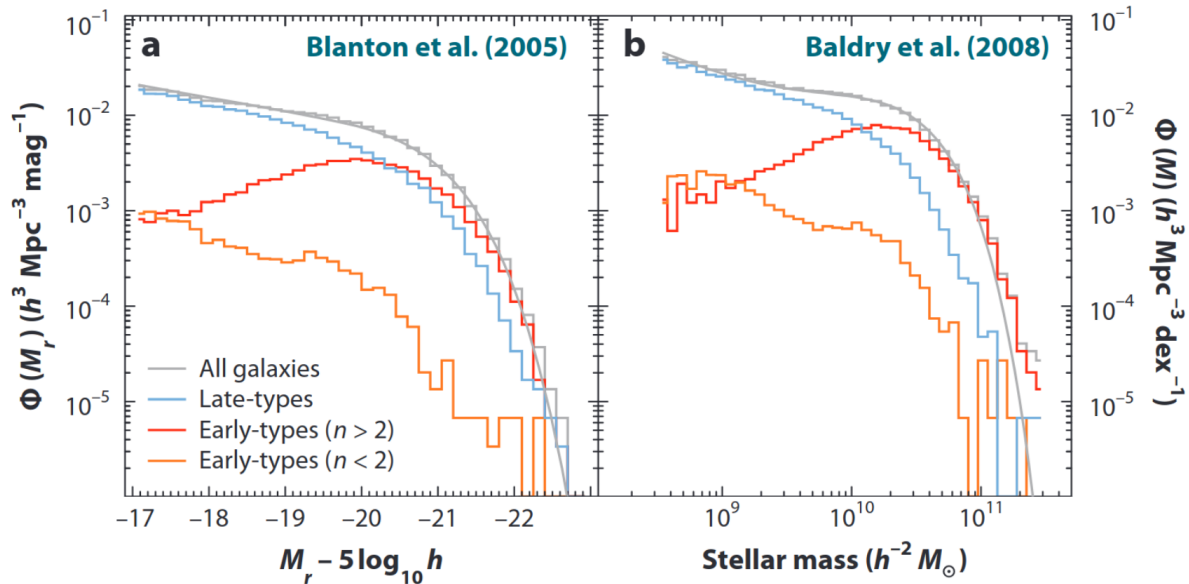
Figure 1.2: Observed galaxy luminosity and mass functions. *Left:* Optical r-band luminosity function from all galaxies (gray histogram), star forming galaxies (blue), red concentrated galaxies (red) and red diffuse galaxies (orange) in SDSS. The Schechter function fit to all galaxies is shown with a grey curve. *Right:* The same colors are used to show the corresponding stellar mass function obtained using a stellar mass-to-light ratio. Figure adapted from Blanton and Moustakas (2009).

the interaction with the virialized halo structure, thus suppressing cooling. Then, star formation only happens once cooling has been able to condense enough cold material into the galactic disk. Finally, feedback due to the stars formed, such as supernova explosions and photoionization, can dissipate and heat the gas counteracting cooling. The authors argue that these baryonic processes can be used to describe the luminosity function, for example, for larger halos, they suggest that gas may not have had enough time to cool down and therefore cannot contribute to the amount of condensed baryons. Additionally, they proposed that efficient cooling in massive halos could supply the necessary gas to fuel the extreme star formation rates of a population of observed massive submillimeter galaxies at $z \geq 2$ (e.g., Smail et al., 1997). On the other hand, the galaxies at the lower end of the halo masses might have their cool gas supply disrupted due to supernova feedback and photoionization. Indeed, Dekel and Silk (1986) presented an analytical model for the mass loss in dwarf galaxies due to supernova feedback and predicted that these reside in dark matter dominated halos which are less clustered. In this context, Benson et al. (2003) studied the shape of the luminosity function using hierarchical clustering models that included these baryonic effects and found that stellar and supernova feedback were not

enough to reproduce the number of high luminosity systems, which were instead predicted in larger numbers. Therefore, the authors concluded that additional mechanisms such as efficient heating and/or gas expulsion were needed to reproduce the observations.

1.2 Active galactic nuclei

In the context of galaxy formation discussed in Section 1.1, cold gas accretion and mergers can efficiently transfer material towards the center of massive galaxies, if the galaxy is hosting a supermassive black hole (SMBH) then this material could be accreted and trigger an active galactic nucleus (AGN; Salpeter, 1964). As a galaxy grows, matter can be transported into a SMBH ($M \sim 10^5 - 10^9 \, \mathrm{M_\odot}$) through a compact ($< 1 \, \mathrm{pc}$) accretion disk, this process releases radiation in all wavelengths and strong winds placing AGN among the brightest objects in the universe (Mo et al., 2010).

The luminosity of an AGN depends on the amount of accreted material, which releases energy due to the gravitational potential of the SMBH. In order to ensure black hole growth, the radiation pressure force generated cannot be larger than the gravitational binding force. This sets a maximum luminosity of an accreting black hole which is given by the Eddington luminosity:

$$L_{\mathrm{Edd}} = \frac{4\pi G c m_{\mathrm{p}}}{\sigma_{\mathrm{T}}} M_{\mathrm{BH}} \approx 1.28 \times 10^{46} \left(\frac{M_{\mathrm{BH}}}{10^9 \, \mathrm{M_\odot}} \right) \, \mathrm{erg \, s^{-1}}, \tag{1.3}$$

where c is the speed of light, m_{p} is the proton mass and σ_{T} is the Thomson scattering cross-section[4]

AGN emission is observed across the whole wavelength range due to the different components of their structure (Mo et al., 2010; Netzer, 2015). Strong emission lines are produced in the accretion disk and appear broad due to large keplerian velocities, this is called the broad line region (BLR). This disk is surrounded by an obscuring dusty torus which can re-process the ionizing radiation of the BLR into infrared emission. This torus is thought to cause the AGN radiation to be directed preferentially through axisymmetric ionization cones. These cones can produce collimated jets of outflowing material and radiation, which can accelerate relativistic electrons producing synchrotron radiation. Farther from the accretion disk, clouds of lower velocity ionized material produce narrow line emission due to photoionization by the AGN, this region is called the narrow line region (NLR).

Additionally, SMBH growth is expected to produce strong episodic feedback capable of regulating the cool gas phase of a galaxy, thus linking both SMBH growth and star formation (Silk and Rees, 1998). In this case, the properties of the black hole would be correlated to the stellar content of galaxies. Indeed, Kormendy and Richstone (1995) had conducted a study of 7 elliptical galaxies which showed that their stellar dynamics were

---

[4]Thomson scattering occurs as charged particles, such as free electrons, and photons interact. The Thomson cross section is defined as $\sigma_{\mathrm{T}} = \frac{8\pi}{3} \left(\frac{q_{\mathrm{e}}^2}{m_{\mathrm{e}} c^2} \right) \approx 6.65 \times 10^{-25} \, \mathrm{cm^2}$, where q_{e} and m_{e} are the charge and mass of an electron, respectively.
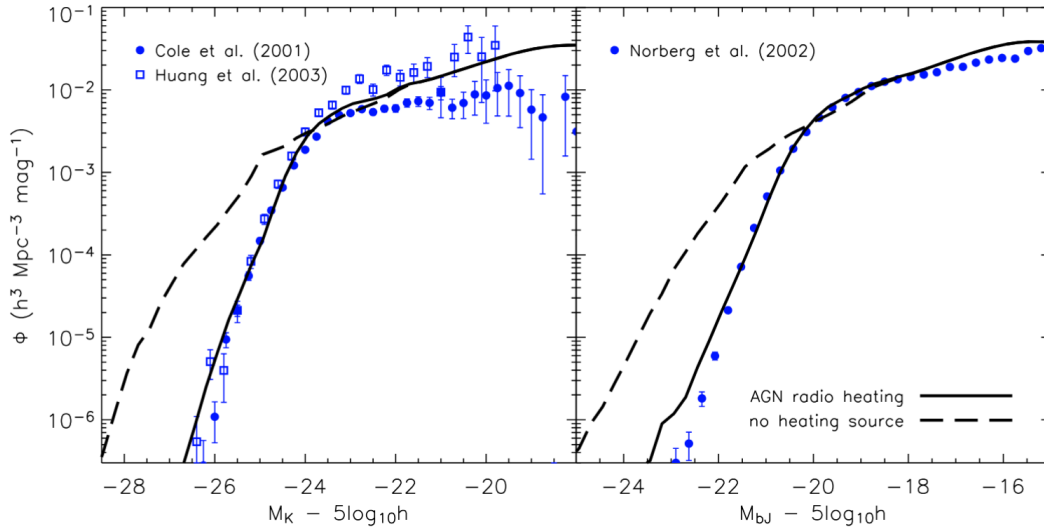
Figure 1.3: Comparison of the galaxy luminosity function from simulations with observations. The blue points show the observed $K-$ and b_J-band luminosity functions on the left and right panels, respectively. The predicted luminosity functions from cosmological simulations with and without AGN heating are shown with solid and dashed lines, respectively). Figure obtained from Croton et al. (2006).

consistent with central SMBHs of $M_{BH} \sim 10^6 - 10^{9.5} \, M_\odot$. Furthermore, the black hole masses derived from this study were proportional to the mass of the galaxy's bulge. Such relationship implies that SMBH growth is tightly linked with galaxy formation. In this context, Kauffmann and Haehnelt (2000a) proposed a model of galaxy formation based on hierarchical growth where an efficient way of transferring mass into SMBHs is through galaxy mergers, which could be an explanation to the observed relationship between M_{BH} and M_{bulge} in elliptical galaxies. Then, Binney (2004) proposed a scenario that could reconcile the high number of luminous galaxies predicted with analytical models of galaxy formation (e.g., Benson et al., 2003) with the observed luminosity function which considers that AGN feedback can suppress gas cooling in massive halos. Later, Di Matteo et al. (2005) and Springel et al. (2005) implemented these ideas into large cosmological simulations which were able to agree with the bright end of the luminosity function. Further work by Croton et al. (2006) showed that AGN feedback is capable of suppressing cooling flows and star formation in massive halos through heating and ejection of material, linking them to the formation of massive elliptical galaxies. Figure 1.3 shows with blue points the K- and b_J-band luminosity function on the left and right panels, respectively. The two panels show the predicted luminosity function from cosmological simulations with and without AGN

heating (solid and dashed lines, respectively) obtained in Croton et al. (2006).

AGN feedback is episodic and present as jets and winds that inject both mechanical and radiative energy into the environment, which ionize, heat and push away surrounding gas (King and Pounds, 2015). For example, UV and X-ray photons from an AGN can ionize neutral atoms and heat them, or they can transfer momentum creating winds. Evidence of AGN feedback in the most massive galaxies at the center of galaxy clusters has been extensively observed in the form of X-ray jets and bubbles that can extend out to hundreds of kiloparsecs, revealing an important mechanism that prevents gas cooling and quenches star formation (Fabian, 2012). Additionally, outflow signatures observed from the BLR imply that AGN feedback can inject mechanic and radiative energy into the surrounding medium (Harrison and Ramos Almeida, 2024b).

1.2.1 Quasars

Due to the anisotropy of the AGN radiation discussed in Section 1.2, different spectral features of the material surrounding a SMBH will be apparent depending on the viewing angle Netzer (2015). In this context, the brightest AGN ($L_{\text{bol}} > 10^{44}\,\text{L}_\odot$; Shen et al. 2020) are being observed through their ionization cones providing a direct view of the accretion disk. These systems, referred to as quasi-stellar radio-objects (QSO) or quasars, were first identified as compact radio sources (Schmidt, 1963) and later associated to accreting massive objects (Salpeter, 1964). The radio emission of a quasar is mainly produced by synchrotron emission (which produces emission in all wavelengths) due to relativistic electrons being accelerated in the magnetic field from the accretion disk, some of these quasars show collimated jets (Fabian, 2012). Additionally, quasars can be routinely detected in optical to near infrarred observed wavelengths (e.g., Lyke et al., 2020) and their emission is characterized by time variability and broad lines (velocity widths $> 1000\,\text{km/s}$), which originate from the BLR.

Due to their large luminosities, quasars can be detected out to large redshifts ($z = 7.6$; Wang et al. 2021), providing a valuable test into the early epochs of the universe. For this reason, quasars have been a repeated target in high-redshift observational studies. For example, Shen et al. (2020) measured the $1.0 < z < 6.0$ evolution of the quasar bolometric luminosity function and showed that the characteristic luminosity peaks at $L_{\text{bol}} = 10^{46.6}\,\text{L}_\odot$ at redshift $z \sim 3$. Additionally, different clustering studies showed that $z = 0.3 - 5.1$ quasars reside in overdense regions implying halo masses of $M_{\text{halo}} \simeq 10^{12}\,\text{M}_\odot$ at all redshifts (Porciani et al., 2004; Croom et al., 2005; Shen et al., 2009; White et al., 2012; Eftekharzadeh et al., 2015; Timlin et al., 2018). To reach such masses, those halos are expected to form at the highest peaks of the cosmic density field (Efstathiou and Rees, 1988) and this mass range suggests that cold-accretion streams can directly fuel the central SMBH during the peak activity time of quasars ($z \sim 3$). Additionally, it was possible to see that not all halos with such high masses were hosting a bright AGN. Therefore, Martini and Weinberg (2001) used the quasar halo masses estimated from clustering studies to compute the fraction of halos that host active quasars at $z = 2 - 3$ and inferred a quasar lifetime of $t_{\text{Q}} = 4 \times 10^7\,\text{yr}$.

Within this framework, quasars are expected to reside in environments where all of the aforementioned processes regulating galaxy formation can happen at the same time and span sub-parsec to kiloparsec scales. Also, their feedback interacts with multiple gas phases ranging from the molecular ($T \leq 100$ K) content within (and possibly beyond) the galaxy, to halo gas heated up to the virial temperatures ($T \sim 10^7$ K). Therefore, to describe the massive end of galaxy formation in a cosmological context requires not only the knowledge of the central engine of quasars, but the inclusion of the larger scale environment in which they reside.

1.3   The circumgalactic medium

In order to build an accurate model of galaxy formation, we require to understand the role of quasars in a cosmological context. As discussed in Section 1.2, cold gas accretion from the cosmic web can feed SMBHs in massive galaxies, which can in turn modify their surrounding gas distribution through AGN feedback and regulate its own growth. In this context, galaxy formation involves multi-scale processes which require a description of the physical mechanisms regulating the balance of cold/hot gas in the vicinity of quasars and galaxies. This diffuse gas interface that surrounds a galaxy's interstellar medium out to the virial radius of of its dark matter halo is defined as the circumgalactic medium (CGM; Tumlinson et al. 2017). The CGM harbors information of the gas exchange between a galaxy and its surroundings caused by the physical processes mentioned in Section 1.1 (gas cooling, star formation, AGN, mergers, feedback), therefore it is multiphase. Indeed, the CGM contains ionized gas as hot as the virial temperature corresponding to $T \sim 10^7$ K for a $M \sim 10^{12}$ M$_\odot$ halo (enough to keep the gas ionized) down to cold $T < 10^4$ K neutral gas Tumlinson et al. (2017); Faucher-Giguère and Oh (2023b). The balance between these phases is regulated by cooling and feedback generating a continuous cycle of inflows and outflows within the CGM, this process is called the baryon cycle (Péroux and Howk, 2020) and it is responsible for shaping the observed properties of galaxies such as stellar and black hole mass.

As discussed in the previous sections and reviewed in Tumlinson et al. (2017), the hot ionized gas ($T \sim 10^7$ K) can be cooled down to $T \leq 10^4$ K through collisional excitation forming cooling flows that feed a galaxy with gas, which at earlier times are more likely to be metal poor. As enough material is condensed into the galaxy it can cool down to $T \leq 100$ K, then star formation proceeds in molecular clouds (Lada and Lada, 2003; McKee and Ostriker, 2007). If the galaxy hosts a SMBH, material reaching the center could trigger an AGN. Mergers are an efficient way to supply large amounts of gas into the galaxy, which can enhance star formation and/or trigger AGN. Stellar winds and supernova inject energy and metals into the interstellar medium and CGM, in low mass halos this can quench star formation. On the other hand, AGN can produce strong winds and outflows that prevent gas cooling, regulating both star formation and SMBH growth. In turn, feedback from stars and AGN will disturb and heat the gas, regulating the baryon cycle. The gas expelled in feedback processes can escape the galaxy's halo (outflows) or it can condense back into the
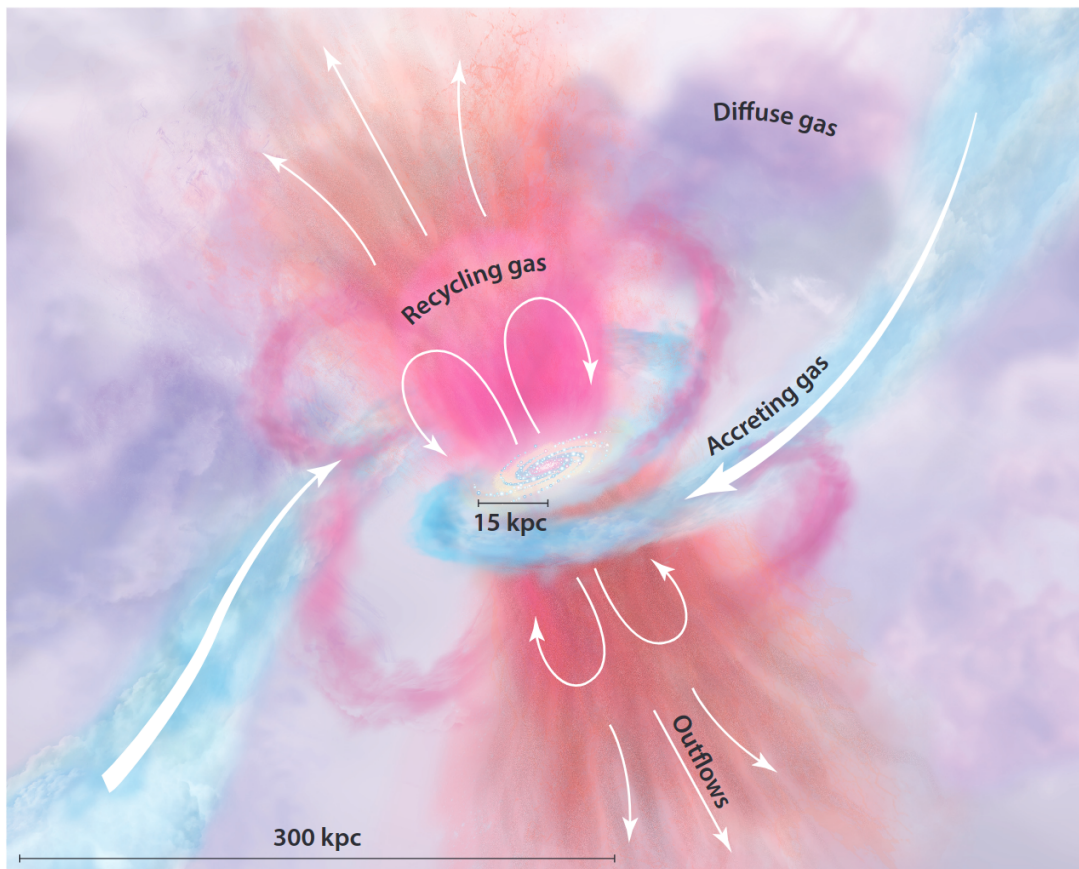
Figure 1.4: Illustration of the CGM. The blue regions represent cool streams of accreting gas from the large-scale cosmic web into the galaxy at the center (represented with white stars), the pink regions represent gas expelled from the galaxy that is condensing back into it, while the orange regions represent material that is ejected from the halo through outflows. Finally, the purple regions represent diffuse gas that is mixed from the other phases. The arrows represent the motions expected in the different gas phases.

interstellar medium (recycling). Figure 1.4 shows an illustration of the CGM in a galaxy halo, with the different colors representing different gas phases (see caption for details) and their motions represented with arrows.

In this context, the long term growth of a galaxy requires the continuous replenishment of the gas supply available for star formation, either through inflows, mergers, or recycling.

Historically, the CGM of galaxies has been probed in absorption lines using background bright quasars, as the UV light from a quasar travels in our direction it is absorbed by any intervening gas. Depending on the gas temperature and density of the galaxy's CGM, different lines will appear in absorption. For example, the presence of Lyman-α (Lyα) absorption in background quasar spectra due to $T \sim 10^4$ K neutral hydrogen revealed column densities of $N_\mathrm{H} \sim 10^{15.5}$ cm^{-2} in the CGM of $2.4 < z < 3.1$ galaxies (Pieri et al.,

2014). The $T \sim 10^4\,$K gas phase has also been probed in absorption of heavier elements such as neutral carbon (Ledoux et al., 2015) and Mg II (Bergeron and Boissé, 1991; Chen et al., 2010), indicating that the cool CGM of $z \sim 0.5 - 2$ galaxies is also enriched with metals. Bouché et al. (2012) studied the Mg II absorption line of 12 quasar sightlines and found that the absorbers preferentially align with the major and minor axis of $z \sim 0.1$ galaxies, suggesting that they are tracing inflows and outflows, respectively. Additionally, absorption lines from highly ionized species such as C IV, N V and O VI can indicate the presence of hot $T > 10^5\,$K CGM gas (Oppenheimer et al., 2012).

Carrying out such absorption studies to detect the CGM of quasars is particularly challenging due to the small number of bright background quasars, as these drop exponentially at high-redshift. Notwithstanding this difficulty, their massive $M \sim 10^{12}\,\mathrm{M_\odot}$, cool $T \sim 10^4\,$K and metal rich gas reservoirs at $z \sim 3$ have been probed in absorption through optically thick hydrogen, Mg II and C IV absorption (Hennawi and Prochaska, 2007; Farina et al., 2013, 2014; Hennawi and Prochaska, 2013; Prochaska et al., 2014; Lau et al., 2016). More recently, Jalan et al. (2019) studied a large sample of 181 projected quasar pairs at $z \sim 3$ and found that the Lyα absorption along the line of sight of the foreground quasars was less than the perpendicular direction, consistent with the hypothesis that we observe quasars through their ionization cones and these can alter the surrounding gas distribution and ionization state.

In summary, absorption studies are a powerful test of the physical conditions in the CGM gas, however they are not able to provide information on the complex gas distribution of the CGM of quasars since each background quasar can only provide information of one line of sight. Instead, observations need to aim to map the CGM directly in emission in order to account for the multi-scale physical conditions.

1.3.1   The CGM of high-redshift quasars in emission

Due to the multi-phase nature of the CGM of quasars, we expect characteristic emission from the different states of the gas. For example, inflowing gas is typically expected to consist of cold $T \sim 10^4\,$K neutral hydrogen and is expected to emit Lyα alpha radiation through gravitational cooling (Dijkstra and Loeb, 2009). Another way of tracing the cold gas is through Mg II 2796 Å and 2803 Å doublet emission (Nelson et al., 2021; Chang et al., 2023), however at $z > 3$ this emission is observed in the near infrared and is more difficult to access. Additionally, we expect the presence of outflows due to AGN or star formation feedback, which can enrich the CGM with metals and produce line emission due to shocks (e.g., Vidal-García et al., 2021). Moreover, the warm ionized CGM gas ($T \sim 10^5 - 7$) is expected to produce UV (C IV, O VI, e.g, Bertone and Schaye 2012; Hayes et al. 2016) and soft X-ray emission (Truong et al., 2023), however due to the low surface brightness is difficult to achieve for quasar halos at high redshifts with current facilities. Also, the densest regions of the CGM could reach low temperatures $T < 100\,$K allowing the formation of molecular gas, which can be detected through CO, CII or dust emission (e.g., Ginolfi et al., 2020; Li et al., 2023), however this emission only traces a small fraction of the bulk of the CGM gas. Finally, the advancement of current space infrared spectroscopy such as

with the James Webb Space Telescope will us to access rest-frame optical emission (Hα, [O III]) of the high redshift CGM.

In summary, the CGM emission is elusive, most of its mass is contained in the hot ionized phase and is diffuse. Regardless, the cold gas $T \sim 10^4$ K phase is relatively significant and carries valuable information on the inflowing material that fuels a galaxy. Therefore, a direct detection of this phase is key to determining the amount of gas available to regulate galaxy and SMBH growth.

The Lyman-α line: A beacon into the CGM of high-redshift quasars

The Lyα line is the strongest (resonant) line from neutral hydrogen produced when an electron decays from the first excited state to the ground state, it is emitted in the UV with a wavelength of $\lambda = 1215.67$ Å. Additionally, due to the abundance of hydrogen, the Lyα line is ubiquitous across astronomical objects and is one of the most powerful probes of the high-redshift universe. The optical depth of the Lyα line is defined in (Draine, 2011) as:

$$\tau_0(\text{Ly}\alpha) = 8.02 \times 10^4 \left(\frac{15 \, \text{km s}^{-1}}{b} \right) \tau(\text{Ly cont}), \tag{1.4}$$

where $\tau(\text{Ly cont}) = 6.3 \times 10^{-18} \, \text{cm}^2 N(\text{H})$ is the optical depth of hydrogen to ionizing radiation, b is the line broadening due to the Doppler effect and $N(\text{H})$ is the number density of hydrogen atoms. If the medium is optically thick to ionizing radiation ($\tau(\text{Ly cont}) > 1$, i.e., fully neutral), then the optical depth of Lyα is much larger ($\sim 10^4$). For this reason, in most cases Lyα photons will easily be scattered many times when encountering neutral hydrogen atoms. When Lyα photons are absorbed and re-emitted by hydrogen atoms they are also diffused in frequency, which decreases their optical depth in the medium until they eventually can escape. Consequently, the Lyα line profile contains valuable information of the distribution and kinematics of the gas, however its interpretation requires careful modeling of the scattering process using radiative transfer simulations.

Specifically, quasars have been targeted for their Lyα emission out to large redshifts (e.g., Fan et al., 2004; Richards et al., 2006; Shen et al., 2020). Their bright rest-frame UV emission can be detected by optical telescopes at redshifts $z > 2$, which is characterized by broad emission lines from their BLR. The most prominent lines in the UV spectra of quasars are the Lyα line and C IV which show linewidths of ~ 1000 km/s.

As discussed in Section 1.2, the radiation produced by an AGN can illuminate the surrounding mass distribution. At $z \sim 3$ this material is expected to be cool $T \sim 10^4$ K infalling gas extending out to 100 kpc, which should radiate Lyα emission as it sets into the gravitational potential of the halo due to collisional excitation (Haiman et al., 2000). Additionally, if the material is being illuminated by the quasar it will also produce low surface brightness (SB $\sim 10^{-18} \, \text{erg s}^{-1} \, \text{cm}^{-2} \, \text{arcsec}^{-2}$) Ly$\alpha$ emission due to photoionization followed by recombination (Haiman and Rees, 2001b).

Particularly, Hennawi and Prochaska (2013) proposed an analytical estimate of the Lyα SB expected in the CGM from photoionization due to the quasar radiation, where

the $T \sim 10^4 \, \mathrm{K}$ gas consists of spherically uniform clouds that are smoothly distributed throughout the halo. In this framework, they discuss two limiting cases: one where the clouds are optically thin $N_{\mathrm{H\,I}} \ll 10^{17.2} \, \mathrm{cm}^{-3}$ and another where the clouds are optically thick $N_{\mathrm{H\,I}} \gg 10^{17.2} \, \mathrm{cm}^{-3}$ to ionizing radiation. For the optically thin case, the gas is expected to be highly ionized and emits via recombination regardless of the strength of the ionizing source, producing Lyα emission that only depends on the clouds density and distribution:

$$\mathrm{SB}_{\mathrm{Ly}\alpha}^{\mathrm{thin}} = \left(\frac{1+z}{3.0}\right)^{-4} \left(\frac{f_{\mathrm{C}}}{1.0}\right) \left(\frac{n_{\mathrm{H}}}{0.1 \, \mathrm{cm}^{-3}}\right) \left(\frac{N_{\mathrm{H}}}{10^{20} \, \mathrm{cm}^{-2}}\right)$$
$$\times \, 7.7 \times 10^{-19} \, \mathrm{erg \, s^{-1} \, cm^{-2} \, arcsec^{-2}}, \tag{1.5}$$

where f_{C} is the covering factor[5], n_{H} is the gas volume density and N_{H} the gas column density (obtained from absorption studies, e.g., Hennawi and Prochaska 2007).

For the optically thick case, the clouds will be shielded from the radiation and only their surface will emit Lyα proportionally to the quasar ionizing radiation and decrease with distance from the quasar:

$$\mathrm{SB}_{\mathrm{Ly}\alpha}^{\mathrm{thick}} = \left(\frac{1+z}{3.0}\right)^{-4} \left(\frac{f_{\mathrm{C}}}{1.0}\right) \left(\frac{R}{100 \, \mathrm{kpc}}\right)^{-2} \left(\frac{L_{\nu_{\mathrm{LL}}}}{10^{30} \, \mathrm{erg \, s^{-1} \, Hz^{-1}}}\right)$$
$$\times \, 6.0 \times 10^{-17} \, \mathrm{erg \, s^{-1} \, cm^{-2} \, arcsec^{-2}}, \tag{1.6}$$

where R is the radius of the halo and $L_{\nu_{\mathrm{LL}}}$ is the ionizing luminosity of the quasar[6].

The extended Lyα emission from the CGM of quasars was was first detected around $z \geq 2$ quasars using deep narrow-band imaging and appeared faint and diffuse, consistent with the photoionization scenario (Hu and Cowie, 1987a; Heckman et al., 1991b), longslit spectra of the same systems revealed broad Lyα linewidths ($\sigma \geq 600 \, \mathrm{km/s}$; Heckman et al. 1991a. The authors suggested that these linewdiths could be due to gravitational infall or outflowing material due to the AGN. These observations confirmed the presence of $T \sim 10^4 \, \mathrm{K}$ gas reservoirs extending out to $\sim 100 \, \mathrm{kpc}$ and revealed asymmetric morphologies. Using deep narrow band imaging techniques, the discovery of additional $z \sim 3 \sim 80 \, \mathrm{kpc}$ Lyα nebulae expanded these observations (Smith et al., 2009) and indicated that the AGN radiation was enough to ionize the halo. With similar technique, Arrigoni Battaia et al. (2016) discovered $\sim 50 \, \mathrm{kpc}$ Lyα nebulae around $z \sim 2$ quasars consistent with the photoionization scenario if the gas density is $\sim 0.6 \times 10^2 \, \mathrm{cm}^{-3}$ (see Equation 1.5). However, Hayes et al. (2011) and Kim et al. (2020) reported the detection of polarized extended Lyα emission, challenging the assumption of photoionization and revealing a component from resonant scattering of Lyα photons. Some works revealed extreme objects extending out

---

[5]In the assumption of spherical uniform clouds from Hennawi and Prochaska (2013), the covering factor is given by $f_{\mathrm{C}} = n_{\mathrm{c}} \sigma_{\mathrm{c}} 4R/3$, where n_{c} is the number density of clouds, σ_{c} is the cloud cross-sectional area and R is the radius of the halo. Essentially this value represents the average fraction of the sky covered by clouds within the halo in our line of sight.

[6]This parameter is computed from the scale factor at the Lyman limit frequency ($\nu_{\mathrm{LL}} = c/912 \, \text{Å} = 3.3 \times 10^{15} \, \mathrm{Hz}$) of a power law fit of the form $L_{\nu} = L_{\nu_{\mathrm{LL}}} (\nu/\nu_{\mathrm{LL}})^{-\alpha}$ to the quasar spectrum.
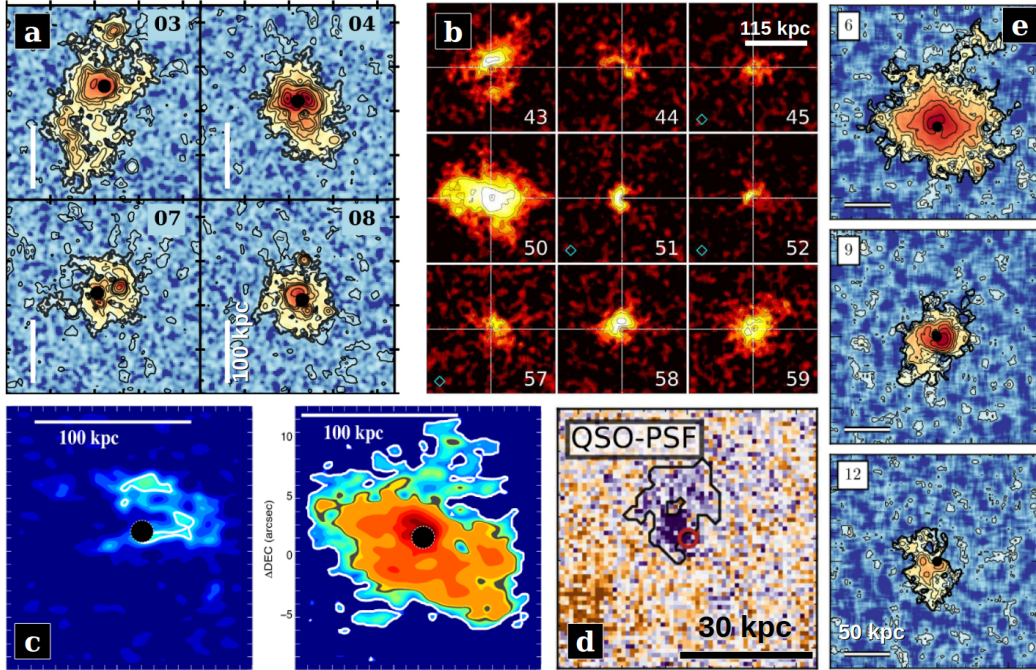
Figure 1.5: Collection of Lyα nebulae around $2 < z < 6$ quasars observed with integral field spectrographs. Each panel shows Lyα SB maps from different studies with a scale bar in physical sizes. *(a)* $z \sim 3.5$ quasars observed with MUSE from Borisova et al. (2016), thick contours indicate levels of $\sim 10^{-18}\,\mathrm{erg\,s^{-1}\,cm^{-2}\,arcsec^{-2}}$. *(b)* $z \sim 3$ quasars observed with MUSE from Arrigoni Battaia et al. (2019a), the lowest contours indicates levels of $\sim 4 \times 10^{-18}\,\mathrm{erg\,s^{-1}\,cm^{-2}\,arcsec^{-2}}$. *(c)* $z \sim 2$ quasars observed with KCWI from Cai et al. (2019), white contours indicate levels of $\sim 10^{-18}\,\mathrm{erg\,s^{-1}\,cm^{-2}\,arcsec^{-2}}$. *(d)* $z \sim 6.2$ quasar observed with MUSE from Farina et al. (2019), the dark contour indicates a level of $\sim 10^{-18}\,\mathrm{erg\,s^{-1}\,cm^{-2}\,arcsec^{-2}}$. *(e)* $z \sim 3.15$ quasars observed with MUSE from Mackenzie et al. (2021b), the lowest contour indicate levels of $\sim 10^{-18}\,\mathrm{erg\,s^{-1}\,cm^{-2}\,arcsec^{-2}}$.

to $\sim$500 kpc associated with multiple active galaxies (Cantalupo et al., 2014; Hennawi et al., 2015). Certainly, studying the origin of the low surface brightness emission from the CGM was challenging due to the high sensitivities required and the lack of precise systemic redshifts necessary to image them with narrow-bands.

Meanwhile, cosmological simulations were carried out to predict the Lyα signal expected from gravitational cooling and photoionization during structure formation (Furlanetto et al., 2005; Dijkstra et al., 2006; Dijkstra and Loeb, 2009; Faucher-Giguère et al., 2010; Rosdahl and Blaizot, 2012b), which suggested that each mechanism is plausible in producing such emission. Some of these simulations included the radiative transfer effects that undergo the Lyα photons (Hansen and Oh, 2006; Gronke et al., 2015), pointing at how the line profiles are affected by the gas distribution and kinematics.

Recently, the development of sensitive optical integral field spectrographs (IFS) such

as the Potsdam Multi Aperture Spectrophotometer (Roth et al., 2005) at the Calar Alto Observatory, the Keck Cosmic Web Imager (KCWI; Morrissey et al. 2018) at the Keck observatory and the Multi Unit Spectroscopic Explorer (MUSE; Bacon et al. 2010) at the Very Large Telescope (VLT) revolutionized this search. Such instruments combine the power of imaging with spectroscopy and can reach sensitivities of SB $\sim 10^{-18}\,\mathrm{erg\,s^{-1}\,cm^{-2}\,arcsec^{-2}}$, which allowed to reveal extended Lyα emission around $z > 2$ quasars without the need for accurate systemic redshifts. Indeed, the detection of extended Lyα emission around $2 < z < 6$ quasars is now routinely reported (Christensen et al., 2006; Borisova et al., 2016; Arrigoni Battaia et al., 2018, 2019a,b; Drake et al., 2019; Farina et al., 2019; Cai et al., 2019; O'Sullivan et al., 2020; Drake et al., 2020; Mackenzie et al., 2021b; Fossati et al., 2021; Lau et al., 2022; González Lobos et al., 2023; Hall and Fu, 2024; Herwig et al., 2024). These works (see Figure 1.5) highlighted that extended Lyα nebulae are common around high-z quasars with a broad range in morphologies (sizes of $\sim 20 - 100\,\mathrm{kpc}$) and opened up the discussion of the different powering mechanisms. For example, Christensen et al. (2006) found that the Lyα nebulae were asymmetric and their luminosity was correlated to the Lyα luminosity of the quasar. Later, Arrigoni Battaia et al. (2019a) presented a large MUSE survey of 61 bright ($-29 < M_\mathrm{i}(z = 2) < -27$) quasars at $z \sim 3$ and found a similar correlation with their luminosities, in addition to quiescent kinematics indicative of gravitational motions. Further, Mackenzie et al. (2021b) characterized the nebulae around 12 fainter ($-27 < M_\mathrm{i}(z = 2) < -24$) quasars at similar redshift and found that their nebulae also appear dimmer and more compact. These studies suggested that, in addition to photoionization followed by recombination, resonant scattering of the Lyα photons from the BLR could be an important powering mechanism. Additionally, some works focused on the kinematics of the Lyα nebulae and revealed that these show relatively quiescent velocity dispersions ($\sigma \sim 300 - 400\,\mathrm{km/s}$) consistent with gravitational motions in $M_\mathrm{halo} \sim 10^{12}\,\mathrm{M_\odot}$ halos (Arrigoni Battaia et al., 2018; O'Sullivan et al., 2020). At the most extreme redshifts available, Farina et al. (2019) discovered with MUSE 12 Lyα nebulae around $z \sim 6$ quasars extending out to $30\,\mathrm{kpc}$ from the quasars which, when accounting for cosmological dimming and comoving distances, were completely consistent with the Lyα SB of nebulae found around $z \sim 3$ quasars discussed above. On the other hand, Cai et al. (2019) presented KCWI observations of 14 Lyα nebulae around $z \sim 2$ quasars, which displayed irregular morphologies and sizes between 50-100 kpc. Importantly, these nebulae were fainter than their higher-redshift counterparts, for which the authors suggested that this is a result of a lower covering factor of the emission. Regarding this, Arrigoni Battaia et al. (2019a) explored the redshift evolution between $z = 2$ and $z = 3$ quasar nebulae and concluded that this drop in emission could be linked to a variation in the neutral gas content, which could be a consequence of the gas being shock heated as the halo reaches a mass of $M_\mathrm{halo} \sim 10^{12.5}\,\mathrm{M_\odot}$ as proposed in Dekel and Birnboim (2006).

From an observational point of view it is not clear which are the main drivers of the extended Lyα emission, however the studies mentioned above hint that photoionization followed by recombination and resonant scattering of Lyα photons could be responsible for the observed emission. Additionally, it is possible that AGN outflows can shock material around producing line emission due to collisional excitation and photoionization, these are

usually associated with ionized material displaying violent kinematics (see e.g., Taniguchi and Shioya, 2000; Vidal-García et al., 2021).

In this context, recent work by Costa et al. (2022) presented cosmological simulations of a $z = 6$ quasar host halo post-processed with Lyα radiative transfer in order to reproduce the extended Lyα emission observed in Farina et al. (2019). These simulations included the effect of collisional excitation, recombination, scattering of Lyα photons from the BLR and quasar outflows. The authors found that a combination of photoionization and collisional excitation was able to agree with observations, however they also found that scattering of Lyα photons from the BLR of the quasar alone was enough to produce consistent ~ 100 kpc nebula. Importantly, they found that outflows were necessary to eject gas in order to allow the Lyα emission to escape and produce extended nebulae. Additionally, Obreja et al. (2024) studied the impact that AGN radiation has on the gas distribution in a $z = 3$ quasar host halo as a function of the opening angle of the ionization cones of the AGN. They found that photoionization from the AGN decreases the amount of gas in the cooling phase by half if the opening angle is $\sim 60°$, highlighting the importance of feedback in regulating the cool gas content. Additionally, these opening angles were able to reproduce the levels of the nebulae Lyα SB observed around $z \sim 3$ quasars. In summary, these simulations are capable of taking into account the impact of feedback of the AGN on CGM scales and require observational constraints on the models implemented, such as the relationship between observed nebulae properties with AGN properties.

The CGM of quasars in additional line emissions

The interpretation of the observed Lyα emission around quasars is complex due to radiative transfer effects and the lack of constraints on the balance between powering mechanisms. One way to help achieve this is through detection of additional line emission such as He II and C IV, which are available at $z \sim 3$ with the same instruments used to detect Lyα nebulae. He II ($\lambda 1640$) occurs primarily by photoionization followed by recombination and it is not resonant, therefore can hint to the strength and extent of quasar radiation. For this, direct comparison of Lyα with He II can constrain the contribution from photoionization followed by recombination. C IV ($\lambda 1548$) is a tracer of the metal enriched region of the CGM of quasars usually associated with outflowing material, this line is also scattered therefore could be more easily detected if the gas is enriched. However, those transitions are much fainter due to their sensitivity to metallicity and higher ionization state required.

These lines were first tentatively detected in longslit spectra around two $z \sim 2 - 3$ quasars with radio jets by Heckman et al. (1991a), however deeper observations were needed to discriminate between powering mechanisms. Arrigoni Battaia et al. (2015b) and Arrigoni Battaia et al. (2015a) conducted a deep narrow-band and spectroscopic search of these lines in already detected Lyα nebulae without successful results, implying dense ($n_{\rm H} \geq 3$) gas reservoirs. The unprecedented SB achievable with MUSE allowed the detection of a ~ 100 kpc He II nebulae associated to a 450 kpc Lyα nebulae at $z = 2.3$ (Cantalupo et al., 2019). The He II was detected in a region associated to a continuum source where gas densities could be enhanced, suggesting a clumpy gas distribution. Moreover, Travascio
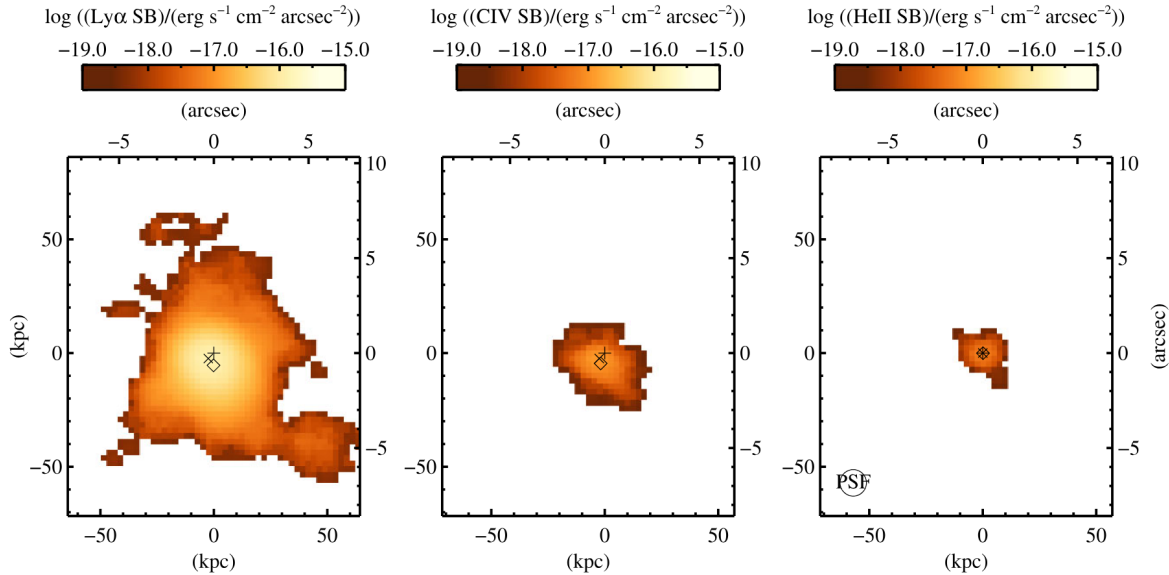
Figure 1.6: KCWI observations of an extremely red quasar at $z = 2.32$ with extended Lyα, C IV and He II emission shown in the left, middle and right panels, respectively. In each panel a plus symbols marks the position of the quasar, a cross symbol indicates the peak of the emission and the diamond symbol represents the centroid of each nebulae. The right panel shows the full width at half maximum of the empirical point spread function of the quasar. Figure obtained from Lau et al. (2022).

et al. (2020) reported the detection at $z = 3.5$ of a 75 kpc C IV nebulae associated to a ~ 100 kpc Lyα nebula, revealing metal enriched gas likely associated to an outflow. These authors found that the C IV emission is associated to the region with brightest Lyα emission and measured a high Lyα velocity dispersion ($\sigma \simeq 700$ km/s), which is consistent with the velocity dispersions found in other systems with outflows.

Further, (Guo et al., 2020) reported both He II and C IV simultaneously around four $z \sim 3$ quasars with already identified Lyα nebula, which showed much more compact emission. Additionally, they stacked 80 previous MUSE observations of quasar with detected Lyα nebulae and resulted in the detection of additional C III] ($\lambda 1909$), indicating CGM metallicities between $0.5 - 1 \, \mathrm{Z}_\odot$. Additionally, their stacking also revealed that the velocity dispersions of the lines increased towards the center of the nebulae, suggesting regions tracing quasar outflows. Moreover, Fossati et al. (2021) conducted a deep MUSE search of 27 $z = 3 - 4.5$ quasars with extended Lyα nebulae and detected C IV and marginally He II emission out to ~ 40 kpc through stacking analysis, consistent with metal enriched gas and a clumpy gas distribution. Finally, Lau et al. (2022) presented KCWI observations of a $z = 2.3$ extremely red quasar (Figure 1.6), which are thought to be dusty and in the early phases of AGN feedback, which showed a ~ 100 kpc Lyα nebulae and associated He II and C IV emission extending out to 33 and 47 kpc, respectively. The authors studied

the kinematics of the Lyα and C IV and proposed that the inner halo is dominated by an outflow.

In summary, these observations showed that the CGM of $z \sim 3$ quasars is enriched with metals and highlighted the need for detection of additional line emission in order to disentangle the physical properties of quasar's CGM. Also, they emphasize the importance of quasar outflows and radiation in producing extended nebulae around $z \sim 3$ quasars.

1.4   Goals and structure of this thesis

This thesis contains the work I have carried out during my PhD, which undertakes an investigation into the role of the CGM in the formation of massive galaxies within the cosmological framework discussed in this chapter. I explored the physical properties and emission mechanisms of the cool $T \sim 10^4 \, \mathrm{K}$ phase of the CGM of high-redshift quasars with the aim to link them to the quasar and host galaxy properties. For this, I used a large sample adding to 123 quasars observed with MUSE at redshift $z \sim 3 - 4.7$ and compared the observed properties of their nebulae such as SB, luminosity and kinematics with quasar properties such as Lyα luminosity, bolometric luminosity, black hole mass, host galaxy dust mass and star formation rates. This thesis contains the work published in González Lobos et al. (2023) and another in preparation.

The structure of this thesis is as follows:

Chapter 2 presents a Python analysis tool that I developed to reveal extended line emission around quasars in MUSE datacubes, including detailed description of the algorithm and how to use it. These Python routines have been used throughout the thesis and in the work presented in Herwig et al. (2024), therefore I aim to make the tool publicly available and provide in this thesis a first documentation.

Chapter 3 presents a pilot study of the CGM around five submillimeter-bright galaxies at $z \sim 3 - 4$ with different quasar contribution and similar halo mass. I detected Lyα nebulae around the systems with quasar and no emission around the systems without AGN contribution. This study concluded that gravitational cooling is likely not a dominant powering mechanism for quasar Lyα nebulae.

Chapter 4 presents a large search of Lyα nebulae around 120 quasars, expanding the work presented in Arrigoni Battaia et al. (2019a) to fainter systems at $z \sim 3$. This survey contains a statistical value that is used to study relationships between the extended emission and quasar properties.

In Chapter 5 I present a summary of the main results of this thesis and discuss the future prospects of my future research.

Chapter 2

Revealing extended circumgalactic emission around quasars: Python code and analysis tools

The study carried out in this thesis focuses on revealing the faint circumgalactic (CGM) line emission around high-redshift ($z \sim 3$) quasars using integral field spectroscopic (IFS) observations (see Chapter 1). To do this I designed a Python code that can reveal this emission using observations carried out with the Multi Unit Spectroscopic Explorer (MUSE; Bacon et al., 2010) at the Very Large Telescope (VLT). This chapter is dedicated to describe the design and usage of the pipeline and it is organized as follows: Section 2.1 introduces the project along with some technical aspects of optical IFS observations and MUSE, Section 2.2 lists the instructions to run the pipeline, Section 2.3 contains a detailed description of the steps of the code and Section 2.4 contains the3, 54, 55 conclusions of this project. The code is available by request in my Github repository: @JaysonAstro and I intend to release it publicly in the future.

2.1 Introduction

2.1.1 How can we observe the emission from the CGM of quasars?

The introduction of modern IFS and their unprecedented surface brightness (SB) limits ($\sim 10^{-18}\,\mathrm{erg\,s^{-1}\,cm^{-2}\,arcsec^{-2}}$) achievable in reasonable observation time (1 hour), such as MUSE at VLT, have been revolutionary in the study of the CGM in emission, leading to routinely reporting faint extended Lyα emission around $2 < z < 6$ quasars (e.g. Borisova et al., 2016; Farina et al., 2019; Arrigoni Battaia et al., 2019a; Mackenzie et al., 2021a; Fossati et al., 2021).

Quasars are one of the most luminous objects in the universe and with their unresolved emission outshine the faint CGM emission we search. Therefore, in order to detect any extended line emission below the quasar spectra we need to remove the quasar's point

spread function (PSF; Møller, 2000). The method of subtracting the quasar's PSF has been extensively tested and described in past works and, in particular, I used the method described in Borisova et al. (2016) and Mackenzie et al. (2021a) as a guideline for developing Python routines that are able to reveal CGM emission around $z \sim 3$ quasars using MUSE observations. These two works used the same technique to extract the quasar nebulae (CubExtractor; Cantalupo et al. in prep.), however they used different parameters (e.g., PSF subtraction radius, PSF width) suited to the different quasar luminosities in their samples. The Python tool I developed considers this case, therefore these parameters can also be adapted to each observation. Finally, the tool I present in this chapter has already been used for the analysis of ~ 100 hours of MUSE observations including the projects presented in Chapters 3 and 4, in addition to the work presented in Herwig et al. (2024).

In summary the method presented in Borisova et al. (2016) and Mackenzie et al. (2021b) consists of building a wavelength dependent empirical model of the quasar's PSF, which is constructed at the quasar location by computing a pseudo narrow-band (NB) at each wavelength and excluding wavelength ranges where the line emission of interest is located. The pseudo-NBs are normalised to the quasar's central flux and then subtracted from the datacube at the quasar location inside a circular aperture of radius proportional to the seeing of the observation. Then, continuum sources are removed from the datacube producing a cube with only extended line emission present. The limitations of this method, as described in Borisova et al. (2016), include that an artifact is introduced at the region of normalization and that it cannot deal with continuum sources blended to the quasar PSF.

2.1.2 Angular resolution and astronomical seeing

When using a telescope to observe a point-like source, such as a distant star or quasar, the image produced is distorted due to the diffraction pattern caused by the aperture used. In the case of an optical telescope this aperture corresponds to the mirror, and for a circular aperture the diffraction pattern can be described with an Airy distribution (Figure 2.1, left panel). The size of brightest region in the Airy pattern defines the (diffraction-limited) angular resolution of the telescope and it is wavelength dependent.

The angular resolution for a circular aperture is defined as:

$$\sin \theta \approx 1.22 \frac{\lambda}{D}$$
$$\theta \approx 1.22 \frac{\lambda}{D} \; ; \; \text{when } \theta \ll 1, \tag{2.1}$$

where θ is the angular resolution in radians, λ is the observed wavelength and D is the diameter of the aperture. The angular resolution from diffraction is, theoretically, the smallest spatial size that can be resolved in an observation, i.e., observing two point sources separated in the sky by a projected distance smaller than the angular resolution are indistinguishable and appear as one.
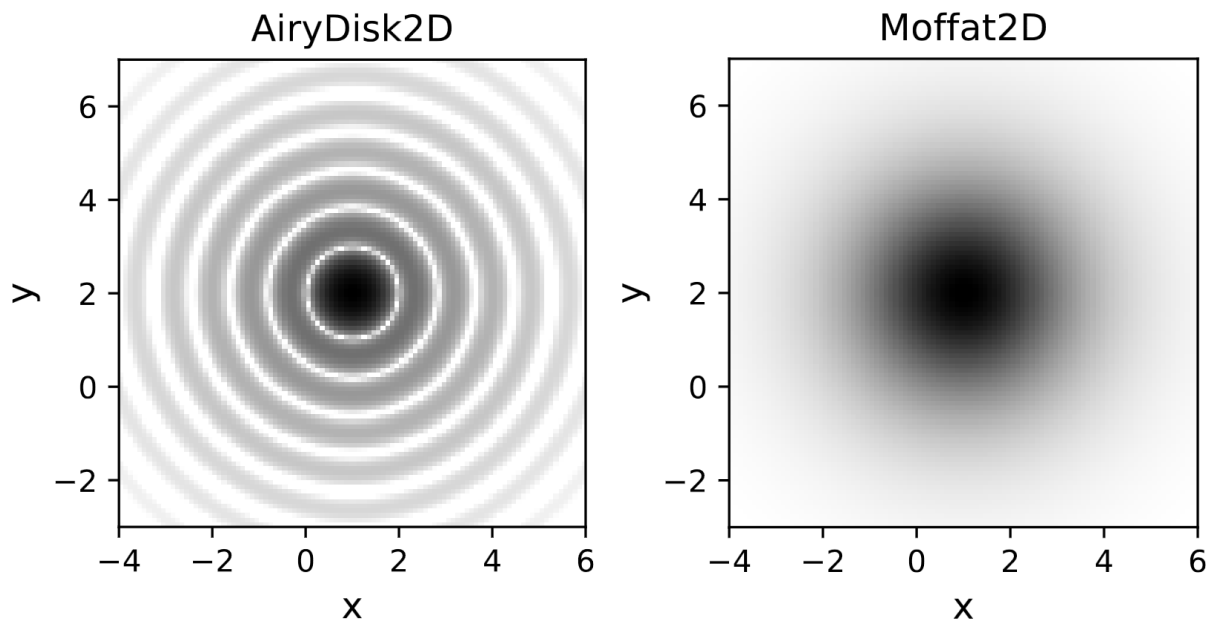
Figure 2.1: Example of 2D Airy and Moffat patterns. *Left:* Image of a 2D model of an Airy diffraction pattern in arbitrary units which results from observing a point source through a circular aperture, *Right:* Image of a 2D model of a Moffat distribution. Adapted from `https://docs.astropy.org/en/stable/modeling/predef_models2D.html`.

In most applicable cases, the light reaching the mirror of a ground-based telescope has to first travel through the Earth's atmosphere, which distorts the image due to turbulence resulting in both blurring and variations in the observed brightness. This effect is called astronomical seeing and degrades the theoretical resolution from diffraction alone. The seeing can vary quickly over time, depends on the observed wavelength and changes when pointing at different locations of the sky. To measure the seeing of an observation, one must measure the angular size of an observed point-source by computing the full width at half maximum (FWHM) of the resulting image.

The combined effect between the diffraction pattern and the atmospheric seeing can be characterized by the PSF and it is used as a measurement of the image quality. The image formed in an instrument when observing an object of any shape is the convolution between the shape and the PSF. For ground-based telescopes the PSF is dominated by the seeing and can be described with a 2D Moffat distribution (Figure 2.1, right panel) of the form:

$$f(x, y) = A \left(1 + \frac{(x - x_0)^2 + (y - y_0)^2}{\gamma^2} \right)^{-\beta}, \qquad (2.2)$$

where A is the amplitude, x_0 and y_0 are the centroid coordinates, γ is the core width and β the power. The FWHM of the Moffat model is the representation of the seeing of the

observation, measured in in angular units, and is given by:

$$\text{FWHM}_{\text{Moffat}} = 2\gamma\sqrt{2^{1/\beta} - 1}. \qquad (2.3)$$

2.1.3   Overview of the MUSE instrument and datacubes

The MUSE instrument (Bacon et al., 2010) is an integral field spectrograph at the VLT that operates in the optical wavelength range of 4650-9300 Å with a spectral resolution ($R = \lambda/\Delta\lambda$) of $R = 2000$ and 4000 at 4600 Å and 9300 Å, respectively. MUSE can benefit from improved spatial resolution compared to other ground-based optical telescopes due to the adaptive optics capabilities of the VLT, which is able to move the secondary mirror in order to correct atmospheric distortions caused by turbulence in real time. Such an instrument is then capable of combining spectroscopy with high-resolution imaging in a 1×1 arcmin^2 field of view (see Table 2.1.3). Additionally, the unprecedented flux limit reached by MUSE (Table 2.1.3) has allowed the study of objects that were too faint to be seen with typical optical imaging instruments. The combination of these characteristics allow us to observe, for example, high redshift extended objects with low surface brightness (see e.g., Wisotzki et al., 2016; Umehata et al., 2019; Bacon et al., 2021; Tornotti et al., 2024). MUSE has two observing modes with different field of view and spatial resolution, the specifications are summarized in Table 2.1.3.

	Wide Field mode (WFM)	Narrow Field Mode (NFW)
Field of view	1×1 arcmin^2	7.5×7.5 arcsec^2
Pixel scale	0.2 arcsec	0.025 arcsec
Spatial resolution	0.3-0.4 arcsec	0.03-0.05 arcsec
Flux limit	3.9×10^{-19} cgs (in 80 hrs)	2.3×10^{-18} cgs (in 1 hr)

Table 2.1: Summary of MUSE capabilities. Adapted from `https://www.eso.org/sci/facilities/develop/instruments/muse.html`

The process of creating datasets from IFS observations is illustrated in Figure 2.2. For the case of MUSE, the instrument splits each field of view into 24 channels that are subsequently divided into 48 slices by integral field units (IFU). The slices corresponding to each channel are sent to the spectrograph which disperses each slice and produces a set of spectra that are then imaged onto a 4K×4K detector. The data from all 48 IFUs is processed using the MUSE data reduction pipeline (Weilbacher et al., 2020) to produce datacubes. Chapters 3 and 4 contain descriptions of the steps performed to reduce raw MUSE data into datacubes using this pipeline.

MUSE datacubes consist of three dimensional (two spatial and one spectral) Flexible Image Transport System (FITS) cubes which contain science (`DATA`) and variance (`STAT`) extensions. When referring to MUSE cubes, I will use the following definitions:
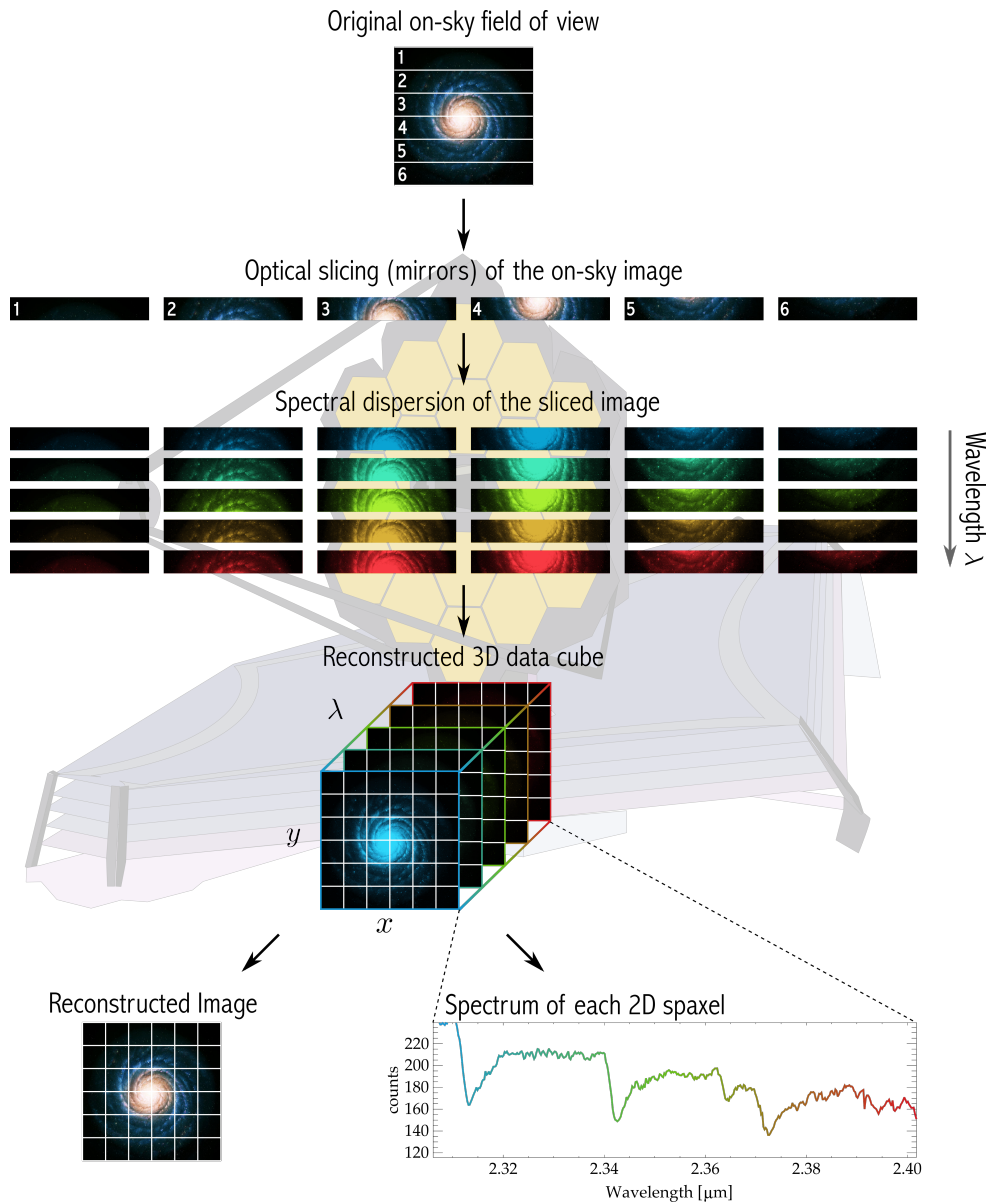
Figure 2.2: Schematic of the resulting datacube from an integral field spectroscopic observation using the Near-Infrared Spectrograph (NIRSpec; Jakobsen et al., 2022; Böker et al., 2022) on the James Webb Space Telescope. The NIRSpec instrument concept is similar to MUSE, but operates at near-infrared wavelengths and a field of view smaller than MUSE ($3'' \times 3''$). The top row shows how the field of view is sliced into channels. The second row shows how the channels are separated into slices. The third row shows the channels as are dispersed by the spectrograph and recorded by the detector. The fourth row shows how the data from the detector can reconstructed as a datacube. The sixth row shows the resulting white image from collapsing the cube at all wavelengths (left) and a spectrum extracted from one spaxel of the cube (right). Image credit: `https://jwst-docs.stsci.edu/methods-and-roadmaps/jwst-integral-field-spectroscopy`.

- **Datacube:** This is a cube which contains science data (`DATA` extension). It has two spatial axes representing sky coordinates in units of degrees, each spatial axis has 380 elements and a scale of 0.2" (5.5×10^{-5} degrees). Additionally, the MUSE datacube contains one spectral axis in units of Angstrom and a total of 3681 elements with scale of 1.25 Å. The data values at each coordinate have flux density units of $10^{-20}\,\mathrm{erg\,cm^{-2}\,s^{-1}\,\mathring{A}^{-1}}$.

- **Variance cube**: A cube containing the associated variance of a datacube (`STAT` extension), with the same axes and dimensions. The units are $10^{-40}\,\mathrm{erg^2\,cm^{-4}\,s^{-2}\,\mathring{A}^{-2}}$.

- **Channel:** Refers to one element of the spectral axis. One spectral channel has a width of 1.25 Å.

- **Voxel:** This is the equivalent of a three-dimensional pixel (or volume pixel), it contains one value of the flux density at a 3D coordinate in the cube.

- **Spaxel:** Corresponds to a column in the cube at a 2D coordinate. Usually this position is chosen as spatial, for which case the column contains the spectral energy distribution at this location.

- **Slice:** Corresponds to a subset of the cube that is obtained using a fixed range of a selected axis, usually chosen as the spectral axis. If the slice is extracted using one spectral channel, then it will contain a 2D image and I will refer to it as layer. The slice can also be extracted using multiple channels, which can also be referred to as a slab.

2.2 Using the pipeline

In this Section I describe the instructions to use the analysis pipeline I developed, after the used has reduced the raw dataset using the MUSE pipeline. This analysis pipeline is designed to combine individual reduced MUSE exposures of quasars and remove the PSF of the quasar together with continuum sources. Figure 2.3 shows a flowchart of the steps performed by the pipeline, which are described in the following sections after an overview of the scripts and requirements.

2.2.1 Overview of the scripts and requirements

The pipeline is separated into two main steps: (i) alignment and combination of single exposures done by the `mask-align-combine.py` script and (ii) subtraction of the quasar's PSF and continuum sources done by the `psf-sub.py` (see Section 2.2 for instructions on how to use the scripts). The code has been optimized to extract faint emission around single quasars in the field, but has been modified in Herwig et al. (2024) for quasar pairs. The following scripts were written by my and contain the different steps of the pipeline:
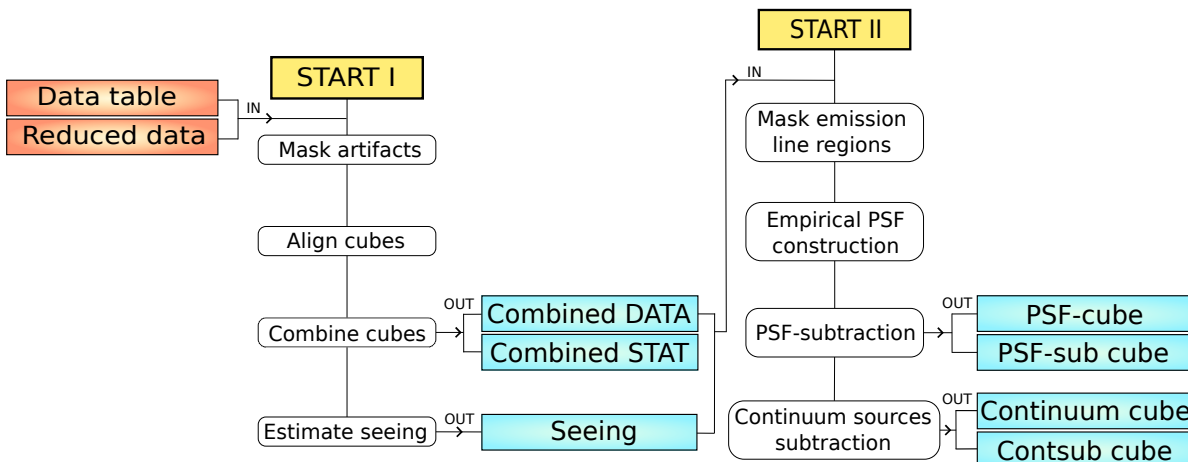
Figure 2.3: Flowchart of the pipeline steps and products. The first segment of the pipeline begins at START I and takes as inputs the (user defined) data table and reduced data (see Section 2.2.2). In this segment the pipeline masks artifacts, aligns exposures, combines datacubes and estimates the seeing as a function of wavelength of the observation (blue). The second segment of the pipeline begins at START II, which uses as input the the products from the previous segment. This step produces a PSF-cube, a PSF-subtracted cube, a continuum cube and continuum-subtracted cube (blue).

- `MUSE-Lya.py`: This is a module that contains functions for alignment, estimation of the seeing as a function of wavelength, combination of data and variance cubes, estimation of the surface brightness (SB) limit and masking circular apertures in a given cube.

- `new-reduceQSOMUSEUM.py`: This is a module that contains generic masks used to remove artifacts when combining single exposures due to the separation of the MUSE IFUs.

- `mask-align-combine.py`: This script uses single reduced exposures of the same field of view and combines them into a final data and variance cube. It first masks artifacts using a white image of the datacube, then aligns each exposure and finally combines using the median. This step has a large memory usage because it needs to load each datacube ($\sim 2\,\mathrm{GB}$) that will be combined at the same time.

- `psf-sub.py`: This script is used to build and subtract the wavelength dependent quasar PSF. Finally, continuum sources are removed and only extended line emission remains in the datacube, if detectable.

The scripts have been tested in Python version 3.6.8 and the following packages are required to be installed in order to use it:

- `NumPy 1.16.3`: Handling and arithmetic of multidimensional arrays (Harris et al., 2020).

- `Astropy 4.1`: Several classes and functions useful for manipulating astronomical datasets (Astropy Collaboration et al., 2013, 2018, 2022). The most used Astropy algorithms for this project are: handling of FITS files, world coordinate systems, implementation of physical units, model fitting, tables, cosmological calculations, convolution.

- `Matplotlib 3.1.3`: Library for data visualization and figure production (Hunter, 2007).

- `SciPy 1.2.1`: Mathematical algorithms for statistics, interpolation, integration (Virtanen et al., 2020).

- `spectral_cube 0.5.0`: Package created for the handling, visualization and manipulation of astronomical datacubes with two spatial and one spectral dimension (Ginsburg et al., 2015; Robitaille et al., 2016).

- `MUSE Python Data Analysis Framework (MPDAF) 3.4`: Tools specifically designed to handle MUSE datasets (Bacon et al., 2016; Piqueras et al., 2017).

- `Photutils 0.7.1`: A package developed for photometry of astronomical sources, source detection, centroid calculation and many other utilities (Bradley et al., 2024).

- `Astronomical Plotting Library in Python (APLpy) 1.1.1`: Package for graph production directly from astronomical data, handles coordinate systems and FITS file headers. This package is fully compatible with Matplotlib (Robitaille and Bressert, 2012).

- `Zurich Atmosphere Purge (ZAP) 2.1`: Tool for removing sky subtraction residuals of MUSE datacubes (Soto et al., 2016).

2.2.2   Data table with source list and directory hierarchy

Additionally to the required Python packages, it is required by the pipeline to create a datatable with the list of systems that will be analyzed, the location of the reduced MUSE data, and the sky coordinates of the quasar that will be subtracted. This table is read and updated as the pipeline performs the different steps. Finally, it is required that the raw data has been already reduced with the MUSE data reduction pipeline (see Weilbacher et al., 2020) and the sky residuals removed with ZAP (Section 2.2.1) before attempting to use this pipeline. Chapters 3 and 4 contain detailed descriptions of the process of data reduction of MUSE observations.

To use the code, an input datatable in `.csv` format is needed for reading the list of systems that will be analyzed. The location and filename of the table is specified inside

of the scripts as a global variable, but it can also be defined with the `--tab-path` option when running the scripts from the command line (Section 2.2). In my case, the global variable for the table filename is:

```
table_dir = '/afs/mpa/temp/valegl2/QSOMUSEUMfaint/'    # path to
  datatable
table_filename = 'data-table.csv'                      # table filename
```

The datatable must contain the path of the parent directory where the reduced individual exposures are located (this is also where the pipeline will automatically create the directories with the final products) and the sky coordinates of the quasar that will be removed. Additionally, columns with each step that the pipeline performs will be created and filled with "yes" in order to keep the progress organized when handling large datasets. An example of a row of the datatable for a system is written below:

```
ID    SOURCE                        DIR
----  ----------  ----------------------------------------
70    J0923+0011 /afs/mpa/temp/valegl3/QSOMUSEUMfaint/J0923


RA           DEC         SEEING   STAR-RA   STAR-DEC
-----------  -----------  -------  ---------  --------
09:23:00.29  +00:11:56.7  0.86       --         --
```

Where `ID` is the identification number of the system (arbitrary) and is used with `--ID` when using the scripts, `SOURCE` is the source name, `DIR` is the parent directory of the MUSE data for the system, `RA` and `DEC` are the coordinates of the quasar in hour angles and degrees, respectively, `SEEING` (see Section 2.3.4) is the angular resolution of the observation in units of arcseconds, `STAR-RA` and `STAR-DEC` are the coordinates of a reference field star that can be optionally used to align the cubes (this example table does not use them).

Finally, each system's individual reduced exposures need to be located in the user-created `/clean` directory inside the parent directory `DIR`, and each system has to have one separated directory. An example of how the files in the `/clean` directory are named for one source is shown in Figure 2.4. It is important that the filename begins with the same keyword as the corresponding `SOURCE` in the datatable. With these files ready, one can start using the pipeline.

2.2.3 Running the scripts

After making sure that all the requirements are fulfilled, the user can now use the pipeline. To run the pipeline, type the following commands in the terminal from the location of the scripts listed in Section 2.2.1:

```
$ python mask-align-combine.py --ID 1 --median-combine --DATA --show-
  plot --tab-path /path-to-table/data-table.csv
$ python mask-align-combine.py --ID 1 --STAT --tab-path /path-to-table/
  data-table.csv
```

```
(valu) valegl@pascal-3-06 /afs/mpa/temp/valegl3/QSOMUSEUMfaint/J0247/clean $ ls -tlsh
total 8.1G
2.7G -rw-r--r-- 1 valegl mpa 2.7G Aug 23  2021 J0247-0023.2_DATACUBE_ZAP.fits
2.7G -rw-r--r-- 1 valegl mpa 2.7G Aug 23  2021 J0247-0023.1_DATACUBE_ZAP.fits
2.7G -rw-r--r-- 1 valegl mpa 2.7G Aug 23  2021 J0247-0023.0_DATACUBE_ZAP.fits
```

Figure 2.4: Example of `/clean` directory where the pipeline looks for individual reduced MUSE exposures for one system. Each file is a cube previously reduced with the MUSE pipeline and sky subtraction performed with ZAP.

The first command will perform a median combine of the `DATA` extensions from the single exposures for `ID 1` of the provided datatable (see Section 2.2.2), the location of the datatable is specified with the option `--tab-path`, otherwise the code will read from the global variables written inside the script. The second line will combine the `STAT` extensions of the same MUSE observations. The command `--show-plot` will pause the pipeline to show figures with the results of aligning the cubes for the user's inspection (see Section 2.3.2).

Once the first step of the pipeline is complete, the user can run the PSF subtraction by typing in the terminal:

```
$ python psf-sub.py --ID 1 --tab-path /path-to-table/data-table.csv
```

The pipeline will create for this example the directories `/combined`, `/psf-sub` and `/contsub` inside the parent directory `DIR` of `ID 1`, which are listed in the datatable. Inside these directories files created during each step of the pipeline will be stored, the steps are described in Section 2.3.

2.3 Description of the code and pipeline steps

2.3.1 Masking of MUSE IFU artifacts

The first step performed by the pipeline is to remove artifacts in individual exposures due to the physical separation of the MUSE IFUs. These separations produce shadows and light leaks, which can be seen as stripes in the collapsed white image of the datacube (Figure 2.5). To remove these artifacts a simple mask is done for each exposure, taking advantage of the observational strategy that is usually done for MUSE observations. This strategy consists of rotating the field of view by 90° and adding a dithering of $< 5''$ between each exposure, which ensures that the pattern of artifacts in the sensor does not overlap when combining the single exposures.

The code uses `mask_fov_generic` within the `new-reduceQSOMUSEUM.py` module which contains a generic mask that is applied to each exposure, assuming the rotation and dithering patterns. Visual inspection is necessary to ensure that the mask is correctly placed on top of the artifacts, so the option `--show-plot` is set to `True` by default within the masking function. The function is by default designed to work with three exposures per system,
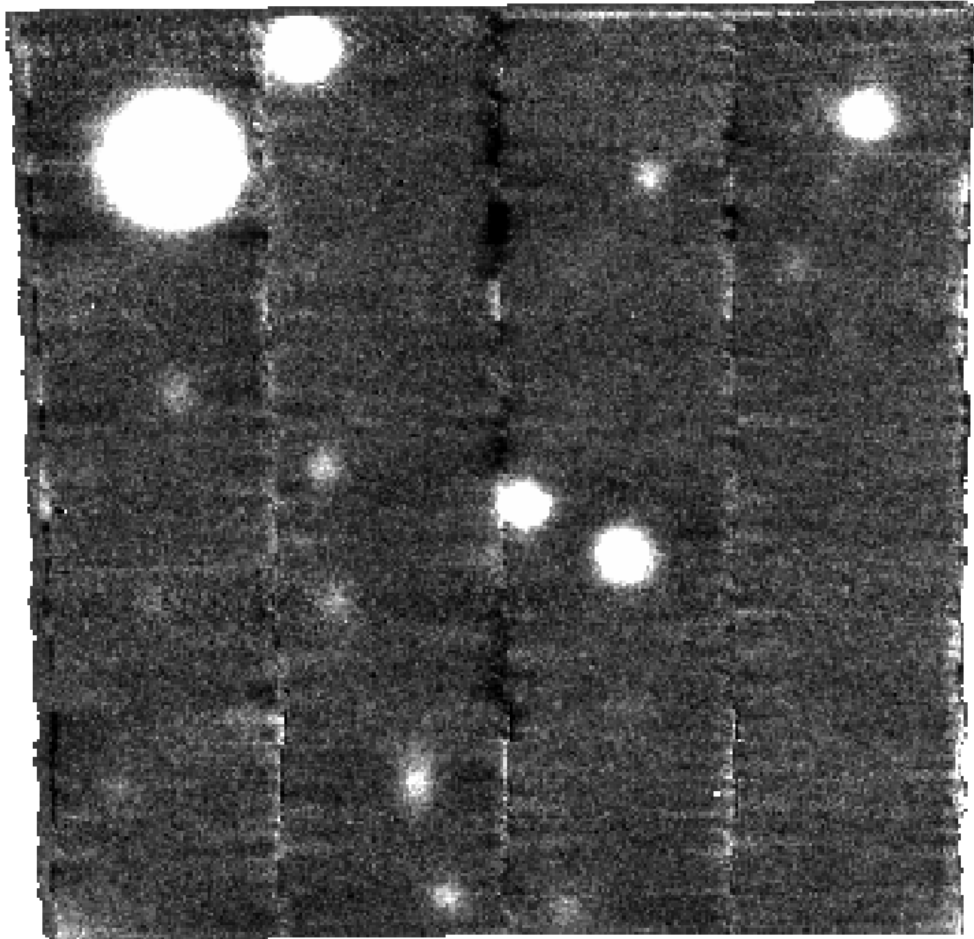
Figure 2.5: Example white image of a single field of view for a quasar observed with MUSE. The image shows the quasar located close to the center of the field, surrounded by other point sources and galaxies. Artifacts due to the separation of the IFUs are seen as stripes across the field. The white image is computed by collapsing (i.e., integrating) the datacube along its whole spectral axis.

however including masks for additional exposures (or dithering angles) is straightforward but needs to be done manually by the user.

2.3.2   Alignment of single exposures

Once the artifacts in each field of view are masked, the pipeline will attempt to align each exposure in preparation for combination. Alignment is done by computing a simple offset between each exposure, with respect to the first exposure. The offset is by default computed using the quasar, but it can be also done by using a field star if its coordinates (`STAR-RA` and `STAR-DEC`) are specified in the input data table (Section 2.2.2) and the option `--star-align` is used when calling the script in the command line. The pipeline will read the coordinates provided in the data table and search for them in the datacube.

The pipeline first recenters the header of the reference cube (by default the first exposure) using the function `recenter_header` within the `MUSE-Lya.py` module. This function uses the reference cube, the reference coordinates (both in degrees and in pixels) and a default radius of `centroid_radius=10` pixels, where computes the centroid of the quasar (or star), within the given radius, by fitting a 2D gaussian model using the white image. Then the header of the reference cube is updated with new reference pixels at the centroid coordinates. After this, the pipeline recenters the other exposures using the same method and computes the offset in pixels with respect to the reference cube. Using these offsets, the pipeline uses the `align_cube` function within the `MUSE-Lya.py` module to align each exposure with respect to the reference cube. To do this, the cubes are inserted in slightly larger cubes by taking into account the computed offsets, forcing the quasar to be located at the same position in the larger cubes. Visual inspection is important for this step, therefore a figure of the white images of the aligned cubes with the position of the quasar overlayed can be produced when specifying the option `--show-plot` when running the `mask-align-combine.py` script.

2.3.3   Combination of single exposures

With each exposure aligned, the pipeline can now combine the single exposures into two final cubes. The pipeline combines the `DATA` and `STAT` extensions (see Section 2.1.3) into separated cubes, which is specified by using the option `--DATA` or `--STAT` when calling the `mask-align-combine.py` script in the command line. Combining the cubes is straightforward, but memory consuming, as all cubes need to be loaded at the same time (on average, MUSE datacubes have sizes of $\sim 2\,\mathrm{GB}$). The functions `combine_data` or `combine_var` will loop over the spectral axis of the final cubes and extract one layer per channel, then will combine the layers of the cubes. For the `DATA` extension it is possible for the user to choose to combine using the mean or median with the options `--mean-combine` or `--median-combine`, however for the `STAT` extension it is always computed the variance of the mean as to properly propagate noise for the median would require bootstrapping on too heavy datacubes.

The combined layer at each channel is inserted into a new cube, which will be the final combined cube. This step is time consuming as the loop over the spectral axis goes over 3681 channels. The combined `DATA` and `STAT` cubes will be stored in a new directory called `/combined` which is created in the parent directory of the system (see Section 2.2.2).

2.3.4 Seeing estimation

With the combined datacube from Section 2.3.3 the PSF-subtraction can be performed with the `psf-sub.py` script. First, the seeing of the observation is estimated to define the radius of aperture to compute and subtract the quasar PSF (Section 2.3.5). As mentioned in Section 2.1.2, the seeing, which is wavelength dependent, can be computed from the FWHM of a Moffat function. The pipeline does this by computing a pseudo NB by collapsing a slice of the cube of $25\,\text{Å}$ (20 channels) at each wavelength, then fitting a Moffat function to the resulting image. The Moffat model is fitted using the `moffat_fit` function of the `MPDAF` package, which takes the $25\,\text{Å}$ pseudo-NB and same parameters as the `recenter_header` from Section 2.3.2.

The resulting seeing as a function of wavelength for one system is shown in Figure 2.6 with a black curve, it is possible to see how the seeing is better at longer wavelengths as expected (Boyd, 1978). The black curve was smoothed with a median filter of 150 channels ($\sim 190\,\text{Å}$), to reduce the spectral variability of the estimation that frequently affects faint quasars. Indeed, in the faint quasar sample presented in Chapter 4 the seeing of some quasars cannot be estimated at every wavelength because the signal-to-noise is too low and the image in the pseudo-NB cannot be modeled with a 2D Moffat distribution. For these cases, the seeing was only estimated at the Lyα peak wavelength (obtained from the quasar spectrum). In any other case, the seeing is estimated at the Lyα peak wavelength of the smoothed seeing curve.
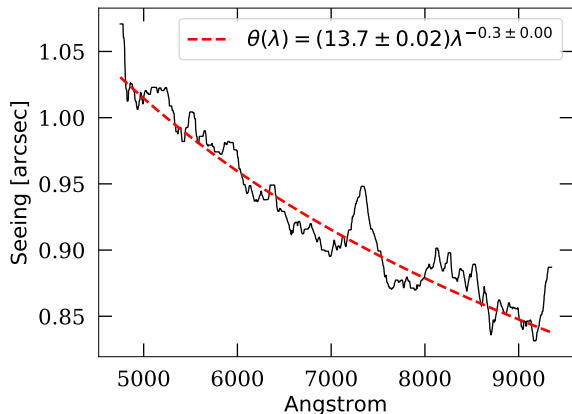
Figure 2.6: Example of the estimated seeing as a function of wavelength for a quasar observed with MUSE. The seeing is measured from the FWHM of a 2D Moffat fit (Equation 2.3) to pseudo-NBs of the observed quasar at each wavelength. The black curve is the seeing smoothed with a median filter of 150 channels. The resulting curve is fitted with a power law of form $\theta(\lambda) = a\lambda^b$ shown with a red dashed curve and parameters shown in the legend. It can be seen how the image quality increases towards longer wavelengths.

2.3.5   PSF construction and subtraction

The method for PSF-subtraction of the quasar relies on empirically determining and removing the wavelength dependent quasar emission (Møller, 2000) from the datacube. For this, I developed the `psf-sub.py` script, which is mostly based on the methods described in Borisova et al. (2016, Section 3.1) and Mackenzie et al. (2021a, Section 2.3), however it is also described in several other works (Cantalupo et al., 2019; Arrigoni Battaia et al., 2018, 2019a; Farina et al., 2019; Cai et al., 2019; O'Sullivan et al., 2020; Fossati et al., 2021).

The script begins by creating a new directory called `/psf-sub` inside the parent directory, where the data products will be stored. Then, the pipeline will re-align the combined cube as done in Section 2.3.2 in order to secure that the quasar coordinates are centered for PSF-subtraction.

To build the quasar PSF at each wavelength, the pipeline will compute a pseudo-NB of width and scale defined as global variables:

```
nb_width = 150              # number of channels
psf_scale = 7               # scale factor
```

centered at the quasar position. The variable `nb_width` is the pseudo-NB width in channels and the value of `psf_scale` will be multiplied by the measured seeing (Section 2.3.4) to define the radius for the aperture where the PSF is subtracted. This radius has to be chosen to ensure that the wings of the PSF distribution are negligible. During the progress of this thesis I noted that there is no optimal fixed NB-width or radius that will ensure quality results for all quasars, therefore visual inspection and adjustment needs to be carried out by the user at this step of the pipeline. For example, for the quasar samples in Borisova et al. (2016) and Arrigoni Battaia et al. (2019a) the PSFs were constructed using a NB-width of 150 channels with a PSF radius scale of 5 times the seeing, while in the fainter sample of Mackenzie et al. (2021a) a NB-width of 400 channels was used. The values I chose for the different projects are listed in the following chapters. The different methods have shown that the description of the CGM of quasars can depend on the parameters chosen, and the data itself, however I found that in general the trends and overall behavior of the extended Lyα emission found in (Arrigoni Battaia et al., 2019a) can be reproduced with this pipeline (4).

Computing the quasar PSF across the whole spectral range will mean that the extended emission, if present, will also be removed from the datacube. That is why the pipeline masks wavelength ranges where we expect extended emission to be observed, which should be close to the wavelength of the quasar broad line emissions. The pipeline blindly searches for line emission in the quasar spectra as the lines are usually shifted from the systemic Shen (e.g., 2016) and the shift is usually luminosity dependent. In the pipeline, this is done by first estimating the wavelength range where we expect quasar line emissions (such as Lyα, Si IV C IV, He II, C III]) from a user-defined redshift range (`z_ini` and `z_end` in the global variables of `psf-sub.py`). Then, an integrated spectrum centered at the quasar is computed inside a 1 arcsec diameter aperture, shown in Figure 2.7 with a black curve. The quasar spectrum

is smoothed using a median filter of 500 channels to produce a "continuum" spectrum[1], shown with a green curve in the same figure. The "continuum" spectrum is constructed this way to remove features from line emission. Additionally, the quasar spectrum is smoothed using a median filter of 50 channels to produce a "smoothed" spectrum (blue curve), which is constructed to highlight broad emission lines. The difference between the smoothed and continuum spectrum, shown with a black curve in the bottom panel of Figure 2.7, is used to determine the location in wavelength of line emission by identifying local peaks. The largest peak is assumed to be Lyα emission for every quasar and is used to set the most likely reference wavelength of the extended emission for the preliminary analysis of the system. The peaks are found using the `find_peaks` function from `scipy.signal` which uses the difference spectrum as data array, a detection threshold and a minimum separation between the local peaks. I choose a threshold of 3σ, where σ is the standard deviation of the difference spectrum at wavelengths redwards from the expected location of the C IV line. The minimum separation for the peaks is computed from the $\Delta\lambda$ between the two closest points from the peak Lyα wavelength where the difference spectrum becomes zero (pink crosses in Figure 2.7). Once the local peaks are identified as line emission, I exclude a conservative wavelength range around them ($\Delta\lambda = 430 - 560\,\text{Å}$) defined by the two closest points from the peak Lyα where the difference spectrum becomes zero plus 150 channels (vertical dashed lines in the figure). This is chosen to ensure that the pseudo-NB will not be computed where we expect extended line emission. Then, these wavelength ranges are excluded when building the pseudo-NBs, instead, the pipeline will use as PSF the next available pseudo-NB at longer wavelength.

The constructed pseudo-NBs are re-scaled, at each wavelength, to match the corresponding flux of the quasar, which is computed inside a normalization region of 5×5 pixels ($1'' \times 1''$) centered at the quasar location. The scale factors are computed using the ratio between the average sigma clip value from the quasar and pseudo-NB inside the normalization region. After re-scaling, negative values are masked from each re-scaled pseudo-NB in order to avoid introducing signal when subtracting. Finally, the re-scaled pseudo-NB is subtracted from the data at the quasar location.

After this step, the pipeline stores a PSF cube built from the stack of re-scaled pseudo-NBs, a PSF-subtracted cube and a Lyα pseudo-NB of $30\,\text{Å}$ inside the `/psf-sub` directory in order to inspect the result from the subtraction. The location of the Lyα wavelength is identified, as first look, in Figure 2.7. The top left panel of Figure 2.8 shows an example of a $30\,\text{Å}$ Lyα pseudo-NB produced by the pipeline when removing the quasar PSF, some extended emission is apparent close to the center of the field of view, however continuum sources are still visible in the field. The subtraction of the quasar PSF introduces an artifact at the normalization region, therefore the $1'' \times 1''$ (5×5 pixels) region at the center of the quasar position is masked and excluded from analysis.

---

[1]This is not intended to characterize the quasar continuum spectrum, but a pathway to find the location of line emissions.
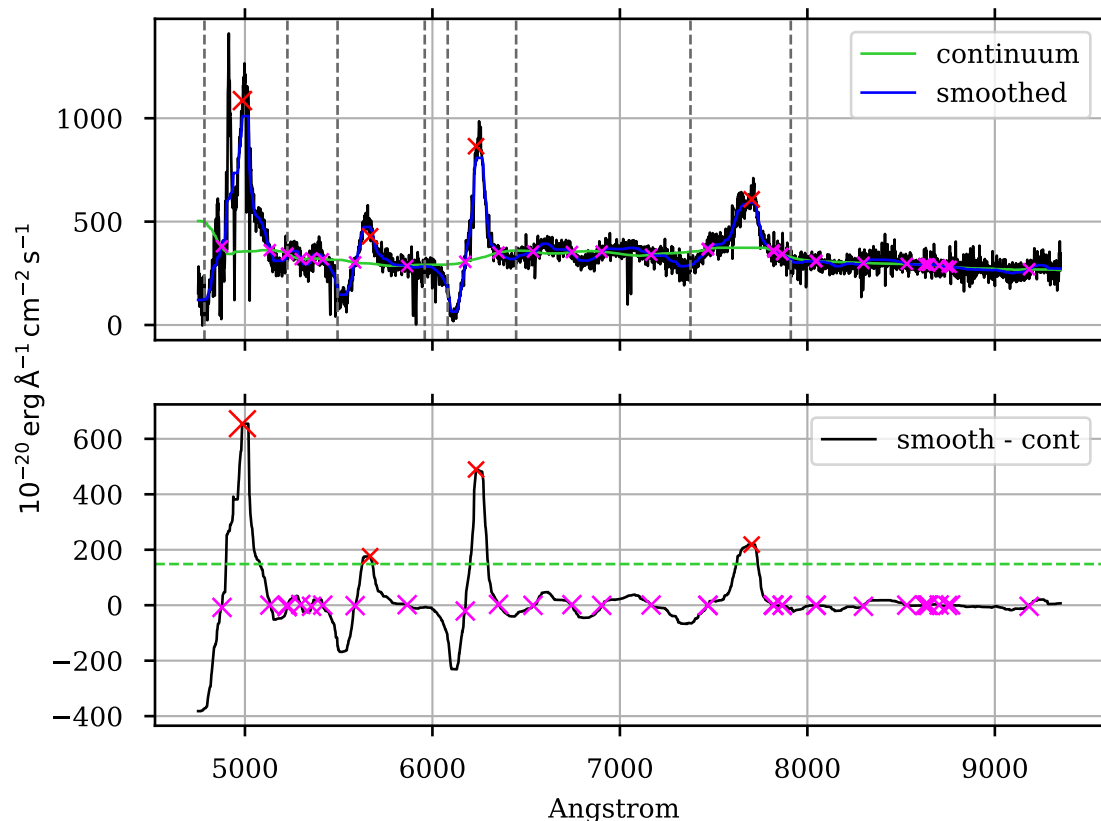
Figure 2.7: Example of identification of the location of quasar broad line emission using a MUSE spectrum. *Top:* The spectrum of the quasar integrated inside a $1\,\mathrm{arcsec}^2$ aperture is shown in black. The "continuum" spectrum (see Section 2.3.5) is shown with a green curve, the smooth spectrum used to highlight line emission features is shown in blue. The dashed vertical lines mark the wavelength ranges around emission lines (red crosses) excluded for computing the pseudo-NB (see text). *Bottom:* The difference between the smooth and continuum spectrum is shown with black. The 3σ intensity threshold is shown with the green dashed line. The positions of local peaks in the difference spectrum are shown with red crosses.
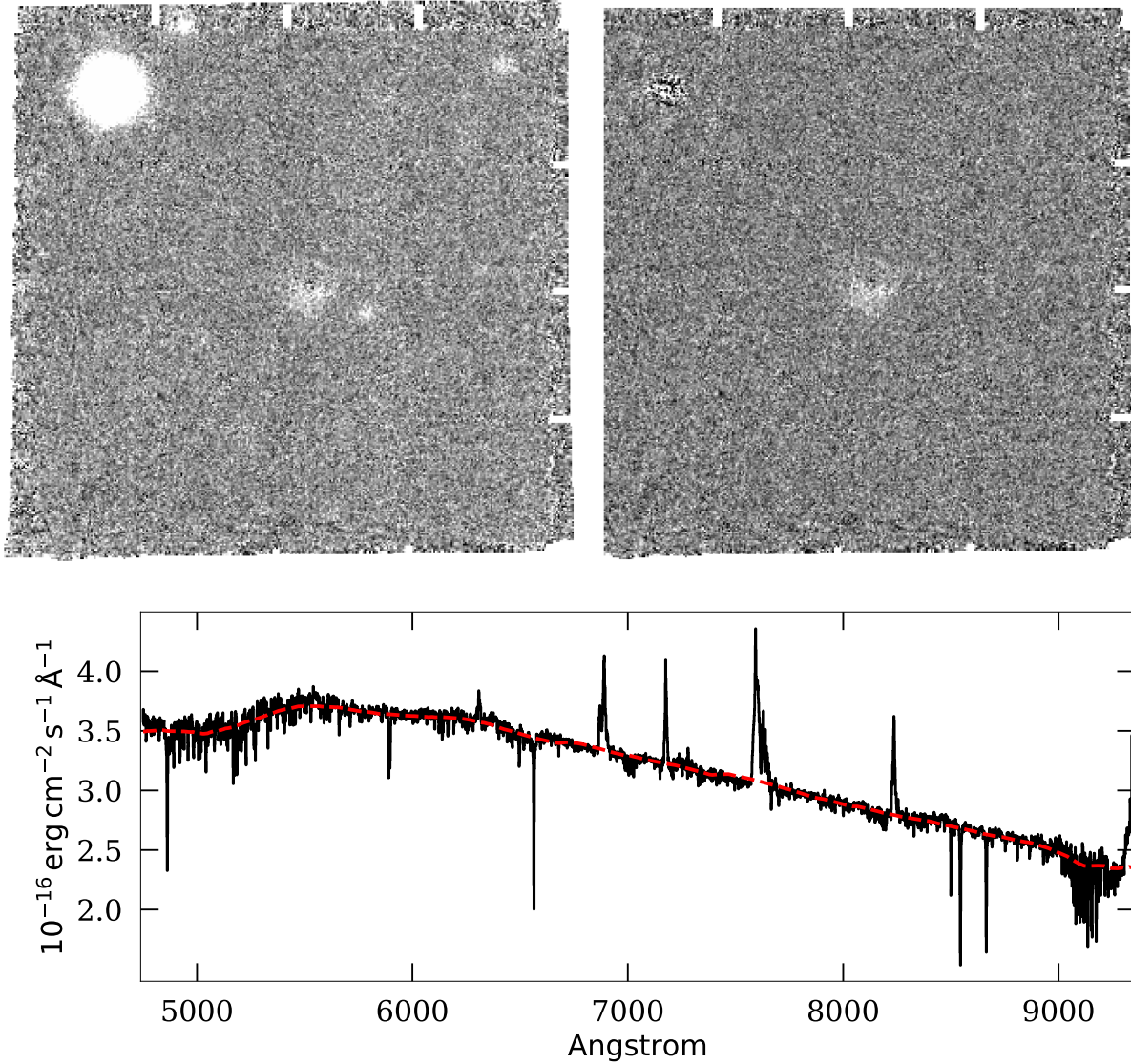
Figure 2.8: Example of PSF- and continuum-subtracted Lyα pseudo-NBs of a quasar field and estimated continuum of a field star. *Top left:* 30 Å pseudo-NBs centered at the wavelength of the Lyα line identified from Figure 2.7 of a PSF-subtracted quasar cube (Section 2.3.5). Some extended emission is apparent close to the quasar position, however there are continuum sources in the field still present. *Top right:* The same pseudo-NB, but after continuum-subtraction. At this stage the datacube is suitable for analysis of extended CGM line emission. *Bottom:* The spectrum of a field star (which is visible in the top left corner of the PSF-subtracted Lyα pseudo-NB) and the estimated continuum (Section 2.3.6) at its location are shown with a solid black and red dashed curve, respectively.

2.3.6   Continuum sources subtraction

Once the quasar PSF has been subtracted, other continuum sources are removed from the datacube in order to produce a cube with only line emission extending outside of the quasar position, if detectable.

The pipeline creates a continuum cube with the `contsubfits` function from the `ZAP` package, which uses a median filter of 300 channels to estimate the continuum at each spaxel of the datacube. After this step, the continuum cube is subtracted from the PSF-subtracted cube. The continuum cube and final subtracted MUSE datacubes are stored in the folder `/contsub` created in the parent directory. The PSF- and continuum- subtracted cube is suitable to search for extended Lyα emission around each quasar. The top right panel of Figure 2.8 shows the 30 Å Lyα pseudo-NB produced by the pipeline when removing continuum sources. This NB is produced as a first approach to check the quality of the subtraction, however further careful analysis needs to be performed in order to characterize the extended emission. Additionally, the bottom panel of Figure 2.8 shows a comparison between the spectrum computed inside a 1 arcsec radius aperture at the location of a field star (black line) and the spectrum extracted from the built continuum cube at the same location and using the same aperture (red dashed line).

2.3.7   Surface brightness limit estimation

The sensitivity of an observation determines the minimum SB that we can detect from an extended source. The pipeline estimates the SB limit using the combined variance cube (see Section 2.3.3). Due to correlated noise between pixels in MUSE data (Bacon et al., 2015), the variance of each channel is rescaled to reflect the variance from the datacube at the same layer. The surface brightness limit will be wavelength dependent, because the background noise varies across the visible range due to sky emission lines. Figure 2.9 illustrates how the background noise of an observation varies across the wavelength range due to sky emission lines, represented as the standard deviation associated to an observed spectrum obtained by integrating inside a 1 arcsec radius aperture at an arbitrary sky location (because it is present in the complete field of view) from a MUSE variance cube.

To estimate the average surface brightness level of an observation at a given wavelength, the `SB_limit_rescale` function within the `MUSE-Lya.py` package first creates a sky mask to perform the calculations only where there is no emission. A sky image is created by computing the average sigma clip value of the white image (with $\sigma = 3$), then setting a threshold of 3× this value to mask out brighter sources. The sky mask is applied to both the variance and datacube. Then, at each layer, I compute the ratio between the mean standard deviation of the variance layer and the standard deviation of the datacube layer. This ratio is used as scale factor which is multiplied to the variance layer.

Using the rescaled variance cube with the sky mask, a 30 Å slab (default value of `nb_width`) centered at the selected wavelength (set by `center_wave`, usually the wavelength of the peak Lyα emission of the quasar), is integrated over the spectral axis and multiplied by the channel width squared to obtain a "variance NB". Then this NB is transformed to
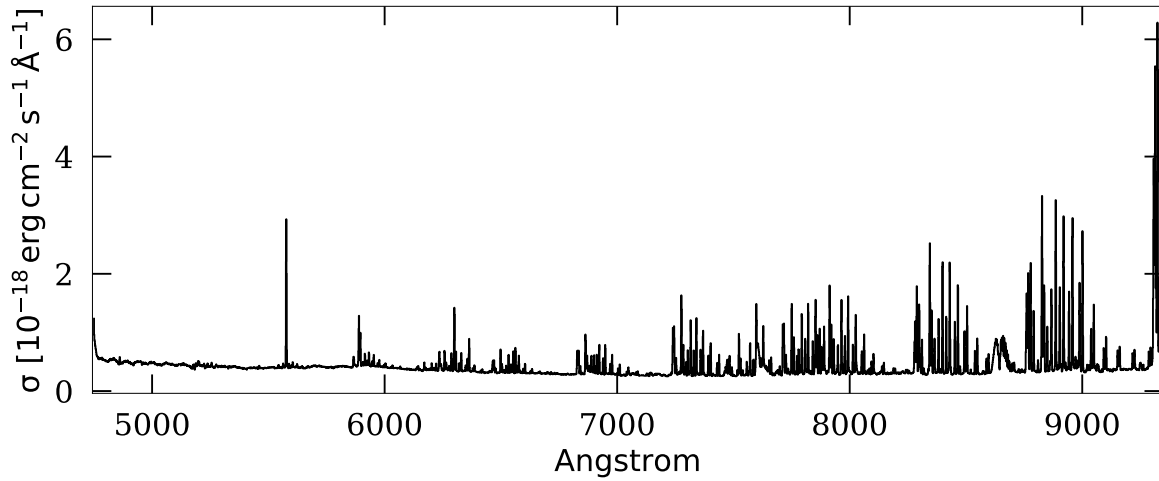
Figure 2.9: Standard deviation associated to an observed spectrum integrated inside a 1 arcsec radius aperture from the corresponding variance cube at an arbitrary location. This figure illustrates how the background noise changes across the wavelength range, highlighting the effect of sky line emissions.

SB units squared by dividing by the area of a pixel squared to obtain a "variance SB", which transformed to σ by taking the square root. Then, I compute the mean of this sigma map to get the mean SB limit per pixel within the 30 Å pseudo-NB. To transform to per arcsec^2, I need to divide by the square root of the number of pixels within one arcsec^2. If one pixel is 0.2″, then there are 25 pixels inside 1 arcsec^2. The SB limit obtained from this step is used to determine the sensitivity of the observations I analyze in Chapters 3 and 4.

2.4 Conclusion

In this chapter I presented how the process of revealing extended line emission around quasars using MUSE observations has been studied and reproduced based on the description presented in past works (Borisova et al., 2016; Farina et al., 2019; Arrigoni Battaia et al., 2019a; Mackenzie et al., 2021a). The method relies in the empirical determination of the quasar PSF and subsequent subtraction together with continuum sources, this process is not trivial and careful analysis of the PSF needs to be done.

When the projects of this thesis started to be elaborated, there were no public tools available to perform the extraction of CGM emission. Therefore, I developed my own individual routines to carry out this task and collected them into this more versatile pipeline with the aim that other people can use it, and improve it, as well. Today, there is one publicly available tool in development that performs a similar task: `q3dfit`[2] (Rupke, 2014; Rupke et al., 2021), however this was designed for JWST data and became available after I already developed this pipeline. It has been compared with already published data in order to test and evolve and has been used for the works presented in Chapters 3 and 4 and others still in preparation by collaborators and myself (Herwig et al. 2024 and González Lobos et al. in prep.). Therefore this Chapter is presented as the first documentation for a tool that will be publicly available in the future.

---

[2]https://q3dfit.readthedocs.io/en/latest/

Chapter 3

Circumgalactic Lyα emission around submillimeter-bright galaxies with different quasar contributions

3.1 Introduction

In the ΛCDM paradigm, galaxies form and evolve embedded in a filamentary cosmic web, and grow by accretion of material from their surrounding medium. In turn, galaxies are expected to modify and pollute their vicinities through several processes (e.g., photoionization, outflows). The gas interface, extending beyond a galaxy's interstellar medium, but bound to the galaxy's halo, is often called the circumgalactic medium (CGM; e.g., Tumlinson et al., 2017). The CGM extends over hundreds of kpc and naturally encodes information on the interactions between a galaxy and its surroundings (e.g., inflows, outflows), making its direct study fundamental for the understanding of galaxy formation and evolution.

The current generation of sensitive integral-field unit (IFU) spectrographs, such as the Multi Unit Spectroscopic Explorer (MUSE; Bacon et al., 2010) at the Very Large Telescope (VLT) and the Keck Cosmic Web Imager (KCWI; Morrissey et al., 2018) at the Keck Observatory, are able to push observations to unprecedented surface brightness limits (SB $\sim 10^{-19}\,\mathrm{erg\,s^{-1}\,cm^{-2}\,arcsec^{-2}}$) allowing us to study the CGM in emission. For example, observations of the Hydrogen Lyman-α (Lyα) emission line surrounding high-z ($2 < \mathrm{z} < 6$) quasars are now routinely reported (e.g., Borisova et al., 2016; Arrigoni Battaia et al., 2018, 2019a; Farina et al., 2019; Cai et al., 2019; O'Sullivan et al., 2020; Mackenzie et al., 2021a; Fossati et al., 2021). The Lyα emission traces large-scale ($\sim 100\,\mathrm{kpc}$), cool (T $\sim 10^4\,\mathrm{K}$), and massive gas reservoirs within the dark-matter halos hosting quasars at these redshfits, which are expected to have masses in the range M $\sim 10^{12} - 10^{13}\,\mathrm{M_\odot}$ (e.g.,

Timlin et al., 2018, and references therein).

The main powering mechanism of the extended Lyα glow is frequently invoked as photoionization from the associated bright quasar followed by recombination in optically thin gas (e.g., Heckman et al., 1991a; Cantalupo et al., 2014; Hennawi et al., 2015; Arrigoni Battaia et al., 2015a; Cai et al., 2018; Arrigoni Battaia et al., 2018). However, the detailed radiative transfer of this resonant line emission, and the balance between different powering mechanisms is still unclear and debated. Hydrodynamical simulations of $z \sim 2$ halos show that photoionization from the central active galactic nucleus (AGN) and star formation from companion galaxies can produce extended Lyα emission (Gronke and Bird, 2017). Also, recent simulations of $z \gtrsim 6$ quasar nebulae showed that scattering of Lyα photons is required to explain the morphology of the extended Lyα emission (Costa et al., 2022). This work also showed that Lyα photons from the quasar's broad-line-regions (BLR), added in post-processing, can contribute to the powering of the extended emission as quasar feedback is able to open channels of least resistance for the propagation of such photons out to CGM scales.

There are at least four possible mechanisms that could act together to power the extended Lyα emission: (i) photoionization from the central AGN or companion galaxies, (ii) shocks powered by galactic/AGN outflows, (iii) gravitational cooling radiation, and (iv) resonant scattering of Lyα. Disentangling their relative roles and making an unique interpretation of observations is challenging (e.g., Arrigoni Battaia et al., 2015b; Mackenzie et al., 2021a), and it is at the root of the difficulties in firmly constraining the physical properties of the emitting gas. Possible avenues to assess the contribution of different powering mechanisms are polarimetric observations of the Lyα emission (e.g., Hayes et al., 2011; Kim et al., 2020), or constraints on additional emission lines such as Hα, C IVλ1549[1] and He IIλ1640, which also aid in determining the ionization state and metallicity of the CGM (e.g., Arrigoni Battaia et al., 2015a). For each of the mechanism, the following expectations hold:

- Photoionization from the central AGN: The AGN illuminates the CGM, which in turn reprocesses the UV emission into a recombination cascade including detectable Lyα, Hα and He II emission (e.g., Heckman et al., 1991a; Christensen et al., 2006; Smith et al., 2009; Geach et al., 2009; Humphrey et al., 2013). If the CGM is already enriched (e.g., from outflows) then extended C IV emission could also be detected.

- Shocks powered by galactic/AGN outflows: The Lyα linewidths observed for nebulae around quasars are generally as expected for quiescent gas in virial equilibrium with the surrounding dark matter halo (Full Width Half Maximum FWHM $\sim 600\,\mathrm{km\,s^{-1}}$; e.g., Arrigoni Battaia et al., 2019a; Cai et al., 2019; O'Sullivan et al., 2020; Lau et al., 2022). However, broader linewidths on tens of kpc around some objects (e.g., Ginolfi et al., 2018; Vidal-García et al., 2021) are evidence for larger turbulence likely caused by outflows from the central AGN. Shocks produced by this outflowing material can produce Lyα emission through collisional excitation and ionization (e.g., Taniguchi and

---

[1]The C IV line is a doublet with wavelengths 1548 Å and 1550 Å.

Shioya, 2000; Taniguchi et al., 2001; Ohyama et al., 2003; Wilman et al., 2005; Mori and Umemura, 2006). The same mechanisms could also allow for the emission of C IV and He II lines.

- Gravitational cooling radiation: As gas cools within dark matter halos, it will radiate away the lost gravitational potential energy through cooling channels. The main result is the emission of Lyα photons produced by collisional excitations (e.g., Haiman et al., 2000; Furlanetto et al., 2005; Dijkstra et al., 2006; Faucher-Giguère et al., 2010; Rosdahl and Blaizot, 2012a). Detecting any other line emission due to this mechanism would be difficult with current facilities.

- Resonant scattering of Lyα photons originating from compact sources: Lyα photons produced by the QSO, the host galaxy and companion galaxies can contribute to an extended Lyα glow as they undergo resonant scattering while propagating outwards through the CGM (e.g., Dijkstra and Loeb, 2008; Hayes et al., 2011; Cen and Zheng, 2013; Cantalupo et al., 2014). C IV is also a resonant transition and it could be detected as extended glow if scattered by a C^{3+}-rich medium. Recombination transitions (e.g.,Hα, He II) are expected to be more compact and narrower than Lyα (e.g., Prescott et al., 2015).

In addition, resonant scattering is expected to take place also for the Lyα photons originating from the first three mechanisms. This results in broader lines and larger nebulae due to the diffusion in space and frequency of the Lyα photons (e.g., Dijkstra 2019).

Stacking analysis of several objects start to reveal extended line emission besides Lyα. Using MUSE data on 80 $z \sim 3$ QSOs (1 hour/source) Guo et al. (2020) reported average C IV, He II, and C III] SB profiles, implying high metallicities in the inner CGM. Moreover, the latest and deepest (4 hours/source with MUSE) survey targeting high-redshift quasars was able to reveal extended emission from Lyα, C IV and tentatively from He II (barely 2σ significance) in their stacked analysis of 27 targets Fossati et al., 2021. They derived line ratios and highlighted the difficulties in modeling the observed metallicities, but conclude that the CGM gas is metal polluted at redshift $z = 3 - 4.5$. In particular, they discussed that resonant scattering of quasar's Lyα photons could be an explanation to the observed ratios and to why their sample shows emission which is more extended in resonant lines (Lyα and C IV) than non-resonant lines (He II).

The longer term goal of our endeavor is to break the degeneracies between different powering mechanisms. In this project, we present the Lyα extended emission around different types of galaxies: unobscured quasars with a companion submillimeter galaxy (SMG; e.g., Smail et al., 1997), SMGs hosting quasars, and SMGs. While all these objects are predicted to reside in similarly massive dark matter halos as quasars ($10^{12-13}\,\mathrm{M}_\odot$; e.g., Wilkinson et al., 2017; García-Vergara et al., 2020; Lim et al., 2020), and to have large star-formation rates, they have different contributions of quasar radiation (from none to bright unobscured quasars). We stress that the clustering of quasars is independent of the luminosity of the quasar ($-28.7 < M_i < -23.8$, Eftekharzadeh et al. 2015), hence looking at different luminosity systems probes the effect of different levels of ionizing radiation in

the same environment. Therefore, once corrected for the cosmological surface brightness dimming, we expect that these systems (i) have similar contributions to the total Lyα emission radiated from gravitational cooling (Haiman et al., 2000), (ii) have different contributions from AGN photoionization, star-formation, and from Lyα resonant scattering, proportional to the AGN luminosity, star-formation activity, and Lyα photon budget in compact sources, respectively, and (iii) have a shock contribution only when evidence of violent kinematics are present on CGM scales.

We emphasize that all our targets have large infrared luminosities ($L_{FIR} \sim 10^{12-13} L_{\odot}$), similar to those of SMGs, and which are caused by dust heated by high rates of obscured star formation, with star formation rates of SFR $\sim 100 - 1000 M_{\odot} yr^{-1}$ (Blain et al., 1999; Casey et al., 2014). In particular, recent works have shown that the distribution of dust in some SMGs appears clumpy and displaced from UV regions, which allows a fraction of their UV photons to escape (e.g., Hodge et al., 2015; Chen et al., 2017). Our observations could therefore estimate what fraction of escaping UV photons from star formation impinge on their CGM. In other words, if cool gas is present around these sources, then we expect that extended Lyα emission due to star formation might be detected when there are enough escaping UV photons reaching the surrounding gas distribution.

This paper is organized as follows. In Section 3.2, we describe in detail the sample, observations and data reduction. In Section 3.3, we describe the analysis carried out in order to reveal the extended emission around our sources. In Section 3.4, we present our results, discuss the properties of the detected extended Lyα emission such as brightness, morphology and kinematics, and report constraints on additional emission lines. In Section 3.5 we compare our observational results with previous literature and discuss the Lyα powering mechanisms mentioned above, showing that the firmest constraint is that against the gravitational cooling scenario. above. We summarize our findings in Section 3.6. We adopt a flat ΛCDM cosmology with $H_0 = 70\,km\,s^{-1}\,Mpc^{-1}$, $\Omega_m = 0.3$ and $\Omega_{\Lambda} = 0.7$, for which the scale of one arcsecond corresponds to 7.0 kpc at the mean redshift of our sources ($z \sim 4$).

3.2   Observations and data reduction

3.2.1   Sample selection

This project exploits the spectral-imaging capabilities of VLT/MUSE to target five systems with strong star formation, including a SMG hosting a QSO with an SMG companion (QSO+SMG), two SMGs hosting a QSO, and two SMGs. In particular, the SMGs are part of the first samples with a firm estimate of their systemic redshifts through the observation of molecular tracers. Our sample is composed as follows:

- One radio-quiet unobscured bright quasar with a submillimeter companion galaxy ∼4 arcsec to the NW of the QSO, BR1202-0725 (e.g., Omont et al., 1996b; Drake et al., 2020);

- Two quasars in SMGs, G09-0902+0101 and G15-1444-0044 (Fu et al., 2017). Even though these sources are bright in the submillimeter, their quasar spectra appear unobscured in the rest-frame UV along the line of sight. They are therefore unobscured QSOs hosted by SMGs. They are about one order of magnitude fainter than the quasar in BR1202-0725;

- Two isolated SMGs (with no AGN) with spectroscopic redshift from [CII] and CO, ALESS61.1 and ALESS65.1 (Swinbank et al., 2012; Birkin et al., 2021).

3.2.2   VLT/MUSE observations and data reduction

The VLT/MUSE data were taken as part of ESO programmes 0103.A-0296(A) and 0102.A-0403(A) in service modes on UT dates between January 2019 and August 2019 (PI: F. Arrigoni Battaia). The observations were taken in wide field mode, resulting in a 0.2" spatial sampling of a $1' \times 1'$ field of view. In this configuration MUSE covers the spectral range $4750 - 9350\,\text{Å}$ with a spectral resolution of $R \sim 2230$ at 6078 Å (the Lyα wavelength at the mean z of the sample). The observing blocks were organized in three exposures of about 15 minutes each with < 5" shifts and 90 degree rotations. The observing conditions were clear and the seeing at the expected Lyα wavelength was of $1.13''$, on average. In addition, for BR1202-0725 we include, re-reduce, and add to our dataset the 48 minutes dataset from Drake et al. (2020), which was taken with MUSE in the same configuration as part of ESO programme $0102.\text{A} - 0428(\text{A})$ (PI: E. P. Farina), with two exposures with a $< 5''$ shift and a 90 degree rotation. These observations were obtained under good weather conditions and a 0.6" seeing. In Table 3.1 we list the total exposure time and the seeing at the Lyα wavelength measured for each field from its final datacube (see Appendix 3.7.1).

The data reduction was performed using the MUSE pipeline version 2.8.3 Weilbacher et al. (2012, 2014, 2020) as described in Farina et al. (2019), which consist of bias and dark subtraction, flat correction, wavelength calibration, illumination correction and standard star calibration. We continue with the removal of sky emission residuals, which we perform using the Zurich Atmospheric Purge software (ZAP; Soto et al. 2016). The reduced datacubes contain both the science data cubes and the associated variance cubes.
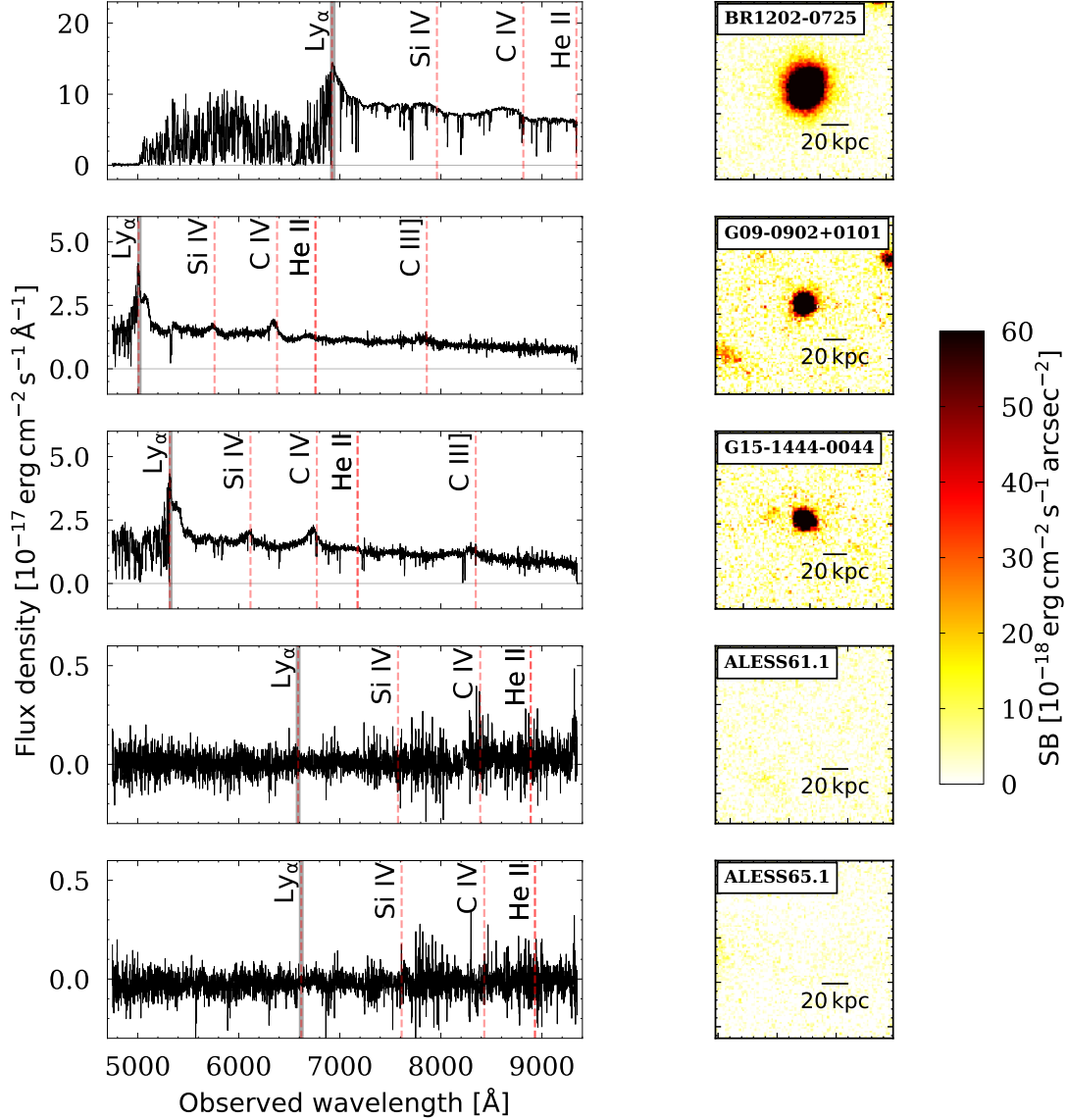
Figure 3.1: Overview of the five targeted systems before subtraction of the unresolved quasar's point spread function and continuum sources (see Section 3.3). *Left:* Integrated spectra of the QSOs and SMGs inside a 3" radius aperture. Vertical dashed lines indicate the positions of the Lyα and quasar broad lines (Si IV, C IV, He II and C III]). The gray shaded region indicates the FWHM of the nebular Lyα emission for the quasars (see Figure 3.2 and Table 3.3) and the 30Å narrow band used for the SMGs (see Figure 3.3). *Right:* 30 Å Surface brightness maps at the expected Lyα wavelength of the targeted QSOs and SMGs before PSF- and continuum-subtraction (see Section 3.3). The maps have a side of 20", corresponding to about 129, 152, 148, 133 and 132 kpc for BR1202-0725, G09-0902+0101, G15-1444-0044, ALESS61.1 and ALESS65.1 respectively.

Table 3.1: Physical properties of the targeted sample and observing log.

ID	Object	Redshift[a]	$\log L_{\mathrm{bol}}^{\mathrm{QSO}}/\mathrm{L}_\odot$ [b]	$\log L_{\mathrm{IR}}^{\mathrm{SF}}/\mathrm{L}_\odot$ [c]	SFR[d] [$\mathrm{M}_\odot\,\mathrm{yr}^{-1}$]	$M_{\mathrm{dust}}^{\mathrm{e}}$ [$10^8\,\mathrm{M}_\odot$]	Seeing[f] [arcsec]	Exp. time [minutes]	SBlim$_{\mathrm{Ly\alpha}}$ [$\times 10^{-18}$ g]	Type
1	BR1202-0725	4.6942 ± 0.0003 ([CII])	47.7	13.7 ± 0.2	5000 ± 2300	23.6 ± 3.1	1.1	126	3.2[i]	QSO+SMG
2	G09-0902+0101	3.120	46.5	13.2 ± 0.1	1600 ± 370	17.4 ± 3.6	1.0	44	3.1	SMG hosting a QSO[h]
3	G15-1444-0044	3.375	46.6	13.3 ± 0.1	2000 ± 460	19.7 ± 2.9	1.0	44	3.3	SMG hosting a QSO[h]
4	ALESS61.1	4.4189 ± 0.0004 (CO(4-3))	–	12.6 ± 0.1	400 ± 90	4.8 ± 0.9	1.3	86	2.5	SMG
5	ALESS65.1	4.4445 ± 0.0005 (CO(4-3))	–	12.6 ± 0.1	400 ± 90	4.7 ± 1.1	1.2	86	2.2	SMG

[a] Redshifts from Carilli et al. (2013), Fu et al. (2017) and Birkin et al. (2021). In brackets we report the line used for precise redshift estimates. For G09-0902+0101 and G15-1444-0044, the redshifts are the best values from Lyke et al. (2020), whose uncertainties are of the order of few hundreds of km s^{-1}.

[b] Bolometric luminosities computed from the observed luminosities at 1450Å using the relation by Runnoe et al. (2012).

[c] IR luminosities at $8 - 1000\,\mu m$ due to star formation re-computed in this work, and consistent within uncertainties with values in Wagg et al. (2012), Fu et al. (2017) and Birkin et al. (2021). For BR1202-0725 we only use the datapoints for the quasar from Omont et al. (1996a) and Iono et al. (2006).

[d] SFR computed using the formula $\mathrm{SFR} = [L_{\mathrm{IR}}^{\mathrm{SF}}/(10^{10}\,\mathrm{L}_\odot)]\,\mathrm{M}_\odot\,\mathrm{yr}^{-1}$ (Fu et al. 2017). The errors reflect only the uncertainty on the IR luminosities.

[e] Dust masses computed assuming a modified blackbody with dust emissivity spectral index $\beta = 2.0$ and fixing the dust temperature only for BR1202-0725 as we only use two datapoints not covering the SED peak ($T_{\mathrm{dust}} = 68\,\mathrm{K}$; Leech et al. 2001). For the other sources we found $T_{\mathrm{dust}} \sim 55\,\mathrm{K}$.

[f] The seeing is estimated by fitting a 2D Moffat model to point sources in each field (see Appendix 3.7.1).

[g] 2σ surface brightness detection level within 1 square arcsecond and 30 Å at the expected Lyα wavelengths, in units of erg s^{-1} cm^{-2} arcsec^{-2}.

[h] The host-galaxies are submillimeter bright with the flux at $870\,\mu m$ of $S_{870} = 14.4$ and $6.0\,\mathrm{mJy}$ for G09-0902+0101 and G15-1444-0044, respectively (Fu et al. 2017).

[i] At the expected Lyα wavelength for BR1202-0725 there are brighter sky lines than for all other sources. This is why the SB$_{\mathrm{lim}}^{\mathrm{Ly\alpha}}$ for BR1202-0725 is comparable to the other sources despite the longer exposure time.

The later are rescaled as usually done in the literature to reflect the empirical variance in the data cubes, since the pipeline underestimates the variance due to correlated noise at pixel level (e.g., Bacon et al. 2015). The scaling factor is found to be on average 1.4, consistent with previous works (e.g., Borisova et al., 2016), and is applied layer by layer to the variance cube. The final variance cubes are used to obtain surface brightness (SB) limits and associated errors of our estimates. After data reduction, we manually mask artifacts that appear due to the edges of the MUSE IFUs. This process needs to be performed for each single exposure before combining. During this step, about $\sim 4\%$ of the pixels are masked on average per exposure. Masking is done by inspection of white images (computed by collapsing the datacube along the spectral axis using the full wavelength range). After masking, each exposure is aligned by performing a 2D gaussian centroid fitting of point sources (stars) in each field for reference, then a simple offset is computed. Finally the datacubes are combined using the median, the variance cubes are also combined by performing error propagation.

At the expected wavelength of the Lyα emission, the final 2σ SB limit is on average $\sim 3 \times 10^{-18} \, \mathrm{erg\,s^{-1}\,cm^{-2}\,arcsec^{-2}}$ for an aperture of 1 square arcsecond and a 30 Å narrow band. We list in Table 3.1 these SB limits.

Finally, Figure 3.1 shows the integrated spectra obtained from our MUSE data inside a 3" radius aperture for each of the systems studied here, together with SB maps of 30 Å narrow-bands centered at the expected Lyα line wavelength before subtracting the quasar's point spread function and continuum sources. We can already see from this figure that there is no detected emission from the SMGs. Note that for BR1202-0725, the observed He II wavelength is located right before the edge of the spectral range (about 9 Å). In Section 3.3 we discuss in detail these observations and their analysis.

3.2.3 Physical properties of the sample

To homogenize our sample, we re-compute some of the galaxies' physical properties in a consistent way for all sources, namely infrared (IR) luminosity, SFRs and dust masses. To do this, we use ancillary submillimeter data. We construct the 8-1000 μm spectral energy distribution using the datapoints from Omont et al. (1996a) (at 1250 μm with IRAM 30 m) and Iono et al. (2006) (at 900 μm with the Submillimeter Array) for BR1202-0725, from Fu et al. (2017) (at 250, 350 and 500 μm with Herschel/SPIRE and 870 μm with ALMA) for G09-0902+0101 and G15-1444-0044, and from Swinbank et al. (2012) (at 250, 350 and 500 μm with Herschel/SPIRE and 870 μm with ALMA) for ALESS61.1 and ALESS65.1. In Table 3.2 we summarize the fluxes of these submillimeter observations.

We estimate the dust masses of each source assuming a modified black body of the form $S_{\nu_0} \propto B_\nu \times [1 - \exp(-\nu/\nu_0)^\beta]$ with $\nu_0 = 2.0 \, \mathrm{THz}$ and dust emissivity spectral index $\beta = 2.0$ (Fu et al., 2017), integrating to obtain the total IR luminosity between $\lambda = 8 - 1000 \, \mu$m. We then use this integrated IR luminosity to estimate the SFR for each source using the formula $\mathrm{SFR} = [L_{\mathrm{IR}}^{\mathrm{SF}}/(10^{10} \, \mathrm{L_\odot})] \, \mathrm{M_\odot \, yr^{-1}}$ from Fu et al. (2017), which assumes a Chabrier (2003) initial mass function. This procedure is reasonable as it has been shown that most of the IR emission in these sources is dominated by star formation in the host galaxy (e.g.,

Table 3.2: Summary of the ancillary data fluxes used to estimate the physical properties of the sample.

ID	S_{250} mJy	S_{350} mJy	S_{500} mJy	S_{870} mJy	S_{900} mJy	S_{1250} mJy
1	–	–	–	–	32 ± 4	12.59 ± 2.28
2	53.7 ± 7.5	56.7 ± 8.6	45.9 ± 9.3	14.4 ± 0.8	–	–
3	47.3 ± 6.6	61.2 ± 8.2	58.8 ± 8.8	6.0 ± 0.6	–	–
4	4.3 ± 1.5	7.4 ± 1.6	10.2 ± 1.7	4.32 ± 0.44	–	–
5	–	7.6 ± 1.4	10.2 ± 1.5	4.24 ± 0.49	–	–

Iono et al. 2006; Fu et al. 2017). The dust masses are derived using equation (3) of Chen et al. (2021), assuming a rest-frame dust mass absorption coefficient $\kappa_{850\,\mu m} = 0.431\,\mathrm{cm^2\,g^{-1}}$ from Li and Draine (2001). For BR1202-0725 we fix the dust temperature to $T_{\mathrm{dust}} = 68\,\mathrm{K}$ (Leech et al., 2001) as we only use the two available datapoints for the quasar, which are not covering the spectral energy distribution (SED) peak. For the other sources we find $T_{\mathrm{dust}} \sim 55\,\mathrm{K}$. If we adopt this same temperature for BR1202-0725 we derive a 20% higher dust mass. The derived dust masses (see Table 3.1) are consistent with dust masses reported in the literature for similar objects. Specifically, the dust masses of ALESS61.1 and ALESS65.1 are in agreement with the values estimated by Birkin et al. (2021).

Further, we provide a rough calculation to show that the halo masses of these systems are within the range expected for quasars and SMGs at these redshifts ($10^{12} - 10^{13}\,\mathrm{M_\odot}$). Specifically, we predict their DM halo masses using the halo mass-stellar mass relation by Moster et al. (2018) at their redshifts. We stress that the obtained estimates are affected by large uncertainties given the scatter in this relation. For the two SMGs, ALESS61.1 and ALESS65.1, we can rely on their stellar masses obtained through SED fitting by Birkin et al. (2021), $\log(M_*/[\mathrm{M_\odot}]) = 10.33^{+0.18}_{-0.01}$ and $\log(M_*/[\mathrm{M_\odot}]) = 10.48^{+0.19}_{-0.13}$, respectively. For the three quasar systems, we instead convert their total gas mass to a stellar mass, assuming the gas to stellar mass ratio at their redshift from Birkin et al. (2021) (e.g., see their Figure 9, left panel). For this step, we homogenize all the measurements obtaining gas masses from the far-IR continuum following equation 3 in Tacconi et al. (2020), assuming a gas-to-dust ratio of 100 (e.g., Riechers et al. 2013). We find $M_{\mathrm{gas}} = 8 \times 10^{10}\,\mathrm{M_\odot}$ for BR1202-0725, and $M_{\mathrm{gas}} = 6.3 \times 10^{10}\,\mathrm{M_\odot}$ and $M_{\mathrm{gas}} = 1.9 \times 10^{10}\,\mathrm{M_\odot}$ for G09-0902+0101 and G15-1444-0044, respectively. The value for BR1202-0725 is consistent with the value computed from CO emission and assuming an $\alpha_{\mathrm{CO}} = 0.8\,\mathrm{M_\odot\,K^{-1}\,km\,s^{-1}\,pc^2}$ (Riechers et al., 2006). We therefore homogenized the values in Birkin et al. (2021) to this α_{CO}. We stress that they targeted 61 SMGs with no clear sign of AGN activity, therefore the used ratio may introduce a systematic bias for our QSOs which are hosted by SMGs. We find stellar masses of $M_* = 6.7^{+5.9}_{-2.1} \times 10^{10}\,\mathrm{M_\odot}$ for BR1202-0725, and $M_* = 8.0^{+10.9}_{-2.8} \times 10^{10}\,\mathrm{M_\odot}$ and $M_* = 2.3^{+2.7}_{-0.8} \times 10^{10}\,\mathrm{M_\odot}$ for G09-0902+0101 and G15-1444-0044, respectively. Therefore, the expected DM halo masses using the halo mass-stellar mass relation by Moster et al. (2018) for the targeted sources are: $\log(M_{\mathrm{DM}}/[\mathrm{M_\odot}]) \sim 12.3$ for BR1202-0725, $\log(M_{\mathrm{DM}}/[\mathrm{M_\odot}]) \sim 12.5$ and $\log(M_{\mathrm{DM}}/[\mathrm{M_\odot}]) \sim 11.9$ for G09-0902+0101 and G15-

1444-0044, and $\log(M_{\rm DM}/[\rm M_\odot]) \sim 11.9$ and $\log(M_{\rm DM}/[\rm M_\odot]) \sim 12.0$ for ALESS61.1, and ALESS65.1, respectively. We quote the halo mass estimates as approximate because of the large uncertainties inherent to the use of the relation in Moster et al. (2018), the use of gas masses to obtain stellar masses, and the uncertainty on the $\alpha_{\rm CO}$ assumed, which could be a factor of 5 higher if $\alpha_{\rm CO}$ is close to the galactic value (Bolatto et al., 2013). Notwithstanding these uncertainties, the values we find are consistent with the range of halo masses from clustering studies (Timlin et al., 2018, and references therein). These estimates are key in placing these systems in the context of galaxy formation, and in quantifying the expected signal for gravitational cooling. Table 3.1 summarizes most of the properties of our targets (redshift, quasar's bolometric luminosity, infrared luminosity due to star formation, SFR, estimated dust mass, seeing at the Lyα wavelength, exposure time and their type) with their respective references.

3.3   Analysis: Revealing the large-scale emission

While SMGs are faint in rest-frame UV, we need to remove the unresolved quasar's point spread function (PSF) to reveal the extended emission around them. In the following subsections we describe the method used to reveal the extended Lyα emission. For this, we develop new Python custom routines that construct and subtract the empirical quasar's PSF, similarly to what is usually done in the literature (e.g., Borisova et al., 2016; Husemann et al., 2018; Farina et al., 2019; O'Sullivan et al., 2020). In summary, we build a wavelength-dependent empirical quasar's PSF which is later subtracted from the datacubes, we then subtract continuum sources in order to obtain datacubes with pure extended line emission. The steps for this method are described below.

3.3.1   PSF Subtraction

The quasars in our sample all outshine the host galaxy at the wavelengths targeted by MUSE. As usually done in the literature, the PSF is computed at each wavelength by constructing pseudo narrow-band images of 150 channels (187 Å) centered at the quasar's position, and inside a box of size 6 times the seeing to ensure that its contribution at the largest radii is negligible. We describe how the seeing is estimated for each observation in Appendix 3.7.1.

We require that the PSF is not computed where we expect the extended line emission, corresponding to wavelength ranges affected by broad quasar lines (such as, e.g., Lyα, CIV, HeII). These wavelength ranges are neglected and their PSF is computed at the first available redshifted pseudo narrow-band. To identify where these wavelength ranges are, we design a custom routine that automatically detects the location of line emission as explained in detail in Appendix 3.7.2. In summary, we find the wavelength of local peaks in the spectra that indicate expected line emission and define a conservative spectral window of about $\Delta\lambda = 430 - 560$ Å ($\Delta v = 24400 - 26000\,\rm km\,s^{-1}$) centered on each line, which is excluded from computing the PSF. Such velocity ranges are much larger than the width

of the discovered emission (Section 3.4).

The empirical wavelength-dependent PSF is then rescaled at each layer to match the quasar's flux within the central $1\,\mathrm{arcsec}^2$. Due to possible cosmic rays, the scaling factor is computed from the average sigma clip of the normalization region. We subtract the rescaled PSF from the original datacube layer by layer, after masking negative pixels (at the edges of the PSF where it approaches the background) in order to not introduce spurious signal. In each field, we finally mask the $1\,\mathrm{arcsec}^2$ normalization region and exclude it from our analysis.

The resulting PSF subtracted datacubes are already able to highlight the extended emission around the quasars. However continuum sources in the field still need to be removed in order to not contaminate the extended emission.

3.3.2   Continuum subtraction

After subtracting the empirical PSF, we remove the contribution from continuum sources in all spaxels of our datacubes. For this, we first create a sky mask using the PSF-subtracted white light image, for which we estimate the noise floor using an average sigma clip algorithm and identify sources above 5 times this threshold. We estimate the continuum of the identified sources by smoothing their spectra at each spaxel using an order 5 polynomial, as done in the MPDAF Python package from Bacon et al. (2016). Finally we subtract the smoothed spectrum from each voxel of the identified sources. This process results in a datacube of only line emission. To check the robustness of our PSF and continuum subtractions we compare with the results from Drake et al. (2020) for BR1202-0725 and find consistent results for the Lyα emission (emission morphology and levels), though our data are deeper.

3.4   Results

The PSF- and continuum-subtracted cubes have been used to extract line emission nebulae associated with the five targets. Below, we focus on the surface brightness maps, integrated spectra, radial profiles and kinematics of the Lyα line emission. We also provide constraints on additional rest-frame UV line emission, C IV, Si IV, He II, and C III][2], when available within the MUSE wavelength range.

3.4.1   Lyα surface brightness maps and nebula spectra

To ease comparison with early narrow-band studies (e.g., Cantalupo et al., 2014), here we obtain SB maps by extracting $30\,\text{\AA}$ narrow-band maps centered at the peak of the Lyα extended emission from the continuum- and PSF-subtracted cubes. The peak is computed from the Gaussian fit to the integrated spectra inside a $3''$ radius aperture centered

---

[2]The C III] transition is a doublet of a forbidden and semi-forbidden transitions with wavelengths 1907 and 1909 Å, respectively.
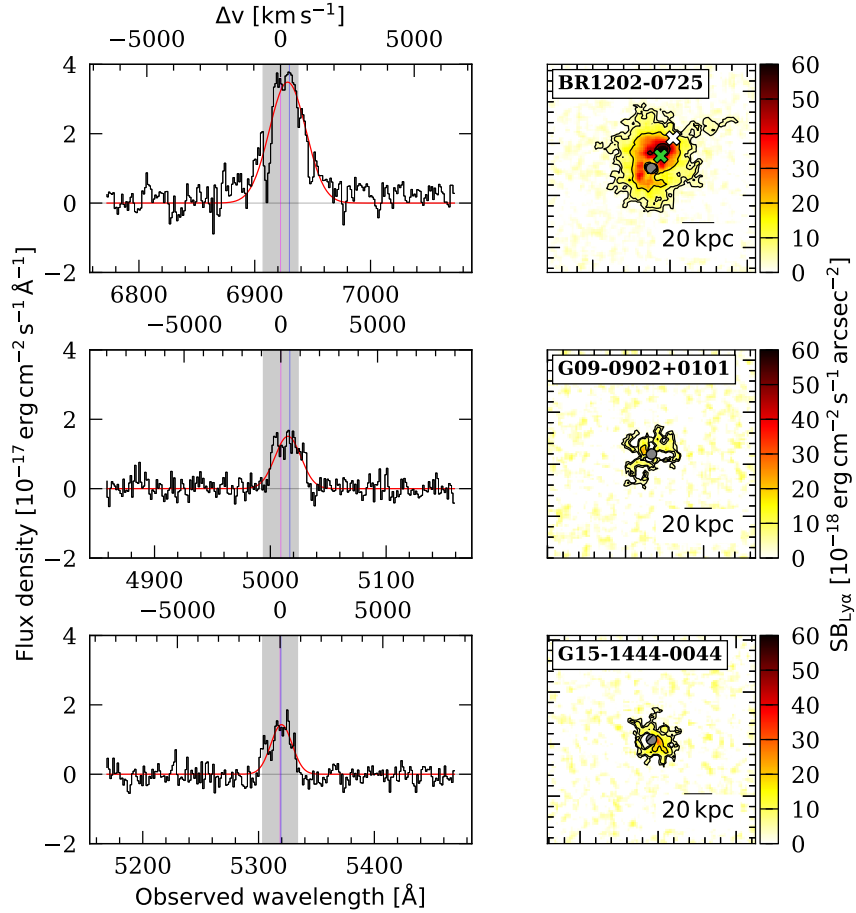
Figure 3.2: Integrated spectra and surface brightness maps of the extended Lyα emission around the three systems with AGN. *Left:* Spectra of the identified Lyα nebulae (black curve), integrated inside the 2σ contour. The gray shaded area shows the channels used to build the surface brightness map. The magenta vertical line indicates the Lyα wavelength from the systemic redshift of the quasars, while the blue vertical line indicates the wavelength at the peak of the Lyα spectra computed from the first moment of the line. Overlayed in red is a Gaussian fit to the spectra. The velocity shift and the FWHM of each system are listed in Table 3.3. The top axis of the spectra panels show the velocity shift with respect to the systemic redshift in $km\,s^{-1}$. *Right:* Lyα surface brightness maps of BR1202-0725 (top), G09-0902+0101 (middle) and G15-1444-0044 (bottom) at the expected wavelength from their systemic redshift (Table 3.1). The maps have a side of 20", corresponding to about 129, 152 and 148 kpc for BR1202-0725, G09-0902+0101 and G15-1444-0044 respectively. A scalebar of 20 kpc is indicated on each map. The black contours indicate surface brightness levels of $[2, 4, 10, 20, 50]\ \sigma$ (see Table 3.1). These maps are smoothed using a 2D box kernel of width of 3 pixels (0.6"). The central $1'' \times 1''$ region used for the quasar PSF normalization is masked and excluded from analysis. For BR1202-0725, we indicate the position of the Lyα emitter (LAE) and SMG companions (Carilli et al., 2013; Drake et al., 2020) with a green and white cross, respectively.
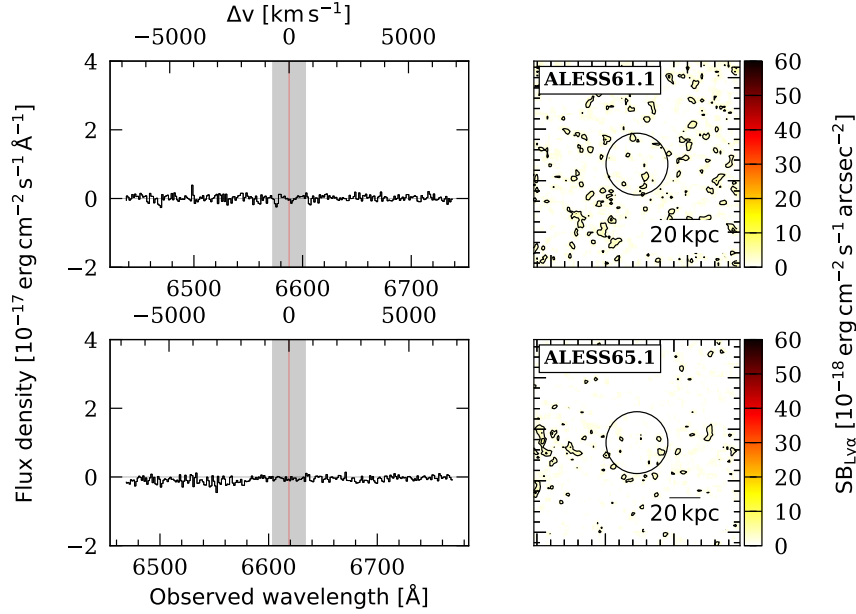
Figure 3.3: Integrated spectra and surface brightness maps of the two observed SMGs. *Left:* Spectra integrated inside of the 2″ radius aperture (black circle) of ALESS61.1 (top) and ALESS65.1 (bottom). The gray shaded area shows the channels used to build the surface brightness map, the magenta vertical line indicates the expected Lyα wavelength. *Right:* Lyα surface brightness maps of the two SMGs at the expected wavelength from their redshift shown in Table 3.1. The maps have a side of 20", which at their redshifts correspond to about 133 and 132 kpc for ALESS61.1 and ALESS65.1, respectively. A scalebar is shown for each map. These maps are smoothed using a 2D box kernel of width of 3 pixels (0.6"). The black circles indicate an aperture of radius 2″ centered at the SMG position.

at the quasar position after masking the $1\,\text{arcsec}^2$ normalization region. To test possible deviations from a Gaussian fit due to e.g. radiative transfer effects, we tested our calculation of the peak by estimating it using the first moment of the flux distribution within $\pm 2.5 \times \text{FWHM}$ of that fit. We found agreement between the two calculations. The SB maps for the quasar fields in our sample are shown in the right panel of Figure 3.2, and highlight the different morphologies and brightness that we find around these sources. Specifically, BR1202-0725 shows the largest Lyα luminosity ($\sim 3 \times 10^{44}\,\text{erg s}^{-1}$, or $\sim 2.7 \times 10^{44}\,\text{erg s}^{-1}$ if we mask the LAE inside a 1.6″ diameter aperture) and extent ($A = 3062\,\text{pkpc}^2$) (see Table 3.3). The two obscured quasars show a factor of ~ 10 times smaller Lyα luminosity and ~ 3 times smaller extent (see Table 3.3). An extended Lyα halo is not detected around the two SMGs at the current depth. This can be appreciated from the 30 Å SB maps at the expected Lyα wavelength shown in the right column of Figure 3.3, and also confirmed by inspecting their integrated spectra within a 2″ radius aperture (see left column of Figure 3.3). Appendix 3.7.3 presents the data shown in Figure 3.2 and 3.3 as χ_{smooth} maps

(e.g., Hennawi and Prochaska 2013).

Given that the detected nebulae are at a different redshifts, we test their extent also by using a common SB threshold corrected for cosmological dimming and compare to another sample presented in Arrigoni Battaia et al. (2023b). This work report luminosity–area relations for Lyα nebulae around $z \sim 2-3$ type-I quasars obtained using different SB thresholds. Because of the redshift of the targets and the sensitivity of our data, to compare the detected nebulae we use the reference relation, the $2\times$ and $4\times$ higher SB thresholds in that work for G09-0902+0101, G15-1444+0044, and BR1202-0725, respectively. By using these specific SB isophote, we find physical areas of 878, 651, 2651 kpc^2 and Lyα nebula luminosities of 7.5×10^{42}, 9.0×10^{42}, 18.9×10^{43} erg s^{-1}, respectively. These values are in agreement with the relations reported in Arrigoni Battaia et al. (2023b), indicating that also type-I quasars hosted by SMGs sit on these luminosity-area relations. Larger samples are needed to confirm this finding.

Further, we extract an integrated spectrum for the Lyα emission of each detected nebula by using all the spaxels within the 2σ contour of that nebula, shown in the left column of Figure 3.2). We fit a simple Gaussian profile to describe the linewidth of the nebulae spectra. We find that all the spectra have consistent broad (FWHM ~ 1500 km s^{-1}) line profiles, with the presence of Lyα absorption features. Such broad lines are not frequently seen around quasars (FWHM ~ 600 km s^{-1}; e.g., Borisova et al. 2016; Arrigoni Battaia et al. 2019a), possibly indicating more turbulent gas reservoirs in the highly star-forming environments targeted here. Interestingly, BR1202-0725 and G09-0902+0101 show integrated Lyα lines with positive shifts of the order of $300-400$ km s^{-1} with respect to the systemic redshift of each system, possibly indicating bulk winds. We note that G15-1444-0044 also show a similar shift when using the maximum of its Lyα line as reference velocity (see Table 3.3). These shifts are larger than the average positive shift found for quasars with good systemic redshifts (from e.g., [CII] 158 μm, 69 ± 36 km s^{-1}; Farina et al. 2019). We examine in detail the presence of an outflow for BR1202-0725 in Section 3.4.3.

Table 3.3: Summary of the properties of the detected nebulae and upper limits for non-detections.

Object	BR1202-0725	G09-0902+0101	G15-1444-0044	ALESS61.1	ALESS65.1
$L_{Ly\alpha}^{QSO\ (a)}$ $[\times 10^{43}\,erg\,s^{-1}]$	193.6 ± 0.1	14.3 ± 0.1	13.1 ± 0.1	–	–
$L_{Ly\alpha}^{Neb\ (b)}$ $[\times 10^{43}\,erg\,s^{-1}]$	30.4 ± 0.5	3.4 ± 0.1	3.3 ± 0.1	< 0.2	< 0.2
$L_{C\,IV}^{Neb\ (c)}$ $[\times 10^{43}\,erg\,s^{-1}]$	< 2.3	< 0.2	< 0.1	< 0.7	< 0.8
$L_{He\,II}^{Neb\ (c)}$ $[\times 10^{43}\,erg\,s^{-1}]$	< 4.5	< 0.1	< 0.1	< 1.0	< 1.0
Lyα Nebula Area$^{(d)}$ [arcsec^2] (pkpc^2)	73.0 (3062)	20.6 (1195)	17.5 (961)	–	–
$SFR_{Ly\alpha}^{Neb(e)}$ $[M_\odot\,yr^{-1}]$	276.9 ± 4.1	30.6 ± 0.9	30.2 ± 0.8	< 2	< 2
$\Delta v_{Neb-Sys}^{Ly\alpha\ (f)}$ $[km\,s^{-1}]$	319 ± 29	465 ± 273	39 ± 272	–	–
$FWHM_{Ly\alpha}^{Neb\ (g)}$ $[km\,s^{-1}]$	1603 ± 57	1578 ± 93	1219 ± 81	–	–
$SB_{Si\,IV}$ $\times[10^{-18}]^{(h)}$	< 0.5	< 0.6	< 0.7	< 0.7	< 1.2
$SB_{C\,IV}$ $\times[10^{-18}]^{(h)}$	< 1.0	< 0.8	< 0.6	< 1.3	< 1.3
$SB_{He\,II}$ $\times[10^{-18}]^{(h)}$	< 1.9	< 0.5	< 0.6	< 1.8	< 1.7
$SB_{C\,III]}$ $\times[10^{-18}]^{(h)}$	–	< 1.2	< 1.8	–	–

$^{(a)}$: Quasars' Lyα luminosities obtained by integrating each quasar spectrum in $\pm$FWHM of the nebular emission.

$^{(b)}$: Lyα luminosities within the 2σ contours of Figure 3.2 for the three quasars. For the two SMGs, 2σ upper limits rescaled assuming a nebula area of $20\,arcsec^2$ (from the 30 Å narrow-band).

$^{(c)}$: 2σ upper limits on the C IV and He II luminosities. For the three quasars, these are obtained for the Lyα nebula area within the the same velocity range as the fitted Lyα line ($\pm$FWHM$_{Ly\alpha}^{Neb}$). For BR1202-0725, most of the velocity range redwards of the He II line falls outside of the spectral range of the MUSE datacube, therefore we use the same velocity span but shifted to the last available channels. While for the SMGs, the limits are obtained assuming a nebula area of $20\,arcsec^2$ within a velocity range equivalent to the Lyα 30 Å narrow-band.

$^{(d)}$: Area of the Lyα nebulae inside the 2σ contour.

$^{(e)}$: SFR obtained from the Lyα luminosities listed in this table, assuming case B recombination and Formula 2 in Kennicutt (1998) (see section 3.5.1).

$^{(f)}$: Velocity shift between the quasars' systemic redshift and the Lyα peak velocity of the integrated nebula spectrum computed as first moment. For completeness, the velocity shifts computed using simply the maximum of each spectrum are 332 ± 29, 444 ± 273, and 382 ± 272 km s^{-1} for BR1202-0725, G09-0902+0101, and G15-1444-0044, respectively.

$^{(g)}$: FWHM of the Gaussian fit of the integrated Lyα emission shown in Figure 3.2.

$^{(h)}$: 2σ surface brightness limits for an aperture equivalent to the nebula area (assuming 20 arcsec^2 for the ALESS SMGs), and in a velocity range equivalent to the 30 Å narrow-band used for Lyα, in units of erg s^{-1} cm^{-2} arcsec^{-2}.
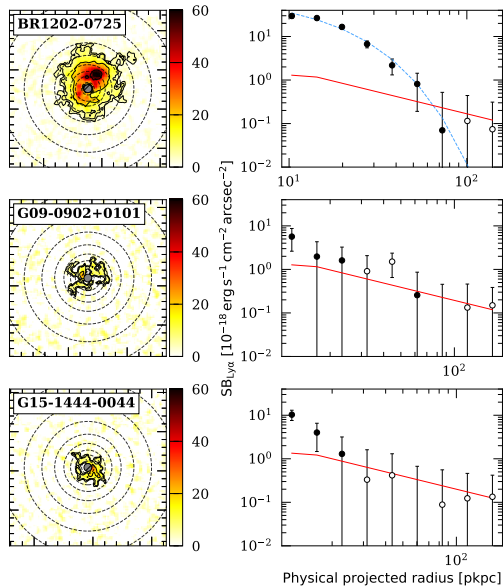
Figure 3.4: Lyα surface brightness radial profiles extraction. *Left:* Smoothed SB maps of the quasar sample (same as in Figure 3.2) with the circular apertures used to extract radial profiles overlaid. The gray circle in each map indicates the 1 arcsec^2 region used for the quasar's PSF normalization, which is neglected in our analysis. *Right:* Extracted radial profiles inside each annulus. Open circles indicate negative values shown here for completeness. The red line represents the 2σ SB limit rescaled to the area of each annulus. The blue dashed curve in the top panel is the best fit of the datapoints above the red line using an exponential function with the form $\mathrm{SB}_{Ly\alpha} = C \exp\left(-r/r_h\right)$, where $C = 85.3 \pm 13.8 \times 10^{-18}\,\mathrm{erg\,s^{-1}\,cm^{-2}\,arcsec^{-2}}$ and $r_h = 11 \pm 1\,\mathrm{pkpc}$.

3.4.2   Lyα surface brightness radial profiles

In order to describe the morphology and relative brightness of our nebulae, we build circularly averaged radial profiles as usually done in the literature (e.g., Arrigoni Battaia et al., 2019a; Fossati et al., 2021). The radial profiles are extracted from the 30 Å SB maps from Figures 3.2, using logarithmically spaced bins starting at about $1.6''$. The left panels of Figure 3.4 show the circular apertures used to extract the profiles overlaid on the SB maps for the detected sources, while the right panels show the individual extracted profiles. Filled circles represent positive mean SB values, while open circles represent negative mean SB values. In the same figure, the solid red line represents the 2σ SB limit within each ring. From these profiles it is evident that the QSO+SMG system BR1202-0725 has a more extended and bright nebula compared to the two SMGs hosting a QSO. We fit the observed SB profile of BR1202-0725 with both an exponential $\mathrm{SB}_{Ly\alpha} = C \exp\left(-r/r_h\right)$ and a power law $\mathrm{SB}_{Ly\alpha} = C r^{\alpha}$ as usually done in the literature, finding a better agreement with an exponential function. The scale length for the best fit is $r_h = 11 \pm 1\,\mathrm{kpc}$. We do not perform any fit on the other two detected nebulae given the limited radial range covered. We discuss further these SB profiles in comparison to other samples in the literature in Section 3.5.2.
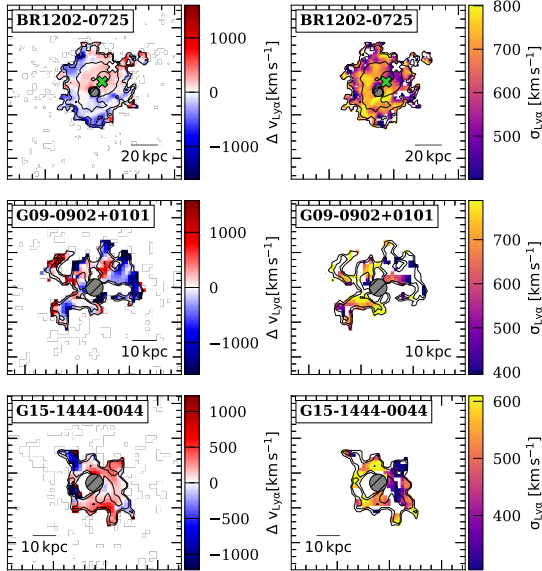
Figure 3.5: Kinematics of the detected Lyα nebulae. Velocity shift $\Delta v_{\mathrm{Ly}\alpha}$ maps (left column) with respect to the Lyα peak wavelength of the nebula (see Figure 3.2), and velocity dispersion $\sigma_{\mathrm{Ly}\alpha}$ maps (right column) of the Lyα nebula around the three quasars, computed from the first and second moment, respectively. The maps are smoothed as in Figure 3.2. The moment calculation is performed only inside the 2σ isophote of each nebula. The position of the LAE and SMG companion of the BR1202-0725 system are marked with a green and white cross, respectively. The side of the maps is 20" for BR1202-0725, and 10" for G09-0902+0101 and G15-1444-0044. A scalebar is shown for each map. The gray circle in each map indicates the 1 arcsec^2 region used for the quasar's PSF normalization, which is neglected in our analysis.

3.4.3 Lyα kinematics

Mean velocity shift and velocity dispersion maps

We compute velocity shift and velocity dispersion maps for our detected sources by building the first and second moment maps within narrow wavelength ranges, which are centered at the peak of their nebula Lyα spectrum and encompass $\pm$FWHM of their gaussian fit (see Table 3.3). Figure 3.5 shows the velocity shift maps and the velocity dispersion maps on the left and right columns respectively. The velocity shift maps are computed with respect to the Lyα line peak of each nebula and highlight the complex kinematics of the nebulae, likely affected by some Lyα resonant scattering. We select the Lyα line peak as reference to keep our sample homogeneous as we do not have an accurate systemic redshift for the SMGs hosting QSOs. We find that BR1202-0725 presents a clear blueshifted and redshifted component at velocities of $\sim \pm 400\,\mathrm{km\,s^{-1}}$. Larger velocity dispersions are seen close to the quasar (FWHM$\sim 1600 - 1800\,\mathrm{km\,s^{-1}}$), while we observe that the companion SMG (indicated with a white cross) is located, in projection, in a region with more quiescent kinematics with respect to the rest of the nebula (FWHM$\sim 1000\,\mathrm{km\,s^{-1}}$). This might be due to the fact that this zone is less turbulent or that dust absorbs some of the Lyα photons (e.g., Laursen et al., 2009). However, we stress that there is a substantial velocity shift between the SMG ($-142.1\,\mathrm{km\,s^{-1}}$, with respect to the systemic z; Drake et al. 2020) and the Lyα emission at its projected location ($\sim +400\,\mathrm{km\,s^{-1}}$), possibly indicating the presence of peculiar velocities between the galaxy and the gas, on top of radiative transfer

effects. Similarly, LAE1 shows a velocity offset of $+42$ km s^{-1} with respect to BR1202-0725 (Drake et al. 2020), which is smaller than the Lyα velocity offset at its projected location. We further study the large velocity components near the quasar in the BR1202-0725 system in Section 3.4.3.

The velocity shift and dispersion maps for G09-0902+0101 and G15-1444-0044 appear noisy, possibly due to their lower surface brightness levels and the complexity of the gas motions on these scales (e.g., Figure B1 in Costa et al., 2022). Deeper observations would be needed to study in detail their kinematics.

Evidence of violent kinematics in BR1202-0725

As mentioned in Section 3.4.3, we observe large Lyα velocity dispersions near the QSO position in the BR1202-0725 system. Indeed, we estimate a large Lyα FWHM (see Table 3.3), which could hint to the presence of large-scale outflows due to the QSO and star-formation activity. Similarly large Lyα FWHM (> 1000 km s^{-1}) has been observed in the CGM around a broad-absorption line (BAL) quasar (Ginolfi et al., 2018), suggesting that we observe broader Lyα emission when there are outflow signatures on small scales.

In this section, we further explore the aforementioned violent kinematics found in the Lyα nebular emission of BR1202-0725. This nebula is bright and therefore we can access the large velocity wings of its Lyα line. Specifically, we investigate the difference in the Lyα line shape in the regions with positive and negative velocity shifts as seen from its first moment map (see Figure 3.5). We show in the top left panel of Figure 3.6 the integrated spectra for regions with negative (blue) and positive (red) velocity shifts, with respect to the peak of the nebular Lyα emission. For the integrated spectrum at positive velocities we subtract the emission coming from a circular region of radius 1.6" centered at the LAE companion position (from Drake et al. 2020; see top-right panel in Figure 3.6) to be sensitive only to the emission from large-scale gas. Assuming this LAE follows a rescaled version of the average SB profile for LAE presented by Wisotzki et al. (2018), extended emission associated with the LAE outside the chosen aperture should be below our 2σ detection threshold, and therefore negligible.

We observe that both these spectra display large linewidths with wings at large velocities ($\Delta v > 1000\,\mathrm{km\,s}^{-1}$). However, the spectrum for the positive velocities shows an excess with a wing out to velocities as high as $\sim 2500\,\mathrm{km\,s}^{-1}$ that can be appreciated in the difference spectrum reported in the middle panel of Figure 3.6. Also, both spectra show the presence of an absorption feature at velocities $-470\,\mathrm{km\,s}^{-1}$. This feature was also reported in Drake et al. (2020), who suggested that it is due to a shell of outflowing material as usually invoked for the case of HzRGs (e.g., van Ojik et al. 1997) and quasar pairs (e.g., Cai et al. 2018; Arrigoni Battaia et al. 2019b).

Further, we investigate from which spatial region the largest velocity shifts are observable. The bottom panels of Figure 3.6 show Lyα SB maps of BR1202-0725 using velocity channels corresponding to the largest velocity shifts, indicated with blue and red shaded regions in the spectra at the top panel respectively. These maps show that the largest velocity shifts are located closer to the quasar position, extending out to about 20 kpc at
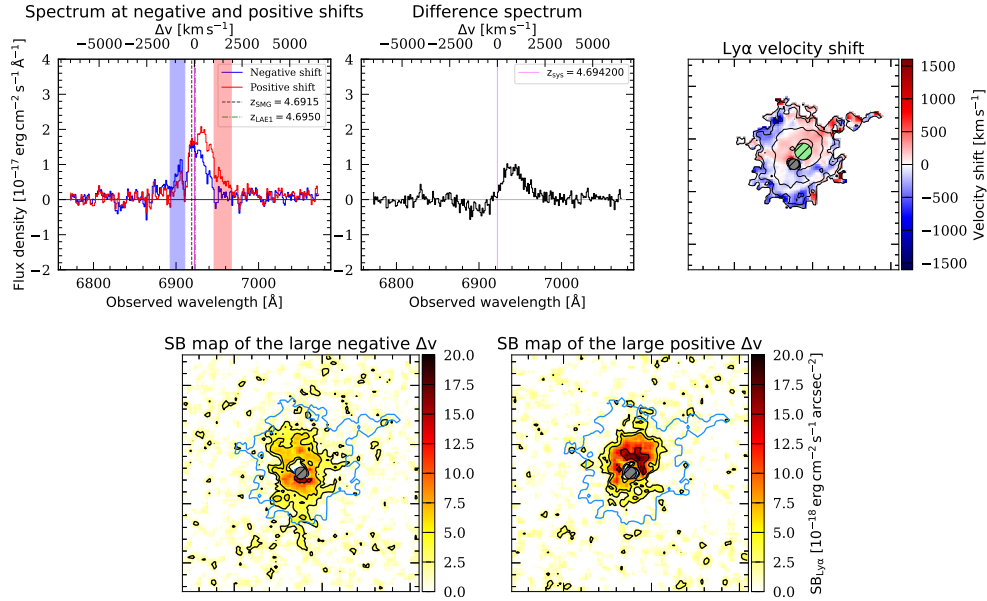
Figure 3.6: Violent kinematics in the Lyα nebula of BR1202-0725. *Top left:* Integrated spectra of regions with negative (blue curve) and positive (red curve) velocity shifts for BR1202-0725, with respect to the peak of the nebular Lyα emission (see Figure 3.2). The spectra are taken after masking the $1'' \times 1''$ region of the quasar's PSF subtraction and a circular region with diameter of 1.6" at the LAE companion position. We indicate with vertical lines the systemic redshift (solid magenta), the redshift of the SMG (black dashed) and LAE (green dot-dashed) companions (Carilli et al., 2013; Drake et al., 2020). *Top middle:* Residual spectrum between the positive and negative shift spectrum. We indicate the systemic redshift with a magenta line. *Top right:* Lyα velocity shift map computed from the first moment using a spectral window of ±FWHM centered at the peak of the nebular Lyα emission (see Table 3.3) and smoothed as in Figure 3.2. The position of the QSO and LAE companion masks are indicated with a gray and green hashed circle, respectively. *Bottom left:* Lyα SB map using the spectral channels with the largest negative shifts of the nebulae, indicated with a shaded blue region in the top left panel. The blue contours indicate the 2σ isophote of the extended emission shown in Figure 3.2. *Bottom right:* Lyα SB map using the spectral channels with the largest positive shifts of the nebulae, indicated with a shaded red region in the top left panel. Both of the SB maps at the bottom are smoothed as in Figure 3.2. All maps have a side of $20''$ and black contours indicating surface brightness levels of $[2, 4, 10, 20, 50]$ σ within the respective wavelength ranges.

the current depth. While all the described features are reminiscent of an outflow, radiative transfer modeling is needed to test this scenario (e.g., Chang et al. 2023). Such a modeling is ongoing and will be presented in a future publication.

3.4.4   Searching for C IV and He II extended emission

As mentioned in the introduction, the emission lines C IV and He II could be used to constrain the powering mechanism responsible for the observed nebulae, the hardness of the ionizing spectrum of the powering source and shock scenarios, the metallicity, and the extent of the enriched halo. For this reason we search for these lines in the final datacubes, together with additional rest-frame UV emission lines, Si IV and C III], that could be used to constrain the physical properties of the extended gas. For all the sources in our sample, we do not detect extended emission in these transitions. For completeness, we present in Figures 3.12, 3.13, 3.14, 3.15 and 3.16 of Appendix 3.7.3 χ_{Smooth} maps obtained for velocity ranges equivalent to the Lyα 30 Å NB and centered at the expected wavelengths for Si IV, C IV, He II and C III], respectively. For the BR1202-0725 system, the He II line is within the datacube spectral range, but the equivalent NB falls outside of the spectral range. Therefore we use the last available channels to compute this χ_{Smooth} map. Since there are no detections for any of these additional lines, we compute 2σ SB upper limits and rescale them to their respective Lyα nebula area and assuming 20 squared arcseconds for the ALESS SMGs, these values are shown in Table 3.3.

We estimate the C IV/Lyα and He II/Lyα ratio upper limits for the three systems with QSOs and discuss them in the context of the Lyα powering mechanisms in Section 3.5.1. These are estimated from the total Lyα luminosity of each nebula and the luminosity upper limits of C IV and He II (shown in Table 3.3). For BR1202-0725, the He II velocity range equivalent to the ±FWHM of the Lyα line is outside of the spectral range, therefore we use the same velocity span encompassing the line, but shifted to the last available channels to estimate this limit. Therefore, we caution that this upper limit may not fully represent the noise in the range ±FWHM of the He II line. However, as the He II line is expected to be narrower than the Lyα emission, the range used surely quantifies the absence of a He II detection in the current observation.

3.5   Discussion

3.5.1   Extended Lyman-α powering mechanisms

The variety of the systems studied here (QSO+SMG, two SMGs hosting a QSO, two SMGs) enables us to discuss the different mechanisms through which extended Lyα nebular emission could be produced. We will consider the following mechanisms: scattering of Lyα photons produced in compact sources, ionizing and Lyα photons produced by ongoing star formation, gravitational cooling radiation, shocks by galactic and/or AGN outflows, and AGN photoionization followed by recombination. In principle, all these mechanisms could

contribute together to the production of the observed extended emission and we discuss their relative roles below. In brief, by revisiting each of the aforementioned mechanisms we show that the firmest conclusion is that gravitational cooling is likely not contributing significantly in powering the observed extended Lyα emission.

Scattering of Lyα photons emitted by compact sources

Lyα photons produced in compact sources can scatter out in the surrounding gas distribution, producing an observable glow. In this scenario, the surface brightness of the extended nebular Lyα emission is therefore expected to be proportional to the Lyα photon budget from the QSO (e.g., Hennawi and Prochaska, 2013) and/or embedded galaxies, and no significant extended He II emission should be detected, as it is a recombination line (e.g., Prescott et al., 2015; Arrigoni Battaia et al., 2015b,a).

For the systems studied here, the dominant contribution of Lyα photons in BR1202-0725, G09-0902+0101 and G15-1444-0044 is clearly the AGN. Indeed, in close proximity to the extended Lyα emission BR1202-0725 has three LAEs ($F_{\mathrm{LAE1}} = (1.54 \pm 0.05) \times 10^{-16}\,\mathrm{erg\,s^{-1}\,cm^{-2}}$, $F_{\mathrm{LAE2}} = (0.54 \pm 0.05) \times 10^{-16}\,\mathrm{erg\,s^{-1}\,cm^{-2}}$ and $F_{\mathrm{LAE3}} = (0.24 \pm 0.03) \times 10^{-16}\,\mathrm{erg\,s^{-1}\,cm^{-2}}$; Drake et al. 2020), but their Lyα emission is only 3% of the quasar budget at those wavelengths (see Table 3.3; $(8.661 \pm 0.004) \times 10^{-15}\,\mathrm{erg\,s^{-1}\,cm^{-2}}$). Instead, G09-0902+0101 and G15-1444-0044 do not show LAEs in close proximity to their extended Lyα glow, while in the SMG fields we do not find evidence for any Lyα emitting sources. We compute an indicative number of Lyα photons available for scattering by integrating the quasar's spectra using the $\pm$FWHM of the nebular emission (luminosities listed in Table 3.3). We find that for each quasar system these photons would be able to power the observed Lyα nebulae, with the quasar Lyα luminosities exceeding by 6.4, 4.3 and 4.0 the nebular luminosities (computed in the same range; Table 3.3) for BR1202-0725, G09-0902+0101 and G15-1444-0044, respectively.

Interestingly, the Lyα luminosity of the quasar in the BR1202-0725 system is 14$\times$ greater than G09-0902+0101 and G15-1444-0044. In this scenario, if the conditions and environment of these three systems are similar, this would predict a 14$\times$ more luminous nebula around BR1202-0725. However, the dust mass in BR1202-0725 is on average 1.3$\times$ greater than in the two SMGs hosting QSOs, likely corresponding to a larger probability of Lyα absorption. Therefore, we would only expect a 10$\times$ more luminous nebula. This calculation aligns well with the observation that the nebula around BR1202-0725 is 9$\times$ more luminous than G09-0902+0101 and G15-1444-0044. Accordingly, the two SMGs, where no strong source of Lyα photons is observed, do not have an extended nebula. Therefore the systems studied here are consistent with a picture in which the extended Lyα level could be regulated by a combination between the QSO's budget of Lyα photons and the dust content of the host galaxy.

To further test this trend, we obtain the nebula and quasar Lyα luminosities for another system with known extended emission and dust mass estimate ($M_{\mathrm{dust}} = (9 \pm 3) \times 10^8\,\mathrm{M_\odot}$; Arrigoni Battaia et al. 2022), finding $L_{\mathrm{Ly\alpha}}^{\mathrm{Neb}} = (33.7 \pm 0.3) \times 10^{43}\,\mathrm{erg\,s^{-1}}$ and $L_{\mathrm{Ly\alpha}}^{\mathrm{QSO}} = (110.0 \pm 0.1) \times 10^{43}\,\mathrm{erg\,s^{-1}}$. We find that also this system follows the aforementioned
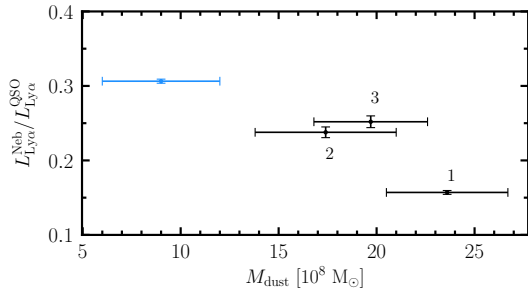
Figure 3.7: Ratio of the nebula and quasar Lyα luminosities versus the dust mass of the central host galaxy for the three quasars in our sample (black with IDs) and for the Fabulous system (blue; Arrigoni Battaia et al. 2022).

tentative trend. To visualize this finding, Figure 3.7 shows how the ratio $L_{\mathrm{Ly\alpha}}^{\mathrm{Neb}}/L_{\mathrm{Ly\alpha}}^{\mathrm{QSO}}$ decreases with M_{dust}.

We stress that previous works looking at variation of Lyα luminosities for quasars' nebulae against the QSO's budget of Lyα photons and/or the QSO's luminosity (e.g., Arrigoni Battaia et al., 2019a; Mackenzie et al., 2021a) found that if a relation is present, its scatter is large. However, those studies did not have any information on the dust properties of the host galaxies, which could be an important factor in finding a trend. Larger samples of QSO Lyα nebulae with well-studied QSO hosts are required to assess the contribution from this scenario.

Moreover, the detected nebulae present an anisotropic distribution and an offset between the quasar position and the peak of the Lyα emission. For example, BR1202-0725 shows no Lyα emission at the position of the dusty SMG (see white cross in Figure 3.2) and the peak of the Lyα distribution is closer to the LAE (see Figure 3.2) where we expect less dust content. The morphological differences and brightest part of the nebulae could therefore be due to the distribution of scattering atoms and dust around each QSO, with the denser regions and the dustier regions showing higher and lower Lyα emission, respectively. Therefore, due to all this, we cannot rule out that resonant scattering of the QSO's Lyα photons can contribute in powering the detected nebulae.

Finally, we stress two important caveats. First, the same morphological and surface brightness differences observed between the detected nebulae could also be due to variations in the gas physical properties (e.g., density, local dust content) in a photoionization scenario (see Section 3.5.1). Secondly, differences in surface brightness could also be produced due to the different local environment in which the extended emission is observed (e.g., presence of companion galaxies) as it is the case for BR1202-0725. We discuss this possibility in Section 3.5.2.

Star formation

The Lyα emission could also be powered by recombination radiation which follows photoionization by the strong star formation of the targeted sources. As any Lyα emission mechanism this process can be followed by resonant scattering, which we do not take into account in this section. In this scenario, the Lyα luminosity is expected to be proportional to the SFR of the embedded sources, modulo the escape fraction of their ionizing

and Lyα photons. We can get a rough estimate of the SFR needed to power the observed extended nebulae by assuming that all of the Lyα luminosity is produced by star formation under case B recombination ($L_{\mathrm{Ly}\alpha} = 8.7 L_{\mathrm{H}\alpha}$) and using the Equation 2 of Kennicutt 1998: $\mathrm{SFR}(\mathrm{M}_\odot\,\mathrm{yr}^{-1}) = L_{\mathrm{H}\alpha}/(1.26 \times 10^{41}\,\mathrm{erg\,s}^{-1})$. For the SMGs we do not find any extended Lyα emission, therefore we report upper limits for their Lyα SFRs. We compute them from their 2σ SB limit (for a $30\,\text{Å}$ narrow band) scaled to a similar nebula area as for the two SMGs hosting a QSO ($20\ \mathrm{arcsec}^2$). All the determined SFR values are listed in Table 3.3.

We compare these derived instantaneous SFRs (timescales up to $\sim 10\,\mathrm{Myr}$; Kennicutt and Evans 2012) with the SFRs estimated from the IR (timescales up to $\sim 100\,\mathrm{Myr}$; Kennicutt and Evans 2012), assuming a constant star-formation history. We find that the available star-formation is larger than that estimated from the Lyα, implying that it would be enough to power the detected Lyα nebulae, also when a very small ($2 - 5\%$) escape of ionizing photons is taken into account. Interestingly, a similar result was found for $z \sim 6$ quasars (median value $\lesssim 1\%$; Farina et al. 2019). However, the fact that we do not detect emission in the surrounding and proximity of the three SMGs in our sample (the two ALESS sources and the SMG companion of BR1202-0725), run counter to the star formation scenario. Indeed, the ratios between the detected nebular emission for the quasars in our sample (which are all hosted by SMG-like galaxies) and the upper limits for SMGs are $> 16-160$, much larger than the ratios between the SFRs for the targeted objects ($4-13$). In other words, if star-formation is the main powering mechanism of extended Lyα the SMGs should have nebulae with $L_{\mathrm{Ly}\alpha} = 4.4 \times 10^{43}\,\mathrm{erg\,s}^{-1}$, which would be detectable in the current dataset if they spread out on scales similar to the nebular emission around the two SMGs hosting a QSO. The fact that we do not detect such emission means that most of the ultraviolet photons produced by star-formation ($> 95\%$, using the 2σ limit) do not escape these galaxies. We stress that the dust contents estimated for the SMGs are the smallest in our sample (Table 3.1). Therefore it would be required a drastic change in dust geometry and dust grain properties between the different sources to ascribe the diversity of Lyα nebulae in this sample to star-formation. Thus, star formation seems to have a minor role in powering the extended emission in these sources.

Gravitational cooling radiation

Large-scale Lyα emission could be produced by gravitational cooling radiation, originating from cold streams accretion. Rosdahl and Blaizot (2012a) and Trebitsch et al. (2016) have done radiative transfer calculations to test this scenario, and found that it can reproduce the sizes and luminosities of extended Lyα emission in massive halos, together with their polarization pattern.

In this scenario, for the high DM halo masses inferred for our sources (see Section 3.2), uncertain analytical and numerical calculations predict the extended Lyα luminosities to be proportional to the DM halo masses, and the peak of the signal to be located at the center of the gravitational potential well (Dijkstra and Loeb, 2009; Faucher-Giguère et al., 2010). We stress upfront that the DM halo masses currently available are highly uncertain

(see caveats in Section 3.2.3). However, it is of interest to check whether they favor a gravitational cooling scenario, also to make predictions for future observations.

For the inferred DM halo masses we would expect G09-0902+0101 to have the brightest Lyα glow, followed by BR1202-0725 (1.6× dimmer), and then G15-1444-0044 and the SMGs (10× dimmer). However, the Lyα nebulae around SMGs hosting a QSO are 9 times fainter than the nebula around the QSO+SMG system. Moreover, in this scenario the SMGs should have extended emission only two times dimmer than BR1202-0725, but they are not detected at the current depth. Therefore there is no clear evidence that gravitational cooling powers these nebulae. This is also supported by recent cosmological simulations of high-redshift QSO halos post-processed with radiative transfer calculations (Costa et al., 2022). the contribution from gravitational cooling is about one order of magnitude lower compared to the effects of recombination and scattering of Lyα photons from the BLRs of quasars. A factor of ten lower emission with respect to the SMGs hosting a QSO cannot be detected in the current dataset.

To search for the gravitational cooling signal one should therefore target obscured isolated galaxies, such as the SMGs studied here. Indeed, in these objects there should be only a very minor contribution from the other mentioned mechanisms. To search for the gravitational cooling signal at a factor of ten lower SB level than for the SMGs hosting QSO studied here, one would need to be able to detect an average signal of the order of $SB_{Ly\alpha} \sim 4 \times 10^{-19}\,\mathrm{erg\,s^{-1}\,cm^{-2}\,arcsec^{-2}}$. This depth could be achieved at high significance (3σ) with a MUSE 75 hours exposure of an individual system or with a stack of multiple systems with an equivalent total exposure time. The detection of this signal would give an independent indication of the halo mass of SMGs and of its cool gas mass fraction.

Shocks by Galactic/AGN outflows

We observe broad Lyα linewidths (FWHM $\sim 1500\,\mathrm{km\,s^{-1}}$, see Table 3.3) in all our nebulae around QSOs. These FWHM are broader than usually reported in the literature (FWHM $<$ $940\,\mathrm{km\,s^{-1}}$, e.g., Borisova et al. 2016; Arrigoni Battaia et al. 2018; Fossati et al. 2021), suggesting the presence of violent kinematics (shocks) driven by the QSO and/or star-formation activity. Indeed, the sound speed in the ambient hot medium ($T \sim 5 \times 10^6\,\mathrm{K}$) for a $10^{12.5}\,\mathrm{M_\odot}$ dark-matter halo is $c_{\mathrm{s}} \approx 260\,\mathrm{km\,s^{-1}}$. Moreover, we observe a positive velocity shift in all our nebulae with respect to the QSO's systemic redshift (Figure 3.2), which could further indicate the presence of bulk outflows as traced by Lyα resonant scattering effects.

In order to build intuition about a shock scenario, we compare C IV/Lyα and He II/Lyα line ratios to those predicted by shock and shock+precursor models from Allen et al. (2008), as done in previous works (e.g., Arrigoni Battaia et al. 2015b; Herenz et al. 2020). When doing this, we imagine the Lyα extended emission as the result of shock fronts propagating at velocity v_{s} in a medium with pre-shock density n_{H}. In such scenario, the Lyα flux follows $F_{\mathrm{Ly\alpha}} \propto n_{\mathrm{H}} v_{\mathrm{s}}^3$ (Allen et al., 2008). We limit the models by Allen et al. (2008) to a realistic set of parameters for the nebulae here studied: $n_{\mathrm{H}} = 0.01, 0.1, 1.0, 10, 100\,\mathrm{cm^{-3}}$, and v_{s} in the range $100 - 1000\,\mathrm{km\,s^{-1}}$ in steps of $25\,\mathrm{km\,s^{-1}}$. We use models with solar
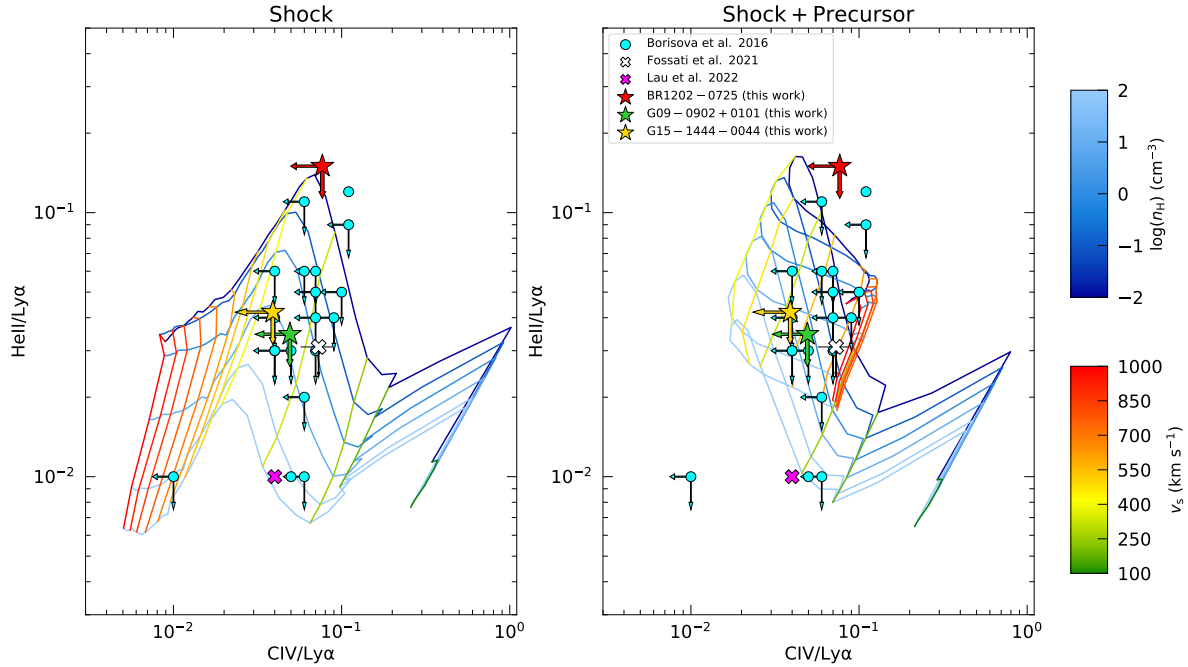
Figure 3.8: $C\,\textsc{iv}/\text{Ly}\alpha$ and $\text{He}\,\textsc{ii}/\text{Ly}\alpha$ line ratio upper limits (2σ) for the sources studied here with detected extended $\text{Ly}\alpha$ nebulae (star symbols). The line ratios are computed from the nebular luminosities listed in Table 3.3. The left panel shows the model grids for the shock scenario, while the right panel shows the model grids for the shock+precursor scenario from Allen et al. (2008). Overlayed are derived line ratios and upper limits for QSO nebulae from Borisova et al. (2016) as cyan circles, stacked nebulae around $z = 3-4.5$ QSOs inside a radial bin of $10 < R/\text{kpc} < 30$ from Fossati et al. (2021) as a white cross, and one extremely red quasar at $z \sim 2.3$ (Lau et al. 2022) as a magenta cross.

metallicity and adopt a magnetic parameter $B/n^{1/2} = 3.23\,\mu\text{G cm}^{3/2}$, which is expected for ISM gas assuming equipartition of magnetic and thermal energy. However, we stress that the selected models do not vary strongly with either of the two latter parameters because of the strong dependence of the ionizing flux on the shock velocity.

In more detail, in the shock models the emission is produced within the region ionized and excited by the shock. While in the shock+precursor scenario, it is taken into account also the component ionized by the extreme ultraviolet and X-ray emission emitted upstream from the shocked region[3]. We caution upfront that these models could underestimate the extended $\text{Ly}\alpha$ emission since the contribution of resonant scattering is not considered. This effect would therefore shift the grids to lower values for both ratios.

Figure 3.8 shows the $C\,\textsc{iv}/\text{Ly}\alpha$ versus the $\text{He}\,\textsc{ii}/\text{Ly}\alpha$ upper limits for our sources in

---

[3]More details on the physical mechanism at play in each model and on the production of different lines can be found in Allen et al. (2008).

comparison to literature data and the model grids taken from Allen et al. (2008). The quasars studied here are shown with star symbols. The values are computed from the integrated luminosities within the nebula area (see Table 3.3). The left panel shows the shock model grids while the right panel shows the shock+precursor model grids. We also compare our data-points to literature data for quasars' nebulae. Specifically, we indicate the line ratios for $z \sim 3.5$ QSO nebulae from Borisova et al. (2016), stacking results for nebulae around $z = 3-4.5$ QSOs inside a radial bin of $10 < R/\text{kpc} < 30$ from Fossati et al. (2021), and one extremely red quasar at $z \sim 2.3$ (Lau et al. 2022). We see that for the systems studied here the shock only scenario allows for larger shock velocities ($v_\text{s} \gtrsim 300$) than the shock+precursor scenario, which restricts velocities to $v_\text{s} \sim 300 - 500 \, \text{km s}^{-1}$. Most of the upper limits in the literature and our most stringent data would require pre-shock densities $n_\text{H} \gtrsim 0.5 \, \text{cm}^{-3}$ for both models. In the next section we show that similarly dense gas is needed in a photoionization scenario where Lyα scattering from the quasar is neglected (e.g., Arrigoni Battaia et al., 2015a).

Photoionization from AGN followed by recombination

Unlike the quasars studied here, the SMGs do not present Lyα emission at the current depth, indicating that AGN are vital for the powering of the observed extended nebulae. We note that even though all the QSOs in our sample are hosted by SMGs, they have a spectra consistent with the average unobscured quasar templates (e.g., Lusso et al. 2015, see Appendix 3.7.4). In section 3.5.1 we discussed the likely contribution of resonant scattering of the AGN Lyα photons in powering the large-scale Lyα emission. Here, instead, we assess the impact of AGN photoionization on the observed Lyα surface brightness following the framework presented in Hennawi and Prochaska (2013). In this scenario, the Lyα signal is produced in the recombination cascade following the gas photoionization due to the central AGN. The cool ($T \sim 10^4 \, \text{K}$) gas is assumed to be organized in small clouds with a single constant hydrogen volume density n_H, constant hydrogen column density N_H, and uniformly distributed within a spherical halo of radius R, such that the clouds covering factor is f_C. The Lyα surface brightness can then be estimated using simple relations for two limiting cases, optically thick ($N_\text{HI} \gg 10^{17.2} \, \text{cm}^{-2}$) and optically thin ($N_\text{HI} \ll 10^{17.5} \, \text{cm}^{-2}$) gas to ionizing radiation.

In the optically thick scenario, a thin surface of the gas clouds will emit Lyα photons proportionally to the number of impinging ionizing photons (determined by the specific luminosity at the Lyman edge, L_{ν_LL}) and decreasing with distance from the quasar as R^{-2}. The Lyα SB in the optically thick regime ($\text{SB}_\text{Ly}\alpha^\text{thick}$) is given by equation 15 of Hennawi and Prochaska (2013).

As done in Arrigoni Battaia et al. (2019b), we estimate L_{ν_LL} of the quasars assuming a spectral energy distribution (SED) described by a power law of the form $L_\nu = L_{\nu_\text{LL}}(\nu/\nu_\text{LL})^{\alpha_\text{UV}}$ and slope $\alpha_\text{UV} = -1.7$ as obtained by Lusso et al. (2015). We show a comparison of the QSOs spectra and assumed SEDs in Figure 3.17 from Appendix 3.7.4, and confirm that these standard QSO templates adjust to our dataset. In particular, we stress that the two SMGs hosting a QSO in our sample are not obscured in their rest-frame UV

along the line of sight, as discovered by Fu et al. (2017). We find $\log(L_{\nu_{\mathrm{LL}}}/[\mathrm{erg\,s^{-1}\,Hz^{-1}}])$ values of 31.8, 30.4 and 30.6 for BR1202-0725, G09-0902+0101 and G15-1444-0044 respectively. We estimate the observed $\mathrm{SB}_{\mathrm{Ly}\alpha}^{\mathrm{thick}}$ at the same distance $R = 13\,\mathrm{kpc}$ for all of the nebulae and compare to the observed values at the same distance, which is the maximum projected distance in common to all studied nebulae. We assume a covering factor of $f_{\mathrm{C}} = 1$ for the clouds ($f_{\mathrm{C}} > 0.5$ as favored by the observed diffuse morphologies, e.g., Arrigoni Battaia et al. 2015b) and hydrogen column density of $N_{\mathrm{H}} = 10^{20.5}\,\mathrm{cm^{-2}}$, as the median value obtained in absorption studies of $z \sim 2$ quasar halos (Lau et al. 2016). In principle the covering factor could be even $f_{\mathrm{C}} > 1$, indicating a clumpy medium with a larger volume filling factor. However we chose a value of 1 to simplify equations and ease comparison with previous works. We derive $\mathrm{SB}_{\mathrm{Ly}\alpha}^{\mathrm{thick}}$ values of 16.5, 2.6 and $2.8 \times 10^{-15}\,\mathrm{erg\,s^{-1}\,cm^{-2}\,arcsec^{-2}}$ for BR1202-0725, G09-0902+0101 and G15-1444-0044 respectively. These values are a factor of $500 - 600$ times greater than the observed values at the same distance, which are 24.6, 4.3 and $5.5 \times 10^{-18}\,\mathrm{erg\,s^{-1}\,cm^{-2}\,arcsec^{-2}}$ for BR1202-0725, G09-0902+0101 and G15-1444-0044 respectively. Therefore we conclude that a pure optically thick regime is unlikely to be found in these systems, unless very small covering factors ($f_{\mathrm{C}} \sim 0.002$) or a very small escape of Lyα photons are considered. This is consistent with several previous works (e.g., Arrigoni Battaia et al. 2015a, 2019b; Farina et al. 2019; Drake et al. 2020).

Consequently, if the quasar directly shines on the surrounding gas, it is more likely in place an optically thin scenario, where the gas is highly ionized and the Lyα recombination signal depends on the gas properties (n_{H}, N_{H}; equation 10 of Hennawi and Prochaska 2013). Considering the Lyα SB in the optically thin regime ($\mathrm{SB}_{\mathrm{Ly}\alpha}^{\mathrm{thin}}$) as the observed average SB at $R = 13\,\mathrm{kpc}$, we estimate the gas volume density n_{H} needed to power the observed Lyα nebulae, assuming once again a covering factor of $f_{\mathrm{C}} = 1$ and hydrogen column density $N_{\mathrm{H}} = 10^{20.5}\,\mathrm{cm^{-2}}$. We find values for n_{H} of 13.3, 0.6 and $1.0\,\mathrm{cm^{-3}}$ for BR1202-0725, G09-0902+0101 and G15-1444-0044, respectively[4]. These large ISM-like values are usually inferred by other observational studies targeting quasar nebulae (see e.g., Hennawi et al., 2015; Arrigoni Battaia et al., 2015a; Cai et al., 2018; Arrigoni Battaia et al., 2019b), however those studies did not have information on the dust content of the QSO's host galaxies. The density values are high for CGM gas compared to those found from simulations for $z \sim 3$ massive systems (Rosdahl and Blaizot, 2012a), which are not able to resolve this gas phase.

Recent observational works showed that the high-z CGM has a multiphase nature, with even molecular gas detections on tens of kpc around some active objects (e.g., high-redshift radio galaxies, Emonts et al. 2016; quasars and SMGs, Vidal-García et al. 2021). It seems therefore realistic that the simulations need large clumping factors[5] to match the observed Lyα surface brightness on CGM scales (e.g, Cantalupo et al., 2014; Arrigoni Battaia et al., 2015a; Cai et al., 2018). However, it is still a matter of debate how strong the clumping needs to be. Large clumping factors are required when assuming only recombination

---

[4]We compute the density values at a specific distance neglecting dust at that location. We stress that changes in the Lyα surface brightness morphology in a photoionization scenario can be due to changes in the density and dust content.

[5]The clumping factor is usually defined as $C = \langle n_{\mathrm{H}}^2 \rangle / \langle n_{\mathrm{H}} \rangle^2$ (e.g., Cantalupo et al., 2014).

($C \sim 1000$, Cantalupo et al. 2014), while a contribution from other mechanisms (i.e., collisional excitation and/or resonant scattering of QSO's Lyα photons) would result in a more moderate clumping.

If the photoionization scenario is the dominant mechanism, we would expect to detect, in deep observations, additional emission lines (e.g., He II) from the quasar's CGM. In particular, in a recombination-only scenario, the He II/Lyα ratio should be ~ 0.3 if Helium is fully doubly ionized (Arrigoni Battaia et al., 2015a; Cantalupo et al., 2019). Lower fractions of fully ionized Helium and the contribution of additional mechanisms in the budget of Lyα photons would result in lower ratios. Stacking analysis of $z \sim 3-4$ quasars clearly detected extended Lyα and C IV, and only marginally He II (e.g., Fossati et al. 2021). That work emphasized that Cloudy photoionization models of gas on CGM scales require scattering of the quasars' Lyα photons to match the observed line ratios using reasonable values for CGM metallicities. Since we detect Lyα emission and do not detect He II, resulting in similar upper limits as Fossati et al. (2021) (He II/Lyα < 0.03), we cannot provide further insights on this problem. Future works are needed to establish the relative contribution of recombination and QSO's Lyα scattered photons to the Lyα glow on CGM scales.

3.5.2   Comparison with previous Lyα SB radial profiles

Figure 3.9 shows the SB radial profiles of the three detected targets as red stars, green and yellow diamonds for BR1202-0725, G09-0902+0101 and G15-1444-0044, respectively, as a function of comoving projected radius, and corrected by cosmological dimming. The profiles are shown only for annulus above the 2σ SB limit for that ring (red line of Figure 3.4). Once again, it is evident that the nebulae associated with the SMGs hosting a QSO are dimmer and more compact than the one around the QSO+SMG system. Further, the same figure shows a comparison with different samples from the literature (see figure caption and legend), highlighting the respective $25-75$ percentile ranges when available. We find that the sources in our sample are outliers for any of the $z \gtrsim 3$ bright quasar samples (Arrigoni Battaia et al., 2019a; Farina et al., 2019; Fossati et al., 2021). However, we find that our faint, but submillimeter-bright $z \sim 3$ quasars present nebulae akin to those found around similarly faint ($i_{\mathrm{mag}} < 19.5$) $z \sim 3$ quasars (Mackenzie et al. 2021a), and that resemble the median profile from the lower redshift ($z \sim 2.3$) sample from Cai et al. (2019). This once again stresses the large difference between nebulae of bright $z \sim 2.3$ quasars and those of bright $z \sim 3$ quasars, which has been argued to be most likely driven by a different halo accretion regime (e.g., Arrigoni Battaia et al. 2019a; Farina et al. 2019; Fossati et al. 2021). For completeness, we also show the observed average SB profile of $z = 2.65$ Lyman Break Galaxies (LBGs) from Steidel et al. (2011). These galaxies are sources at the lower end of the halo masses probed by our sample (median halo mass of $M_{\mathrm{DM}} = 9 \times 10^{11}\,\mathrm{M}_\odot$; Steidel et al. 2011), and show both signatures of Lyα emission and absorption on galaxy scales, but they do not have an AGN contribution. LBGs clearly have an SB profile fainter than sources hosting QSOs, further stressing the importance of AGN in powering strong Lyα emission.
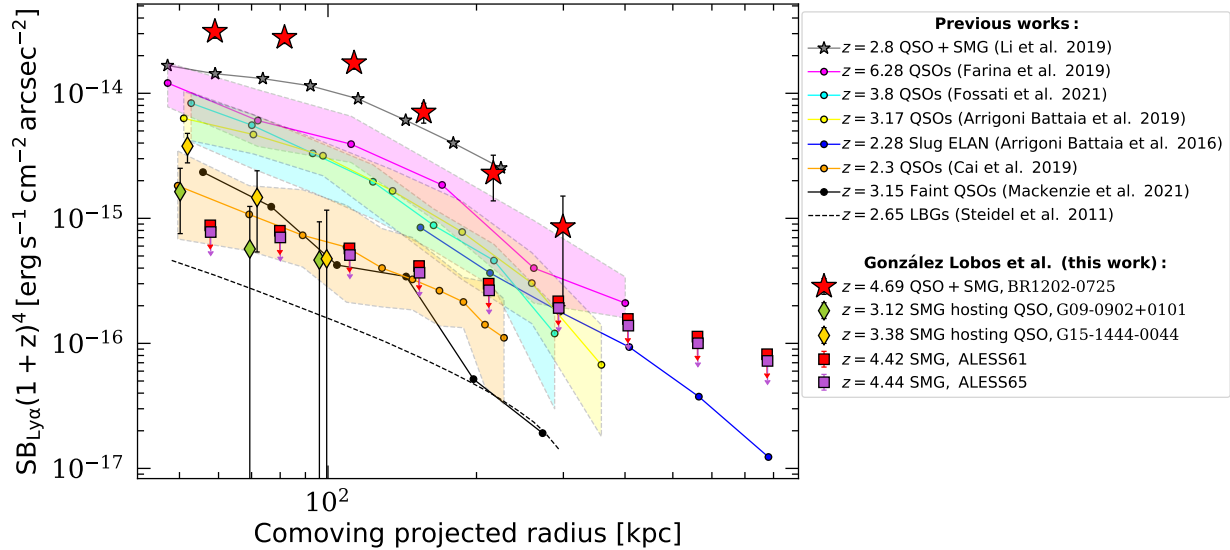
Figure 3.9: Circularly averaged SB as a function of comoving projected radius of the nebulae detected in our quasar sample (red stars, green and yellow diamonds for BR1202-0725, G09-0902+0101 and G15-1444-0044, respectively), corrected for cosmological dimming. The red and purple squares with arrows indicate the upper limits for ALESS61.1 and ALESS65.1, respectively. Different profiles from the literature are indicated as colored circles with their respective $25-75$ percentile ranges when available. The $z = 3.17$ sample of the QSO MUSEUM from Arrigoni Battaia et al. (2019a) is shown in yellow. The SB profile (taken from Arrigoni Battaia et al. 2016) of the $z = 2.28$ Slug Enormous Lyα Nebula (ELAN) is shown in blue (Cantalupo et al. 2014). The $z = 6.2$ quasar sample from Farina et al. (2019) is shown in magenta. The $z = 3.8$ quasar sample from Fossati et al. (2021) is shown in cyan. The $z = 2.3$ quasar sample from Cai et al. (2019) is shown in orange. The median profile of the faint quasar sample at $z = 3$ from Mackenzie et al. (2021a) is shown with black connected circles. We computed the SB profile of the galaxy group SMMJ02399 comprising a quasar and an SMG at $z = 2.8$ from Li et al. (2019) (gray connected circles). Finally, the fit to the observed SB profile for $z = 2.65$ LBGs from Steidel et al. (2011) is shown with the black dashed curve.

On the other hand, the QSO+SMG system BR1202-0725 has clearly an enhanced brightness with respect to all other profiles. This could be due to several factors, like (i) the merger state of this system with interacting galaxies (an SMG, a QSO host and a LAE), likely providing a larger reservoir of cool gas with respect to individual halos and possible supply for diffuse star formation (e.g., Decarli et al. 2019), (ii) the presence of dense gas on CGM scales, as directly evident from the presence of a bridge of [C II] emission between the QSO and the SMG (Drake et al., 2020), and (iii) presence of galactic and AGN winds/outflows that could enhance densities in their surroundings and/or favor the escape of Lyα photons (e.g., Costa et al. 2022). To confirm whether brighter SB profiles are typical for QSO+SMG systems, we extract the radial profile for the SMMJ02399 system at $z = 2.8$ (gray points) from Li et al. (2019). This system is also known to have a multiphase CGM with a cold diffuse molecular phase extending out to at least ~ 20 kpc (Vidal-García et al. 2021). We also find that this system is at the high end of the radial profiles, even though its redshift is lower. This finding further suggests that QSO+SMG systems are the pinnacle of Lyα emission at each redshift. Further evidence of this comes from the comparison of the SB radial profile of the $z \sim 2.28$ Slug Enormous Lyα Nebula (ELAN, blue points) from Arrigoni Battaia et al. (2016) with the profiles of similar bright quasars at $z \sim 2$ (Cai et al., 2019). The Slug ELAN is known to host an SMG undergoing ram-pressure stripping within the halo of a bright QSO (Chen et al. 2021). Similar to the aforementioned cases, the SB profile of the Slug ELAN is above the average $z \sim 2$ quasars' profile. However, its SB profile is not as high as the one found for BR1202-0725 and SMMJ02399, possibly indicating a difference in the densities and reservoir of cool material around these systems from high to low redshift (e.g., Arrigoni Battaia et al. 2019a). In the same figure we also indicate the 2σ upper limits for the SB inside each ring for the SMGs, as the red (ALESS61.1) and purple (ALESS65.1) squares with arrows. We find that the Lyα SB for isolated SMGs is at least a factor of 2 fainter than that of quasars at similar redshifts.

Finally, we compare the scale length $r_\mathrm{h} = 11 \pm 1$ kpc obtained for BR1202-0725 in Section 3.4.2 with those reported for the average profiles of type-I quasars at bracketing redshifts $z \sim 3$ and $z \sim 6$. We find that BR1202-0725 sitting at $z = 4.6942$ has a scale length smaller (larger) than the sample at $z \sim 3$ ($z \sim 6$) when looking at physical scales, $r_\mathrm{h} = 15.7$ kpc (Arrigoni Battaia et al. 2019a) and $r_\mathrm{h} = 9.4$ (Farina et al. 2019), respectively. This would translate to similar scale lengths in comoving units as can be appreciated in Figure 3.9. Larger samples of quasar's nebulae at $z \sim 5$ are needed to firmly constrain these values.

3.6   Summary

With VLT/MUSE, we targeted five z $\sim 3 - 4$ submillimeter-bright systems to unveil extended Lyα emission, discuss the contribution of different powering mechanisms, as well as compare our results to the plethora of z > 2 quasar observations. Specifically, our observations comprise systems with different degrees of quasar illumination: a QSO+SMG system (BR1202-0725), two SMGs hosting a QSO (G09-0902+0101 and G15-1444-0044),

and two SMGs (ALESS61.1 and ALESS65.1). All these objects are expected to sit in halos as massive as those hosting quasars (section 3.2). Below, we summarize our observational findings:

- We find that our targets have very different Lyα morphologies and brightness levels. The QSO+SMG system presents the highest levels of Lyα emission, probably reflecting the richness of its halo environment in terms of mass and density of the cool gas phase (top panel of Figure 3.2 and section 3.5.2). We do not detect any extended Lyα emission around the two SMGs.

- All the detected Lyα nebulosities present more violent kinematics (FWHM$\gtrsim 1200\,\mathrm{km\,s^{-1}}$) with respect to nebulae around quasars at similar redshifts (FWHM$\sim 600\,\mathrm{km\,s^{-1}}$; Arrigoni Battaia et al. 2019a; Fossati et al. 2021). In particular, we find evidence of large-scale outflows in the BR1202-0725 system (Figure 3.4.3).

- None of the targeted systems show extended emission in other rest-frame UV lines besides Lyα down to $\sim 10^{-18}$ erg s^{-1} cm^{-2} arcsec^{-2} (2σ in 30 Å; Section 3.4.4).

- The two SMGs hosting a QSO have CGM Lyα profiles about 3 times fainter than the typical z $\sim$ 3 quasar halo, resembling the median profile of similarly faint quasars Mackenzie et al. (2021a) (Figure 3.9; section 3.5.2). We also find that their Lyα emission is at similar levels than the emission around bright z $\sim$ 2 quasars, further indicating the remarkable difference between the Lyα emission around bright z $\sim$ 2 quasars and higher redshift quasars (e.g., Arrigoni Battaia et al. 2019a; Farina et al. 2019; Fossati et al. 2021).

We then discuss our observational results in the context of the relative roles of the different Lyα powering mechanisms presented in Section 3.1: resonant scattering of Lyα photons for embedded sources, gravitational cooling radiation, shocks by galactic/AGN outflows, and photoionization from AGN or star-formation followed by recombination. We briefly summarize our results here.

Cooling radiation is unlikely to be the main powering mechanism, because we would expect the Lyα emission to scale proportionally to the halo mass (see Section 3.5.1). Therefore, we should have detected similar levels of Lyα emission for the similar halo masses of our sample (e.g., Haiman et al., 2000; Rosdahl and Blaizot, 2012a). We propose that more observations of obscured systems, such as isolated SMGs, could provide test cases for this scenario.

We cannot rule out that resonant scattering of Lyα photons emitted by compact sources could have a significant contribution to the observed nebulae. Indeed, we observe that the extended Lyα level is consistent with being regulated by the budget of QSO Lyα photons modulo the dust content on galaxy scales. Sources with no Lyα emission on small scales, i.e. the SMGs, do not show extended Lyα emission. However, due to the small size of our sample we cannot provide firm constraints on the relationship between the extended Lyα

luminosity and the budget of QSO Lyα photons. Therefore larger samples of QSO Lyα nebulae with information on their host galaxies are needed.

Regarding the star-formation scenario, by comparing the inferred $\text{SFR}_{\text{Ly}\alpha}$ between our nebulae (Table 3.3) to the derived SFR from their total IR luminosity (Table 3.2), we show that the available star-formation in these systems should be enough to power the Lyα nebulae (see Section 3.5.1). However, the fact that we do not detect extended Lyα emission around the SMGs suggests that photoionization due to star-formation followed by recombination (and resonant scattering) has a minor role in powering these nebulae likely because most of the UV and Lyα photons from star-formation do not escape these dusty galaxies.

Also, the aforementioned presence of large Lyα linewidths and positive velocity shifts (Table 3.3) of the QSO's nebulae motivates us to test a large-scale outflow scenario in Section 3.5.1. We compare the C IV/Lyα and He II/Lyα line-ratio upper limits with shock and shock+precursor models from Allen et al. (2008). We find that the ratios for our systems agree with the models with shock velocities $v_{\text{s}} \geq 300 \, \text{km s}^{-1}$ for the shock only scenario and $v_{\text{s}} \sim 300 - 500 \, \text{km s}^{-1}$ for the shock+precursor scenario. Both cases allow for a high pre-shock density of $n_{\text{H}} \geq 1 \, \text{cm}^{-3}$, usually not resolved in cosmological simulations and expected within the interstellar-medium.

Moreover, we find that the AGN presence is essential for powering the observed Lyα halos, as only systems with quasars show an extended Lyα glow, highlighting the importance of photoionization from the central AGN as a contribution to the extended Lyα emission. We test the contribution of photoionization from the quasar followed by recombination in Section 3.5.1, under the assumption of two limiting scenarios: optically thick and optically thin to ionizing radiation. Assuming the quasar is illuminating the gas, we find that our data favors an optically thin scenario, which requires an average volume density of $n_{\text{H}} \sim 1 - 10 \, \text{cm}^{-3}$, as frequently found in previous studies (e.g., Arrigoni Battaia et al. 2015b; Hennawi et al. 2015; Cai et al. 2018).

Summarizing, we find evidence against gravitational cooling radiation to be the main powering mechanism of the detected extended Lyα emission. On the other hand, photoionization, outflows and resonant scattering of Lyα photons from compact sources are likely contributors to the observed Lyα nebulae. Our pilot work opens the path to the analysis of CGM emission around high-z massive systems taking into account the properties of quasar's hosts (e.g., Muñoz-Elgueta et al. 2022) and embedded galaxies, frequently overlooked in the study of large-scale emission. Future large statistical samples together with statistical investigations of mock observations are needed to confirm and extend our findings. Moreover, future JWST observations of extended Hα emission around QSOs could help disentangling the powering mechanisms discussed in this work.

3.7 Appendix

3.7.1 Seeing as a function of wavelength

As mentioned in Section 3.3, we subtract the wavelength-dependent unresolved quasar's PSF in order to reveal extended Lyα emission. The PSF is subtracted centered at the quasar position and out to six times the seeing, this value is chosen so that the PSF profile becomes consistent with zero. To estimate the seeing we perform a 2D Moffat fit to pseudo narrow-bands (width of 25 Å) of stacked point sources in each field as a function of wavelength.

The 2D Moffat model is given by:

$$f(x, y) = A \left(1 + \frac{(x - x_0)^2 + (y - y_0)^2}{\gamma^2} \right)^{-\beta}, \qquad (3.1)$$

where A is the scale amplitude, x_0 and y_0 are the point source centroid coordinates, γ is the core width of the model, and β is the power of the model. The seeing is obtained from the FWHM of the Moffat profile, given by $\mathrm{FWHM} = 2\gamma\sqrt{2^{1/\beta} - 1}$. We show in Table 3.1 the seeing at the expected Lyα wavelength of each field.

We show in Figure 3.10 an example of the wavelength-dependent FWHM and β of one of the quasar's empirical PSF, i.e. for BR1202-0725. We exclude wavelengths significantly affected by the Lyα forest (< 5600 Å) and indicate with gray shaded regions the wavelength ranges where extended Lyα emission is conservatively expected and therefore the PSF is kept constant (see Section 3.3.1 and Appendix 3.7.2). We find an expected decrease with wavelength of the FWHM and a close to constant β parameter consistent with the trend and values found in previous MUSE studies ($\beta \sim 1.7$; e.g., Fusco et al., 2020). In Figure 3.10 we also show a power-law fit to the FWHM as a function of wavelength, which is consistent with the seeing at the Lyα wavelength reported in Section 3.1 from point sources. This fit excludes the gray shaded regions as these are constant by construction.

3.7.2 Line emission identification

As mentioned in Section 3.3.1, in order to not subtract the extended emission we are interested in, we construct the wavelength-dependent empirical PSF of each quasar only where there is no line emission. For this, we create a routine that identifies peaks of line emission at the expected wavelengths. This routine is only intended to identify the location in wavelength of the line emissions, instead of characterizing the line emission of the quasar. We detect line emission by integrating a spectrum at the quasar location inside a 1 arcsecond diameter aperture, shown in Figure 3.11. We then use a median filter to create two smoothed spectra, one that highlights the QSO spectrum broad lines (smooth spectrum) and another that smooths out the broad line features ("continuum" spectrum[6]). The

---

[6]In practice, this is not intended to be a perfect characterization of the quasar continuum, but it allows us to quickly identify the location of the line emission.
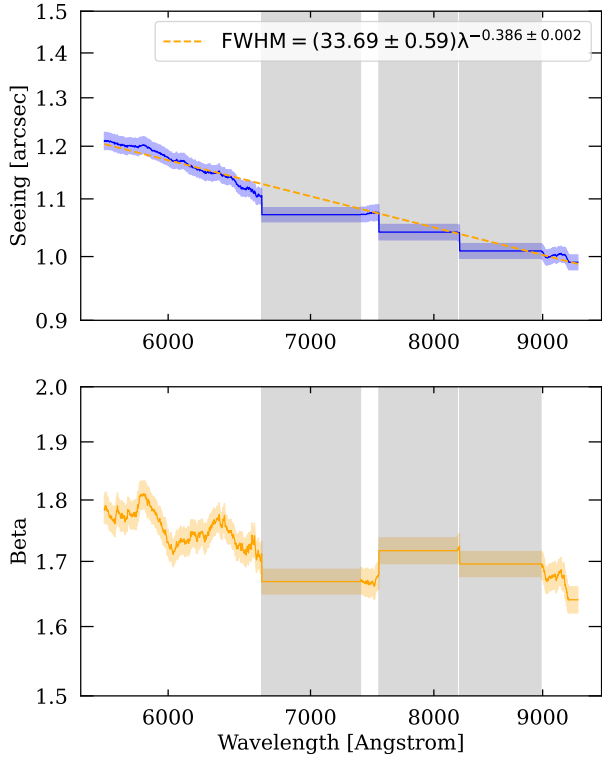
Figure 3.10: Properties of the wavelength dependent Moffat fit used to estimate the seeing for BR1202-0725. *Top:* Seeing (FWHM of the Moffat fit) as a function of observed wavelength of BR1202-0725's PSF (blue) with its respective 1σ uncertainty as shaded region. The power law fit is shown with a dashed orange line and the fitted parameters are shown in the legend. *Bottom:* Beta parameter of the fitted Moffat profile as a function of wavelength with its respective 1σ uncertainty.

smooth spectrum uses a median filter of 50 spectral channels ($62.5\,\text{Å}$), while the "continuum" spectrum uses a median filter of 500 spectral channels ($625\,\text{Å}$). We find where these two spectra intersect by creating a difference spectrum between the smooth and continuum spectrum, we then identify the lines by finding positive peaks in the difference spectrum that are above a 3σ threshold. The peaks are found using `scipy.signal.find_peaks` in combination with the 3σ threshold and a minimum separation between the local peaks. The 3σ threshold is computed from the RMS of the difference spectrum redwards of the C IV line, because we do not expect to detect more line emissions at these wavelengths due to the redshift of our sources. In Figure 3.11 we show an example of line emission identification for G09-0902+0101. Where the top panel shows the spectrum and the locations of line emission are marked with red crosses, the vertical dashed lines show the regions where we find the wavelength ranges for each line. These ranges are excluded when we build the empirical PSF, and instead use the next available PSF redwards of the line emission.

3.7.3   Si IV, C IV, He II and C III] analysis

We conduct a search for other extended line emission besides Lyα, such as Si IV, C IV, He II and C III]. However, we do not find extended emission in these lines for any target (Section 3.4.4). For completeness, we build χ_{Smooth} maps (e.g., Hennawi and Prochaska 2013) centered at the expected wavelength of each line and using a narrow-band window that reflects the $30\,\text{Å}$ narrow-band used for Lyα. The χ_{Smooth} maps for the systems studied
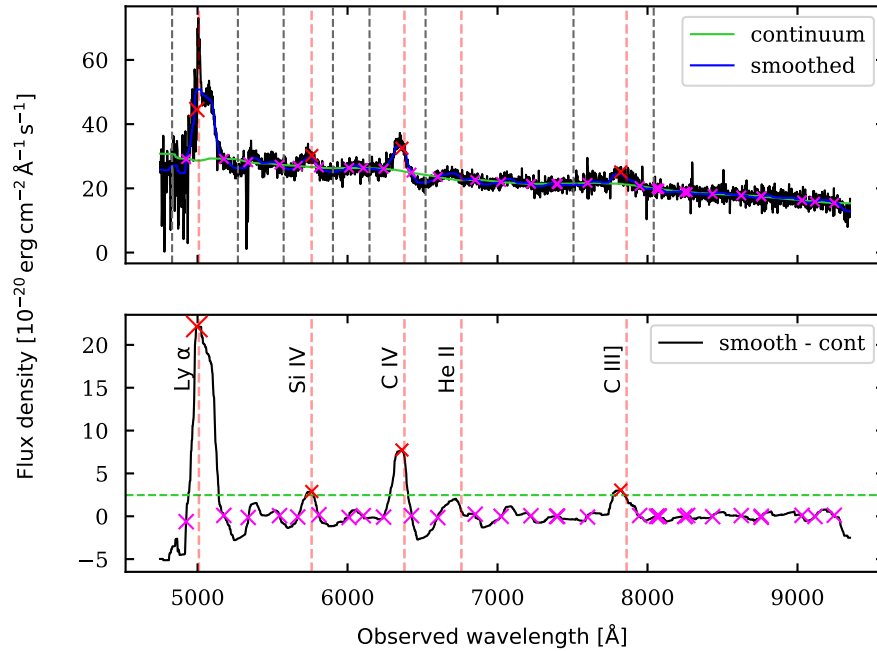
Figure 3.11: Example of the quasar's broad line emission identification for G09-0902+0101. *Top:* Integrated spectrum inside a 1 arcsecond diameter aperture of G09-0902+0101 is shown in black. Overlayed are a smoothed spectrum (blue) and "continuum" spectrum (green), constructed by using a median filter of 50 and 500 channels respectively. The red and pink crosses indicate detected peaks of line emission and the intersection between the smooth and "continuum" spectra respectively. The vertical gray lines indicate the regions where each line emission is excluded to build the PSF (see Section 3.3.1). *Bottom:* Difference spectrum between the smooth and continuum spectrum of the top panel. The green dashed line indicates the 3σ threshold for line identification. We indicate with a red dashed line the position of the quasar's Lyα and broad line emissions, with their respective label.

here are shown in Figures 3.12, 3.13, 3.14, 3.15 and 3.16, these maps are best suited for visualizing the presence of extended emission (if any), and to appreciate the noise in the data. The χ_{Smooth} maps are computed using equation (2) from Farina et al. (2019), given by:

$$\text{SMOOTH}[\chi_{x,y,\lambda}] = \frac{\text{CONVOL}[\text{DATA}_{x,y,\lambda} - \text{MODEL}_{x,y,\lambda}]}{\sqrt{\text{CONVOL}^2[\sigma^2_{x,y,\lambda}]}}, \tag{3.2}$$

where $\text{DATA}_{x,y,\lambda}$ is the original datacube, $\text{MODEL}_{x,y,\lambda}$ is the empirical PSF of the quasar obtained in Section 3.3.1, $\sigma^2_{x,y,\lambda}$ is the variance datacube. CONVOL is a spatial convolution using a 2D box kernel with of 3 pixels width (0.6") and CONVOL^2 is a spatial convolution using the square of the width of the kernel used for CONVOL. Different noise properties depends also on the vicinity to sky lines. For example, the He II velocity range of BR1202-0725 displays sky lines, therefore we subtract the residuals from the data before computing the χ_{Smooth} map.

3.7.4   QSO spectral energy distribution fitting

As mentioned in Section 3.5.1, we model the number of quasars' ionizing photons impinging on optically thick gas estimating the specific luminosity at the Lyman edge ($L_{\nu_{\text{LL}}}$) for the three quasars in our sample. As shown in Arrigoni Battaia et al. (2019b), a QSO SED can be parametrized by different power-laws, with the extreme ultra-violet portion described by a power law of the form $L_\nu = L_{\nu_{\text{LL}}}(\nu/\nu_{\text{LL}})^{\alpha_{\text{UV}}}$ with slope $\alpha_{\text{UV}} = -1.7$ (as obtained in Lusso et al. (2015)), and a slope $\alpha_{\text{opt}} = -0.46$ below 1 Ryd (Vanden Berk et al. 2001). Figure 3.17 shows a comparison of the MUSE QSO spectra and the assumed SED (following Arrigoni Battaia et al. 2019b), which confirms that a standard QSO template adjust to the sample studied here.
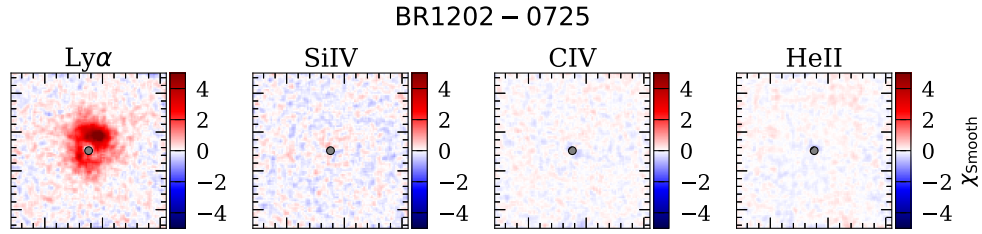
Figure 3.12: Lyα, Si IV, C IV and He II χ_{Smooth} maps using a velocity window equivalent to the 30 Å narrow-band used for the Lyα SB maps for BR1202-0725. The side of the maps is 20", corresponding to 129 kpc. We show with a circle the $1'' \times 1''$ normalization area of the quasar's PSF-subtraction.
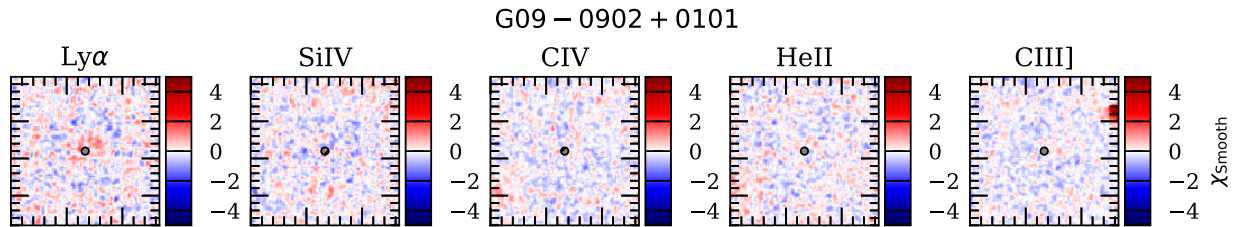
Figure 3.13: Lyα, Si IV, C IV, He II and C III] χ_{Smooth} maps using a velocity window equivalent to the 30 Å narrow-band used for the Lyα SB maps for G09-0902-0101. The side of the maps is 20", corresponding to 152 kpc. We show with a circle the $1'' \times 1''$ normalization area of the quasar's PSF-subtraction.
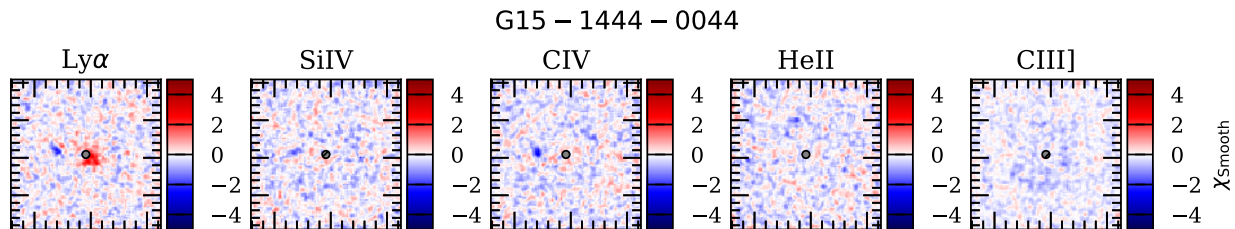
Figure 3.14: Same as Figure 3.13, but for G15-1444-0044. The 20" side of the maps corresponds to 148 kpc.
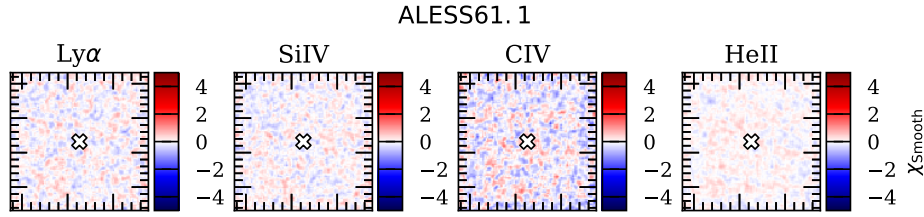
Figure 3.15: Lyα, Si IV, C IV, and He II χ_{Smooth} maps using a velocity window equivalent to the 30 Ånarrow-band used for the Lyα SB maps for ALESS61.1. The side of the maps is 20", corresponding to 133 kpc. We show with a white cross the position of the SMG.
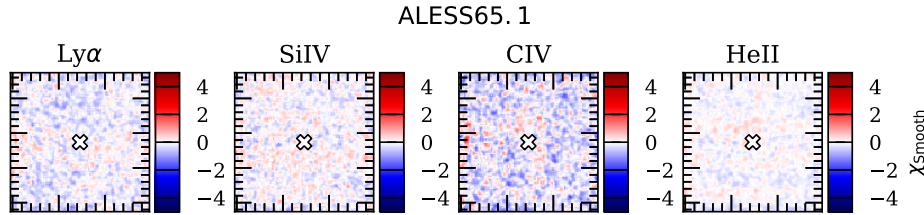
Figure 3.16: Same as Figure 3.15, but for ALESS65.1. The 20" side of the maps corresponds to 132 kpc.
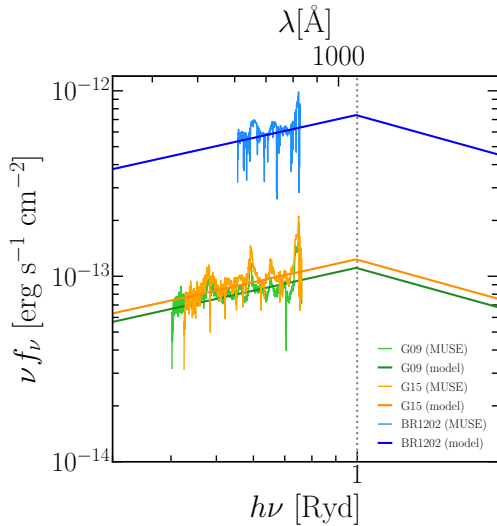
Figure 3.17: Comparison of the SED of the three quasars studied here used as incident radiation field in the modeling. The blue, orange and green solid lines indicate the input spectrum with slope $\alpha_{\mathrm{UV}} = -1.7$ (Lusso et al., 2015) for BR1202-0725, G09-0902+0101 and G15-1444-0044 respectively. The curves of the same color indicate the MUSE spectrum of each quasar extracted within a 1.5" radius aperture.

Chapter 4

QSO MUSEUM III: the circumgalactic medium in Lyα emission around 120 $z \sim 3$ quasars covering the full luminosity range of SDSS quasars

The contents of this chapter will appear in in González Lobos et al. 2024 in prep.

4.1 Introduction

A large fraction of the baryons in the universe are thought to reside in regions between the interstellar medium of galaxies and their host dark-matter halo virial radius. This material, currently referred to as the circumgalactic medium (CGM; Tumlinson et al. 2017), has been determined to be multiphase, including cold (10-100 K; e.g., Emonts et al. 2016; Vidal-García et al. 2021; Emonts et al. 2023), cool ($\sim 10^4$ K; e.g., Werk et al. 2014; Wisotzki et al. 2016; Nateghi et al. 2024) and warm/hot ($> 10^5$ K; e.g., Predehl et al. 2020; Di Mascolo et al. 2023; Zhang et al. 2024) gas. The importance of the CGM in galaxy evolution has become clearer in the past two decades and its phases are currently under intense scrutiny (Faucher-Giguère and Oh 2023a). Indeed, the CGM stores information on the complex interplay of several processes that happen when a galaxy first forms and successively shape galaxy formation and evolution, including gas inflows from the larger scales of the intergalactic medium (IGM; e.g., Kereš et al. 2005; Decataldo et al. 2024), galactic or active galactic nucleus (AGN) winds/outflows (e.g., Springel et al. 2005; Stinson et al. 2006; Wright et al. 2024), radiation (e.g., Ciotti and Ostriker 1997; Obreja et al. 2019) and interactions with and gas stripping of satellite galaxies, whose activity could also affect the CGM (e.g., Hopkins et al. 2006; Anglés-Alcázar et al. 2017).

The CGM of AGN is the optimal case study to encompass all of the aforementioned

processes involved in quiescent systems with infalling gas. AGN, more specifically those identified by the observation of their broad emission lines, i.e. quasars, are known to reside in relatively massive halos up to $z \sim 6$ ($M_{\mathrm{DM}} \sim 10^{12.5}$ M$_\odot$; White et al. 2012; Farina et al. 2019; Fossati et al. 2021; de Beer et al. 2023; Costa 2024). At high redshifts, halos of this mass are rare and should be characterized by (i) the presence of overdense environments around these systems which could contribute to their growth through infall and mergers (e.g., Kauffmann and Haehnelt 2000b), and (ii) the presence of several satellite galaxies, some of which are active companions as demonstrated by recent observations (e.g., Decarli et al. 2017; Fossati et al. 2021; Chen et al. 2021; Bischetti et al. 2021; Arrigoni Battaia et al. 2022; Nowotka et al. 2022; Arrigoni Battaia et al. 2023a). Also, quasars host galaxies are more massive and more star forming than typical galaxies at the same cosmic epoch (e.g., Walter et al. 2009; Pitchford et al. 2016; Molina et al. 2023), implying that their CGM and environment need to provide enough material to sustain such activity.

Importantly, quasars, accreting super-massive black holes (SMBHs), are indicative of very high radiative energy which may expel, enrich and highly ionize the gas reservoir within the host and its surroundings, a process known as AGN feedback (e.g., Fabian 2012; King and Pounds 2015). To reach their exceptional masses ($M_{\mathrm{BH}} \sim 10^8 - 10^{10}$ M$_\odot$), SMBHs grow mostly at the center of their host galaxies in a cycle of accretion and feedback, regulating their own growth (e.g., Di Matteo et al. 2005). Indeed, quasars have been observed to be highly variable (e.g., MacLeod et al. 2012), with typical variability timescales of the order of 10^{5-6} years (Schawinski et al. 2015; Eilers et al. 2017) and ages of $10^6 - 10^8$ years (Martini 2004). The quasars "shut-down" phase is loosely constrained to 10^{4-5} years based on the geometry and extent of few quasar light echoes and the recombination time scale of narrow line emission (e.g., Lintott et al. 2009; Schirmer et al. 2013; Davies et al. 2015). The impact of quasars on their surrounding reservoir and environment is therefore not only almost instantaneous, but also cumulative (e.g., Harrison and Ramos Almeida 2024a).

The quasar number density, and therefore their activity is at its apex at $z \sim 2$ (e.g., Shen et al. 2020). This is fortunate as the quasars CGM at their peak activity can therefore be probed both in absorption against bright background sources and directly in emission. Absorption line studies of the CGM of $z \sim 2-3$ quasars revealed cool ($T \sim 10^4$ K) massive ($M \sim 10^{11}$ M$_\odot$) and metal rich ($Z \sim 0.5$ Z$_\odot$) gas reservoirs as traced by optically thick absorbers, whose spatial distribution is highly anisotropic likely due to quasar illumination mainly along our line of sight (e.g., Hennawi and Prochaska, 2007; Prochaska et al., 2014; Lau et al., 2016). However, such studies are based on statistical samples as only one line of sight is available per foreground quasar. Detailed information on the morphology, physical properties and kinematics of the CGM around individual quasars require direct observations.

The direct detection of the CGM of $z \sim 2-3$ quasars has been a long-sought aim since the early predictions of the possible presence of extended glows of Hydrogen Lyα emission around AGN (Rees 1988; Haiman and Rees 2001a), which should result from the quasar illuminating its surrounding distribution of infalling gas. Several spectroscopic and narrow-band studies were successful in unveiling their CGM gas out to distances

of $< 50\,\mathrm{kpc}$ (e.g., Hu and Cowie 1987b; Weidinger et al. 2005; Christensen et al. 2006; Hennawi and Prochaska 2013; Arrigoni Battaia et al. 2016), but were hampered by the shallow sensitivity of past instrumentation and the lack of statistical samples of detections and the lack of accurate quasar systemic redshifts. Notwithstanding these difficulties, these pioneering works were able to (i) unveil the Lyα signal out to scales of ~ 500 kpc for the most exceptional systems (Cantalupo et al. 2014; Hennawi et al. 2015), (ii) constrain, in a photoionization scenario, the cool gas emitting Lyα to be dense, and metal enriched in some cases (Heckman et al. 1991b,a), (iii) show that the kinematics of the CGM are relatively quiescent, possibly dominated by infall (Weidinger et al. 2004), and (iv) start to investigate correlations between nebulae and QSO properties (Christensen et al. 2006).

The development of integral field spectrographs, such as the Multi Unit Spectroscopic Explorer (MUSE, Bacon et al., 2010) at the Very Large Telescope (VLT) and the Keck Cosmic Web Imager (KCWI, Morrissey et al., 2018) at the Keck Observatory revolutionized this field of research by allowing to map with unprecedented surface brightness limits ($\mathrm{SB}_{\mathrm{Ly}\alpha} \sim 10^{-18}\,\mathrm{erg\,s^{-1}\,cm^{-2}\,arcsec^{-2}}$) the CGM of $2 < z < 6$ bright quasars. It was therefore possible to uncover a large diversity of Lyα nebulae (sample of ~ 100 at $z \sim 3$) with sizes up to $\sim 100\,\mathrm{kpc}$ in only one hour of telescope time per object (Borisova et al., 2016; Farina et al., 2017; Arrigoni Battaia et al., 2018; Ginolfi et al., 2018; Cai et al., 2018; Arrigoni Battaia et al., 2019a,b; Farina et al., 2019; Cai et al., 2019; Travascio et al., 2020; Drake et al., 2020; Lau et al., 2022; González Lobos et al., 2023).

The origin of the extended Lyα emission is subject of debate, even if quasars provide enough ionizing photons in principle to keep the surrounding gas ionized. Indeed, important parameters are frequently not known, including fraction of volume illuminated by each quasar or quasar ionization cones opening angle, geometry of the host galaxy and its position with respect to the quasar ionization cones, presence of winds/ouftlows. Several mechanisms can act together and, through their combination, produce the observed Lyα glow: recombination radiation following gas ionization by the quasar radiation (e.g., Cantalupo et al. 2005; Kollmeier et al. 2010; Costa et al. 2022), shocks (e.g., Mori et al. 2004), resonant scattering of Lyα photons from the quasar broad line regions (e.g., Cantalupo et al. 2014; Costa et al. 2022), gravitational cooling radiation (e.g., Haiman et al. 2000; Dijkstra et al. 2006). Furthermore, Lyα photons produced on CGM scales could resonantly scatter shaping the nebulae morphology and the spectral shape of the Lyα emission (Costa et al. 2022). Overall, the aforementioned observational studies more frequently highlighted the importance of photoionization due to the quasar radiation followed by recombination in optically thin gas. In this framework, the Lyα SB scales as the product of the gas mass and density ($\mathrm{SB}_{\mathrm{Ly}\alpha}^{\mathrm{thin}} \propto n_{\mathrm{H}} M_{\mathrm{gas}}$; Hennawi and Prochaska, 2013). In this scenario, the observed Lyα SB implies densities of the cool gas of $n_{\mathrm{H}} \gtrsim 1\,\mathrm{cm}^{-1}$ (Hennawi et al., 2015; Arrigoni Battaia et al., 2015b, 2019b), which are comparable to star-forming regions in the interstellar medium of galaxies. Moreover, extended He II and C IV emission has been detected in some individual cases or using stacking analysis of tens of systems (Arrigoni Battaia et al., 2018; Cantalupo et al., 2019; Guo et al., 2020; Travascio et al., 2020; Fossati et al., 2021; Lau et al., 2022; Sabhlok et al., 2024), indicating that the CGM of $2 < z < 6$ quasars is metal enriched and ionized.

Most of these studies focused on the CGM of the brightest quasars, however recent work by Mackenzie et al. (2021b) targeted with MUSE 12 $z \sim 3$ quasars selected to be fainter ($-23.8 < M_i(z = 2) < -27.1$) than previous studies and detected Lyα nebulae in all of them. The Lyα nebulae of fainter quasars reported in that work were on average fainter and less extended than brighter systems, indicating a correlation between the Lyα SB of the nebula and the quasar UV and Lyα luminosities. The authors discussed that the observed relation could originate due to several reasons: a possible dependency with halo mass, resonant scattering dominating the emission around faint quasars, unresolved inner regions of the nebulae or an unresolved component from the interstellar medium of the host galaxy, however evidence was inconclusive to discern between those.

In this framework, I report on the continuation of the largest effort to date to map the CGM of $z \sim 3$ quasars: the Quasar Snapshot Observations with MUse: Search for Extended Ultraviolet Mission survey (QSO MUSEUM, Arrigoni Battaia et al. 2019a; Herwig et al. 2024). Arrigoni Battaia et al. (2019a), hereafter QSO MUSEUM I, detected with MUSE a diversity of Lyα nebulae around 61 bright quasars at $z = 3.17$. QSO MUSEUM I show that (i) quasars with very similar bolometric luminosities can be surrounded by very different extended Lyα emission (in extent and SB level; see also Arrigoni Battaia et al. 2023b), (ii) the motions traced by the Lyα emission have amplitudes consistent with gravitational motions expected in dark matter haloes hosting $z \sim 3$ quasars, (iii) there is an evolution of the level of Lyα emission around $z \sim 2$ and $z \sim 3$ quasars, and (iv) the nebulae are likely powered by a combination of photoionization and resonant scattering of Lyα photons.

In this work, I have extended the QSO MUSEUM survey to a total of 120 single quasar fields, by targeting with MUSE 59 fainter systems $-27 < M_i(z = 2) < -24$ at $z = 3.1$. With this large sample I can now test the findings presented in Mackenzie et al. (2021b) in addition to the link between SMBH properties, AGN feedback and extended Lyα nebulae. This paper is organized as follows: in Section 4.2 we provide an overview of the sample selection and data reduction, Section 4.3 highlights our main observational findings (SB levels, luminosities, morphology, kinematics), while in Section 4.4 we discuss the implications of the observations in light of quasar variability, powering mechanisms and CGM physical properties. Section 4.5 summarizes the work. We adopt a flat ΛCDM cosmology with $H_0 = 70 \, \mathrm{km \, s^{-1} \, Mpc^{-1}}$, $\Omega_\mathrm{m} = 0.3$ and $\Omega_\Lambda = 0.7$. In this cosmology, 1 arcsec corresponds to $\sim 7.5 \, \mathrm{kpc}$ at the median redshift of the sample ($z = 3.1$).

4.2   Observations and Data Reduction

4.2.1   Sample selection

The QSO MUSEUM survey (Arrigoni Battaia et al., 2019a) targeted with MUSE 61 quasars covering a range of absolute i-band magnitudes normalized at $z = 2$ of $-29.67 < M_i(z = 2) < -27.03$ and redshift $3.03 < z < 3.46$. These quasars represent the brightest objects not targeted by the MUSE Guaranteed Time Observation (GTO) team (i.e. Borisova et al.
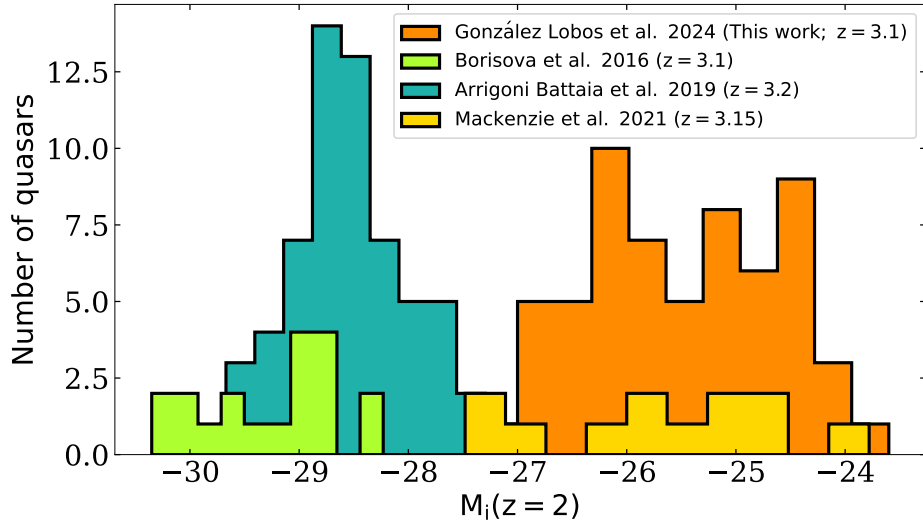
Figure 4.1: Overview of $z \sim 3$ quasar samples with MUSE observations. Histograms of the absolute i-band magnitude normalized at $z = 2$ (following Ross et al., 2013) of the QSO MUSEUM III survey: 59 faint quasars from this study (orange), and 61 bright from the QSO MUSEUM I survey (Arrigoni Battaia et al., 2019a) (dark green). For comparison, we show the 19 bright quasars from Borisova et al. (2016) (light green) and the 12 faint from Mackenzie et al. (2021b) (yellow). In the legend we indicate the median redshift of each sample.

2016). In this work, we extend the survey by targeting 58 additional quasars covering a fainter range of magnitudes $-27 < M_i(z = 2) < -24$. Additionally, we include the $z = 3.4$ quasar discovered around ID 31 in Arrigoni Battaia et al. (2019a) (see their Appendix C). This sample has been constructed from the public spectroscopic quasar catalog of the Sloan Digital Sky Survey / Baryon Oscillation Spectroscopic Survey (SDSS/BOSS) data release 14 (DR14) (Pâris et al., 2018), selecting objects as in QSO MUSEUM I, but now in a more limited redshift range of $3 < z < 3.2$ and a uniform magnitude distribution. The redshift range is chosen to target the lowest redshift accessible by MUSE in Lyα emission (close to the quasars' activity peak), and to avoid contamination from stronger and more frequent sky lines at higher redshift (longer wavelengths). Figure 4.1 shows the $M_i(z = 2)$ distribution of the QSO MUSEUM sample from Arrigoni Battaia et al. (2019a) (dark green) and the 59 fainter quasars presented in this work (orange). This extended sample makes up the largest search to date for nebular emission around $z \sim 3$ quasars (120 systems). Additionally, we show in the same figure, the similarly faint quasar sample from Mackenzie et al. (2021b) (yellow) and the bright quasars targeted by Borisova et al. (2016) (light green).
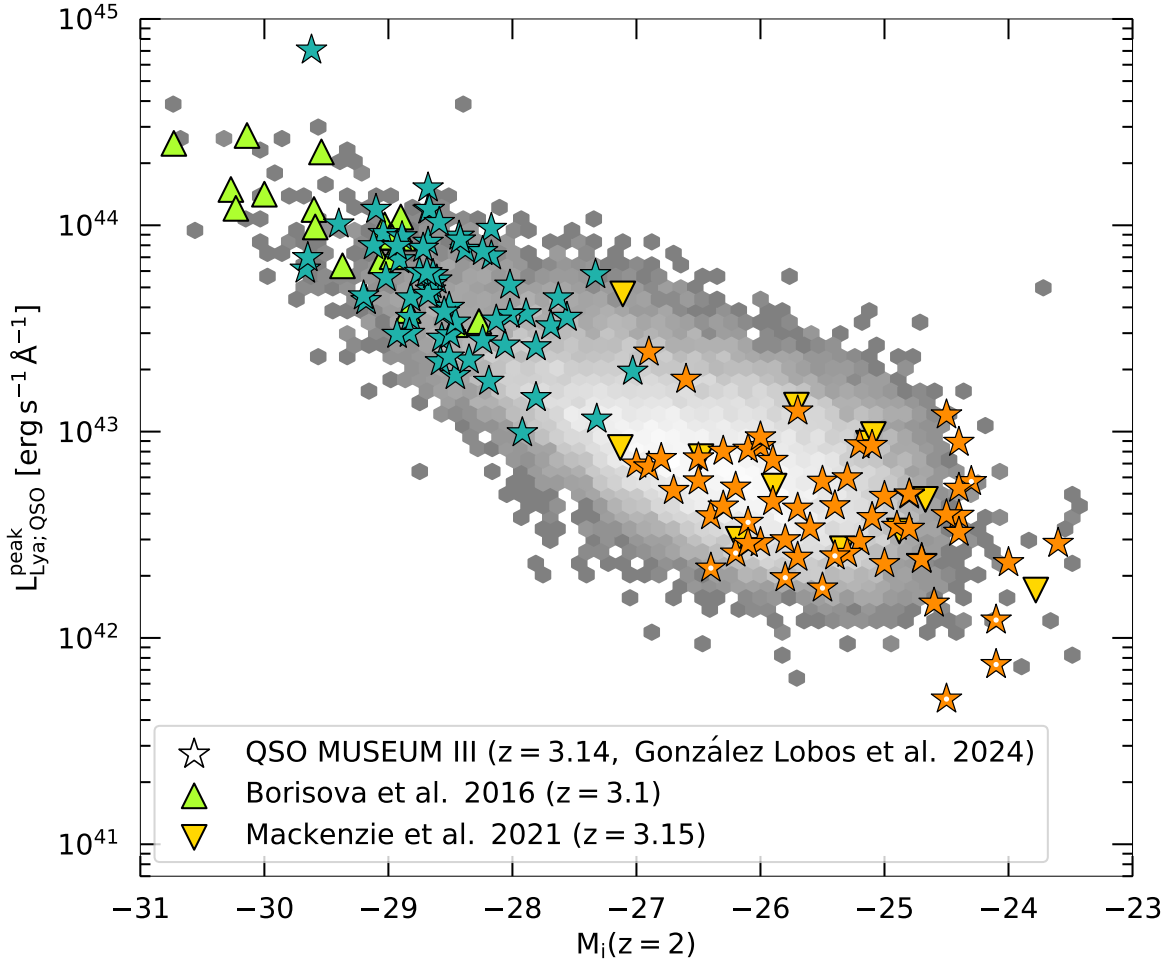
Figure 4.2: Overview of the luminosity distribution of observed $z \sim 3$ quasars. The figure shows the quasar peak Lyα luminosity density as a function of its absolute i-band magnitude normalized at $z = 2$ ($M_i(z = 2)$, following Ross et al., 2013). The QSO MUSEUM III faint and bright quasars are shown with orange and dark green stars, respectively. The systems with no Lyα nebula detected are marked with a white dot (see Section 4.3.1). In addition, we show the location of the 17 brighter quasars targeted in (Borisova et al., 2016) (light green triangles) and the 12 fainter objects from Mackenzie et al. (2021b) (yellow triangles). For comparison, we show the 2-D number density of $3.0 < z < 3.46$ quasars from the SDSS DR17 (Abdurro'uf et al., 2022) increasing from gray to white. Section 4.2.2 explains how the luminosities are derived.

4.2.2 Physical properties of the targeted quasars

The physical properties of the targeted quasars are summarized in Figures 4.2 and 4.3. The distribution of the peak Lyα luminosity density as a function of $i-$band absolute magnitude normalized at $z = 2$ (following Ross et al., 2013) of the bright and faint quasars is shown in Figure 4.2 with dark green and orange stars, respectively. The peak Lyα luminosity density is computed from the MUSE datacube by integrating a spectrum inside a 1.5" radius aperture centered at the quasar location. In addition, we compute using the MUSE datacubes the values from the sample of 17 quasars targeted in Borisova et al. (2016) and 12 quasars from Mackenzie et al. (2021b) and show them with light green and yellow triangles, respectively. For comparison, I compute the values from the SDSS DR17 (Abdurro'uf et al., 2022) $3.0 < z < 3.46$ quasars. For this, I crossmatch the quasars from Rakshit et al. (2020) at this redshift range and download each quasar spectrum with the AstroQuery[1] Python module (Ginsburg et al., 2019), specifically using the `query_specobj` and `get_spectra` functions within it. Then, I search in the quasar spectra for the peak flux density at the Lyα alpha wavelength and construct the density map shown with a gray scale in Figure 4.2. This figure illustrates how the QSO MUSEUM survey covers the parameter space of the SDSS quasar population. Specifically, the 120 quasars in QSO MUSEUM III encompass a wide range of quasar UV luminosities (six orders in $M_i(z = 2)$) and in peak Lyα quasar luminosity $L_{\text{Ly}\alpha;\text{QSO}}^{\text{peak}}$ (three orders).

Further, for all the QSO MUSEUM III targeted quasars we estimated their black-hole mass and accretion rates (parametrized by the so-called Eddington ratio). These quantities are computed using the output from the fit to the quasar spectra obtained with the public Python code PyQSOFit[2] (Guo et al., 2018) as described in Appendix 4.6.1, where also the definition of quantities are reported. The typical uncertainties on the estimate of the black hole masses (Equation 4.5) are of the order of 0.5 dex as the calculations are based on the C IV broad line. Figure 4.3 shows the Eddington ratio as a function of black hole mass for the QSO MUSEUM III sample with the same symbols as in Figure 4.2. The outlier green star at the top right corresponds to ID 26, which is also the brightest quasar targeted (see Appendix 4.6.2). The MUSE data of this system is also noisy both using the data reduction presented here and as reported in Arrigoni Battaia et al. (2019a), however I compared with SDSS data of this quasar and found consistent spectra. Therefore, the values reported for the luminosities, black hole mass and Eddington ratio of this system are robust. Additionally, we show in Figure 4.3 the number density for SDSS quasars in the same redshift range from Rakshit et al. (2020), who used almost the same method to estimate such quantities (see details in Appendix 4.6.1). Finally, we show the relation between the quasar peak Lyα luminosity density and their bolometric luminosity (computed using the monochromatic luminosity $L_\lambda(1350\,\text{Å})$; see Appendix 4.6.1) for the 120 quasars in Figure 4.3.

---

[1]https://github.com/astropy/astroquery
[2]https://github.com/legolason/PyQSOFit
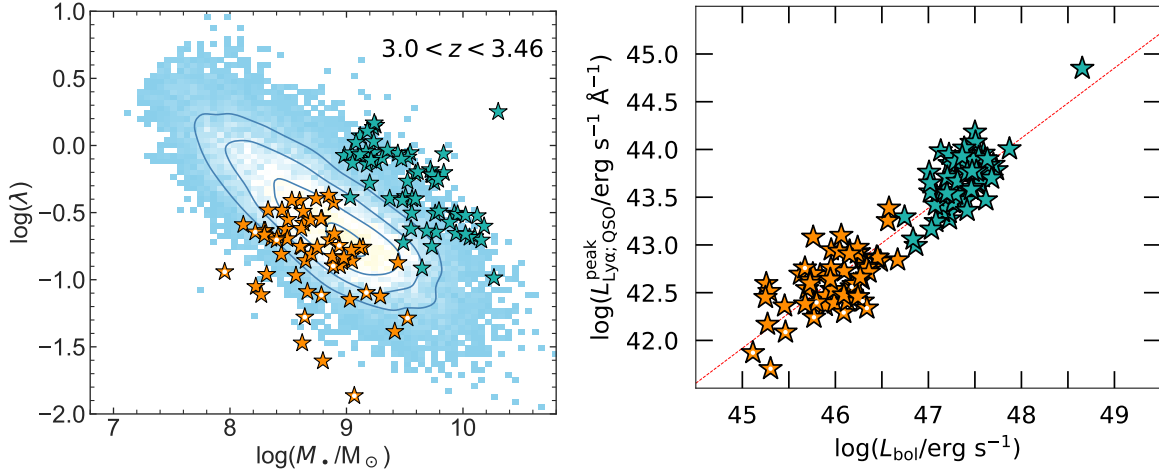
Figure 4.3: Eddington ratio versus black hole mass and peak Lyα luminosity density versus bolometric luminosity of the targeted sample. *Left:* The Eddington ratio versus black hole mass for the QSO MUSEUM III sample (same symbols as in Figure 4.2) are compared with the values for SDSS quasars in the same redshift range (blue, 2-D number density histogram; Rakshit et al. 2020). The contours indicate the iso-proportions of the density at 0.2, 0.4, 0.68 and 0.95 levels, indicating that 20%, 40%,68%, and 95% of the quasars are outside that contour, respectively. *Right:* The peak Lyα luminosity density versus bolometric luminosity are shown with the same symbols. The bolometric luminosity is computed using the monochromatic luminosity $L_\lambda(1350\,\text{Å})$ (see Appendix 4.6.1). The red dashed line represents a power law fit to the data of the form $\log(L^{\text{peak}}_{\text{Ly}\alpha;\,\text{QSO}}/\text{erg}\,\text{s}^{-1}\,\text{Å}^{-1}) = 8.96 + 0.73\log(L_{\text{bol}}/\text{erg}\,\text{s}^{-1})$.

4.2.3   Observations

The observations were carried out with the MUSE instrument on the VLT 8.2m telescope YEPUN (UT4) over roughly 6.5 years (2014-2021). The data for the faint sample were taken as part of the European Southern Observatory (ESO) program 0106.A-0297(A) (PI: F. Arrigoni Battaia) in service mode on UT dates between 06-11-2020 and 10-03-2021 with good weather conditions (46.5% with clear sky, 46.5% with photometric sky, 7% with thin clouds; details in Table 4.1)[3]. The observations were taken using the Wide Field Mode of MUSE, which covers a field of view of $1' \times 1'$ with a 0.2" pixel scale and a spectral range of 4750-9350 Å with a channel width of 1.25 Å and resolving power of $R \sim 1750$ at 4984 Å (the expected Lyα wavelength at the median redshift of the sample). The observational strategy is the same as in Arrigoni Battaia et al. (2019a), which consists of three exposures of 900 seconds each per field with a dither of < 5" and 90 degree rotations with respect to each other. The average seeing at the expected Lyα wavelength of the 59 systems is 1.03".

---

[3]from the ESO program, we removed two bad observations: the field corresponding to J0244-0059 was incorrect and contained a standard star in the science datacube and the field of J1103+0913 showed sky fringes in the datacube which can also be seen in the data processed by ESO.

Table 4.1: Summary of the MUSE observations for the faint sample.

ID	Name	RA	Dec	$M_i\,(z=2)^a$	$\mathrm{Seeing_{Ly\alpha}}$	$\mathrm{SBlimit}^b$ $_{30\,\text{\AA}\,\mathrm{Ly\alpha}}$	Sky
		[J2000]	[J2000]	[mag]	[arcsec]	$[10^{-18}\,\mathrm{cgs}]$	Conditions^c
62	J0203-0443	02:03:57.00	-04:43:10.2	-24.6	0.69	2.28	PH
63	J0229-0029	02:29:56.55	-00:29:53.9	-26.1	2.02	2.26	CL
64	J0159-0032	01:59:45.45	-00:32:28.4	-24.7	0.77	2.28	CL
65	J0829+1426	08:29:39.91	+14:26:25.7	-25.0	1.08	2.33	PH
66	J0200-0606	02:00:12.60	-06:06:15	-27.0	0.58	1.81	CL
67	J0247-0023	02:47:46.86	-00:23:53.4	-26.9	0.71	1.94	PH
68	J0809+0643	08:09:49.16	+06:43:10.8	-24.5	0.93	1.85	CL
69	J0834+1012	08:34:15.33	+10:12:31.2	-25.4	0.83	2.06	PH
70	J0923+0011	09:23:00.29	+00:11:56.7	-24.8	0.86	1.89	PH
71	J0823+0531	08:23:07.22	+05:31:35.4	-26.2	0.97	1.97	CL
72	J0227-0113	02:27:21.91	-01:13:24.6	-24.1	0.93	2.04	PH
73	J1038+0919	10:38:40.81	+09:19:14.3	-25.0	1.4	2.17	CL
74	J0203-0153	02:03:33.76	-01:53:08.4	-25.6	1.52	1.92	PH
75	J0210-0945	02:10:03.52	-09:45:20.5	-26.0	0.79	2.37	TN
76	J0155-0732	01:55:25.44	-07:32:16.3	-26.6	1.08	1.97	PH
77	J0151+0023	01:51:25.83	+00:23:32.7	-24.4	0.77	2.0	PH
78	J0030+0047	00:30:42.91	+00:47:43.3	-24.0	0.91	2.82	TN
79	J0148-0055	01:48:09.00	-00:55:08.8	-24.4	0.78	1.87	PH
80	J0017+0316	00:17:44.80	+03:16:06.1	-26.9	0.87	2.31	CL
81	J0925+0344	09:25:41.80	+03:44:37.0	-25.2	0.96	2.26	CL
82	J0125-0005	01:25:29.50	-00:05:13.5	-24.1	1.23	4.75	TN
83	J0843+1916	08:43:19.90	+19:16:28.8	-24.8	1.15	2.29	CL
84	J0752+1244	07:52:54.22	+12:44:51.5	-25.1	0.94	2.26	PH
85	J0018-0026	00:18:17.73	-00:26:59.0	-26.2	0.88	2.0	TN
86	J0747+1429	07:47:14.29	+14:29:54.3	-26.5	1.59	1.93	CL
87	J0245-0036	02:45:23.32	-00:36:19.0	-24.9	1.0	1.82	CL
88	J0801+0534	08:01:30.16	+05:34:37.0	-25.7	1.15	2.07	CL
89	J0840+0141	08:40:58.35	+01:41:45.0	-26.0	1.15	1.73	CL
90	J1016+0833	10:16:25.72	+08:33:09.8	-25.2	0.97	2.5	CL
91	J0159+0025	01:59:22.99	+00:25:30.8	-24.3	0.69	2.28	PH
92	J0234-0044	02:34:41.17	-00:44:43.7	-24.4	1.0	2.1	PH
93	J0243-0038	02:43:00.58	-00:38:18.0	-24.5	0.86	1.98	PH
94	J0140-0202	01:40:20.33	-02:02:43.0	-25.5	0.78	1.94	PH
95	J0252-0333	02:52:42.99	-03:33:39.4	-25.8	0.95	2.27	PH
96	J0939+0451	09:39:29.36	+04:51:47.4	-25.1	0.74	2.13	PH
97	J0208-0922	02:08:02.86	-09:22:43.0	-26.8	1.0	1.92	PH
98	J0212-0602	02:12:48.13	-06:02:16.9	-25.7	1.0	2.15	CL
99	J1205+1059	12:05:12.55	+10:59:34.6	-24.5	2.11	2.22	CL
100	J1001-0007	10:01:22.20	-00:07:52.7	-25.3	0.8	2.41	TN
101	J1145-0209	11:45:19.45	-02:09:43.9	-25.9	0.98	2.05	CL
102	J1057+0804	10:57:37.23	+08:04:11.2	-26.1	0.79	2.2	CL
103	J1244-0027	12:44:08.39	-00:27:26.1	-26.0	1.31	2.27	CL
104	J1216+0454	12:16:29.25	+04:54:34.8	-25.7	1.67	1.93	CL
105	J1048+0449	10:48:04.72	+04:49:00.3	-24.8	1.34	2.03	CL
106	J0920-0048	09:20:56.50	-00:48:07.0	-25.8	0.86	1.65	PH
107	J0223-0309	02:23:04.27	-03:09:51.5	-25.3	0.97	1.91	PH
108	J1301-0020	13:01:12.26	-00:20:48.9	-26.5	1.0	2.1	PH
109	J0823+0340	08:23:25.59	+03:40:59.4	-26.7	1.0	2.03	CL
110	J0832+0450	08:32:20.15	+04:50:28.3	-25.5	0.95	2.0	CL
111	J1022+0418	10:22:25.90	+04:18:24.2	-26.4	1.01	2.11	PH
112	J1101+0314	11:01:05.12	+03:14:03.9	-26.3	1.67	2.09	CL
113	J0207-0306	02:07:16.83	-03:06:48.4	-25.9	1.02	2.43	CL
114	J1200+1528	12:00:26.16	+15:28:16.1	-25.4	0.96	1.87	CL
115	J0252-0057	02:52:53.28	-00:57:28.0	-24.4	0.67	2.07	PH
116	J0840+0636	08:40:26.81	+06:36:32.8	-26.3	1.06	2.08	CL
117	J1244+0327	12:44:06.42	+03:27:43.2	-24.7	1.27	1.86	CL
118	J1153-0141	11:53:02.24	-01:41:13.2	-26.4	1.11	1.94	CL
119	J1019+0845	10:19:17.81	+08:45:50.0	-26.1	0.81	2.03	CL
120	UM670-comp.	01:17:22.24	-08:41:43.5	-23.6	0.8	2.22	CL

^{a} Absolute $i-$band magnitude normalized to $z=2$ following Ross et al. (2013).
^{b} 1σ SB limit within $1\,\mathrm{arcsec^2}$ and a $30\,\text{\AA}$ narrow-band centered at the observed Lyα wavelength in units of $10^{-18}\,\mathrm{erg\,s^{-1}\,cm^{-2}\,arcsec^{-2}}$.
^{c} Sky conditions during the observations as described in the ESO observational log: PH-photometric; CL-clear; TN-thin cirrus.

We summarize these observations in Table 4.1.

Additionally, we include in this work the MUSE observations of the 61 quasars from the QSO MUSEUM I survey (Arrigoni Battaia et al., 2019a) and list their observations in Table 4.5. These data were taken as part of the ESO programmes 094.A-0585(A), 095.A-0615(A/B), and 096.A-0937(B) (PI: F. Arrigoni Battaia). The 120 systems are reduced and analyzed in this work using the exact same methods as described in Sections 4.2.4 and 4.2.5.

4.2.4   Data Reduction

The data reduction for the whole sample comprised of 120 quasars was performed using the MUSE pipeline version 2.8.3 (Weilbacher et al., 2012, 2014, 2020) following the method described in Farina et al. (2019) consisting in subtraction of bias and dark field, flat field correction, wavelength calibration, illumination correction and standard star flux calibration. We remove the sky emission in each datacube using the Zurich Atmospheric Purge (ZAP; Soto et al., 2016) software. The MUSE pipeline underestimates the variance due to the noise correlation between pixels (Bacon et al., 2015), therefore we rescale each layer of the variance cubes to reflect the variance in the datacubes. The rescaled variance cubes are used to compute the surface brightness (SB) limits and errors in our estimations.

Following the method presented in González Lobos et al. (2023), the three[4] reduced exposures of each target are median combined after masking artifacts due to the separation of the MUSE IFUs (consisting of $\sim 4\%$ of the field of view). The final products are a final science datacube and a variance datacube obtained by taking into account propagation of errors during the combination. This final variance datacube is once again checked against the data by rescaling each layer to the variance in the corresponding science layer after combining.

The average 2σ SB limit within $1\,\mathrm{arcsec}^2$ in a $30\,\text{Å}$ pseudo narrow-band (NB) at the observed Lyα wavelength of the sample is $2.2 \times 10^{-18}\,\mathrm{erg\,s^{-1}\,arcsec^{-2}\,cm^{-2}}$ (see Table 4.1 for the individual SB limits). Per channel (1.25 Å) and within the same aperture and at the same wavelength. These SB limits are in very well agreement to those reported in Arrigoni Battaia et al. (2019a) despite the different analysis tools used in this work.

4.2.5   Revealing extended emission around quasars

The unresolved bright emission from a quasar can easily outshine the fainter emission from the surrounding CGM (e.g., Heckman et al., 1991b,a; Møller, 2000).Therefore in order to characterize the extended CGM emission we need to subtract the point spread function (PSF) of the quasar, as it has been frequently described in the literature (e.g., Borisova et al., 2016; Husemann et al., 2018; Farina et al., 2019; O'Sullivan et al., 2020; González Lobos et al., 2023). In this work, we modify the Python routines developed and described in González Lobos et al. (2023) to reveal extended emission around quasars with different

---

[4]The fields of ID 8 and 37 had in total 12 and 6 exposures respectively (see Table 2 of Arrigoni Battaia et al. 2019a).

luminosities. For the bright objects we use parameters similar to those in Borisova et al. (2016) and Arrigoni Battaia et al. (2019a), while for the faint sample we use parameters similar to the one presented in Mackenzie et al. (2021b).

Specifically, the PSF for faint quasars is constructed empirically using pseudo-NBs of 400 channels computed at each wavelength of the datacubes. This choice of pseudo-NB width is made to increase the signal to noise in the constructed PSF, similar to the 300 channels used in Mackenzie et al. (2021b) and larger than the 150 channels used for brighter quasars (Borisova et al. 2016; Arrigoni Battaia et al. 2019a). Each pseudo-NB is normalized to the emission inside a region of $1\,\mathrm{arcsec}^2$ centered at the quasar coordinates, computed from the sigma clipped (3σ) average, and then subtracted from the datacube at the quasar position out to a radius of three times the seeing (see Table 4.1).

Finally, we mask the $1\,\mathrm{arcsec}^2$ region located at the quasar position used for normalizing the pseudo-NB and exclude it from our analysis. Indeed this region is affected by PSF residuals (e.g., Borisova et al. 2016). We refer the reader to González Lobos et al. (2023) for more details on the algorithm.

After the PSF-subtraction, any extended emission could be still contaminated by the presence of continuum sources. We remove them using a median-filtering approach (e.g., Borisova et al. 2016) using the `contsubfits` function (with default parameters) within the ZAP[5] (Soto et al., 2016) software. Such a method has been already used in other works targeting extended emission around quasars (Arrigoni Battaia et al. 2019b,Herwig et al. in prep.).

4.3   Results

The final datacubes obtained in Section 4.2.5 contain only extended line emission, if detectable. We build Lyα SB maps, integrated spectra, velocity shift and velocity dispersion maps using such PSF- and continuum-subtracted datacubes, and present them in Figures 4.4, 4.5, 4.6, 4.7, 4.8 and 4.9, respectively. In the following sections, we describe how nebulae are detected, analyzed, and our findings.

4.3.1   Nebula detection

Using the PSF- and continuum subtracted datacubes, we extract a spectrum inside a 1.5" radius aperture centered at the quasar location, after masking the $1\,\mathrm{arcsec}^2$ normalization region (see Section 4.2.5). We use this spectrum to find Lyα emission by setting a 3σ detection threshold based on the variance associated to the spectrum within the same aperture, then finding the peak emission above this threshold. We set the redshift of the detected nebulae using the wavelength of the peak Lyα emission from this method and list them in Table 4.2, where non-detections are marked with dashed lines. We report the detection of 110 nebulae out of the 120 targeted quasars, all the non-detections occur in the fainter quasar sample that is presented in this work. We further check both the detections

---

[5]`https://github.com/musevlt/zap`

Table 4.2: Properties of the quasar and extended Lyα emission

ID	$z_{\mathrm{Ly}\alpha;\mathrm{peak}}^{\mathrm{QSO}}$	$z_{\mathrm{Ly}\alpha;\mathrm{peak}}^{\mathrm{Neb}}$	$L_{\mathrm{Ly}\alpha;\mathrm{peak}}^{\mathrm{QSO}}$ erg s^{-1} Å^{-1}	Luminosity 10^{42} erg s^{-1}	Area arcsec^2 (pkpc^2)	$\Delta v_{\mathrm{gauss}}$ km s^{-1}	Δv_{m1} km s^{-1}	FWHM$_{\mathrm{gauss}}$ Å (km s^{-1})	$\Delta\lambda_{\mathrm{m2}}$ Å (km s^{-1})
62	3.043	3.043	1.5×10^{42}	5.22±0.52	5.56 (326.99)	15.89±75.22	50.35±81.05	23.3 (1421)	9.63 (587)
63	3.137	$--$	$--$	$--$	$--$	$--$	$--$	$--$	$--$
64	3.058	3.053	2.4×10^{42}	8.89±0.55	10.24 (600.99)	-105.41±27.0	-13.12±28.16	12.76 (776)	4.32 (262)
65	3.031	3.031	4.9×10^{42}	23.52±0.9	21.68 (1278.0)	23.74±30.4	26.27±22.06	17.06 (1044)	6.78 (415)
66	3.143	3.145	7×10^{42}	44.31±1.13	45.08 (2597.65)	32.02±23.84	85.05±15.86	17.98 (1070)	7.17 (427)
67	3.138	3.136	6.7×10^{42}	17.99±0.93	17.68 (1020.67)	51.35±42.64	31.19±41.8	23.9 (1424)	9.48 (565)
68	3.059	3.059	1.2×10^{43}	58.92±0.96	41.88 (2455.21)	146.56±11.45	175.08±7.57	13.64 (828)	5.67 (344)
69	3.148	3.146	4.4×10^{42}	23.07±1.06	20.48 (1179.75)	-49.81±59.86	-81.21±43.96	28.1 (1671)	12.6 (749)
70	3.145	3.142	4.9×10^{42}	15.38±0.67	15.44 (890.15)	30.74±22.13	70.05±20.97	14.44 (859)	6.14 (365)
71	3.186	3.201	5.4×10^{42}	34.79±1.45	29.52 (1681.86)	721.35±57.89	675.07±46.49	32.97 (1937)	13.62 (800)
72	3.105	$--$	$--$	$--$	$--$	$--$	$--$	$--$	$--$
73	3.081	3.07	2.3×10^{42}	32.89±1.36	35.48 (2075.26)	-510.38±44.87	-470.12±39.03	27.04 (1637)	10.38 (628)
74	3.182	3.184	3.4×10^{42}	23.87±1.13	26.24 (1500.16)	155.95±45.77	213.02±40.23	25.08 (1478)	10.14 (598)
75	2.996	2.994	8.5×10^{42}	44.71±1.05	30.16 (1790.89)	95.17±22.72	128.66±12.66	15.61 (963)	6.49 (401)
76	3.193	3.196	1.8×10^{43}	17.54±1.02	11.6 (661.52)	388.84±46.42	423.45±48.91	27.03 (1588)	11.15 (655)
77	3.113	3.111	3.9×10^{42}	33.5±0.93	27.12 (1573.45)	-60.28±17.62	-82.81±16.37	17.19 (1031)	7.29 (437)
78	3.092	3.098	2.3×10^{42}	19.18±1.15	12.0 (698.8)	409.0±97.63	388.02±68.17	32.97 (1984)	14.25 (858)
79	3.156	3.149	8.9×10^{42}	23.38±0.75	19.6 (1128.48)	-231.52±16.26	-285.72±15.45	14.3 (849)	6.04 (359)
80	3.028	3.023	2.4×10^{43}	74.65±1.29	48.84 (2883.52)	-235.23±11.03	-209.74±7.34	12.49 (765)	4.99 (306)
81	3.026	3.027	2.9×10^{42}	16.61±0.48	15.56 (917.99)	-262.11±7.22	-271.83±6.85	6.44 (395)	2.52 (154)
82	3.042	$--$	$--$	$--$	$--$	$--$	$--$	$--$	$--$
83	3.091	3.091	5×10^{42}	19.04±0.97	15.44 (899.39)	177.15±41.11	185.38±42.31	24.23 (1460)	10.46 (630)
84	3.046	3.045	3.8×10^{42}	23.46±0.9	22.2 (1305.18)	-63.77±25.86	-62.4±22.69	17.01 (1037)	7.0 (427)
85	3.139	$--$	$--$	$--$	$--$	$--$	$--$	$--$	$--$
86	3.189	3.191	7.5×10^{42}	38.1±1.46	36.92 (2107.8)	153.59±51.62	151.69±35.11	28.01 (1648)	11.83 (696)
87	3.146	3.159	3.5×10^{42}	12.18±0.78	11.72 (673.38)	742.06±91.8	792.57±70.34	32.97 (1956)	13.28 (788)
88	3.035	3.029	2.5×10^{42}	12.85±0.77	16.2 (955.38)	-374.45±51.52	-416.33±44.27	21.51 (1316)	8.75 (535)
89	3.143	3.152	2.9×10^{42}	5.63±0.51	7.96 (457.98)	467.31±54.34	492.59±57.72	18.52 (1101)	7.07 (420)
90	3.043	3.044	8.6×10^{42}	34.51±1.18	32.72 (1924.06)	105.08±21.07	125.01±18.76	15.51 (946)	6.86 (418)
91	3.045	$--$	$--$	$--$	$--$	$--$	$--$	$--$	$--$
92	3.115	3.112	5.3×10^{42}	14.78±0.81	15.84 (918.81)	-40.14±38.89	-46.52±38.39	20.78 (1246)	9.27 (556)
93	3.046	$--$	$--$	$--$	$--$	$--$	$--$	$--$	$--$
94	3.178	3.181	5.7×10^{42}	20.42±0.88	20.92 (1196.75)	89.09±24.2	96.75±27.59	18.86 (1113)	7.61 (449)
95	3.024	$--$	$--$	$--$	$--$	$--$	$--$	$--$	$--$
96	3.118	3.12	8.6×10^{42}	73.94±1.44	48.68 (2819.3)	-70.61±17.01	-91.26±13.14	20.08 (1203)	7.96 (477)
97	3.092	3.096	7.4×10^{42}	14.47±0.77	16.8 (977.54)	220.94±32.48	274.6±31.37	17.83 (1074)	6.55 (394)
98	3.074	3.077	4.3×10^{42}	22.24±1.02	17.32 (1011.75)	1.27±47.73	30.23±45.52	29.1 (1762)	12.37 (749)
99	3.105	3.106	4×10^{42}	11.72±0.76	10.04 (583.07)	202.81±66.97	215.04±60.73	27.17 (1631)	11.99 (720)
100	3.059	3.06	2.6×10^{42}	8.17±0.65	7.36 (431.4)	179.48±55.87	278.02±61.02	21.58 (1310)	8.36 (507)
101	3.084	3.078	7.3×10^{42}	26.66±1.24	25.24 (1473.92)	-232.66±54.09	-286.72±49.81	30.99 (1873)	10.71 (648)
102	3.193	3.197	8.2×10^{42}	44.26±1.23	34.88 (1988.94)	41.52±14.66	20.9±14.43	15.62 (918)	6.3 (370)
103	3.01	3.002	9.4×10^{42}	32.57±1.28	22.28 (1320.96)	-22.62±72.81	96.71±45.67	32.97 (2028)	12.31 (756)
104	3.14	3.143	1.3×10^{43}	43.01±1.27	27.92 (1609.38)	35.71±28.7	3.26±23.41	24.15 (1439)	10.64 (634)
105	3.188	3.188	3.4×10^{42}	22.51±1.02	19.08 (1089.76)	137.82±45.99	222.9±39.35	25.48 (1500)	10.59 (623)
106	3.181	3.18	3×10^{42}	5.38±0.47	7.56 (432.52)	111.13±56.69	144.73±56.55	19.54 (1152)	6.47 (382)
107	3.086	3.083	6×10^{42}	15.08±0.88	18.2 (1061.85)	-108.68±54.37	-157.97±53.68	26.78 (1617)	10.32 (623)
108	3.092	3.092	5.8×10^{42}	30.23±1.23	25.88 (1507.21)	-140.75±43.3	-157.37±36.72	26.64 (1606)	10.25 (618)
109	3.076	3.077	5.2×10^{42}	29.45±1.22	26.76 (1563.05)	59.98±53.91	179.66±43.53	29.84 (1805)	12.42 (751)
110	3.098	$--$	$--$	$--$	$--$	$--$	$--$	$--$	$--$
111	3.043	3.045	3.9×10^{42}	6.47±0.55	8.56 (503.17)	170.88±61.55	154.25±55.59	18.89 (1151)	6.09 (372)
112	3.101	3.103	4.4×10^{42}	38.03±1.2	40.56 (2356.89)	212.43±24.1	217.13±18.86	17.19 (1033)	7.32 (440)
113	3.105	3.108	4.6×10^{42}	39.69±1.66	34.32 (1992.45)	47.93±41.95	32.96±41.28	28.62 (1719)	11.64 (699)
114	3.148	$--$	$--$	$--$	$--$	$--$	$--$	$--$	$--$
115	3.116	3.116	3.3×10^{42}	12.71±0.49	12.36 (716.36)	-83.13±11.97	-96.78±12.4	9.45 (567)	4.01 (240)
116	3.069	3.069	8×10^{42}	22.27±1.0	19.16 (1120.93)	14.07±41.89	-17.75±39.61	26.26 (1591)	10.73 (650)
117	3.186	3.186	2.4×10^{42}	30.33±1.19	34.08 (1947.36)	67.38±36.68	60.03±33.03	24.52 (1444)	9.76 (575)
118	3.108	$--$	$--$	$--$	$--$	$--$	$--$	$--$	$--$
119	3.176	3.175	2.9×10^{42}	19.03±0.82	21.8 (1248.54)	-10.89±22.65	2.22±21.95	14.8 (874)	6.02 (356)
120	3.407	3.406	2.8×10^{42}	3.56±0.31	3.52 (192.32)	94.36±26.5	112.72±31.65	11.58 (648)	4.56 (255)

and non-detections by building SB maps from NB images and consider detected nebulae above 2σ (section 4.3.2). We report results on the stacking of non detections and discuss their properties of the associated quasars in Section 4.3.2 and 4.4.2.

4.3.2   Lyman-α SB maps and spectra

We use the redshift of the nebulae identified in Section 4.3.1 to build Lyα SB maps computed from 30 Å pseudo-NBs centered at the Lyα line. This wavelength range is chosen to allow comparison with previous studies. As done in all previous works (e.g., Borisova et al. 2016), we compute the residual background of each SB map after masking the location of continuum sources present in the original white image. We then subtract the background level from each SB map. The resulting SB maps for the 59 faint quasars and the 61 bright quasars are shown in Figures 4.4 and 4.23, respectively, after smoothing using a 2D Box kernel of 3 pixels. For non detections, we build the SB maps in a 30 Å pseudo-NB centered at the peak Lyα emission of the quasar spectra. The SB maps of Figure 4.4 correspond to $\sim 150 \times 150$ kpc at the median redshift of the sample and show that the nebulae around the fainter quasars appear dimmer and more compact than their bright quasar counterparts (Figure 4.23), consistent with the findings presented in Mackenzie et al. (2021b). As done in previous works, the detected nebulae are defined out to their 2σ isophote in the Lyα SB maps. We use this isophote to characterize the nebulae physical properties in Section 4.3.3.

For the 59 faint quasars, we integrate the spectra inside the 2σ isophotes and present them in Figures 4.5, 4.6 and 4.7 with red curves, after normalizing by their maximum flux density. For the non-detections, we show the spectrum integrated within a 1.5" radius aperture in gray without normalization. For comparison, we show the quasar spectra within a 1.5" radius aperture in black after normalizing by their peak. The blue dashed line represents the wavelength of the peak Lyα emission of the quasar. We see that the Lyα emission of the detected nebulae resembles, in most cases, the Lyα emission of the quasars even though it is narrower, i.e, with similar absorption features and small shifts in wavelength compared to the Lyα line of the quasar. However, there are cases (like ID 71, 73, 81, 92) in which the Lyα emission occurs at wavelengths corresponding to absorption in the quasar spectrum. This result is similar to what has been found in the smaller sample studied in Mackenzie et al. (2021b). The resulting spectra for the 61 bright quasars from Arrigoni Battaia et al. (2019a) are presented in Figures 4.24, 4.25 and 4.26 of Appendix 4.6.2.

4.3.3   Nebulae morphology, area, integrated luminosity and kinematics

We characterize the nebulae by computing their integrated Lyα luminosity, area within the 2σ isophote, morphology, velocity shift with respect to the quasar Lyα line and linewidth, which we summarize in Table 4.2. Additionally, we obtain the spatial kinematics of the nebulae using the first and second moment maps which we present in Figures 4.8 and 4.9.
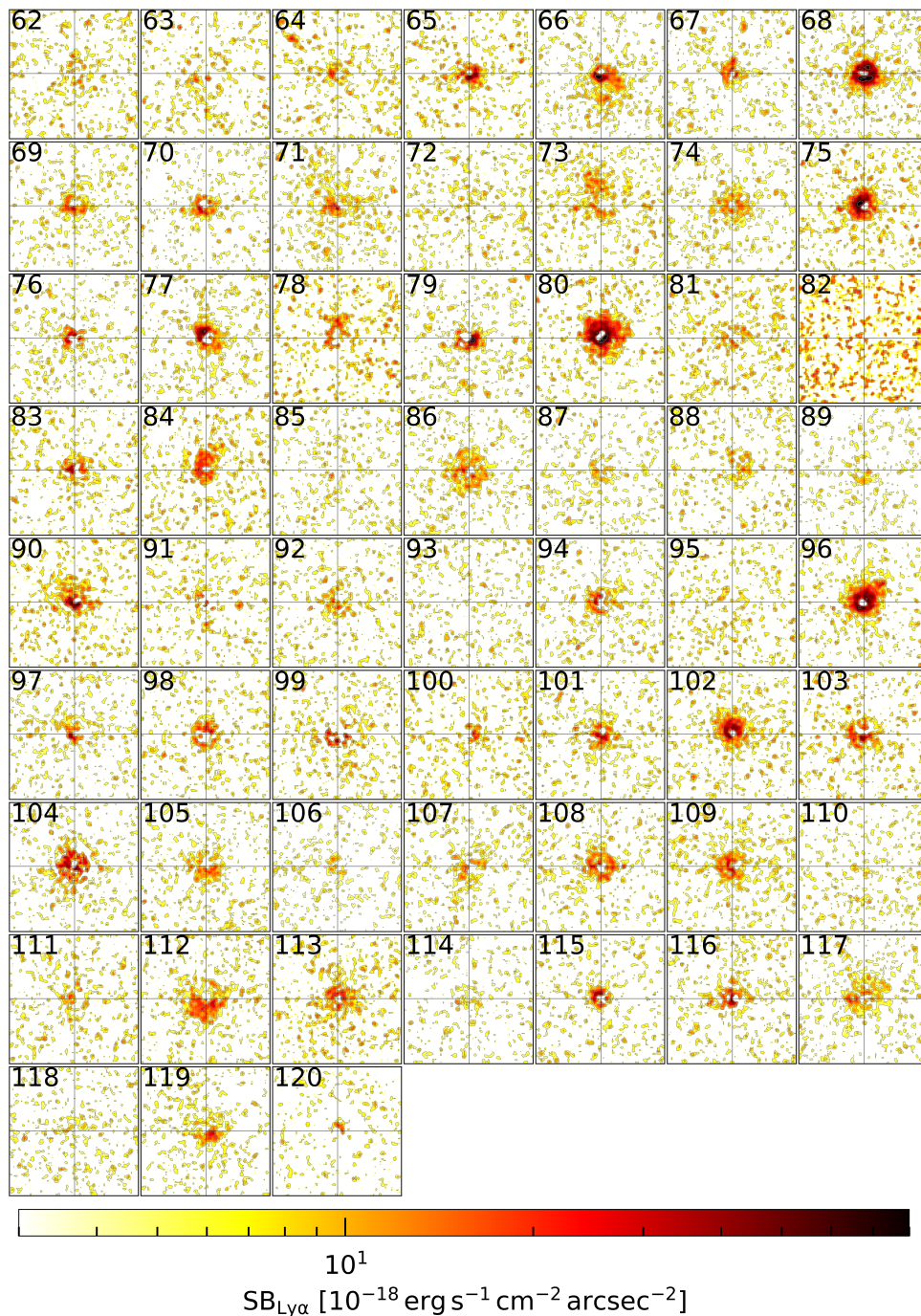
Figure 4.4: QSO MUSEUM III atlas of the faint quasars' Lyα nebulae. Lyα SB maps around the 59 faint quasars after PSF- and continuum-subtraction (see Section 4.2.5), computed from 30 Å pseudo-NBs centered at the peak Lyα wavelength of the nebula. Each image shows maps with projected sizes 10" × 10" (∼ 75 × 75 kpc at the median redshift of the sample). In each map, a black crosshair indicates the location of the quasar. The contours indicate levels of [2, 4, 10, 20, 50] times the Lyα SB limit within the pseudo-NB (Table 4.1).
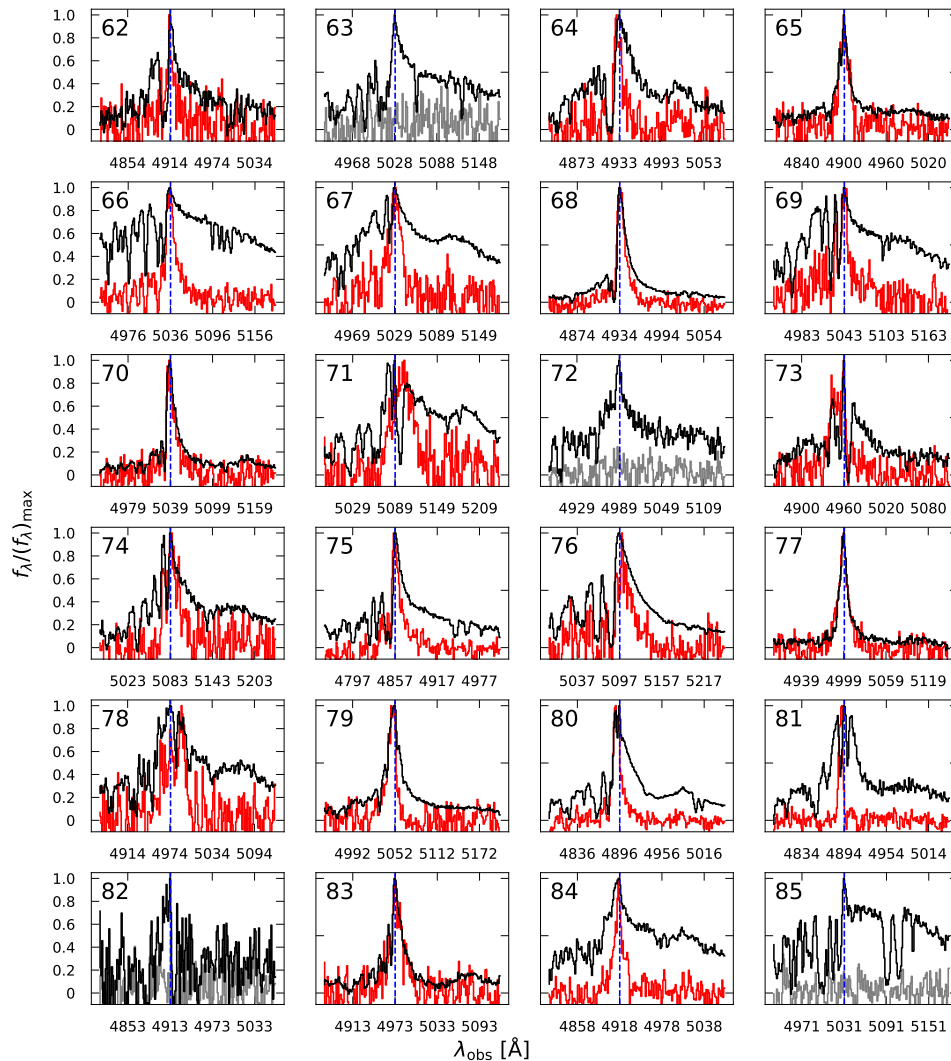
Figure 4.5: One-dimensional spectrum around the Lyα line of ID 62-85 of the targeted faint quasars. The ID of each system is shown in the top left corner of each panel. In each panel, the black line is a spectrum integrated from the MUSE datacube inside a 1.5" radius aperture centered at the quasar location and normalized by its peak. We indicate the wavelength of the peak of the Lyα emission of each quasar with a blue vertical line. The red line in each panel shows the integrated spectrum of detected nebular integrated from the PSF- and continuum-subtracted datacubes within the 2σ isophotes from Figure 4.4, after normalizing by its peak. The gray lines are the spectra integrated within a 1.5" radius aperture from subtracted cubes where we found no extended Lyα emission. We mask the 1"$\times$1" PSF normalization region when we extract a spectrum from a subtracted datacube.
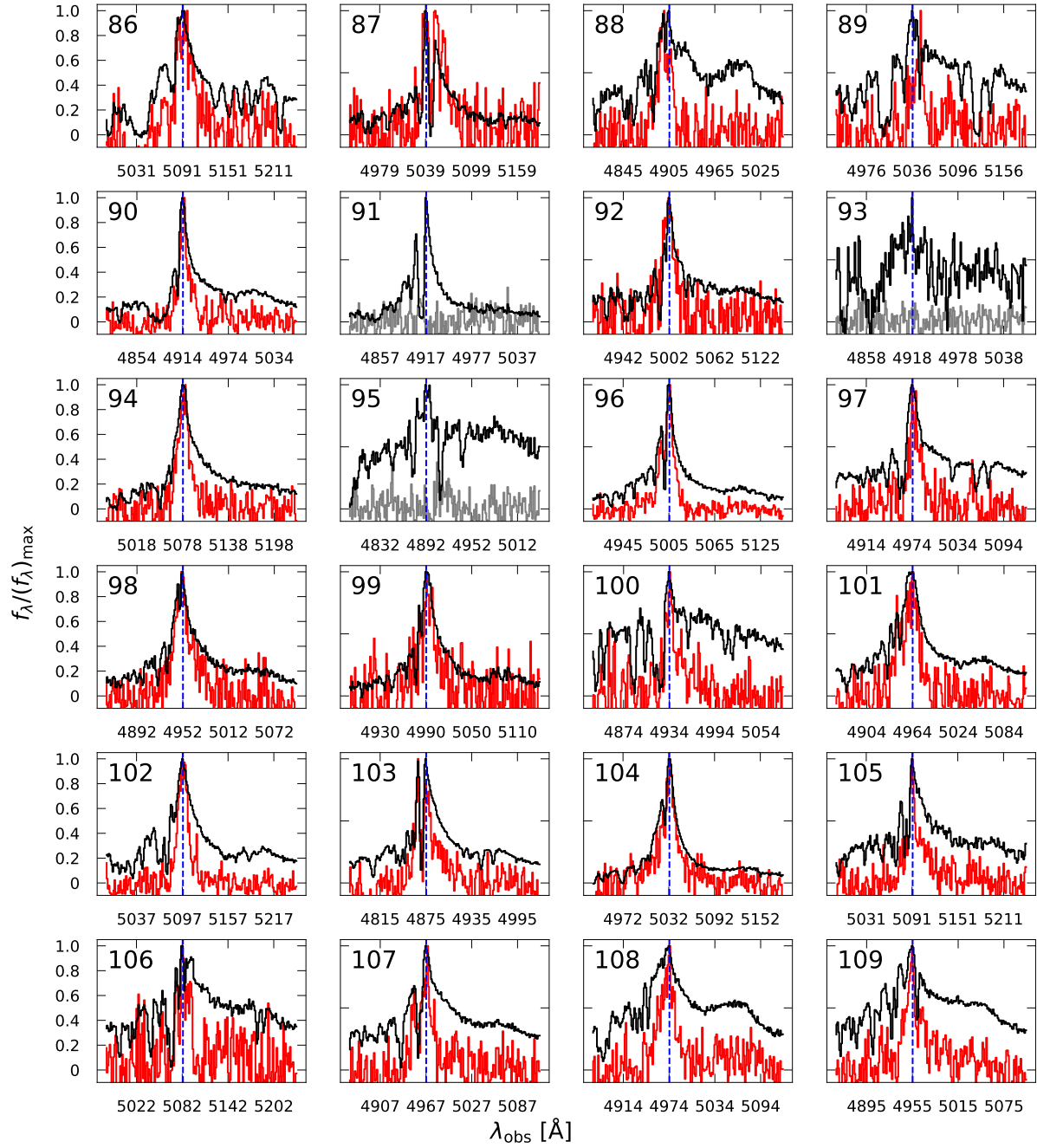
Figure 4.6: Same as Figure 4.5 but for ID 86-109.
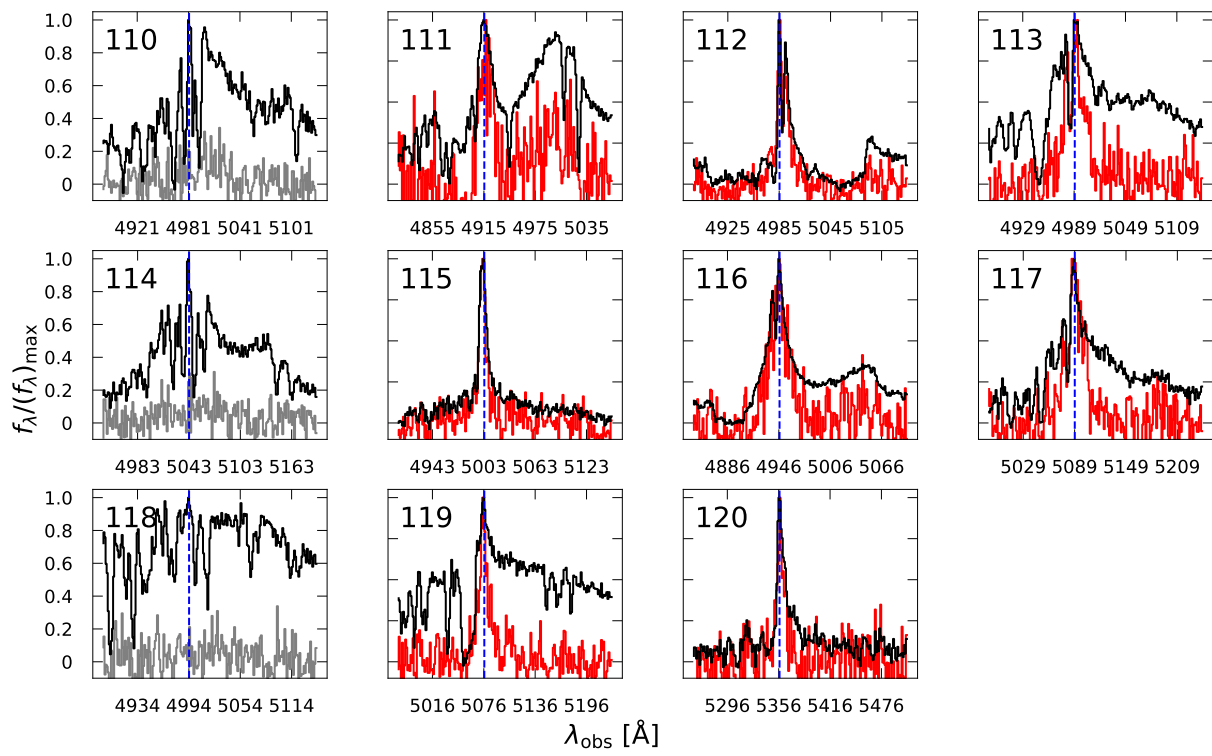
Figure 4.7: Same as Figure 4.5 but for ID 110-120.
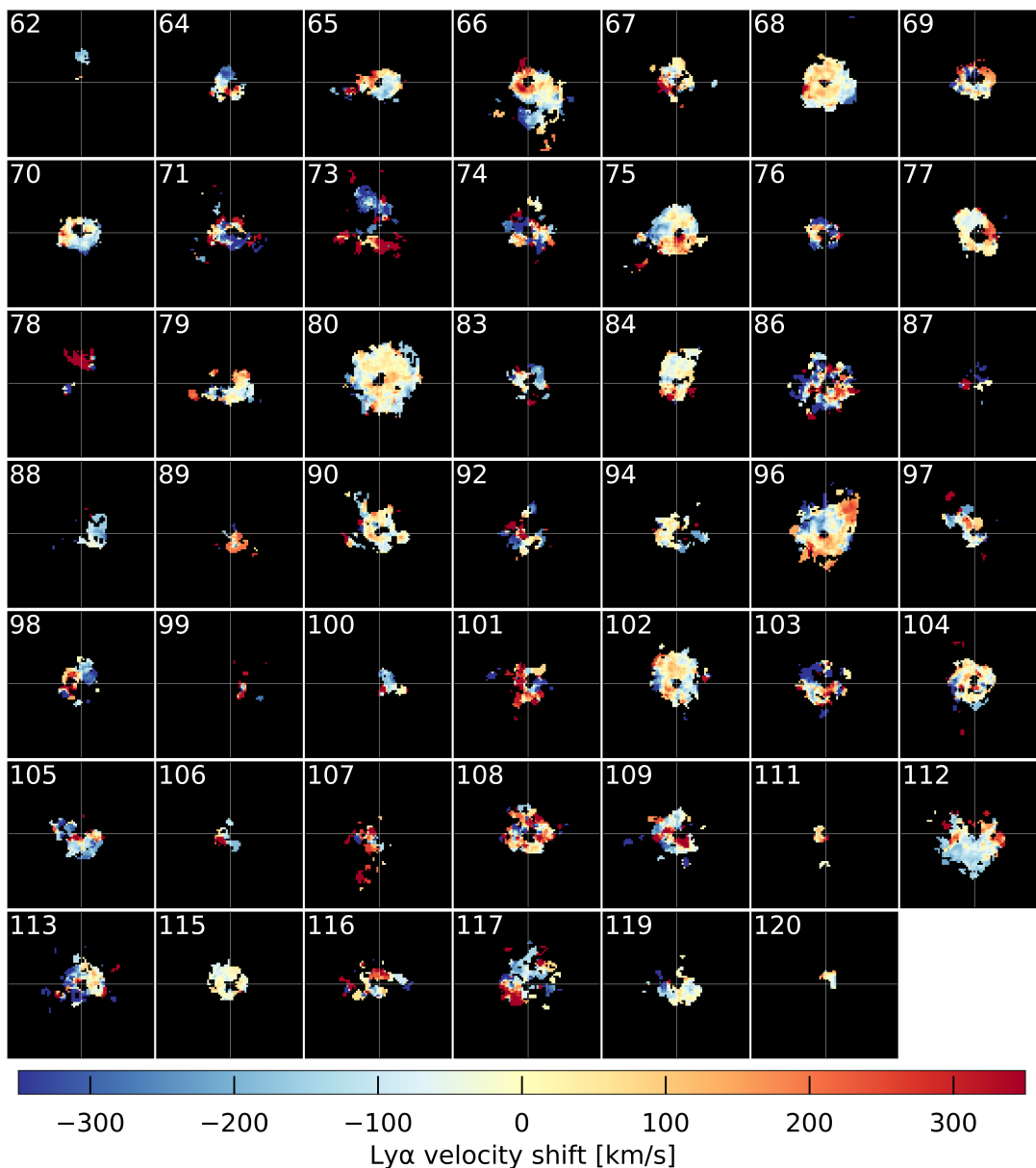
Figure 4.8: Lyα velocity shift maps of the detected nebulae around $z \sim 3$ faint quasars. The Lyα velocity shift map is computed from the first moment of the PSF- and continuum-subtracted datacubes within a $\pm\mathrm{FWHM}_{\mathrm{Ly}\alpha}$ with respect to the wavelength of the peak of the Lyα emission of the nebula (Table 4.2).The panels are shown using a projected scale of $8'' \times 8''$ ($\sim 60 \times 60\,\mathrm{kpc}$) and a white crosshair indicates the location of the quasar. The ID of each system is shown at the top left corner of each panel.
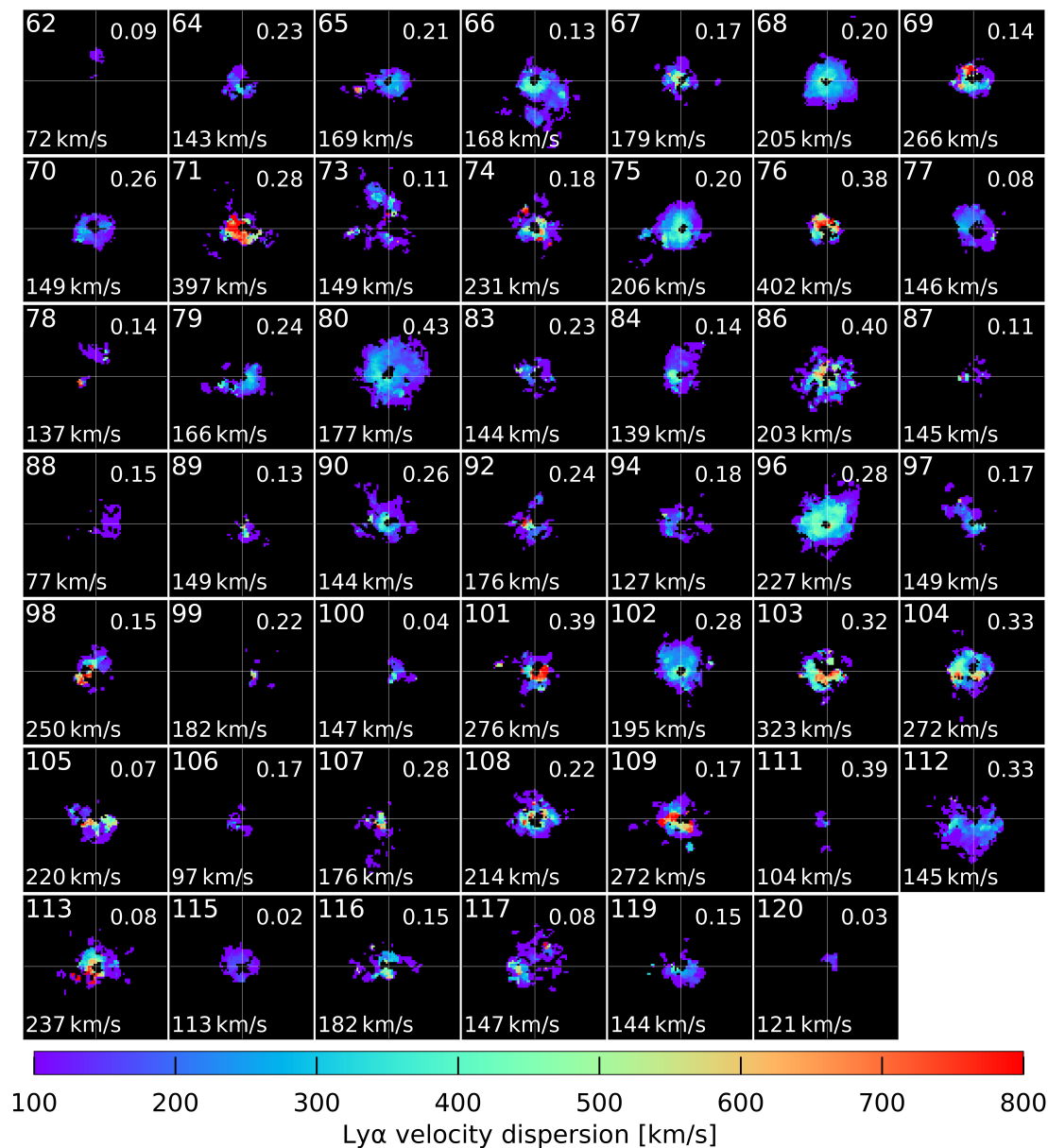
Figure 4.9: Lyα velocity dispersion maps of the detected nebulae around $z \sim 3$ faint quasars. The Lyα velocity dispersion map is computed from the second moment of the PSF- and continuum-subtracted datacubes within a $\pm \mathrm{FWHM_{Ly\alpha}}$ centered at the wavelength of the peak of the Lyα emission of the nebula (Table 4.2).The panels are shown with the same projected scale of $8'' \times 8''$ ($\sim 60 \times 60\,\mathrm{kpc}$) and a white crosshair indicates the location of the quasar. The ID of each system and the average velocity dispersion within the mask are shown at the top and bottom left corner of each panel, respectively. The velocity dispersion of the faint quasars is on average lower than their bright counterparts (Figure 4.28).

First, we characterize the Lyα line using the spectra integrated inside the 2σ isophotes by fitting a gaussian in order to obtain the centroid wavelength and the full width at half maximum (FWHM). We set an upper limit of 14 Å for the standard deviation when performing the gaussian fit. We estimate the total Lyα luminosity of the nebulae by integrating the spectra within a wavelength range of ±FWHM centered on the Lyα line. This choice of wavelength range is made to ensure that we are considering most of the flux distribution into the calculation of the luminosity. The centroid of the gaussian fit is used to compute the velocity shift of the nebula with respect to the quasar's peak Lyα emission, we list these values in Table 4.2.

We also note that a gaussian function is, in general, not a good representation of the Lyα line profile due to absorption features and possible radiative transfer effects affecting the propagation of Lyα photons. Therefore, we compute, for comparison, the first and second moment of the Lyα flux distribution to estimate the line centroid and linewdith independently from any model assumption. We find good agreement between the estimates from the gaussian fit and flux weighted moments of the Lyα line flux distribution. We list in Table 4.2 the flux weighted first moment of the line in terms of the velocity shift with respect to the quasar peak Lyα wavelength and the linewidth obtained from the second moment of the flux distribution.

In order to describe the kinematics of the observed nebulae, we compute the velocity shift and velocity dispersion maps shown in Figures 4.8 and 4.9 for the faint quasars and Figures 4.27 and 4.28 for the bright quasars. These maps are computed using the first and second moment of a pseudo-NB constructed within the ±FWHM range obtained from the gaussian fit and centered at the peak Lyα wavelength of the nebulae. We restrict the calculation of the moment maps to regions with SNR> 3 in the SB maps. The datacubes are spatially smoothed with a gaussian kernel of 0.5" before the SNR calculation, then this mask is applied to the PSF- and continuum- subtracted cubes before computing the first and second moment maps. The velocities are computed with respect to the wavelength of the peak of each extended Lyα emission. We see from the velocity shift maps that the nebulae kinematics of the faint sample (Figure 4.8) are complex and diverse, with some nebulae presenting velocity components that span $\sim 200-400$ km/s across the peak Lyα of the nebula (e.g., ID 66, 73, 96). Other nebulae appear to have more quiescent kinematics with velocities diverging < 100 km/s from the Lyα (e.g., ID 68, 80). We note that the maps for the faint quasars carry little information on the individual nebular kinematics as the maps are not able to resolve the smallest coherent structures. On the other hand, the velocity shift maps of the bright sample (Figure 4.27) display similar variety of complex velocity structures, with both quiescent and disturbed features in their nebulae. In particular, the largest velocity gradients for the bright quasars span a larger range than the faint nebulae of up to ~ 600 km/s across the peak Lyα wavelength. From the velocity dispersion maps of the faint quasars (Figure 4.9) we see that most of the nebulae show quiescent kinematics with velocity dispersions around $100-200$ km/s and show an tendency to increase up to $300-400$ km/s towards the location of the quasar. On the other hand, the bright quasar nebulae (Figure 4.28) have in general larger velocity dispersions and a similar tendency to increase up to $500-600$ km/s towards the center. For both samples

we see some cases where the velocity dispersion quickly increases to much higher values $(800 - 1000 \text{ km/s})$ at the center. We further explore these findings in Section 4.3.4.

We observe from the Lyα SB maps that the nebulae display a wide variety of morphologies, with some nebulae appearing centrally concentrated around the quasar position (e.g., ID 1, 39, 68, 80 among others), others appear lopsided towards one direction from the quasar (e.g., ID 11, 36, 66, 109, 112) and finally some cases show large scale coherent structures (e.g., ID 13, 50, 56, 96). The strength of these effects could have an origin on the different powering mechanisms of extended Lyα nebulae, such as photoionization due to anisotropic quasar radiation or resonant scattering (e.g, Costa et al., 2022). Moreover, the origin could be related to the gas distribution of each system (e.g., Cai et al., 2019) or viewing angle (e.g, Costa et al., 2022). Finally, the environment or presence of companions could affect the observed Lyα nebulae morphology (see e.g., González Lobos et al., 2023; Herwig et al., 2024). Therefore, we attempt to quantify the observed nebulae morphologies using two different measurements. First, we quantify the asymmetry of the SB maps as previously done in the literature (e.g., Arrigoni Battaia et al. 2019a; Herwig et al. 2024), defined as the ratio between the semiminor and semimajor axis within the 2σ isophotes used to describe the area of the detected nebulae (Tables 4.2 and 4.5). This can be described using the Stokes parameters:

$$\alpha = \frac{(1 - \sqrt{Q^2 + U^2})}{1 + \sqrt{Q^2 + U^2}} \tag{4.1}$$

Where Q and U are the Stokes parameters computed from the flux weighted second order moments of the image following Equation 1 in Arrigoni Battaia et al. (2019a) within the 2σ isophote. The value of α corresponds to the aspect ratio of the isophote, where $\alpha = 1$ represents a circular distribution. The left panel of Figure 4.10 shows the resulting α as a function of integrated Lyα nebula luminosity (Tables 4.2 and 4.5) within the same isophote for the faint (orange) and bright (dark green) quasars. We see that most of the observed nebulae have values of $\alpha > 0.5$, i.e., the nebulae tend to be rounder. Also, the median α of the faint sample (orange dot-dashed line) is smaller than of the bright quasars (green dot-dashed line), indicating that faint quasars present slightly more elongated nebulae. Indeed, we observe that 5 of the dimmest nebulae ($L_{\text{neb}} < 10^{44} \text{ erg s}^{-1}$) are associated with values representing more elongated distributions. For comparison, we show the median value of α from Arrigoni Battaia et al. (2019a) with a thin green dot-dashed line which is consistent with our re-calculation. Further, we show the α reported in the faint quasar sample from Mackenzie et al. (2021b) with a gray dotted line which appears to be consistent with the faint quasars presented in this work. Finally, the median value reported in Herwig et al. (2024) for associated projected quasar pairs is shown with a red dashed line, which showed an elongated morphology tracing the separation of the pairs. Notwithstanding these observations, there is no clear indication of a trend between α and $L_{\text{Ly}\alpha;\text{neb}}$ of the observed nebulae, which is also seen in those three works.

Finally, we use the same 2σ isophotes to compute the lopsidedness of the nebulae as done in Arrigoni Battaia et al. (2023b). In that work, the authors defined the asymmetry
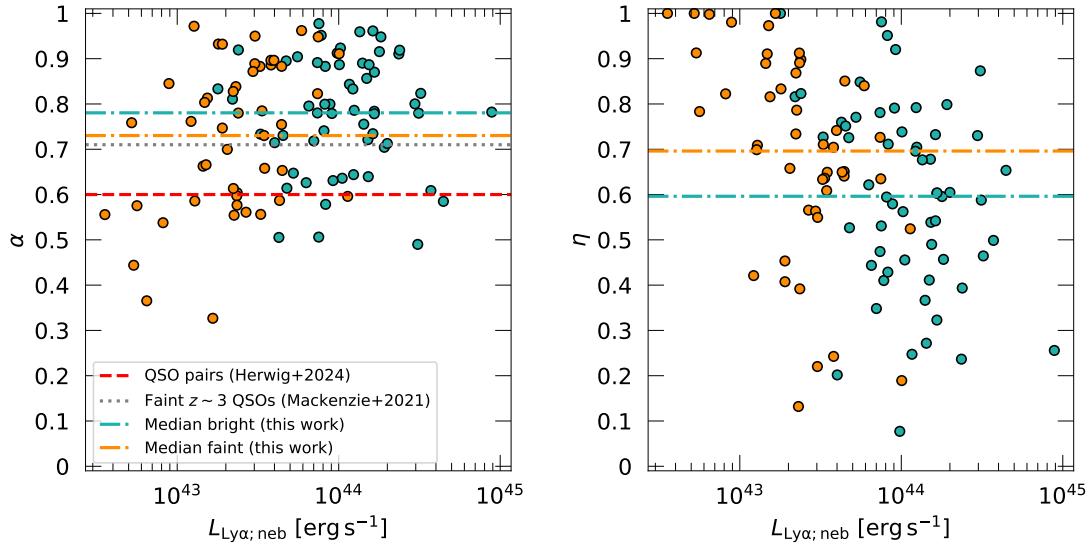
Figure 4.10: Level of elongation (α) and lopsidedness (η) of the observed nebulae. *Left:* Elongation (α) computed from the Stokes parameters (see Section 4.3.3) within the 2σ isophote of the detected nebulae as a function of their nebula Lyα luminosity. Larger values of α indicate rounder distributions. *Right:* Nebula lopsidedness (η) as presented in Arrigoni Battaia et al. (2023b) and described in the text. High values correspond to all emission being in one side of the quasar. In both panels, the orange and dark green points indicate the faint and bright sample of QSO MUSEUM III, respectively. The median values of the faint and bright sample are indicated with dot dashed lines of the same colors. Additionally, we show the median values of α reported in Mackenzie et al. (2021b) and Herwig et al. (2024).
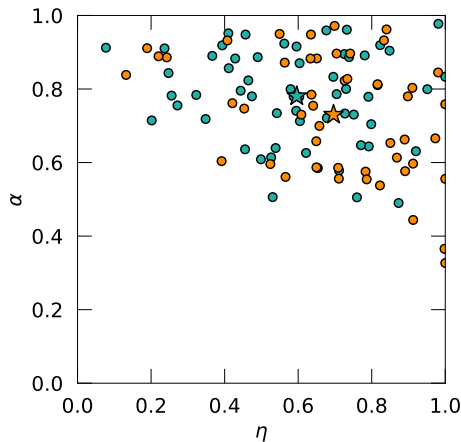
Figure 4.11: Comparison of elongation (α) and lopsidedness (η) of the detected nebulae. The bright and faint quasars are shown with green and orange dots, respectively. Similarly, the median values of each sample are shown with stars.

based on the ratio of areas $\eta = (A_{\max}^{\text{neb}} - A_{\min}^{\text{neb}})/A_{\max}^{\text{neb}}$. Where $A_{\max}^{\text{neb}}$ and $A_{\min}^{\text{neb}}$ are computed as the maximum and minimum area on both sides of an imaginary line that crosses the quasar position. In this case, η represents the level of lopsidedness of the nebulae, i.e., a value of $\eta = 1$ corresponds to all of the emission being on one side of the quasar. We plot η as a function of nebula Lyα luminosity within the 2σ isophote in the right panel of Figure 4.10 using orange and green colors for the faint and bright sample, respectively. This figure shows that the dimmest nebulae appear more lopsided with respect to brighter nebulae. This is similar to the results found in Arrigoni Battaia et al. (2023b), where at a fixed SB cut the smallest and dimmest nebulae appear more lopsided. In this case, we do not use a fixed SB cut, but the systems studied here are found to lie close to the Luminosity-Area relationship presented in that work for a SB threshold of $2.46 \times 10^{-17} \text{erg s}^{-1} \text{cm}^{-2} \text{arcsec}^{-2}$ (see their Table 1). We see that the systems with $\alpha < 0.5$ and $\eta \sim 1$ correspond to ID 62, 81 and 99 which have very low signal to noise and their morphology appears irregular. For these systems the 2σ isophote appears on one side of the quasar, which is a consequence of their clumpy SB morphology due to low luminosities. Also, we note that some bright systems also appear lopsided and this could be indication of larger scale structures. However, we see that there is no clear trend with η and the nebula Lyα luminosity in this sample. Finally, Figure 4.11 shows a comparison of the estimated values of α versus η for the bright and faint quasars using green and orange dots, respectively. This figure indicates that most of the nebulae tend to have a circular morphology and their emission tends to be preferentially towards one side of the quasar, i.e., the nebulae emission is asymmetric with respect to the quasar position. However, we note that the values of η span from centered to lopsided nebulae and no clear indication of following a trend with luminosity or α. We briefly discuss the possible origin of these observations in Section 4.4.2.

4.3.4 Surface brightness and velocity dispersion radial profiles

The nebulae presented in this work show a diversity of morphologies, luminosities and kinematics and we attempt to quantify their differences by building radial profiles using the SB maps of Figures 4.4 and 4.23 and the velocity dispersion maps of Figures 4.9 and 4.28 as usually done in the literature (Arrigoni Battaia et al., 2019a; González Lobos et al., 2023). The Lyα SB radial profiles are computed by averaging the maps inside annuli with logarithmically increasing radius centered at the quasar position, then corrected by cosmological dimming. We extract the SB radial profiles for all systems and compute the median profile for the faint and bright sample and show them in the top left panel of Figure 4.12 with orange and blue triangles, respectively. These profiles are cut to the 2σ detection limit of the stack and the shaded areas represent their mean uncertainty. For comparison, we show the median profile of 12 similarly faint $z \sim 3$ quasars from Mackenzie et al. (2021b) and the QSO MUSEUM I (Arrigoni Battaia et al., 2019a) with a yellow and purple line, respectively. The similarities of the observed profiles and those studies show that our analysis results in comparable Lyα nebulae. Additionally, we construct a stacked SB map for the non detections by median combining 30 Å pseudo-NB images centered
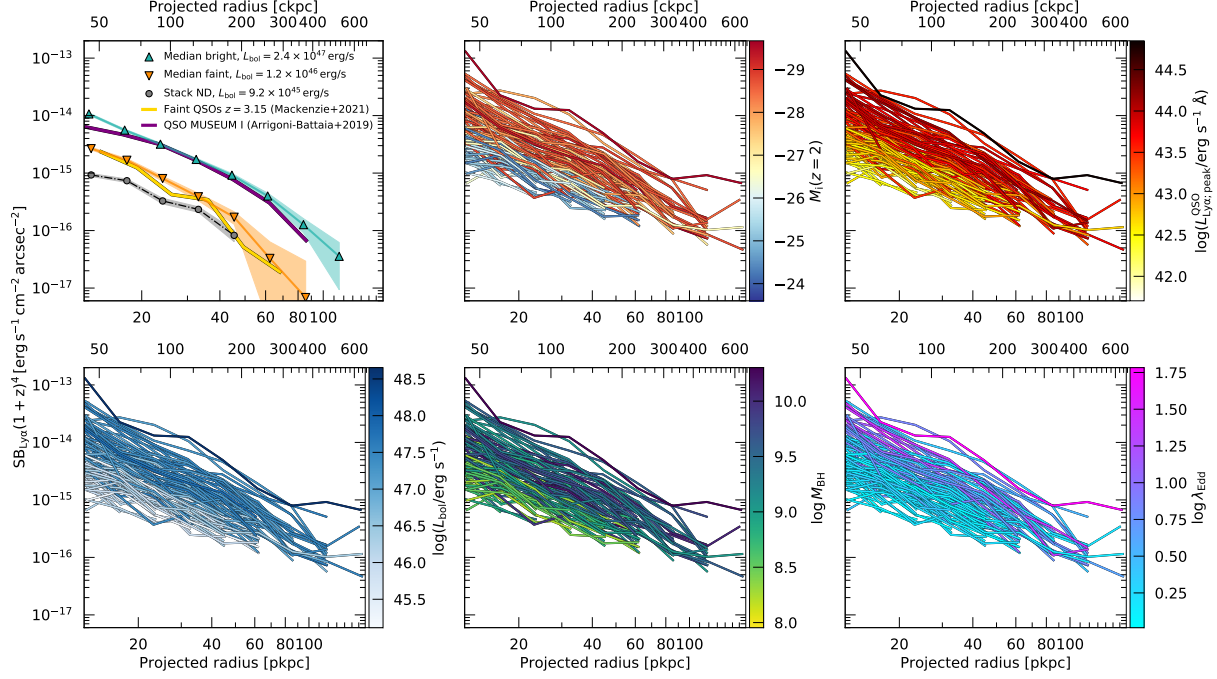
Figure 4.12: Lyα SB radial profiles of the QSO MUSEUM III nebulae. The profiles of each detected nebulae are computed by averaging the Lyα SB maps of Figures 4.4 and 4.23 inside annuli with logarithmically increasing radius centered at the quasar location, after masking the $1'' \times 1''$ normalization region. We cut the profiles when they reach values below the 2σ SB limit or are negative, and only plot profiles that have at least two points satisfying this criteria (108/110 profiles). The Lyα SB is corrected by cosmological dimming and is shown as a function of physical (bottom axis) and comoving (top axis) projected distances. *Top left:* Median profiles of the faint and bright sample (orange and green triangles) and stacked non detections (gray circles). Additionally, the median profiles from Mackenzie et al. (2021b) and Arrigoni Battaia et al. (2019a) are shown with a yellow and purple line, respectively. *Top middle:* The profiles are color coded by the absolute *i*-band magnitude normalized to $z = 2$ of the quasar. *Top right:* The profiles are color coded by the peak of the Lyα luminosity density of the quasar. *Bottom left:* The profiles are color coded by the bolometric luminosity of the quasar, computed from the monochromatic luminosity at 1350Å (Appendix 4.6.1). *Bottom middle:* The profiles are color coded by their quasar's black-hole mass. *Bottom right:* The profiles are color coded by their quasar's Eddington ratio.
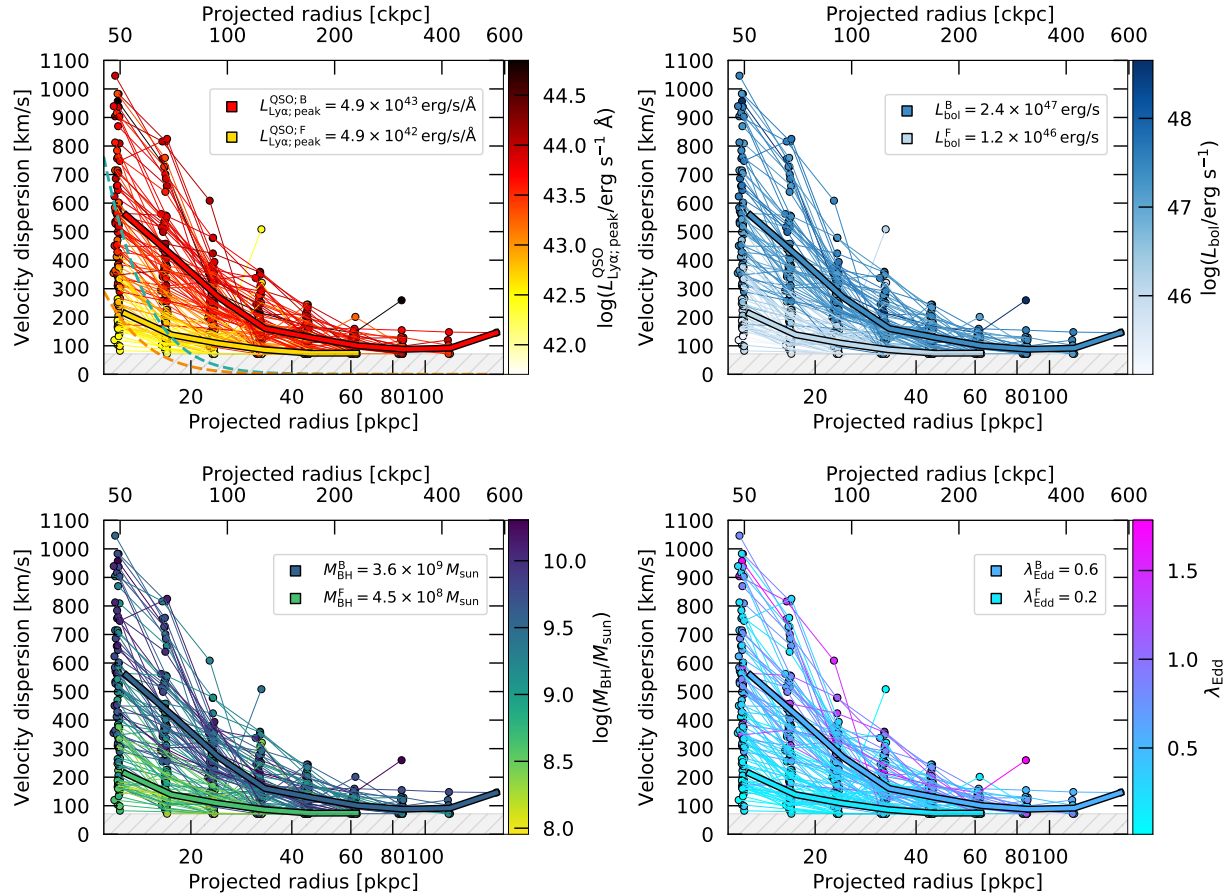
Figure 4.13: Individual Lyα velocity dispersion radial profiles of the QSO MUSEUM III nebulae. Each profile is computed by averaging the Lyα velocity dispersion maps from Figures 4.9 and 4.28 inside the 3>SNR mask, using the same annuli as the profiles from Figure 4.12. *Top left:* The profiles are color coded by the peak Lyα luminosity density of the quasar. *Top right:* The profiles are color coded by the bolometric luminosity of the quasar. *Bottom left:* The profiles are color coded by the black hole mass of the quasar. *Bottom right:* The profiles are color coded by the Eddington ratio of the quasar. Additionally, we show in each panel the median velocity dispersion profile of the faint and bright samples, color coded by each property with the median value of each bin indicated at the top right corner of the panel. The average Moffat seeing of the observations is shown in the top left panel with dashed lines, which is re-scaled to the median profile of the bright (blue) and faint (orange) sample. In each panel, the MUSE spectral resolution limit (72 km/s) is shown with a dashed gray area.

at the wavelength of the peak of the quasar Lyα emission. This decision is based on the frequent observation that Lyα nebulae peak emission occurs at a similar wavelength of the quasar Lyα peak emission (Arrigoni Battaia et al. 2019a; Cai et al. 2019). We similarly propagate the associated variances to obtain errors. The stacked map shows a clear detection of which we show its SB profile in the top left panel of Figure 4.12 with gray circles. This SB profile is at the low end of all the observed individual nebulae and bolometric luminosities, confirming that these sources are just below our detection limit for individual systems.

In the rest of the panels of Figure 4.12, we show the extracted individual Lyα SB radial profiles for the detected nebulae. In these, we show datapoints lying above the 2σ Lyα SB limit (rescaled to the area of each annuli). We only show profiles that have two or more datapoints above the rescaled SB limit, corresponding to a total of 108 profiles. Further, the Lyα SB profiles of Figure 4.12 are color coded by their quasar properties: the absolute i-band magnitude normalized at $z = 2$ (top middle), the quasar's peak Lyα luminosity density (top right), the quasar's bolometric luminosity (bottom left), the quasar's black hole mass (bottom middle) and their Eddington ratio (bottom right). We see from these plots that the profiles span almost 2 orders of magnitude in their SB level and their shapes are similar across the whole sample. We further study the shape of the SB profiles by fitting a power and exponential function in Section 4.4.1. Here, we observe that, in general, the profiles of nebulae around the faint sample have Lyα SB about one order of magnitude lower than the nebulae around bright quasars. Also, the extended Lyα around the bright quasars is detected out to projected distances of ~ 100 pkpc, while for the faint quasars the Lyα is detected mostly out to 60 pkpc. Additionally, the SB profile normalization factor increases as the peak Lyα luminosity and bolometric luminosity of the quasar increase. Such trend is not as clearly apparent with the absolute magnitude, as the profiles present larger Lyα SB scatter at a fixed quasar magnitude. Similarly, the black hole masses show scatter across the range of Lyα SB. Finally, there is a tendency for the brightest nebulae to also present the most extreme Eddington ratios, suggesting a potential link between nebula SB and extent and AGN accretion rate. Finally, we overlay in the top left panel the median SB profile of the faint and bright sample, with shaded areas representing their mean error with orange and blue shades, respectively. Details on the calculation of the median profiles is described in detail in Section 4.4.1. We observe that stacking highlights that the profile shapes for the faint and bright samples are strikingly similar, however the SB normalization factor of the bright sample is about 8 times larger than the faint. The median values of each AGN property within the faint and bright sample bins are shown in the legend of Figure 4.13.

Further, we present in Figure 4.13 radial profiles that were constructed similarly to the SB profiles, but using the velocity dispersion maps of Figures 4.9 and 4.28. These profiles are computed by averaging inside each annuli only where there is velocity dispersion data (within the SNR> 3 mask of Figures 4.9 and 4.28). We overlay in the figure the spectral resolution limit (72 km/s) of MUSE with a shaded gray region. Note that the profiles approach this limit as the distance to the center increases, indicating that we need higher spectral resolution to resolve the lines at such distances. However, the velocity dispersion

profiles tend to increase towards the quasar position. We color code the profiles by their quasar properties such as the peak Lyα luminosity density of the quasar (top left), the quasar's bolometric luminosity (top right), the black hole mass (bottom left) and Eddington ratio (bottom right). We see a wide range of velocity dispersions, ranging from ~ 100 km/s up to ~ 1000 km/s within the innermost regions of the CGM of the targeted quasars (~ 12 kpc). This scatter decreases to about 300 km/s as the projected distance increases (~ 40 kpc), due to the steep decrease on the velocity dispersion of the nebulae around the brightest quasars. Indeed, we show the median velocity dispersion profile for the faint and bright quasar sample in Figure 4.13 with thicker lines, which indicate that the velocity dispersion of bright quasar nebulae are about three times larger than fainter quasars at ~ 12 kpc and only two times larger at ~ 20 kpc. If we compare the velocity dispersion radial profiles to properties such as black hole masses and Eddington ratios we observe a similar behavior but with less pronunciation, probably because of the larger scatter of these properties across the range of luminosities probed with our sample. We show in the top left panel of this figure the average Moffat profiles of the observations rescaled to the faint and bright median profiles with blue and orange dashed lines respectively, to show that the trend is not affected by residuals of the quasar PSF-subtraction.

4.4 Discussion

By targeting 59 additional faint ($-27 < M_{\mathrm{i}}(z=2) - 24$) $z \sim 3$ quasars, this work expands the current catalog of known Lyα nebulae with 49 additional detections, which translates into covering two orders of magnitude fainter systems than the bolometric luminosities studied in the QSO MUSEUM I survey (see Figure 4.3), and representing a factor of $4\times$ more nebulae than currently available at these quasar luminosities. This wider dynamic range allows us to study the CGM in emission of quasars across the faint and bright end of the observed $z \sim 3$ quasar population (Figure 4.2) and link it to their AGN properties in addition to the physical mechanisms powering the emission.

4.4.1 Stacked Lyα SB and velocity dispersion radial profiles and their dependence on quasar properties

We design figures that contain all in once the aforementioned results as a function of quasar properties. In the left panel of Figure 4.14 we show the bolometric luminosity as a function of black hole mass of the 110 quasars with detections in a log-log plot, color coded by the peak Lyα luminosity density of the quasars. In this plot, quasars with similar Eddington ratios follow gray dashed diagonal lines. The size of the symbols is proportional to the ratio between the total luminosity of the Lyα nebula and its area in kpc^2 within their 2σ isophote, basically tracing the mean physical Lyα surface brightness of the nebula. This plot illustrates both the correlation between the quasar Lyα luminosity and their bolometric luminosity (Figure 4.3), and the increase in Lyα surface brightness for brighter systems as it was also observed in the Lyα SB profiles of Figure 4.12. Additionally, we
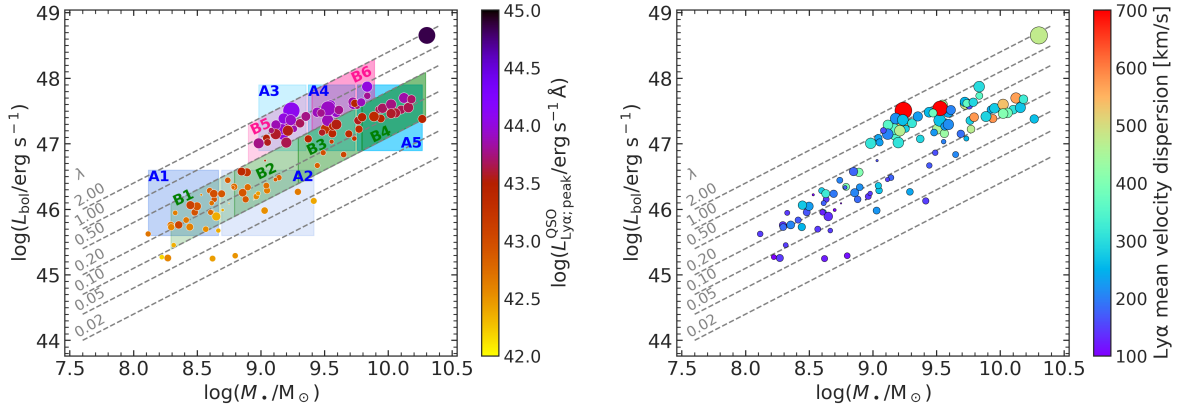
Figure 4.14: Comparison of observed quasar properties with nebulae properties. We show for each detected nebulae, their quasar bolometric luminosity as a function of black hole mass. The size of each point is proportional to the integrated Lyα luminosity of the nebula divided by the total nebula area, with larger symbols having larger ratios. Different values of constant Eddington ratios ($\lambda_{\rm Edd}$) are shown with gray dashed lines. *Left:* The points are color coded by the peak Lyα luminosity density of each quasar (Table 4.5). *Right:* The points are color coded by the mean velocity dispersion shown in the maps of Figures 4.9 and 4.28. Additionally, we overlay in the left panel the bins covering different quasar properties described in Section 4.4.1.

show in the right panel of Figure 4.14 the same properties but color coded by the mean velocity dispersion measured in the second moment maps of Figures 4.9 and 4.28. We see that the nebulae have a tendency to present larger average velocity dispersions with increasing bolometric luminosity (and hence also peak Lyα quasar luminosity), which was also observed in the velocity dispersion radial profiles of Figure 4.13. Therefore, we observe from Figure 4.14 that the nebulae become brighter and more turbulent with increasing bolometric luminosity and black hole mass.

We explore the main drivers of these trends by computing the median Lyα SB profiles using several bins encompassing different quasar properties. Stacking is done by first re-binning the profiles and their uncertainties into a common grid of projected comoving distances using a cubic spline interpolation, then we compute the median value at each radial bin. Since the stacking procedure decreases the noise potentially revealing fainter emission than in individual profiles, we also include in the stack the datapoints falling below the 2σ Lyα SB limit of each individual profile. We compute the mean uncertainty of each stacked radial bin by propagating their variances. Similarly, we re-scale the 2σ Lyα SB limit of the stacked bins and use it to cut the stacked profile at the radial distance at which it falls below the 2σ detection limit.

To stack the profiles, first we build equally spaced bins of the peak Lyα luminosity density of the quasar and show their median Lyα SB profiles in the top left panel Figure 4.15 and color code them by by the median peak Lyα luminosity of the quasars within the bin
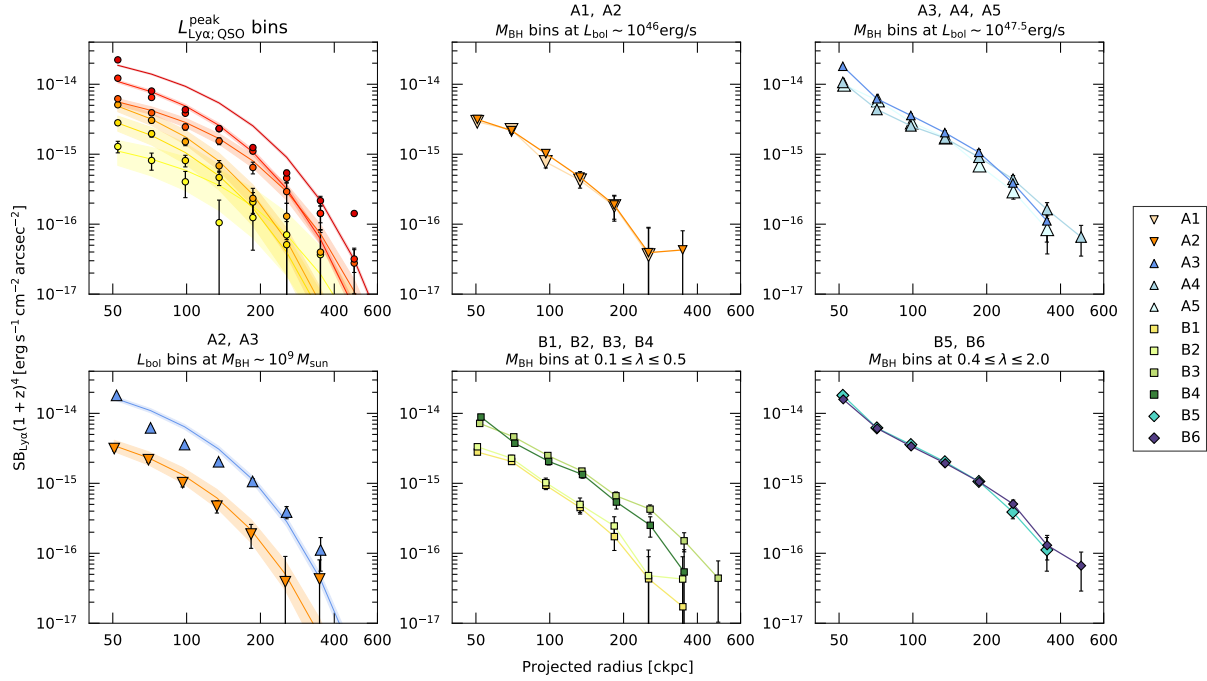
Figure 4.15: Lyα SB radial profiles binned at different quasar properties. The panels show the median Lyα SB corrected by cosmological dimming as a function of projected comoving distances. *Top left:* Median profiles within equally spaced bins of peak Lyα luminosity density of the quasars (see Section 4.4.1), color-coded by the median $L_{\text{Ly}\alpha;\text{peak}}^{\text{QSO}}$ of the bin and using the same color-scale as the individual radial profiles of Figure 4.12. We plot an exponential fit (see Section 4.4.1) to each profile with a shaded area of the same color as the datapoints. *Top middle:* Median profiles within bins A1 and A2 of Figure 4.14, representing $M_{\text{BH}} \sim 10^{8.3}$ and $10^{9.1}\,\text{M}_\odot$ at fixed $L_{\text{bol}} \sim 10^{46}\,\text{erg\,s}^{-1}$. *Top right:* Median profiles within bins A3, A4 and A5 representing $M_{\text{BH}} \sim 10^{9.2}$, $10^{9.6}$ and $10^{10}\,\text{M}_\odot$ at fixed $L_{\text{bol}} \sim 10^{47.5}\,\text{erg\,s}^{-1}$. *Bottom left:* Median profiles within bins A2 and A3 representing two bins of bolometric luminosity $L_{\text{bol}} \sim 10^{46}$ and $L_{\text{bol}} \sim 10^{47.5}\,\text{erg\,s}^{-1}$ at a fixed black hole mass of $M_{\text{BH}} \sim 10^9\,\text{M}_\odot$. We plot an exponential fit to each profile with a shaded area of the same color as the datapoints. *Bottom middle:* Median profiles within bins B1, B2, B3 and B4 representing M_{BH} bins of $\sim 10^{8.5}$, $10^{9.0}$, $10^{9.5}$ and $10^{10}\,\text{M}_\odot$ at $\lambda_{\text{Edd}} \sim 0.2$. *Bottom right:* Median profiles within bins B5 and B6 representing M_{BH} bins of $\sim 10^{9.2}$ and $10^{9.7}\,\text{M}_\odot$ at $\lambda_{\text{Edd}} \sim 1.0$. The legend indicates the symbol used for each bin, while the median values of their bolometric luminosity and black hole mass are indicated in the legend of Figure 4.16.
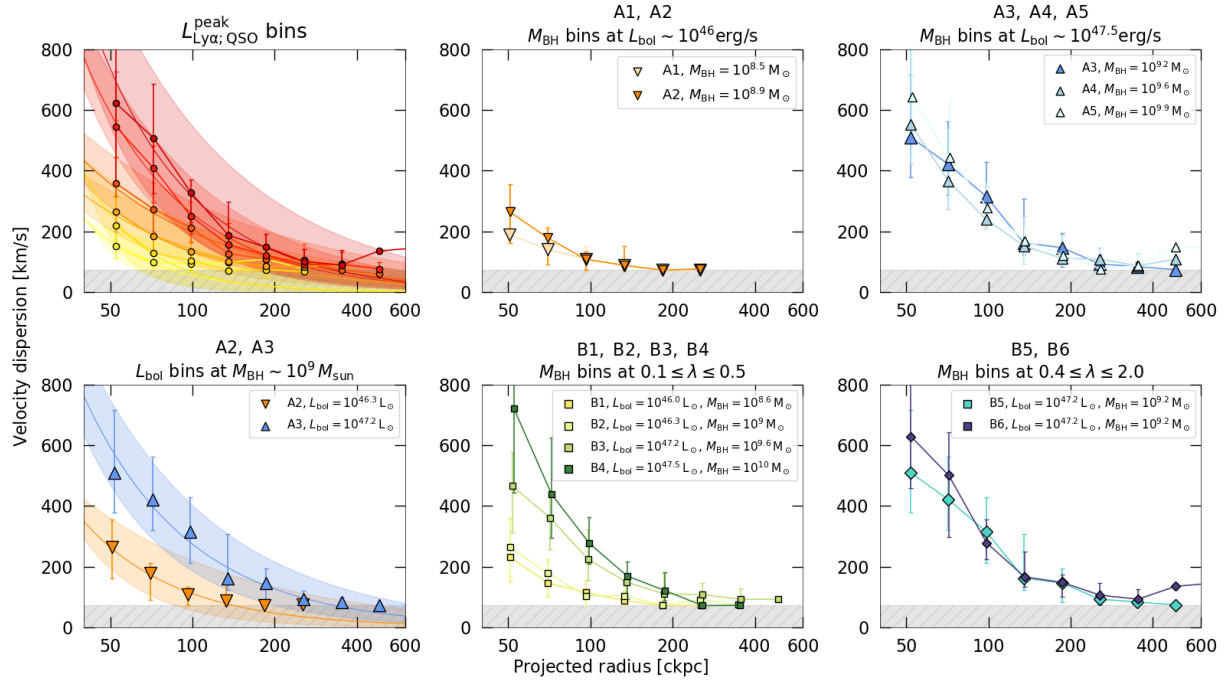
Figure 4.16: Velocity dispersion profiles binned at different quasar properties. Similarly to Figure 4.15, we show the median velocity dispersion profiles within the same bins and using the same layout. The top left panel shows a power law fit to the median profiles at different peak quasar Lyα luminosity bins with solid lines and shaded areas indicating their 1σ uncertainty.

using the same color scale as the radial profiles shown in the middle panel of Figure 4.12. The bins are $\log(L_{\mathrm{Ly\alpha;peak}}^{\mathrm{QSO}}/\mathrm{erg\,s^{-1}\,\AA^{-1}}) = 42.5$ to 44 and sizes of 0.3 dex, resulting in 6 bins with 20, 23, 16, 9, 23 and 29 stacked profiles each. Within this range of peak Lyα luminosity densities, the SB level of the stacked profiles have a tendency to increase from $\mathrm{SB}_{\mathrm{Ly\alpha}}(1+z)^4 \sim 10^{-15}$ to 10^{-14} erg s^{-1} cm^{-2} arcsec^{-2} in their inner region (~ 50 ckpc or ~ 12.5 pkpc) and maintain a similar order of magnitude difference as the projected distance increases, this suggest that the profiles in general have a similar shape between each other. Additionally, we stack the profiles in the same way but using equally spaced bolometric luminosity bins starting with $\log(L_{\mathrm{bol}}/\mathrm{erg\,s^{-1}}) = 45$ to 48.7 and sizes of 0.6 dex, resulting in 5 bins with 8, 31, 21, 31 and 28 profiles each. We do not show these profiles, however a similar trend is observed between the SB level and the bolometric luminosity as expected from the relationship between the bolometric luminosity and the peak Lyα luminosity density of the quasar illustrated in Figure 4.3 and the individual radial profiles of Figure 4.12.

It is clear form these observations that the Lyα SB level of the nebulae is correlated with the quasar luminosities, however we want to test whether other AGN properties could also be linked to it. For this, we construct bins at different black hole masses and Eddington ratios that span the range of properties of the targeted quasars (Figure 4.14), these bins are overlayed and labeled in the left panel of Figure 4.14. Bins A1 and A2 are constructed to cover the low end of bolometric luminosities ($L_{\mathrm{bol}} \sim 10^{46}$ erg s^{-1}) and black hole masses between $\log(M_{\mathrm{BH}}/\mathrm{M}_\odot) = 8.1 - 8.6$ and $\log(M_{\mathrm{BH}}/\mathrm{M}_\odot) = 8.6 - 9.5$, respectively. Bins A3, A4 and A5 are constructed to cover the higher end of bolometric luminosities ($L_{\mathrm{bol}} \sim 10^{47.5}$ erg s^{-1}) and black hole masses of $\log(M_{\mathrm{BH}}/\mathrm{M}_\odot) = 9.0 - 9.4$, $\log(M_{\mathrm{BH}}/\mathrm{M}_\odot) = 9.4 - 9.7$ and $\log(M_{\mathrm{BH}}/\mathrm{M}_\odot) = 9.7 - 10.2$, respectively. Bins B1, B2, B3 and B4 are constructed to cover the lower end of Eddington rations ($\lambda_{\mathrm{Edd}} \sim 0.2$) and black hole mass bins of $\log(M_{\mathrm{BH}}/\mathrm{M}_\odot) = 8.3$ to 10.3 and sizes of 0.5 dex. Note that the uncertainties in the estimation of the black hole masses are of the order of $\log(M_{\mathrm{BH}}/\mathrm{M}_\odot) \sim 0.5$ (Appendix 4.6.1), therefore these large black hole mass bin sizes could be considered, for this test, a fixed black hole mass range. Finally, bins B5 and B6 are constructed to cover the higher end of Eddington ratios ($\lambda_{\mathrm{Edd}} \sim 1.0$) and black hole mass bins of $\log(M_{\mathrm{BH}}/\mathrm{M}_\odot = 8.9 - 9.4$ to $9.4 - 9.9$. We stack the Lyα SB profiles inside these bins using the same method described above and plot the resulting profiles in Figure 4.15, where each panel corresponds to a set of bins indicated at their top. The top middle panel of this figure shows that the increasing black hole mass at low bolometric luminosity (bins A1 and A2) does not have an impact in the median SB profile, indicating that the Lyα radiation around faint quasars is independent of the black hole mass. Similarly, at high bolometric luminosity but different black hole mass (bins A3, A4, A5) there is no apparent evolution of the profiles. However, the bottom left panel of Figure 4.15 shows that at fixed black hole mass ($M_{\mathrm{BH}} \sim 10^9\,\mathrm{M}_\odot$), the lower end of bolometric luminosities (bin A2) has around 7 times dimmer nebulae than the higher end of bolometric luminosities (bin A2), confirming the trend observed between individual radial profiles and bolometric luminosity of Figure 4.12. On the other hand, if we compare the bins with low Eddington ratios and different black hole masses (bins B1, B2, B3 and B4) we see a slight increase in the SB level

of the stacked profiles, more likely originating from the increase in bolometric luminosity than the increase in black hole mass, as we do not see changes in profiles due to black hole mass. Finally the two bins at high Eddington ratio (B5 and B6) show very similar profiles despite the different black hole mass and bolometric luminosity.

Similarly, we use the same bins to compute median Lyα velocity dispersion radial profiles which are shown in Figure 4.16 using the same colors as in Figure 4.15. The stack is carried out by computing the median value at each projected distance bin and masking out values that fall below the spectral resolution limit (72 km/s). These plots show that all profiles seem to approach the resolution limit at projected distances between 100 and 200 ckpc. Additionally, we see that the velocity dispersion profiles follow similar trends as the SB radial profiles as a function of bolometric luminosity. Indeed, the velocity dispersions become higher towards the center with increasing peak Lyα luminosity density of the quasar and bolometric luminosity. This effect is clearly seen in the bottom left panel where the velocity dispersion increases from 300 km/s to 500 km/s in the center for bins A2 and A3, respectively. This trend could indicate a link between the kinematics in the inner CGM to the AGN activity, which we further discuss in Section 4.4.2. Similarly to Figure 4.15, the velocity dispersion profiles do not seem to be strongly affected by the changes in black hole mass.

With these tests we confirm that the increase in SB level and velocity dispersion of the nebulae is correlated to the bolometric luminosity, therefore we focus in quantifying these differences by fitting the median profiles inside the quasar luminosity bins described above with a power or exponential law. We perform the fits using a Markov Chain Monte Carlo (MCMC) approach, which is implemented in the `emcee`[6] module for Python (Foreman-Mackey et al., 2013). For reference, we show in the top left panels of Figures 4.15 and 4.16 the resulting exponential and power law fits with a solid line and shaded regions representing their 1σ uncertainty, using the same colors as the datapoints of each corresponding median profile. Additionally, we fit the median profiles of the non detections, bin A2 and bin A3 with the same method. For the Lyα SB, we fit the profiles using both a power law of the form $\mathrm{SB}_{\mathrm{Ly}\alpha}(1 + z)^4 = \mathrm{SB}_0 \times r^\beta$ and exponential function of the form $\mathrm{SB}_{\mathrm{Ly}\alpha}(r) = \mathrm{SB}_0 \times e^{-(r/R_h)}$. On the other hand, for the median velocity dispersion profiles within the same bins, we fit only a power law of the form $\sigma = \sigma_{50}(r/50\,\mathrm{ckpc})^\beta$. Figure 4.17 summarizes the results of the MCMC fit to the median profiles inside $L^{\mathrm{QSO}}_{\mathrm{Ly}\alpha;\mathrm{peak}}$ and L_{bol} bins as a function the median luminosity of the bin with a dot-dashed red line and solid blue line, respectively. The top row shows the power law fit parameters to the stacked SB profiles, which shows that the normalization factor SB_0 of the median profiles tends to increase up to an order of magnitude with increasing quasar luminosity and the power β ranges between -2.25 to -1.75. Similarly, the middle row shows the fitted parameters for the exponential function, which shows a similar behavior in the normalization factor. The characteristic radius R_h of the exponential fit appears to be constant at $\sim 50\,\mathrm{ckpc}$. The fitted parameters of the stacked non detections are shown with a white diamond, while the fits of bins A2 bin A3 are shown with light blue and dark blue squares. The fitted

---

[6]`https://emcee.readthedocs.io/en/stable/index.html`
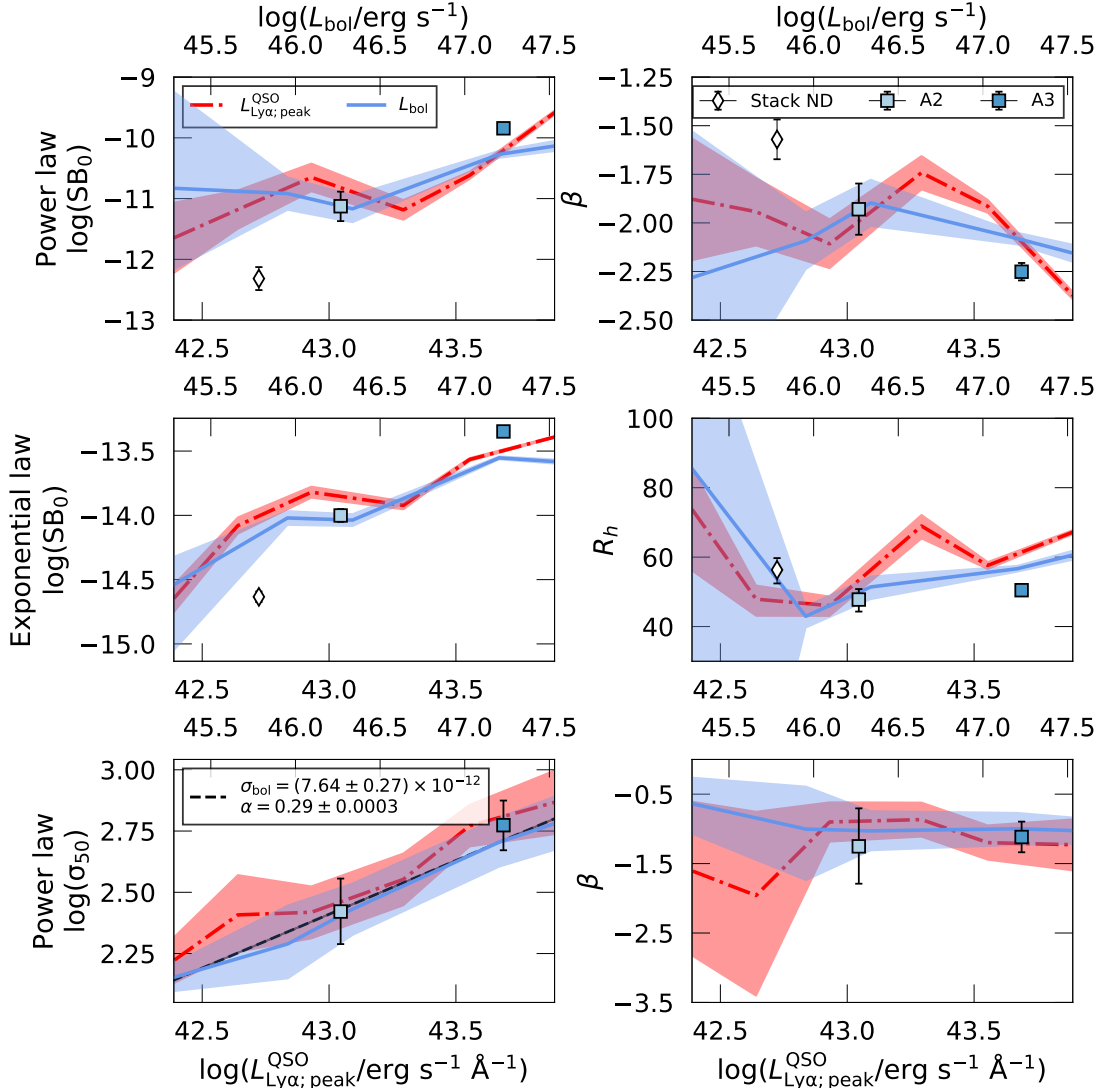
Figure 4.17: Fitted parameters from a power and exponential law to the stacked SB and velocity dispersion profiles as a function of their median quasar luminosities. The first row shows the fitted $\log(SB_0)$ (left) and β (right) parameters of a power law versus the median peak Lyα luminosity density (top axis, red dot dashed line) and bolometric luminosity (bottom axis, blue line) of the quasar, with their respective uncertainties as shaded areas. The second row shows the $\log(SB_0)$ and R_h parameters of an exponential law fit as a function of their median quasar luminosities. The bottom row shows the fitted $\log(\sigma_{50})$ and β of a power law fit to the median velocity dispersion profiles as a function of their quasar luminosity. We also show in the left panel a power law fit to the normalization factor as a function of bolometric luminosity of the form $\sigma_{50} = \sigma_{bol}(L_{bol}/\mathrm{erg/s})^\alpha$ and parameters shown in the legend with a black dashed line and 1σ uncertainty shaded area. Finally, the fitted parameters for the profile of the stacked non detections are shown with a white diamond and errorbars representing the 1σ uncertainty, while the fitted parameters of bins A2 ans A3 are shown with light blue and dark blue squares, respectively.

values for these three bins follow similar tendencies as the luminosity bins. Interestingly, the profile obtained by stacking the non detections has a lower normalization factor than the lowest luminosity bin (which has comparable median luminosity). This could indicate that at these low luminosities there is potentially a mechanism that can suppress the detection of extended Lyα emission, such as host galaxy orientation (e.g., Costa et al., 2022), small opening angles (Obreja et al., 2024) and/or molecular and dust content of the host galaxy (Muñoz-Elgueta et al., 2022; González Lobos et al., 2023), which we further discuss in Section 4.4.2.

Additionally, we assess the goodness of the power law versus exponential fits for the stacked non detections, bin A2 and bin A3 by calculating the root-mean-square-deviation (RMSD) between the profiles and their fitted functions as:

$$\mathrm{RMSD} = \sqrt{\frac{(\mathrm{SB_{Ly\alpha}} - \mathrm{fit})^2}{\sigma^2}}, \tag{4.2}$$

where σ is the error associated to the Lyα SB. We find that the exponential function is a better fit to the profile of stacked non detections than a power law (RMSD of 2.9 and 4.2, respectively). Similarly, bin A2 is also better described with an exponential than power law (RMSD of 1.6 and 3.3, respectively). Opposite to this, bin A3 is better described with a power law rather than an exponential law (RMSD of 3.6 and 13.04, respectively). This is a consequence of the increased SB towards the center of the nebula in comparison to the points at larger distance (see Figure 4.15), which biases the fit towards larger normalization factors. If this first point is not considered in the fit, an exponential law can be a good description of the profile in bin A3. Overall, these tests show that not a single power or exponential law can describe the observed SB radial profiles, however they are a robust representation.

Finally, the bottom row of Figure 4.17 shows the fitted parameters to the median velocity dispersion profiles for a power law of the form $\sigma = \sigma_{50}(r/50\,\mathrm{ckpc})^\beta$. From the bottom right panel, we see that the power remains constant at $\beta \sim -1.0$. On the other hand, we observe that the normalization factor σ_{50} is related to the bolometric luminosity through a power law. We further fit a power law of the form $\sigma_{50} = \sigma_{\mathrm{bol}}(L_{\mathrm{bol}}/\mathrm{erg\,s^{-1}})^\alpha$ and show in that panel with a dashed black line and list the parameters in the legend of this panel. This indicates that all of the observed inner velocity dispersions scale tightly with the quasar bolometric luminosities, suggesting that the Lyα emission could be tracing AGN winds/outflows at these scales.

4.4.2 Insights on the powering mechanisms for extended Lyα emission

As mentioned in section 4.1, there are several physical mechanisms than can collectively power extended Lyα nebulae around quasars, such as photoionization due to the quasar (and nearby sources) radiation followed by recombination, resonant scattering of Lyα photons originating from the broad line region of the quasar, shocks due to galactic/AGN winds

and outflows and gravitational cooling. In this work, we have confirmed, with similar observations, the findings presented in Mackenzie et al. (2021b) regarding the correlation between quasar Lyα and UV luminosities and Lyα SB of the nebulae. Moreover, in Section 4.4.1 we discussed that the Lyα and bolometric luminosities of the quasars are the main AGN properties linked to the observed Lyα SB and velocity dispersions.

Figure 4.18 summarizes the effect that the bolometric luminosity of the quasar has on the Lyα SB level and velocity dispersion by comparing the median radial profiles within bins A2 and A3 with a solid orange line and blue dashed line, respectively. Additionally, we show the median profile of the stacked non detections with gray dots and shaded region indicating its 1σ uncertainty. The legend indicates the median values of the bolometric luminosity and Eddington ratio in each bin. The left panel shows the median Lyα SB corrected by cosmological dimming as a function of projected distance in comoving kiloparsec, with the shaded areas representing the 25 and 75 percentiles of the stacked profiles. The shapes of the Lyα SB profiles are similar, however the profile of bin A2 is on average a factor of 5 times lower than that of bin A3. Additionally, the median profile of the stacked non detections is on average 2 times dimmer than the median profile of bin A2. In the same panel, we show the simulated profile obtained by assuming the illumination of a galaxy in a $10^{12.3}\,\mathrm{M}_\odot$ halo by the ultraviolet background (UVB) only (Obreja et al. 2024). The fact that the two profiles are very similar suggests that faint quasars are associated with very small opening angles. Additionally, we show in the same panel the Lyα SB profile around Lyman break galaxies (LBGs; Steidel et al. 2011), which are expected to be hosted in $M \sim 10^{12}\,\mathrm{M}_\odot$ halos.

On the other hand, the right panel of Figure 4.18 shows the median velocity dispersion profiles within the same bins. We see that the velocity dispersion in bin A2 is on average a factor of 2 times lower than the velocity dispersions in bin A3, while the median bolometric luminosity of bin A2 is an order of magnitude smaller than the median bolometric luminosity of A3. Additionally, we show in the same panel the intrinsic Lyα velocity dispersion (σ_i) obtained by de Beer et al. (2023) using mock observations of cosmological simulations in halos with $M = 10^{12}$ and $10^{12.6}\,\mathrm{M}_\odot$ at $z = 3.017$ with a black dashed line and a red dot-dashed line, respectively. Those simulations are carried out under the assumption of maximal quasar fluorescence and the median σ_i is computed first within a projected distance of $40 - 100\,\mathrm{ckpc}$, which translates to $9.76 - 24.4\,\mathrm{pkpc}$ at the median redshift of our sample. Therefore, in order to compare the shapes of the velocity dispersion profiles, we re-scaled the profiles from de Beer et al. (2023) to match the median velocity dispersion at the average projected distance of $17\,\mathrm{pkpc}$ of bin A2. Note that from our observations we are not able to recover the intrinsic velocity dispersion, however de Beer et al. (2023) indicated that the velocity dispersions of the mock observations are able to trace well the intrinsic velocity dispersions derived from gravitational motions given their halo mass. We see that the observed velocity dispersion profile is much narrower than the σ_i from de Beer et al. (2023), indicating that the same assumption cannot be made and other mechanisms could be contributing to the observed shape. In this case, we see that the differences in the velocity dispersion profiles are affected by the bolometric luminosities due to AGN activity, which is also shown as the relationship in the bottom left panel of Figure 4.17.
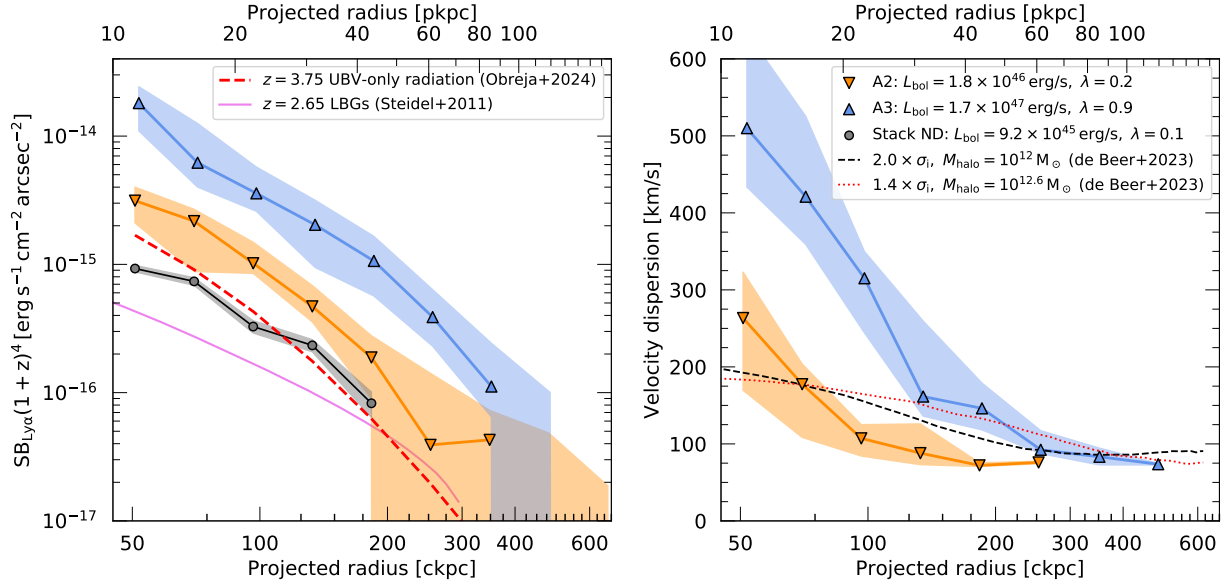
Figure 4.18: Median Lyα SB and velocity dispersion of stacked radial profiles. *Left:* Lyα SB corrected by cosmological dimming as a function of projected comoving distance for the stacked non detections in gray dots and bins A2 and A3 with orange and blue triangles, respectively. The simulated profile obtained from the illumination of a galaxy in a $10^{12.3}\,\mathrm{M}_\odot$ halo by the ultraviolet background (UVB) only (Obreja et al. 2024) is shown with a red dashed line. The profile around LBGs (Steidel et al., 2011) is shown with a magenta line. *Right:* Velocity dispersion as a function of projected comoving distances of bins A2 and A3 with orange and blue triangles, respectively, and their shaded region representing the 25th to 75th percentiles. Additionally, we show with a black dashed line and a red dot-dashed line the intrinsic Lyα velocity dispersion (σ_{int}) from de Beer et al. (2023) using cosmological simulations of haloes at $z = 3.017$ with $M_{\mathrm{halo}} = 10^{12}$ and $10^{12.6}\,\mathrm{M}_\odot$, respectively, after rescaling to match the velocity dispersion at 17 pkpc of bin A2 (see Section 4.4.2). Their median properties physical such as peak Lyα luminosity density of the quasar, bolometric luminosity, black hole mass and Eddington ratio of the bins are indicated in the legend.

This is also supported by the larger median Eddington ratio of bin A3 ($\lambda_{\rm Edd} \sim 0.9$) with respect to bin A2 ($\lambda_{\rm Edd} \sim 0.2$). Note that $\lambda_{\rm Edd}$ scales linearly with quasar bolometric luminosity and is inversely proportional to the black hole mass, however bins A2 and A3 span a similar range of black hole masses (see Figure 4.14). These findings can suggest that the observed velocity dispersion profile shapes are correlated with the intensity of AGN feedback in these systems. In this case, the large velocity dispersions at the center could be tracing winds/outflows and then quickly decay towards a quiescent state.

Further, we would like to discuss the interplay that can happen between the aforementioned powering mechanisms and their possible impact on the nebulae that we observe. In the context of photoionization due to the quasar radiation followed by recombination, we expect the gas, if illuminated by the quasar, to be almost fully ionized on the scales spanned by the Lyα nebulae that we see in this work (Mackenzie et al., 2021b). In this case, the illuminated gas will be optically thin to ionizing radiation, resulting in a Lyα SB level that is independent of the ionizing luminosity, but instead depends on the physical properties of the gas such as the hydrogen volume and column densities ($\rm SB_{Ly\alpha} \propto n_H N_H$; Equation 10 in Hennawi and Prochaska 2013). This can be translated to a dependence in n_H and mass reservoir in the cool phase M_H (Hennawi and Prochaska 2013). To explain the changes in Lyα SB that we see, there is therefore the need of a change of n_H and/or M_H. In this framework, if we assume a fixed M_H or similarly the median value of column density obtained in absorption studies of quasar CGM $N_H = 10^{20.5}\,{\rm cm}^{-2}$ (Lau et al., 2016), we find that the median Lyα SB profiles of the faint and bright quasar nebulae imply gas densities of $n_H \sim 0.5$ and $2\,{\rm cm}^{-3}$, respectively, at a fixed projected distance of $R \sim 20\,{\rm kpc}$, the median redshift of our sample, and assuming a covering fraction of $f_C = 1$ (Arrigoni Battaia et al., 2015b). As expected, these values are consistent with the densities estimated in previous works (e.g., Hennawi et al. 2015; Arrigoni Battaia et al. 2019b). Thus, if the recombination scenario in optically thin gas were the dominant mechanism powering the nebulae, then the observed Lyα SB may imply that the bright quasars reside in denser gas reservoirs. Similarly, at fixed n_H the change in SB could be due to a more ($4\times$) massive reservoir of cool gas around bright quasars. However, both faint and bright quasars at $z \sim 3$ seem to reside in similarly massive halos as estimated by clustering measurements White et al. (2012); Timlin et al. (2018). Also, at low redshift it is expected a relation between black hole mass and halo X-ray temperature, hence halo mass (e.g., Gaspari et al. 2019). If this relation holds also out to $z \sim 3$, we should see a trend of increasing velocity dispersion as a function of black hole mass. Indeed, the velocity dispersion of Lyα nebulae has been used to determine the quasar halo mass (Arrigoni Battaia et al. 2019a; Farina et al. 2019; de Beer et al. 2023). Here, we do not see any evidence of such a trend (see Figures 4.16 and 4.18). Hence, we do not expect drastic changes in n_H and M_H around the targeted quasars, modulo the effect of the quasars' feedback itself which may increase densities in the inner halo because of entrained material for stronger winds/outflows (e.g., Costa et al. 2014), but simultaneously reduce the reservoir of cool gas because of the stronger ionizing radiation (e.g., Obreja et al. 2024). Then, other mechanisms would be required to provide enough gas densities or cool gas mass to power the observed nebulae, such as stripped satellite galaxies. But once again this effect would need to be more pronounced around

brighter quasars. Something that has to be tested observationally (e.g., Chen et al. 2021; Bischetti et al. 2021). Another way to change the amount of cool gas mass photoionized by the quasars is to change the fraction of volume they can illuminate (Obreja et al. 2024). In other words, if the ionization cone of the AGN increases with the luminosity of the quasar then brighter quasars would be able to increase the nebula SB levels in the recombination scenario. We further discuss this effect later in this section.

Regarding a scenario in which the Lyα nebulae are predominantly powered by resonant scattering, it is possible to expect that the Lyα luminosity of the nebulae is correlated with the Lyα luminosity of the quasar (and consequently the bolometric luminosity). In this case, Lyα photons produced in the broad line region of the quasar are scattered through the surrounding gas distribution until they escape the CGM. For this reason, the observed flux distribution contains information on the Lyα source as well as the location and kinematics of the last scattering event (e.g., Blaizot et al. 2023). On the other hand, the fraction of neutral hydrogen available to scatter Lyα photons is inversely proportional to the luminosity of ionizing radiation of the quasar, which can be directed anisotropically along its ionization cones. Indeed, this is consistent with the predicted SB profile from a galaxy illuminated by the UVB only and the observed profile of stacked non detections (Figure 4.18) Further, dust absorption could also impact the detection of extended Lyα emission (González Lobos et al. 2023). Hence, an indication of the amount of dust associated to the non detections may help in assessing their degree of obscuration, such as inferred from future ALMA observations. Finally, we require detailed assessment of radiative transfer effects that shape the observed line profiles in order to interpret of the observed relationship between nebula Lyα properties and bolometric luminosity.

Recent radiative transfer cosmological simulations carried out by Costa et al. (2022) have shown that resonant scattering of Lyα photons from the broad line region of the AGN can produce Lyα emission out to scales of $\sim 100\,\mathrm{kpc}$ in $z \sim 6$ quasar host halos. Additionally, this work highlighted that to reproduce the Lyα nebulae it is required that AGN outflows clear the gas within the nucleus to allow Lyα photons to escape and scatter in the CGM. This could be consistent with our observations, where the brightest nebulae are associated to the largest velocity dispersions (Figure 4.18), which could arise in the case if AGN outflows are able to increase the gas densities and inject turbulence in the cool ISM and CGM gas. Moreover, the brightest nebulae are also associated to the largest Eddington ratios, indicating that AGN feedback is stronger in these systems. On the other hand, the same simulation by Costa et al. (2022) predicted that host galaxy orientation affects the way we would see Lyα nebulae because of AGN outflows preferentially escaping along the minor axis, producing a diversity of morphologies. For example, lopsided and dim nebulae can be reproduced in the case of galaxies viewed close to edge-on, while more symmetric and brighter nebulae can occur for galaxies viewed closer to face-on. The fact that we observe a broad range of nebular morphologies and the dimmest nebulae are also lopsided (Figure 4.10, see also Arrigoni Battaia et al. 2023b) could be a consequence of viewing angle. A similar diversity could be present also among Lyα nebulae around faint quasars, with the fainter nebulae being associated to quasars hosted by more edge-on galaxies. Finally, in the same simulations by Costa et al. (2022) it is also shown that the

effect of resonant scattering increases the observed linewidths, although they predict an increase also in the outskirts. Nevertheless, the simulations at $z \sim 6$ from Costa et al. (2022) trace smaller physical scales than observed here. Finally, part of the increase in velocity dispersion could be due to a larger effect of Lyα resonant scattering for brighter quasars (e.g., Mackenzie et al. 2021b).

Moreover, Costa et al. (2018) estimated that the bolometric luminosity threshold L_{ths} over which an AGN is able to power mechanical outflows can be computed as the luminosity at which the outbound radiation pressure acceleration balances the inward gravitational acceleration on the entirety of ISM gas:

$$\frac{L_{\text{ths}}}{c} = \frac{GM_{200}^2}{R_{\text{ISM}}^2} \frac{M_{\text{ISM}}}{M_{200}} \frac{M_{\text{ISM}} + M_\star + M_{\text{DM}}(< R_{\text{ISM}})}{M_{200}}, \tag{4.3}$$

where G is the gravitational constant, c the speed of light, $R_{\text{ISM}} \approx 0.1R_{200}$ is the outer boundary of the ISM, and M_{ISM}, $M_\star$ and $M_{\text{DM}}(< R_{\text{ISM}})$ are the gas, star and dark matter masses within the ISM region. A typical $z \sim 3$ quasar host dark matter halo has $M_{200}=10^{12.5}M_\odot$ and $R_{200} \approx 100$ kpc. If we assume a Navarro-Frenk-White dark matter profile (Navarro et al., 1997) and use the concentration–halo mass relation for $z = 3$ of Dutton and Macciò (2014) $M_{\text{DM}}(< R_{\text{ISM}})/M_{200} \approx 0.056$. We can estimate the ISM mass fraction M_{ISM}/M_{200} using the EAGLE simulation (the dashed green curve in figure 2 of Mitchell and Schaye, 2022, for $z = 2$) to be 8% for our target halo mass, where we assumed the cosmic baryon fraction value of the Planck cosmology $f_b = \Omega_b/\Omega_M = 0.157$. For the stellar mass fraction, we can use the z-appropriate relation of Moster et al. (2018) to get $M_\star/M_{200} \approx 0.027$. Plugging all these numbers in the equation above, an AGN at $z = 3$ has to have a bolometric luminosity of at least 1.08×10^{48} erg/s for radiation pressure to push away all of the ISM. This limit luminosity is computed assuming a spherical symmetric ISM distribution, however quasars are typically associated with star forming galaxies, which have their ISM organized in a disk. Therefore, the amount of ISM that needs to be removed for the AGN radiation to escape the ISM is lower. For example, if we assume the AGN needs to remove only the ISM within a typical ionization bi-cone of angle $\alpha = 60°$ (e.g. Obreja et al., 2024), the limit luminosity becomes $[1-\cos(\alpha/2)] \times 1.08 \times 10^{48}erg/s=1.4 \times 10^{47}$erg/s. Interestingly, this new L_{bol} limit coincides with the minimum luminosity of the QSO MU-SEUM bright sample, which has larger average Lyα SB than the QSO MUSEUM faint sample as given by the points' sizes in Figure 4.14. In this case, the observed Lyα SB of the bright nebulae is produced because the AGN has been able to push enough ISM material, allowing the photons to escape and scatter. Moreover, the observed nebulae associated to the quasars above this bolometric luminosity show increased average velocity dispersions with respect to the faint quasars (see right panel of Figure 4.14). Indeed, this is also observed in Figure 4.18, where we show the median Lyα SB and velocity dispersion profiles within bins A2 and A3 with an orange solid line and blue dashed line, respectively. In particular, the median velocity dispersion profiles (right panel) show that the nebulae around brighter quasars ($L_{\text{bol}} \sim 10^{47}$ erg/s) have enhanced velocity dispersions that decrease more steeply with projected distance than the velocity dispersion of nebulae around fainter quasars. This is also supported by the larger median Eddington ratio of bin
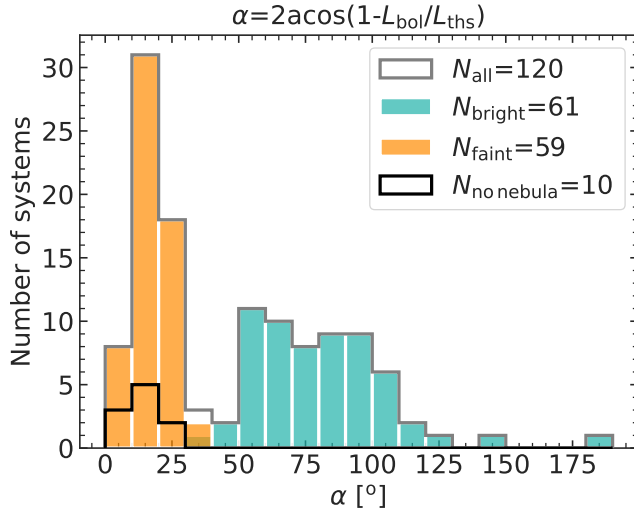
Figure 4.19: Distribution of the opening angle estimated for the targeted quasars as a function of their bolometric luminosity. The histogram shows the number QSO MUSEUM faint (orange) and bright (dark green) quasars with the estimated opening angle using the luminosity necessary to push their ISM and allow the escape of Lyα photons as discussed in Costa et al. (2018). The values of bins A2 and A3 are shown with blue squares. The thick black lines represent the non detections.

A3 ($\lambda_{\rm Edd} \sim 0.9$) with respect to bin A2 ($\lambda_{\rm Edd} \sim 0.2$) which could indicate stronger AGN feedback in these systems.

Assuming that to see a Lyα nebula around a quasar there is the need of an AGN outflow (Costa et al. 2022), using the above reasoning we could estimate how the opening angle of the targeted quasars changes as a function of their $L_{\rm bol}$ by requiring:

$$L_{\rm bol} = L_{\rm ths} \times [1 - \cos(\alpha/2)]. \tag{4.4}$$

Figure 4.19 shows the results of solving for α in Equation 4.4 with $L_{\rm ths} = 1.08 \times 10^{48}$ erg/s for the full sample, which shows that brighter quasars would have larger opening angles. In this case bright quasars would be able to ionize a larger mass of cool gas (boosting the Lyα SB signal in a recombination scenario) or to illuminate with their Lyα photons more gas (important in a scattering scenario). In the same figure we show the median opening angles of the subsamples A2 (faint) and A3 (bright), which represent bins at roughly fixed $M_{\rm BH} \sim 10^9$ M$_\odot$. We find that their median opening angles should be 21º and 65º, respectively. This means that the ratio of illuminated volumes is ~ 9, which is very similar to the ratio of their SB levels (~ 7). Additionally, quasars associated with non detections are at the low end of the distribution of opening angles. In the context proposed by Costa et al. (2022), if the AGN outflow is not powerful enough due to low accretion rates (i.e., low $\lambda_{\rm Edd}$) then it would be inefficient in opening channels for the propagation of Lyα photons and producing extended Lyα nebulae. The fact that the quasars in our sample associated to non-detected Lyα nebulae also have the lowest $\lambda_{\rm Edd}$ could be a consequence of this scenario if the same feedback mechanisms are in play at $z \sim 3$.

It has been argued that so different opening angles might result in observable difference in the asymmetries of the nebulae (Mackenzie et al. 2021b). We do not find such differences in agreement with previous studies, but we think that the absence of differences is due to the fact that at small opening angles the level of emission is comparable to the level of
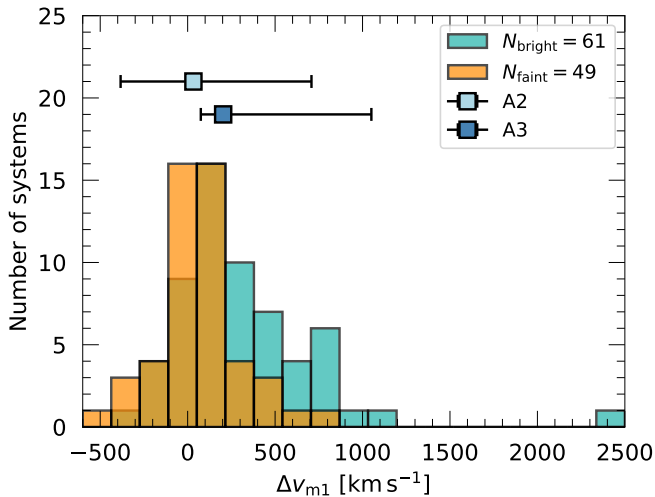
Figure 4.20: Distribution of nebula Lyα velocity shift with respect to the quasar Lyα. The plot shows histograms of the bright and faint nebulae Lyα velocity shifts (v_{m1}) computed from the first moment of the flux distribution reported in Tables 4.2 and 4.5 with green and orange colors, respectively. The number of systems inside bins A2 and A3 (Figure 4.14) are shown as a function of their median v_{m1} with blue squares. The size of each bin corresponds to $163\,\mathrm{km\,s^{-1}}$.

the Lyα emission due to UVB and host galaxy (Obreja et al. 2024; see also Figure 4.18), hence washing out any geometrical difference due to quasar illumination alone. Also, small opening angles for faint quasars better explain the more frequent presence of narrow Lyα nebulae with very similar spectrum to some portions of the Lyα emission of the quasar itself (see Figures 4.5, 4.6 and 4.7). Such emission is likely due to ISM and inner CGM, also potentially not illuminated by the quasar (see also Mackenzie et al. 2021b). We stress that a luminosity dependent opening angle means that the fraction of obscured or type-II AGN f_N would vary as a function of L_bol. Specifically, following geometrical arguments $f_\mathrm{N} = \cos(\alpha/2)$, resulting in $f_N^\mathrm{faint} = 0.93^{+0.06}_{-0.24}$ and $f_N^\mathrm{bright} = 0.42^{+0.09}_{-0.15}$. These values are in overall agreement with those obtained using infrared luminosities and X-ray surveys (see e.g., Figure 4 in Treister et al. 2008; Marconi et al. 2004). Even though these fractions are still matter of debate, we argue that statistical studies of quasar CGM could help in assessing this problem further.

The last two powering mechanisms to discuss are gravitational cooling and shocks due to galactic/AGN outflows. Given the dependence of the SB levels with the quasar L_bol we can exclude a gravitational cooling scenario, which would instead depend mainly on the mass of the system studied (e.g., Dijkstra and Loeb 2008; Faucher-Giguère et al. 2010). Conversely, fast shocks are expected to provide additional ionizing photons and boost collisions. In such a case, the flux in Lyα emission is expected to scale as $F_\mathrm{Ly\alpha} \propto n_\mathrm{H} v_\mathrm{shock}^3$, with v_shock being the shock speed (Allen et al. 2008). Given the presence of increased Lyα SB and velocity dispersions around more accreting and active quasars we cannot exclude that shocks, and hence also collisions do not play any role in powering Lyα nebulae around quasars. If only shock speed would be responsible for the difference in Lyα SB in the A2 and A3 samples at roughly fixed M_BH, bright quasars would push 2× faster outflows at fixed n_H. This is not far from the scaling invoked by Fiore et al. (2017) between L_bol and the outflow velocity v_{out}, with $v_\mathrm{out} \propto L_\mathrm{bol}^{1/5}$. While this relation, if valid, is computed on smaller scales, it could be that shock velocities may follow similar relations and therefore contribute

to the powering of the Lyα nebulae. The exquisite spatial resolution of JWST (Gardner et al. 2006) may help us in uncovering morphological and velocity signatures of shocks in the Lyα nebulae surrounding quasars as traced by rest-frame optical emission lines (e.g., [OIII]). In the same scenario, the presence of winds/outflows from the AGN can cause the peak of the observed Lyα flux distribution to appear broader and redshifted with respect to the intrinsic emission due to radiative transfer effects (see e.g.,Chang et al. 2023). This is supported by the observed increased velocity dispersions on nebulae associated to quasars with larger Eddington ratios. Additionally, if the most luminous quasars are producing stronger feedback then their Lyα emission could appear more redshifted with respect to fainter quasars. In Figure 4.20, we show the collection of velocity shifts (Δv_{m1}) of the nebulae computed from the first moment of their Lyα flux distribution with respect to the peak Lyα wavelength described in Tables 4.2 and 4.5 of the bright and faint quasars with green and orange bins, respectively. Additionally, we plot in the same figure the number of nebulae in bins A2 and A3 as a function of their median Δv_{m1}, with the errorbars representing the velocity range covered by each bin. We see that most of the nebulae have redshifts similar to the quasar's Lyα, however the bright quasar sample shows more systems with velocity shifts $\gtrsim 200\,\mathrm{km/s}$. We also studied the distribution of velocity shifts derived from the gaussian fits ($\Delta v_{\mathrm{gauss}}$ in Tables 4.2 and 4.5) and found consistent results. This comparison is robust and in order to interpret the kinematics of the observed nebulae we require precise information on the systemic redshifts of the quasars together with radiative transfer modeling of the individual Lyα line profiles of the nebulae.

4.5   Summary

In this work, I have presented the largest effort to date to map the CGM around 120 $z \sim 3$ quasars in Lyα emission (QSO MUSEUM III). We were able to detect 110 nebulae around the targets using MUSE observations and characterized their Lyα SB level, kinematics, morphology (area and asymmetry) and quasar properties. Specifically, the addition of 60 new faint quasar fields allowed to detect $2\times$ fainter nebulae than previous studies (Mackenzie et al., 2021b) and to conduct a statistical study of their properties.

We find a large variety of nebulae luminosities and extents that we have characterized using radial profiles which we link to their quasar properties. From this study, we learn that the observed Lyα SB of the nebulae increase with the peak Lyα luminosity density and bolometric luminosity of the quasar. Additionally, we show that the nebulae kinematics also reflect their quasar luminosity, because brighter nebulae present, on average, increased velocity dispersions.

Finally, we discuss the physical mechanisms that could drive the observed relationship such as recombination radiation, resonant scattering, shocks and outflows from AGN feedback and gravitational cooling. We argue that the most likely mechanisms producing the extended Lyα emission are a combination of recombination radiation, resonant scattering and shocks due to outflows. In particular, we discuss the importance of the quasar opening angle both for producing Lyα photons that will scatter and for illuminating the surround-

ing gas distribution which in turn produces recombination radiation, which impacts the observation of the brightest nebulae as well as the non-detections.

In conclusion, I presented a statistical sample that allowed me to assess the different factors that impact the observed Lyα emission of the CGM of quasars. However, given the complexity of the CGM and the interplay of these parameters we require samples covering the full range of quasars and a detailed characterization of these properties. Additionally, radiative transfer models for quasar host halos at $z \sim 3$ and detection of additional line emissions (Hα, He II and C IV) are required to assess the balance between powering mechanisms and metal enrichment in the CGM.

4.6 Appendix

4.6.1 Estimating quasar properties from their 1-D spectra

In this appendix we describe how we obtained an estimate of the black-hole mass and accretion rates of the targeted SMBHs. We rely on the only available broad emission line observed for all the sample, C IV, and that allow us to derive single-epoch black hole masses using the Vestergaard and Peterson (2006) estimator

$$\log M_{\mathrm{BH}}(\mathrm{C\,IV}) \quad = \quad \log \left\{ \left[\frac{\mathrm{FWHM}(\mathrm{C\,IV})}{1000\,\mathrm{km\,s^{-1}}} \right]^2 \left[\frac{\lambda L_\lambda(1350\,\mathring{A})}{10^{44}\,\mathrm{erg\,s^{-1}}} \right]^{0.53} \right\} \quad + \quad 6.66 \quad (4.5)$$

where FWHM(C IV) is the width of the C IV broad-emission line and $L_\lambda(1350\,\mathring{A})$ is the monochromatic luminosity of the quasar at rest-frame 1350 Å. This estimator has a 0.5 dex intrinsic uncertainty. To obtain those quantities we use the standard technique of modeling the 1-D quasar spectrum with a linear combination of a pseudo-continuum, broad and narrow emission lines (e.g., Shen et al. 2019). Specifically, we fit the spectra with PyQSOFit (Guo et al. 2018) which gives in output the aforementioned quantities. We fit for the following emission lines: Lyα, N Vλ1240$\mathring{A}$, C IVλ1549$\mathring{A}$, C IIIλ1909$\mathring{A}$. For these lines we use the same fitting parameters and number of Gaussians as specified in previous works (see Table 1 in Rakshit et al. 2020). Upon visual inspection of each obtained model spectrum, we (i) introduced the fit of Si IVλ1397$\mathring{A}$, 1402$\mathring{A}$, (ii) mask absorption features close or on top of the C IV broad emission line, and (iii) refine the wavelength ranges for the continuum estimation, when needed and re-run the fitting. The values obtained for FWHM(C IV), $\lambda L_\lambda(1350\,\mathring{A})$ and M_{BH} for the full sample are reported in Tables 4.3 and 4.4, while we show four examples of our fit of the C IV range in Figure 4.21.

Once we have M_{BH}, we can compute the theoretical maximum luminosity for the case when radiation pressure and gravity are in equilibrium in a spherical geometry, i.e., the Eddington luminosity (Eddington 1926)

$$L_{\mathrm{Edd}} = \frac{4\pi G M_{\mathrm{BH}} m_{\mathrm{p}} c}{\sigma_{\mathrm{T}}} = 1.26 \times 10^{38} \left(\frac{M_{\mathrm{BH}}}{M_\odot} \right) \mathrm{erg\,s^{-1}} \qquad (4.6)$$
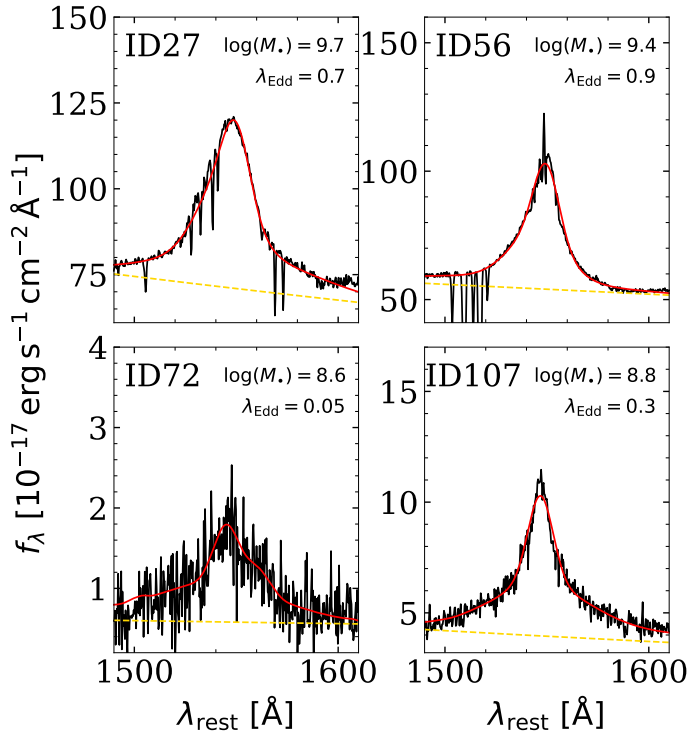
Figure 4.21: Four examples of C IV and continuum fit using PYQ-SOFIT. Each panel shows the 1-D spectrum (black) of one targeted quasar (ID in the top-left corner) together with the estimated continuum (yellow dashed line) and the best fit (red). The black hole mass and Eddington ratio obtained from this fit are listed in the top-right corner (see text for details).

where σ_T is the Thomson scattering cross section, G is the gravitational constant, m_p is the proton mass, and c is the speed of light. The Eddington luminosity is usually compared with the quasar bolometric luminosity (L_{bol}) to assess the activity and hence accretion rate of the SMBH. A so-called Eddington ratio is usually defined as $\lambda_{Edd} = L_{bol}/L_{Edd}$. We computed L_{bol} from the monochromatic luminosity $L_\lambda(1350\,\text{Å})$ as done in Rakshit et al. (2020) using the bolometric correction factor given in Shen et al. (2011) and adapted from Richards et al. (2006)

$$L_{bol} = 3.81 \times L_\lambda(1350\,\text{Å}). \tag{4.7}$$

This estimate can have up to 0.3 dex of uncertainty. The computed L_{bol}, together with corresponding λ_{Edd} values are all also listed in Tables 4.3 and 4.4.

To verify the obtained M_{BH} and λ_{Edd}, we compared them with the values from the automated fit of Rakshit et al. (2020) for the sources in common between the two studies and cataloged as good fits in that work. Figure 4.22 shows the result of this comparison. The largest differences are found at the lowest and highest end of the black hole mass distribution, and the the low end of the bolometric luminosities. These differences are due to the fact that Rakshit et al. (2020) fit >500000 sources and hence visual inspection of all the obtained models was not possible, while we improve the fit of several sources after visual inspection.
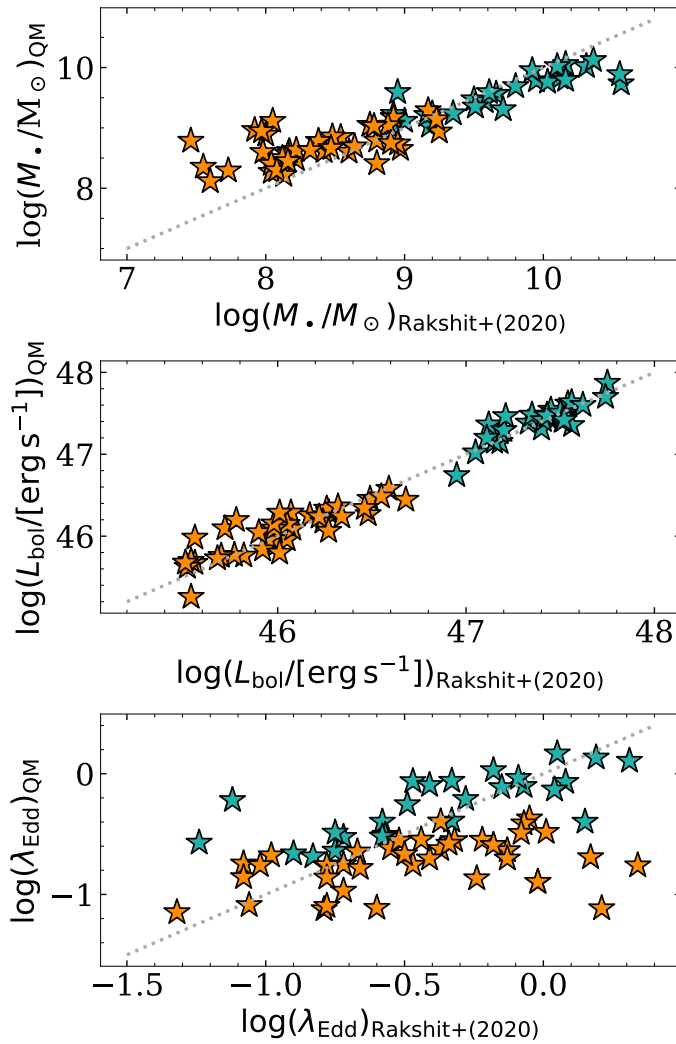
Figure 4.22: Comparison of SMBH properties with respect to previous work. The obtained $M_{\rm BH}$, $L_{\rm bol}$ and $\lambda_{\rm Edd}$ are compared with those found in Rakshit et al. (2020) for a subsample of the QSOMUSEUM objects (see text for details). Datapoints for bright quasars studied in QSO MUSEUM I are shown in green, while those for fainter quasars added in this work are shown in orange. In each panel, the dotted gray line indicates the one to one relation.

Table 4.3: PyQSOfit results: QSO MUSEUM I

ID	z	$L_{\mathrm{Ly}\alpha;\mathrm{peak}}^{\mathrm{QSO}}$ erg s^{-1}Å^{-1}	$L_\lambda(1350)$Å erg s^{-1}	L_{bol} erg s^{-1}	FWHM(C IV) km s^{-1}	M_{BH} M$_{\mathrm{sun}}$	L_{Edd} erg s^{-1}	λ_{Edd}
1	3.166	5.4×10^{43}	$5 \pm 1.0 \times 10^{46}$	$1.9 \pm 0.007 \times 10^{47}$	3724 ± 9	$1.7 \pm 1.0 \times 10^{9}$	$2.2 \pm 0.012 \times 10^{47}$	0.88 ± 0.01
2	3.133	6.1×10^{43}	$1.4 \pm 1.0 \times 10^{47}$	$5.4 \pm 0.012 \times 10^{47}$	5653 ± 50	$6.8 \pm 1.0 \times 10^{9}$	$8.6 \pm 0.153 \times 10^{47}$	0.63 ± 0.01
3	3.11	9.1×10^{43}	$1 \pm 1.0 \times 10^{47}$	$3.9 \pm 0.013 \times 10^{47}$	4415 ± 18	$3.5 \pm 1.0 \times 10^{9}$	$4.4 \pm 0.037 \times 10^{47}$	0.88 ± 0.01
4	3.219	4.3×10^{43}	$8.7 \pm 1.0 \times 10^{46}$	$3.3 \pm 0.006 \times 10^{47}$	7142 ± 38	$8.4 \pm 1.0 \times 10^{9}$	$1.1 \pm 0.011 \times 10^{48}$	0.31 ± 0.0
5	3.32	3.6×10^{43}	$5.9 \pm 1.0 \times 10^{46}$	$2.3 \pm 0.005 \times 10^{47}$	6542 ± 33	$5.8 \pm 1.0 \times 10^{9}$	$7.3 \pm 0.074 \times 10^{47}$	0.31 ± 0.0
6	3.029	7×10^{43}	$1.3 \pm 1.0 \times 10^{47}$	$5 \pm 0.034 \times 10^{47}$	8035 ± 34	$1.3 \pm 1.0 \times 10^{10}$	$1.7 \pm 0.015 \times 10^{48}$	0.3 ± 0.0
7	3.117	8×10^{43}	$1.1 \pm 1.0 \times 10^{47}$	$4.1 \pm 0.019 \times 10^{47}$	5381 ± 17	$5.3 \pm 1.0 \times 10^{9}$	$6.7 \pm 0.046 \times 10^{47}$	0.61 ± 0.0
8	3.132	7.1×10^{43}	$4.4 \pm 1.0 \times 10^{46}$	$1.7 \pm 0.019 \times 10^{47}$	3958 ± 14	$1.8 \pm 1.0 \times 10^{9}$	$2.3 \pm 0.021 \times 10^{47}$	0.74 ± 0.01
9	3.301	1×10^{44}	$2 \pm 1.0 \times 10^{47}$	$7.4 \pm 0.025 \times 10^{47}$	5185 ± 19	$6.8 \pm 1.0 \times 10^{9}$	$8.6 \pm 0.064 \times 10^{47}$	0.87 ± 0.01
10	3.227	8.8×10^{43}	$7.9 \pm 1.0 \times 10^{46}$	$3 \pm 0.077 \times 10^{47}$	4976 ± 26	$3.9 \pm 1.0 \times 10^{9}$	$4.9 \pm 0.084 \times 10^{47}$	0.62 ± 0.02
11	3.078	9.9×10^{42}	$1.9 \pm 1.0 \times 10^{46}$	$7.3 \pm 0.039 \times 10^{46}$	6446 ± 52	$3.1 \pm 1.0 \times 10^{9}$	$3.9 \pm 0.063 \times 10^{47}$	0.19 ± 0.0
12	3.376	4.9×10^{43}	$9.1 \pm 1.0 \times 10^{46}$	$3.5 \pm 0.016 \times 10^{47}$	7284 ± 33	$9 \pm 1.0 \times 10^{9}$	$1.1 \pm 0.011 \times 10^{48}$	0.31 ± 0.0
13	3.164	5.2×10^{43}	$1 \pm 1.0 \times 10^{47}$	$3.8 \pm 0.006 \times 10^{47}$	5660 ± 31	$5.7 \pm 1.0 \times 10^{9}$	$7.2 \pm 0.078 \times 10^{47}$	0.53 ± 0.01
14	3.126	1.9×10^{43}	$4.4 \pm 1.0 \times 10^{46}$	$1.7 \pm 0.003 \times 10^{47}$	5278 ± 38	$3.2 \pm 1.0 \times 10^{9}$	$4.1 \pm 0.058 \times 10^{47}$	0.42 ± 0.01
15	3.141	1.2×10^{44}	$7.7 \pm 1.0 \times 10^{46}$	$2.9 \pm 0.008 \times 10^{47}$	3319 ± 4	$1.7 \pm 1.0 \times 10^{9}$	$2.1 \pm 0.006 \times 10^{47}$	1.36 ± 0.01
16	3.142	2.2×10^{43}	$4.4 \pm 1.0 \times 10^{46}$	$1.7 \pm 0.003 \times 10^{47}$	7152 ± 61	$5.9 \pm 1.0 \times 10^{9}$	$7.4 \pm 0.127 \times 10^{47}$	0.23 ± 0.0
17	3.34	2.2×10^{43}	$3.7 \pm 1.0 \times 10^{46}$	$1.4 \pm 0.013 \times 10^{47}$	6814 ± 33	$4.9 \pm 1.0 \times 10^{9}$	$6.2 \pm 0.067 \times 10^{47}$	0.23 ± 0.0
18	3.265	7.6×10^{43}	$6 \pm 1.0 \times 10^{46}$	$2.3 \pm 0.006 \times 10^{47}$	4966 ± 21	$3.3 \pm 1.0 \times 10^{9}$	$4.2 \pm 0.035 \times 10^{47}$	0.54 ± 0.0
19	3.188	4.5×10^{43}	$8.7 \pm 1.0 \times 10^{46}$	$3.3 \pm 0.014 \times 10^{47}$	8736 ± 58	$1.3 \pm 1.0 \times 10^{10}$	$1.6 \pm 0.021 \times 10^{48}$	0.21 ± 0.0
20	3.395	5.6×10^{43}	$1 \pm 1.0 \times 10^{47}$	$4 \pm 0.005 \times 10^{47}$	7594 ± 43	$1.1 \pm 1.0 \times 10^{10}$	$1.3 \pm 0.015 \times 10^{48}$	0.3 ± 0.0
21	3.219	1.5×10^{44}	$8.3 \pm 1.0 \times 10^{46}$	$3.2 \pm 0.009 \times 10^{47}$	3322 ± 6	$1.8 \pm 1.0 \times 10^{9}$	$2.2 \pm 0.009 \times 10^{47}$	1.41 ± 0.01
22	3.176	4.5×10^{43}	$9.4 \pm 1.0 \times 10^{46}$	$3.6 \pm 0.011 \times 10^{47}$	9147 ± 51	$1.4 \pm 1.0 \times 10^{10}$	$1.8 \pm 0.02 \times 10^{48}$	0.2 ± 0.0
23	3.061	2.8×10^{43}	$6.3 \pm 1.0 \times 10^{46}$	$2.4 \pm 0.025 \times 10^{47}$	11518 ± 40	$1.8 \pm 1.0 \times 10^{10}$	$2.3 \pm 0.021 \times 10^{48}$	0.1 ± 0.0
24	3.062	9.7×10^{43}	$3.6 \pm 1.0 \times 10^{46}$	$1.4 \pm 0.005 \times 10^{47}$	3809 ± 10	$1.5 \pm 1.0 \times 10^{9}$	$1.9 \pm 0.011 \times 10^{47}$	0.72 ± 0.0
25	3.307	4×10^{43}	$7.8 \pm 1.0 \times 10^{46}$	$3 \pm 0.017 \times 10^{47}$	8552 ± 41	$1.1 \pm 1.0 \times 10^{10}$	$1.4 \pm 0.014 \times 10^{48}$	0.21 ± 0.0
26	3.181	7.1×10^{44}	$1.2 \pm 1.0 \times 10^{48}$	$4.5 \pm 0.017 \times 10^{48}$	5519 ± 17	$2 \pm 1.0 \times 10^{10}$	$2.5 \pm 0.016 \times 10^{48}$	1.78 ± 0.01
27	3.318	6.8×10^{43}	$1.1 \pm 1.0 \times 10^{47}$	$4.4 \pm 0.016 \times 10^{47}$	5244 ± 22	$5.3 \pm 1.0 \times 10^{9}$	$6.6 \pm 0.057 \times 10^{47}$	0.66 ± 0.01
28	3.344	2.6×10^{43}	$3.8 \pm 1.0 \times 10^{46}$	$1.4 \pm 0.003 \times 10^{47}$	5856 ± 25	$3.6 \pm 1.0 \times 10^{9}$	$4.6 \pm 0.039 \times 10^{47}$	0.31 ± 0.0
29	3.18	3×10^{43}	$6.4 \pm 1.0 \times 10^{46}$	$2.4 \pm 0.02 \times 10^{47}$	7896 ± 39	$8.7 \pm 1.0 \times 10^{9}$	$1.1 \pm 0.012 \times 10^{48}$	0.22 ± 0.0
30	3.357	1.2×10^{44}	$8.4 \pm 1.0 \times 10^{46}$	$3.2 \pm 0.011 \times 10^{47}$	3266 ± 8	$1.7 \pm 1.0 \times 10^{9}$	$2.2 \pm 0.012 \times 10^{47}$	1.47 ± 0.01
31	3.131	5×10^{43}	$1.3 \pm 1.0 \times 10^{47}$	$4.8 \pm 0.038 \times 10^{47}$	8700 ± 55	$1.5 \pm 1.0 \times 10^{10}$	$1.9 \pm 0.025 \times 10^{48}$	0.25 ± 0.0
32	3.069	1.8×10^{43}	$3.2 \pm 1.0 \times 10^{46}$	$1.2 \pm 0.005 \times 10^{47}$	7486 ± 57	$5.4 \pm 1.0 \times 10^{9}$	$6.8 \pm 0.105 \times 10^{47}$	0.18 ± 0.0
33	3.125	8.9×10^{43}	$4.4 \pm 1.0 \times 10^{46}$	$1.7 \pm 0.008 \times 10^{47}$	3579 ± 6	$1.5 \pm 1.0 \times 10^{9}$	$1.9 \pm 0.008 \times 10^{47}$	0.9 ± 0.01
34	3.223	1.1×10^{43}	$1.8 \pm 1.0 \times 10^{46}$	$6.8 \pm 0.084 \times 10^{46}$	7888 ± 79	$4.5 \pm 1.0 \times 10^{9}$	$5.6 \pm 0.119 \times 10^{47}$	0.12 ± 0.0
35	3.247	5.8×10^{43}	$2.7 \pm 1.0 \times 10^{46}$	$1 \pm 0.003 \times 10^{47}$	3296 ± 5	$9.6 \pm 1.0 \times 10^{8}$	$1.2 \pm 0.004 \times 10^{47}$	0.84 ± 0.0
36	3.197	3.3×10^{43}	$3.2 \pm 1.0 \times 10^{46}$	$1.2 \pm 0.006 \times 10^{47}$	3364 ± 21	$1.1 \pm 1.0 \times 10^{9}$	$1.4 \pm 0.018 \times 10^{47}$	0.88 ± 0.01
37	3.13	7.5×10^{43}	$5.1 \pm 1.0 \times 10^{46}$	$1.9 \pm 0.006 \times 10^{47}$	3245 ± 9	$1.3 \pm 1.0 \times 10^{9}$	$1.7 \pm 0.01 \times 10^{47}$	1.18 ± 0.01
38	3.348	8.3×10^{43}	$9.1 \pm 1.0 \times 10^{46}$	$3.5 \pm 0.007 \times 10^{47}$	4460 ± 23	$3.4 \pm 1.0 \times 10^{9}$	$4.2 \pm 0.044 \times 10^{47}$	0.82 ± 0.01
39	3.1	1×10^{44}	$6.4 \pm 1.0 \times 10^{46}$	$2.4 \pm 0.023 \times 10^{47}$	3281 ± 5	$1.5 \pm 1.0 \times 10^{9}$	$1.9 \pm 0.011 \times 10^{47}$	1.28 ± 0.01
40	3.342	7.7×10^{43}	$8 \pm 1.0 \times 10^{46}$	$3 \pm 0.015 \times 10^{47}$	4185 ± 107	$2.8 \pm 1.1 \times 10^{9}$	$3.5 \pm 0.177 \times 10^{47}$	0.87 ± 0.04
41	3.321	2.8×10^{43}	$4.8 \pm 1.0 \times 10^{46}$	$1.8 \pm 0.006 \times 10^{47}$	5496 ± 28	$3.7 \pm 1.0 \times 10^{9}$	$4.6 \pm 0.047 \times 10^{47}$	0.4 ± 0.0
42	3.042	8.5×10^{43}	$6.1 \pm 1.0 \times 10^{46}$	$2.3 \pm 0.007 \times 10^{47}$	3546 ± 9	$1.7 \pm 1.0 \times 10^{9}$	$2.2 \pm 0.012 \times 10^{47}$	1.07 ± 0.01
43	3.087	2.6×10^{43}	$3.1 \pm 1.0 \times 10^{46}$	$1.2 \pm 0.005 \times 10^{47}$	4950 ± 11	$2.3 \pm 1.0 \times 10^{9}$	$3 \pm 0.109 \times 10^{47}$	0.4 ± 0.01
44	3.197	3×10^{43}	$6.7 \pm 1.0 \times 10^{46}$	$2.5 \pm 0.018 \times 10^{47}$	6582 ± 44	$6.2 \pm 1.0 \times 10^{9}$	$7.8 \pm 0.109 \times 10^{47}$	0.32 ± 0.01
45	3.312	3×10^{43}	$1.1 \pm 1.0 \times 10^{47}$	$4.1 \pm 0.018 \times 10^{47}$	5411 ± 135	$5.4 \pm 1.1 \times 10^{9}$	$6.9 \pm 0.342 \times 10^{47}$	0.6 ± 0.03
46	3.385	7.9×10^{43}	$1.1 \pm 1.0 \times 10^{47}$	$4.3 \pm 0.005 \times 10^{47}$	5681 ± 16	$6.1 \pm 1.0 \times 10^{9}$	$7.7 \pm 0.045 \times 10^{47}$	0.56 ± 0.0
47	3.156	3.7×10^{43}	$3.7 \pm 1.0 \times 10^{46}$	$1.4 \pm 0.009 \times 10^{47}$	3529 ± 11	$1.3 \pm 1.0 \times 10^{9}$	$1.6 \pm 0.012 \times 10^{47}$	0.85 ± 0.01
48	3.197	3.7×10^{43}	$3.9 \pm 1.0 \times 10^{46}$	$1.5 \pm 0.005 \times 10^{47}$	5286 ± 91	$3 \pm 1.0 \times 10^{9}$	$3.8 \pm 0.132 \times 10^{47}$	0.39 ± 0.01
49	3.109	1.5×10^{43}	$2.8 \pm 1.0 \times 10^{46}$	$1.1 \pm 0.003 \times 10^{47}$	6275 ± 57	$3.6 \pm 1.0 \times 10^{9}$	$4.5 \pm 0.083 \times 10^{47}$	0.24 ± 0.0
50	3.197	3.4×10^{43}	$5.2 \pm 1.0 \times 10^{46}$	$2 \pm 0.006 \times 10^{47}$	5585 ± 50	$3.9 \pm 1.0 \times 10^{9}$	$4.9 \pm 0.088 \times 10^{47}$	0.4 ± 0.01
51	3.138	5.1×10^{43}	$4.2 \pm 1.0 \times 10^{46}$	$1.6 \pm 0.007 \times 10^{47}$	3279 ± 10	$1.2 \pm 1.0 \times 10^{9}$	$1.5 \pm 0.01 \times 10^{47}$	1.05 ± 0.01
52	3.144	4.6×10^{43}	$5.4 \pm 1.0 \times 10^{46}$	$2.1 \pm 0.011 \times 10^{47}$	3975 ± 35	$2 \pm 1.0 \times 10^{9}$	$2.6 \pm 0.046 \times 10^{47}$	0.81 ± 0.02
53	3.149	2×10^{43}	$1.5 \pm 1.0 \times 10^{46}$	$5.5 \pm 0.047 \times 10^{46}$	4101 ± 24	$1.1 \pm 1.0 \times 10^{9}$	$1.4 \pm 0.017 \times 10^{47}$	0.41 ± 0.01
54	3.109	3.6×10^{43}	$2.8 \pm 1.0 \times 10^{46}$	$1 \pm 0.013 \times 10^{47}$	3543 ± 10	$1.1 \pm 1.0 \times 10^{9}$	$1.4 \pm 0.012 \times 10^{47}$	0.74 ± 0.01
55	3.188	3.5×10^{43}	$4.2 \pm 1.0 \times 10^{46}$	$1.6 \pm 0.01 \times 10^{47}$	3815 ± 21	$1.6 \pm 1.0 \times 10^{9}$	$2 \pm 0.024 \times 10^{47}$	0.77 ± 0.01
56	3.089	5.8×10^{43}	$6.9 \pm 1.0 \times 10^{46}$	$2.6 \pm 0.016 \times 10^{47}$	3930 ± 15	$2.2 \pm 1.0 \times 10^{9}$	$2.8 \pm 0.023 \times 10^{47}$	0.92 ± 0.01
57	3.406	2.3×10^{43}	$6.8 \pm 1.0 \times 10^{46}$	$2.6 \pm 0.017 \times 10^{47}$	7283 ± 172	$7.7 \pm 1.0 \times 10^{9}$	$9.7 \pm 0.46 \times 10^{47}$	0.27 ± 0.01
58	3.037	5.9×10^{43}	$8.6 \pm 1.0 \times 10^{46}$	$3.3 \pm 0.017 \times 10^{47}$	4990 ± 31	$4.1 \pm 1.0 \times 10^{9}$	$5.2 \pm 0.066 \times 10^{47}$	0.64 ± 0.01
59	3.118	3.8×10^{43}	$7.6 \pm 1.0 \times 10^{46}$	$2.9 \pm 0.023 \times 10^{47}$	8271 ± 79	$1.1 \pm 1.0 \times 10^{10}$	$1.3 \pm 0.026 \times 10^{48}$	0.22 ± 0.0
60	3.183	4.4×10^{43}	$2.7 \pm 1.0 \times 10^{46}$	$1 \pm 0.006 \times 10^{47}$	4203 ± 13	$1.6 \pm 1.0 \times 10^{9}$	$2 \pm 0.014 \times 10^{47}$	0.52 ± 0.0
61	3.061	5.9×10^{43}	$7.7 \pm 1.0 \times 10^{46}$	$2.9 \pm 0.012 \times 10^{47}$	4366 ± 24	$3 \pm 1.0 \times 10^{9}$	$3.7 \pm 0.041 \times 10^{47}$	0.79 ± 0.01

Table 4.4: Continuation PyQSOfit results: QSO MUSEUM III

ID	z	$L^{\mathrm{QSO}}_{\mathrm{Ly\alpha;peak}}$ $\mathrm{erg\,s^{-1}\,Å^{-1}}$	$L_\lambda(1350\,Å)$ $\mathrm{erg\,s^{-1}}$	L_{bol} $\mathrm{erg\,s^{-1}}$	FWHM(C IV) $\mathrm{km\,s^{-1}}$	M_{BH} $\mathrm{M_{sun}}$	L_{Edd} $\mathrm{erg\,s^{-1}}$	λ_{Edd}
62	3.051	1.5×10^{42}	$4.9 \pm 1.1 \times 10^{44}$	$1.9 \pm 0.216 \times 10^{45}$	3963 ± 247	$1.7 \pm 1.1 \times 10^{8}$	$2.1 \pm 0.292 \times 10^{46}$	0.09 ± 0.02
63	3.14246	3.6×10^{42}	$3.9 \pm 1.0 \times 10^{45}$	$1.5 \pm 0.024 \times 10^{46}$	6806 ± 296	$1.5 \pm 1.1 \times 10^{9}$	$1.9 \pm 0.163 \times 10^{47}$	0.08 ± 0.01
64	3.064	2.4×10^{42}	$1.5 \pm 1.0 \times 10^{45}$	$5.9 \pm 0.28 \times 10^{45}$	3214 ± 25	$2 \pm 1.0 \times 10^{8}$	$2.5 \pm 0.075 \times 10^{46}$	0.23 ± 0.01
65	3.0328	4.9×10^{42}	$1.8 \pm 1.0 \times 10^{45}$	$6.9 \pm 0.243 \times 10^{45}$	3497 ± 97	$2.6 \pm 1.1 \times 10^{8}$	$3.3 \pm 0.19 \times 10^{46}$	0.21 ± 0.01
66	3.139	7×10^{42}	$1.2 \pm 1.0 \times 10^{46}$	$4.7 \pm 0.033 \times 10^{46}$	6883 ± 136	$2.8 \pm 1.0 \times 10^{9}$	$3.5 \pm 0.139 \times 10^{47}$	0.13 ± 0.01
67	3.1279	6.7×10^{42}	$8 \pm 1.0 \times 10^{45}$	$3 \pm 0.027 \times 10^{46}$	5450 ± 59	$1.4 \pm 1.0 \times 10^{9}$	$1.7 \pm 0.039 \times 10^{47}$	0.17 ± 0.0
68	3.062	1.2×10^{43}	$1.5 \pm 1.0 \times 10^{45}$	$5.8 \pm 0.194 \times 10^{45}$	3420 ± 20	$2.3 \pm 1.0 \times 10^{8}$	$2.8 \pm 0.061 \times 10^{46}$	0.2 ± 0.01
69	3.135	4.4×10^{42}	$5.1 \pm 1.0 \times 10^{45}$	$1.9 \pm 0.025 \times 10^{46}$	5517 ± 130	$1.1 \pm 1.0 \times 10^{9}$	$1.4 \pm 0.067 \times 10^{47}$	0.14 ± 0.01
70	3.15	4.9×10^{42}	$1.1 \pm 1.0 \times 10^{45}$	$4.2 \pm 0.158 \times 10^{45}$	2823 ± 59	$1.3 \pm 1.0 \times 10^{8}$	$1.6 \pm 0.076 \times 10^{46}$	0.26 ± 0.02
71	3.195	5.4×10^{42}	$5.8 \pm 1.0 \times 10^{45}$	$2.2 \pm 0.029 \times 10^{46}$	3958 ± 58	$6.2 \pm 1.0 \times 10^{8}$	$7.8 \pm 0.233 \times 10^{46}$	0.28 ± 0.01
72	3.106	1.2×10^{42}	$7.6 \pm 1.1 \times 10^{44}$	$2.9 \pm 0.219 \times 10^{45}$	5716 ± 411	$4.4 \pm 1.2 \times 10^{8}$	$5.5 \pm 0.825 \times 10^{46}$	0.05 ± 0.01
73	3.088	2.3×10^{42}	$7.5 \pm 1.1 \times 10^{44}$	$2.8 \pm 0.206 \times 10^{45}$	3944 ± 210	$2.1 \pm 1.1 \times 10^{8}$	$2.6 \pm 0.295 \times 10^{46}$	0.11 ± 0.01
74	3.182836	3.4×10^{42}	$2.4 \pm 1.0 \times 10^{45}$	$9.1 \pm 0.246 \times 10^{45}$	4090 ± 94	$4.1 \pm 1.0 \times 10^{8}$	$5.2 \pm 0.249 \times 10^{46}$	0.18 ± 0.01
75	3.003	8.5×10^{42}	$4.7 \pm 1.0 \times 10^{45}$	$1.8 \pm 0.024 \times 10^{46}$	4517 ± 89	$7.2 \pm 1.0 \times 10^{8}$	$9 \pm 0.36 \times 10^{46}$	0.2 ± 0.01
76	3.199	1.8×10^{43}	$9.6 \pm 1.0 \times 10^{45}$	$3.7 \pm 0.04 \times 10^{46}$	3881 ± 32	$7.8 \pm 1.0 \times 10^{8}$	$9.8 \pm 0.17 \times 10^{46}$	0.38 ± 0.01
77	3.114389	3.9×10^{42}	$4.7 \pm 1.2 \times 10^{44}$	$1.8 \pm 0.37 \times 10^{45}$	4218 ± 538	$1.9 \pm 1.3 \times 10^{8}$	$2.3 \pm 0.649 \times 10^{46}$	0.08 ± 0.03
78	3.0983	2.3×10^{42}	$2 \pm 1.0 \times 10^{45}$	$7.8 \pm 0.273 \times 10^{45}$	4438 ± 119	$4.5 \pm 1.1 \times 10^{8}$	$5.6 \pm 0.318 \times 10^{46}$	0.14 ± 0.01
79	3.1554	8.9×10^{42}	$2.4 \pm 1.0 \times 10^{45}$	$9 \pm 0.211 \times 10^{45}$	3513 ± 25	$3 \pm 1.0 \times 10^{8}$	$3.8 \pm 0.071 \times 10^{46}$	0.24 ± 0.01
80	3.032	2.4×10^{43}	$9.9 \pm 1.0 \times 10^{45}$	$3.8 \pm 0.024 \times 10^{46}$	3671 ± 12	$7 \pm 1.0 \times 10^{8}$	$8.9 \pm 0.063 \times 10^{46}$	0.43 ± 0.0
81	3.027	2.9×10^{42}	$2.1 \pm 1.0 \times 10^{45}$	$7.9 \pm 0.205 \times 10^{45}$	3692 ± 141	$3.1 \pm 1.1 \times 10^{8}$	$3.9 \pm 0.304 \times 10^{46}$	0.2 ± 0.02
82	3.041824	7.4×10^{41}	$3.4 \pm 1.2 \times 10^{44}$	$1.3 \pm 0.276 \times 10^{45}$	3207 ± 657	$9 \pm 1.5 \times 10^{7}$	$1.1 \pm 0.482 \times 10^{46}$	0.11 ± 0.05
83	3.094	5×10^{42}	$1.5 \pm 1.0 \times 10^{45}$	$5.7 \pm 0.245 \times 10^{45}$	3193 ± 106	$2 \pm 1.1 \times 10^{8}$	$2.5 \pm 0.174 \times 10^{46}$	0.23 ± 0.02
84	3.046	3.8×10^{42}	$4.1 \pm 1.0 \times 10^{45}$	$1.6 \pm 0.024 \times 10^{46}$	5290 ± 178	$9.2 \pm 1.1 \times 10^{8}$	$1.2 \pm 0.078 \times 10^{47}$	0.14 ± 0.01
85	3.135	2.6×10^{42}	$5.2 \pm 1.0 \times 10^{45}$	$2 \pm 0.024 \times 10^{46}$	4843 ± 149	$8.7 \pm 1.1 \times 10^{8}$	$1.1 \pm 0.068 \times 10^{47}$	0.18 ± 0.01
86	3.1899	7.5×10^{42}	$7.3 \pm 1.0 \times 10^{45}$	$2.8 \pm 0.023 \times 10^{46}$	3517 ± 32	$5.5 \pm 1.0 \times 10^{8}$	$6.9 \pm 0.128 \times 10^{46}$	0.4 ± 0.01
87	3.157	3.5×10^{42}	$1.3 \pm 1.0 \times 10^{45}$	$5 \pm 0.188 \times 10^{45}$	4544 ± 205	$3.7 \pm 1.1 \times 10^{8}$	$4.6 \pm 0.429 \times 10^{46}$	0.11 ± 0.01
88	3.035	2.5×10^{42}	$2.6 \pm 1.0 \times 10^{45}$	$9.8 \pm 0.203 \times 10^{45}$	4429 ± 134	$5 \pm 1.1 \times 10^{8}$	$6.3 \pm 0.388 \times 10^{46}$	0.15 ± 0.01
89	3.151	2.9×10^{42}	$3.7 \pm 1.0 \times 10^{45}$	$1.4 \pm 0.034 \times 10^{46}$	5327 ± 230	$8.8 \pm 1.1 \times 10^{8}$	$1.1 \pm 0.097 \times 10^{47}$	0.13 ± 0.01
90	3.049	8.6×10^{42}	$3.7 \pm 1.0 \times 10^{45}$	$1.4 \pm 0.024 \times 10^{46}$	3713 ± 27	$4.3 \pm 1.0 \times 10^{8}$	$5.4 \pm 0.093 \times 10^{46}$	0.26 ± 0.01
91	3.044482	5.7×10^{42}	$1.2 \pm 1.0 \times 10^{45}$	$4.7 \pm 0.198 \times 10^{45}$	3086 ± 22	$1.6 \pm 1.0 \times 10^{8}$	$2.1 \pm 0.055 \times 10^{46}$	0.23 ± 0.01
92	3.119	5.3×10^{42}	$3.3 \pm 1.0 \times 10^{45}$	$1.2 \pm 0.025 \times 10^{46}$	3761 ± 46	$4.1 \pm 1.0 \times 10^{8}$	$5.2 \pm 0.138 \times 10^{46}$	0.24 ± 0.01
93	3.046	5.1×10^{41}	$5.3 \pm 1.1 \times 10^{44}$	$2 \pm 0.202 \times 10^{45}$	10286 ± 944	$1.2 \pm 1.2 \times 10^{9}$	$1.5 \pm 0.281 \times 10^{47}$	0.01 ± 0.0
94	3.1832	5.7×10^{42}	$2.4 \pm 1.0 \times 10^{45}$	$9 \pm 0.2 \times 10^{45}$	4059 ± 48	$4 \pm 1.0 \times 10^{8}$	$5.1 \pm 0.134 \times 10^{46}$	0.18 ± 0.01
95	3.035525	2×10^{42}	$3.2 \pm 1.0 \times 10^{45}$	$1.2 \pm 0.026 \times 10^{46}$	5170 ± 243	$7.7 \pm 1.1 \times 10^{8}$	$9.7 \pm 0.919 \times 10^{46}$	0.13 ± 0.01
96	3.117	8.6×10^{42}	$2.9 \pm 1.0 \times 10^{45}$	$1.1 \pm 0.024 \times 10^{46}$	3392 ± 26	$3.1 \pm 1.0 \times 10^{8}$	$4 \pm 0.076 \times 10^{46}$	0.28 ± 0.01
97	3.097	7.4×10^{42}	$7.5 \pm 1.0 \times 10^{45}$	$2.8 \pm 0.025 \times 10^{46}$	5376 ± 356	$1.3 \pm 1.1 \times 10^{9}$	$1.6 \pm 0.217 \times 10^{47}$	0.17 ± 0.02
98	3.075	4.3×10^{42}	$1.4 \pm 1.0 \times 10^{45}$	$5.4 \pm 0.187 \times 10^{45}$	3854 ± 46	$2.8 \pm 1.0 \times 10^{8}$	$3.5 \pm 0.105 \times 10^{46}$	0.15 ± 0.01
99	3.109	4×10^{42}	$1.4 \pm 1.0 \times 10^{45}$	$5.3 \pm 0.252 \times 10^{45}$	3262 ± 38	$2 \pm 1.0 \times 10^{8}$	$2.5 \pm 0.085 \times 10^{46}$	0.22 ± 0.01
100	3.055	2.6×10^{42}	$3.5 \pm 1.0 \times 10^{45}$	$1.3 \pm 0.024 \times 10^{46}$	9271 ± 363	$2.6 \pm 1.1 \times 10^{9}$	$3.3 \pm 0.258 \times 10^{47}$	0.04 ± 0.0
101	3.08	7.3×10^{42}	$5.1 \pm 1.0 \times 10^{45}$	$1.9 \pm 0.023 \times 10^{46}$	3288 ± 28	$4 \pm 1.0 \times 10^{8}$	$5 \pm 0.089 \times 10^{46}$	0.39 ± 0.01
102	3.196	8.2×10^{42}	$4.5 \pm 1.0 \times 10^{45}$	$1.7 \pm 0.025 \times 10^{46}$	3773 ± 87	$4.9 \pm 1.0 \times 10^{8}$	$6.2 \pm 0.288 \times 10^{46}$	0.28 ± 0.01
103	3.0164	9.4×10^{42}	$4.6 \pm 1.0 \times 10^{45}$	$1.7 \pm 0.025 \times 10^{46}$	3510 ± 20	$4.3 \pm 1.0 \times 10^{8}$	$5.4 \pm 0.073 \times 10^{46}$	0.32 ± 0.01
104	3.14	1.3×10^{43}	$3 \pm 1.0 \times 10^{45}$	$1.2 \pm 0.02 \times 10^{46}$	3163 ± 39	$2.8 \pm 1.0 \times 10^{8}$	$3.5 \pm 0.093 \times 10^{46}$	0.33 ± 0.01
105	3.193	3.4×10^{42}	$2.5 \pm 1.0 \times 10^{45}$	$9.6 \pm 0.257 \times 10^{45}$	6504 ± 198	$1.1 \pm 1.1 \times 10^{9}$	$1.3 \pm 0.084 \times 10^{47}$	0.07 ± 0.0
106	3.1906	3×10^{42}	$3.2 \pm 1.0 \times 10^{45}$	$1.2 \pm 0.021 \times 10^{46}$	4408 ± 88	$5.6 \pm 1.0 \times 10^{8}$	$7.1 \pm 0.29 \times 10^{46}$	0.17 ± 0.01
107	3.091393	6×10^{42}	$5.7 \pm 1.0 \times 10^{45}$	$2.2 \pm 0.026 \times 10^{46}$	3946 ± 47	$6 \pm 1.0 \times 10^{8}$	$7.6 \pm 0.187 \times 10^{46}$	0.28 ± 0.01
108	3.0858	5.8×10^{42}	$5.7 \pm 1.0 \times 10^{45}$	$2.2 \pm 0.024 \times 10^{46}$	4493 ± 114	$7.9 \pm 1.1 \times 10^{8}$	$9.9 \pm 0.505 \times 10^{46}$	0.22 ± 0.01
109	3.0667	5.2×10^{42}	$6 \pm 1.0 \times 10^{45}$	$2.3 \pm 0.024 \times 10^{46}$	5238 ± 92	$1.1 \pm 1.0 \times 10^{9}$	$1.4 \pm 0.049 \times 10^{47}$	0.17 ± 0.01
110	3.12	1.7×10^{42}	$1.5 \pm 1.0 \times 10^{45}$	$5.9 \pm 0.246 \times 10^{45}$	5589 ± 207	$6.1 \pm 1.1 \times 10^{8}$	$7.7 \pm 0.592 \times 10^{46}$	0.08 ± 0.01
111	3.033	3.9×10^{42}	$4.4 \pm 1.0 \times 10^{45}$	$1.7 \pm 0.026 \times 10^{46}$	3167 ± 33	$3.4 \pm 1.0 \times 10^{8}$	$4.3 \pm 0.095 \times 10^{46}$	0.39 ± 0.01
112	3.1108	4.4×10^{42}	$2.3 \pm 1.0 \times 10^{45}$	$8.8 \pm 0.223 \times 10^{45}$	2962 ± 34	$2.1 \pm 1.0 \times 10^{8}$	$2.7 \pm 0.071 \times 10^{46}$	0.33 ± 0.01
113	3.1053	4.6×10^{42}	$4.9 \pm 1.0 \times 10^{45}$	$1.8 \pm 0.032 \times 10^{46}$	7382 ± 324	$1.9 \pm 1.1 \times 10^{9}$	$2.5 \pm 0.217 \times 10^{47}$	0.08 ± 0.01
114	3.142	2.5×10^{42}	$1.6 \pm 1.0 \times 10^{45}$	$6.3 \pm 0.199 \times 10^{45}$	3530 ± 66	$2.5 \pm 1.0 \times 10^{8}$	$3.2 \pm 0.13 \times 10^{46}$	0.2 ± 0.01
115	3.116568	3.3×10^{42}	$5.1 \pm 1.1 \times 10^{44}$	$2 \pm 0.219 \times 10^{45}$	7592 ± 378	$6.3 \pm 1.1 \times 10^{8}$	$7.9 \pm 0.916 \times 10^{46}$	0.02 ± 0.0
116	3.07	8×10^{42}	$3.7 \pm 1.0 \times 10^{45}$	$1.4 \pm 0.025 \times 10^{46}$	4936 ± 253	$7.6 \pm 1.1 \times 10^{8}$	$9.5 \pm 0.984 \times 10^{46}$	0.15 ± 0.02
117	3.172	2.4×10^{42}	$1.2 \pm 1.0 \times 10^{45}$	$4.7 \pm 0.214 \times 10^{45}$	5155 ± 174	$4.6 \pm 1.1 \times 10^{8}$	$5.8 \pm 0.418 \times 10^{46}$	0.08 ± 0.01
118	3.0854	2.2×10^{42}	$5.7 \pm 1.0 \times 10^{45}$	$2.2 \pm 0.026 \times 10^{46}$	9254 ± 373	$3.3 \pm 1.1 \times 10^{9}$	$4.2 \pm 0.34 \times 10^{47}$	0.05 ± 0.0
119	3.19	2.9×10^{42}	$4.6 \pm 1.0 \times 10^{45}$	$1.7 \pm 0.027 \times 10^{46}$	5232 ± 185	$9.5 \pm 1.1 \times 10^{8}$	$1.2 \pm 0.085 \times 10^{47}$	0.15 ± 0.01
120	3.407	2.8×10^{42}	$4.7 \pm 1.1 \times 10^{44}$	$1.8 \pm 0.232 \times 10^{45}$	6354 ± 817	$4.2 \pm 1.3 \times 10^{8}$	$5.3 \pm 1.399 \times 10^{46}$	0.03 ± 0.01

4.6.2   QSO MUSEUM I

In this Appendix we present the maps and physical properties obtained in Section 4.3 but for the QSO MUSEUM bright sample (Arrigoni Battaia et al., 2019a).

Table4.5 shows the ID, redshift of the peak Lyα emission of the quasar, redshift of the peak Lyα emission of the associated nebula, peak Lyα luminosity density of the quasar, integrated luminosity within the 2σ isophote, area contained in the 2σ isophote, velocity shift between the centroid obtained from fitting a gaussian to the 2σ isophote spectrum and the Lyα of the quasar, velocity shift between the flux weighted first moment of the Lyα line of the nebula and the Lyα of the quasar, FWHM computed from the gaussian fit to the 2σ isophote spectrum and linewidth measured from the flux weighted second moment of the Lyα line of the nebula.

Figure 4.23 shows the Lyα SB maps computed from 30 Å pseudo-NBs centered at the peak Lyα emission of the nebula.

Figures 4.24, 4.25 and 4.26 show the integrated spectrum within the 2σ isophotes of Figure 4.23 and the quasar spectrum integrated within a 1.5" radius aperture in red and black, respectively, after normalizing them to the maximum value. The vertical dashed blue line represents the wavelength of the peak Lyα emission of the quasar.

Figure 4.27 shows the velocity shift maps computed using the second moment map of pseudo-NBs centered at the peak Lyα emission of the nebula and within the $\pm$FWHM of the nebula spectrum (Table 4.5. The maps are constructed with the same SNR mask as in Section 4.3.3 for the faint sample. Similarly, Figure 4.28 shows the velocity dispersion maps constructed using the same pseudo-NBs.

Table 4.5: Properties of the quasar and extended Lyα emission of the QSO MUSEUM I

ID	$z_{\text{Ly}\alpha;\text{peak}}^{\text{QSO}}$	$z_{\text{Ly}\alpha;\text{peak}}^{\text{Neb}}$	$L_{\text{Ly}\alpha;\text{peak}}^{\text{QSO}}$ erg s^{-1} Å^{-1}	Luminosity 10^{42} erg s^{-1}	Area arcsec^2 (pkpc^2)	Δv_{gauss} km s^{-1}	Δv_{m1} km s^{-1}	FWHM$_{\text{gauss}}$ Å (km s^{-1})	$\Delta\lambda_{\text{m2}}$ Å (km s^{-1})
1	3.166	3.154	5.4×10^{43}	124.68±2.59	44.56 (2562.85)	237.84±60.53	204.4±22.13	32.97 (1950)	14.94 (884)
2	3.161	3.164	6.1×10^{43}	88.27±2.78	74.2 (4258.63)	126.87±46.91	36.96±25.53	24.96 (1478)	8.13 (482)
3	3.115	3.123	9.1×10^{43}	166.09±2.93	81.32 (4706.22)	344.77±66.8	303.65±19.5	32.97 (1974)	15.45 (925)
4	3.228	3.23	4.3×10^{43}	97.86±2.25	75.32 (4265.7)	248.83±28.57	264.73±14.72	19.05 (1110)	7.85 (458)
5	3.325	3.328	3.6×10^{43}	77.9±2.2	56.92 (3159.92)	623.61±35.16	567.57±21.78	23.74 (1351)	9.12 (519)
6	3.041	3.04	7×10^{43}	17.86±1.06	7.8 (458.99)	956.08±163.79	973.62±69.64	32.97 (2006)	16.59 (1009)
7	3.118	3.121	8×10^{43}	105.13±2.58	38.96 (2255.96)	368.54±107.54	359.48±27.02	32.97 (1972)	15.1 (903)
8	3.125	3.131	7.1×10^{43}	162.74±1.79	136.84 (7906.42)	511.21±16.62	486.83±7.74	21.01 (1254)	8.58 (512)
9	3.306	3.313	1×10^{44}	152.41±3.33	65.68 (3657.67)	444.49±36.71	440.88±20.57	29.85 (1707)	12.14 (694)
10	3.245	3.245	8.8×10^{43}	322.09±3.39	161.08 (9095.48)	-75.36±19.66	-119.06±8.34	23.86 (1387)	9.84 (572)
11	3.068	3.1	9.9×10^{42}	40.12±1.04	40.24 (2339.93)	2402.76±16.77	2415.26±11.1	12.5 (752)	4.61 (277)
12	3.386	3.396	4.9×10^{43}	62.88±1.93	33.36 (1826.3)	641.05±22.74	647.5±19.83	20.22 (1135)	8.0 (449)
13	3.168	3.169	5.2×10^{43}	308.56±3.42	269.4 (15448.68)	218.19±11.19	217.45±6.04	15.76 (932)	6.47 (382)
14	3.139	3.127	1.9×10^{43}	42.61±1.88	19.76 (1142.75)	-123.03±93.13	24.4±50.01	32.97 (1965)	13.01 (775)
15	3.145	3.142	1.2×10^{44}	235.68±3.01	103.56 (5971.22)	47.26±17.44	67.85±9.46	23.91 (1422)	9.46 (562)
16	3.186	3.19	2.2×10^{43}	73.87±2.4	55.68 (3178.93)	170.38±65.53	126.8±32.82	29.83 (1756)	13.63 (803)
17	3.349	3.351	2.2×10^{43}	142.92±2.23	115.0 (6354.27)	76.26±12.61	71.63±7.57	15.45 (876)	6.25 (354)
18	3.278	3.289	7.6×10^{43}	296.53±3.29	97.6 (5461.66)	891.67±15.01	862.96±8.41	22.45 (1290)	8.9 (512)
19	3.215	3.223	4.5×10^{43}	182.49±3.08	116.24 (6592.98)	759.03±31.18	809.72±15.94	28.9 (1687)	10.4 (607)
20	3.42	3.447	5.6×10^{43}	82.56±2.45	37.8 (2047.7)	1089.96±97.4	1077.01±32.53	32.97 (1833)	17.14 (953)
21	3.22	3.222	1.5×10^{44}	238.44±3.09	102.2 (5797.18)	55.32±8.26	96.14±6.82	17.19 (1004)	6.85 (400)
22	3.23	3.231	4.5×10^{43}	151.53±2.72	72.8 (4122.58)	80.54±21.19	65.02±13.53	22.05 (1285)	9.1 (531)
23	3.145	3.137	2.8×10^{43}	70.11±1.58	45.8 (2643.23)	-299.96±22.95	-331.48±16.1	21.46 (1278)	8.05 (479)
24	3.056	3.057	9.7×10^{43}	191.62±2.04	86.24 (5057.42)	104.2±29.99	122.52±10.74	30.97 (1882)	12.55 (762)
25	3.343	3.353	4×10^{43}	75.19±2.18	40.32 (2226.71)	487.54±79.25	453.35±31.25	32.97 (1869)	15.27 (866)
26	3.179	3.177	7.1×10^{44}	886.44±23.8	53.84 (3082.22)	-80.67±83.9	-70.14±29.48	32.97 (1946)	15.8 (933)
27	3.333	3.333	6.8×10^{43}	116.49±2.39	67.4 (3737.51)	-1.5±26.39	-15.77±14.62	22.0 (1252)	8.75 (498)
28	3.359	3.355	2.6×10^{43}	47.76±1.77	33.88 (1870.41)	66.02±41.52	68.43±34.38	29.38 (1662)	11.79 (667)
29	3.222	3.223	3×10^{43}	22.0±1.62	15.6 (884.7)	305.51±106.81	339.04±82.66	32.97 (1924)	15.5 (904)
30	3.36	3.36	1.2×10^{44}	312.9±5.88	22.4 (1235.5)	-92.58±69.76	-127.79±19.58	32.97 (1866)	16.23 (918)
31	3.205	3.197	5×10^{43}	73.82±2.29	47.12 (2686.76)	-156.3±51.11	-138.62±29.7	29.01 (1702)	11.75 (689)
32	3.099	3.102	1.8×10^{43}	82.97±2.02	88.92 (5168.04)	235.38±24.66	204.86±18.8	22.24 (1337)	8.98 (540)
33	3.134	3.139	8.9×10^{43}	149.06±2.65	58.84 (3394.4)	-34.03±19.07	-68.46±14.46	26.16 (1561)	10.74 (641)
34	3.243	3.254	1.1×10^{43}	90.7±1.86	88.84 (5006.84)	697.89±16.83	682.55±14.06	20.36 (1181)	8.17 (474)
35	3.245	3.245	5.8×10^{43}	162.81±2.14	71.96 (4063.17)	160.56±13.95	204.87±9.53	23.65 (1373)	9.26 (538)
36	3.191	3.204	3.3×10^{43}	166.12±2.3	134.4 (7652.51)	841.47±15.38	847.49±9.54	20.66 (1212)	8.17 (479)
37	3.128	3.127	7.5×10^{43}	178.67±1.86	92.44 (5345.34)	16.83±17.55	-12.68±7.0	21.55 (1287)	9.02 (539)
38	3.354	3.352	8.3×10^{43}	123.59±2.28	18.36 (1014.27)	-116.15±87.94	-215.57±19.45	32.97 (1868)	18.67 (1058)
39	3.097	3.097	1×10^{44}	166.4±2.41	66.44 (3865.52)	159.76±15.25	248.98±8.55	19.04 (1145)	6.89 (415)
40	3.339	3.341	7.7×10^{43}	140.41±2.56	73.36 (4061.99)	59.36±20.49	54.06±15.44	26.68 (1516)	10.46 (594)
41	3.335	3.338	2.8×10^{43}	65.31±1.79	50.44 (2794.71)	233.2±33.91	235.95±20.2	22.33 (1269)	9.17 (521)
42	3.035	3.033	8.5×10^{43}	154.21±2.29	60.88 (3587.43)	51.35±23.54	93.89±10.41	21.04 (1286)	8.82 (539)
43	3.125	3.124	2.6×10^{43}	92.2±1.76	68.88 (3985.45)	178.08±21.5	197.13±14.0	21.67 (1294)	8.59 (513)
44	3.229	3.234	3×10^{43}	45.23±1.9	28.52 (1613.88)	680.73±90.68	829.47±46.48	32.97 (1918)	13.83 (804)
45	3.362	3.37	3×10^{43}	23.91±1.57	18.8 (1034.73)	426.85±89.38	505.39±57.42	26.84 (1515)	9.65 (545)
46	3.391	3.4	7.9×10^{43}	135.04±3.14	93.0 (5087.3)	459.7±41.83	505.75±19.39	26.24 (1471)	10.99 (616)
47	3.155	3.16	3.7×10^{43}	372.29±2.57	155.8 (8949.64)	551.11±5.78	534.81±3.29	14.1 (835)	5.93 (351)
48	3.208	3.218	3.7×10^{43}	102.48±2.03	89.4 (5075.73)	838.52±24.85	794.28±13.66	21.09 (1233)	8.75 (511)
49	3.135	3.14	1.5×10^{43}	81.02±1.58	91.76 (5292.55)	285.54±17.61	320.69±12.84	19.19 (1143)	6.95 (414)
50	3.214	3.206	3.4×10^{43}	444.95±2.99	199.4 (11348.57)	-621.77±7.53	-612.76±4.06	18.17 (1066)	7.24 (424)
51	3.134	3.138	5.1×10^{43}	47.28±1.24	46.8 (2700.48)	226.7±12.2	203.04±9.92	11.2 (668)	4.51 (269)
52	3.139	3.137	4.6×10^{43}	55.56±1.64	33.24 (1918.42)	-0.3±26.61	68.44±22.45	23.92 (1425)	9.37 (558)
53	3.153	3.167	2×10^{43}	52.39±1.46	70.68 (4054.7)	816.36±21.8	827.12±16.76	17.79 (1053)	7.61 (450)
54	3.109	3.114	3.6×10^{43}	100.94±2.03	82.08 (4758.68)	254.12±19.58	293.99±14.84	22.23 (1333)	8.57 (514)
55	3.193	3.19	3.5×10^{43}	75.38±1.89	31.96 (1825.04)	-40.51±35.92	-2.15±24.68	31.11 (1830)	12.37 (728)
56	3.091	3.098	5.8×10^{43}	200.0±2.49	110.28 (6414.74)	428.01±11.65	414.14±7.68	17.96 (1081)	7.24 (436)
57	3.454	3.464	2.3×10^{43}	32.82±2.05	16.56 (893.95)	196.95±53.84	174.01±47.43	23.73 (1313)	10.11 (559)
58	3.05	3.047	5.9×10^{43}	82.02±1.49	46.96 (2759.77)	-31.31±11.53	20.94±6.87	12.03 (733)	4.43 (270)
59	3.156	3.16	3.8×10^{43}	122.36±2.83	63.2 (3630.88)	21.31±49.54	17.42±21.57	27.17 (1612)	11.81 (701)
60	3.179	3.18	4.4×10^{43}	100.63±2.0	42.48 (2430.38)	206.0±22.08	237.85±14.47	22.3 (1315)	9.32 (549)
61	3.061	3.067	5.9×10^{43}	113.63±2.8	79.24 (4638.0)	586.26±53.71	571.12±28.0	32.97 (1998)	12.52 (759)
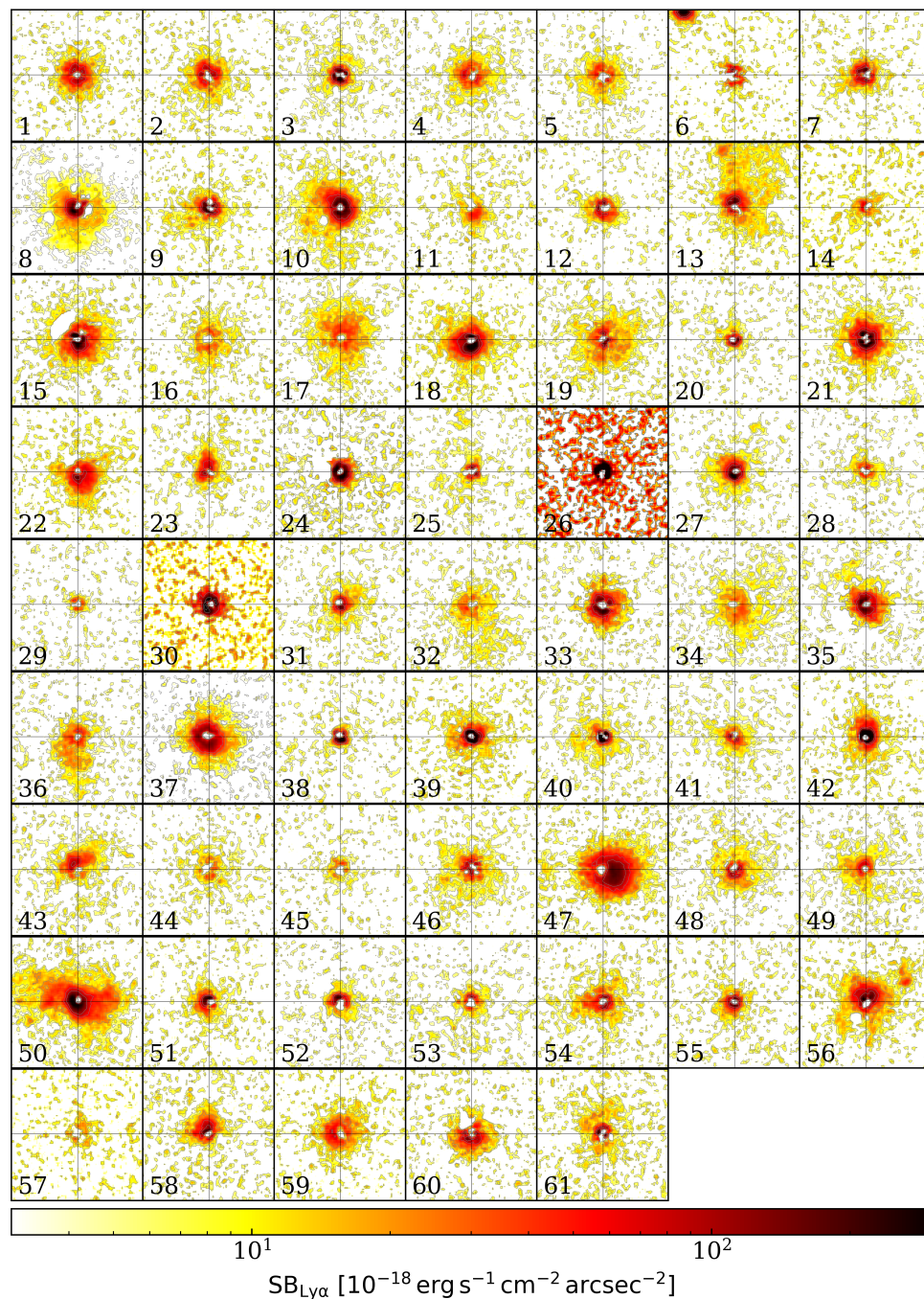
Figure 4.23: Lyα SB maps around the QSO MUSEUM bright sample from Arrigoni Battaia et al. (2019a), after PSF- and continuum subtraction (see Section 4.2.5), from 30 Å NBs centered at the peak Lyα wavelength of the nebula. Each image shows maps of 15" × 15" (about 110 kpc x 110 kpc at the median redshift of the sample) centered on the quasar position. In each map, The gray crosshair indicates the location of the quasar. The contours indicate levels of [2, 4, 10, 20, 50] times the SB limit of each observation.
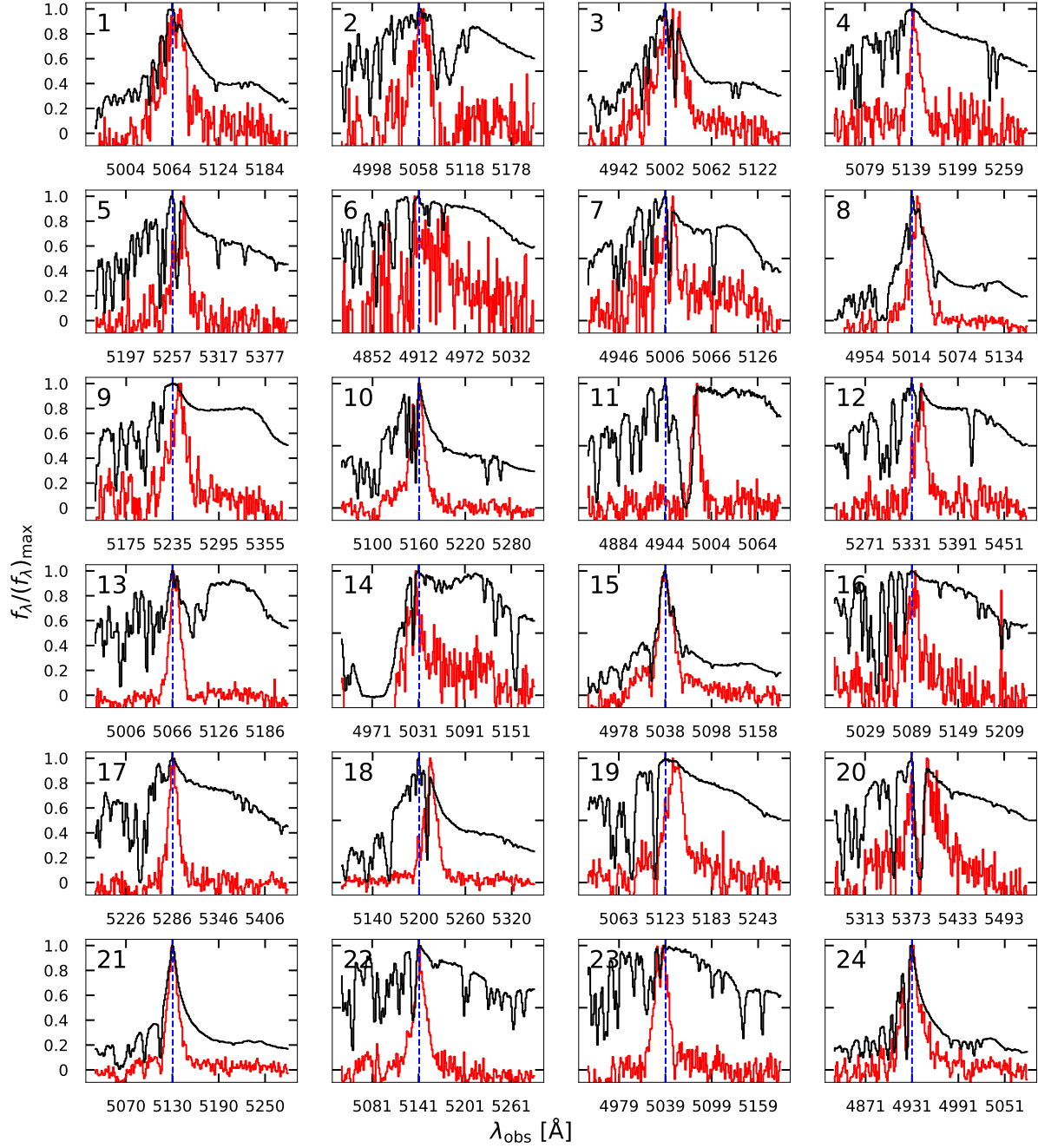
Figure 4.24: Same as Figure 4.5, but for the QSO MUSEUM bright sample.
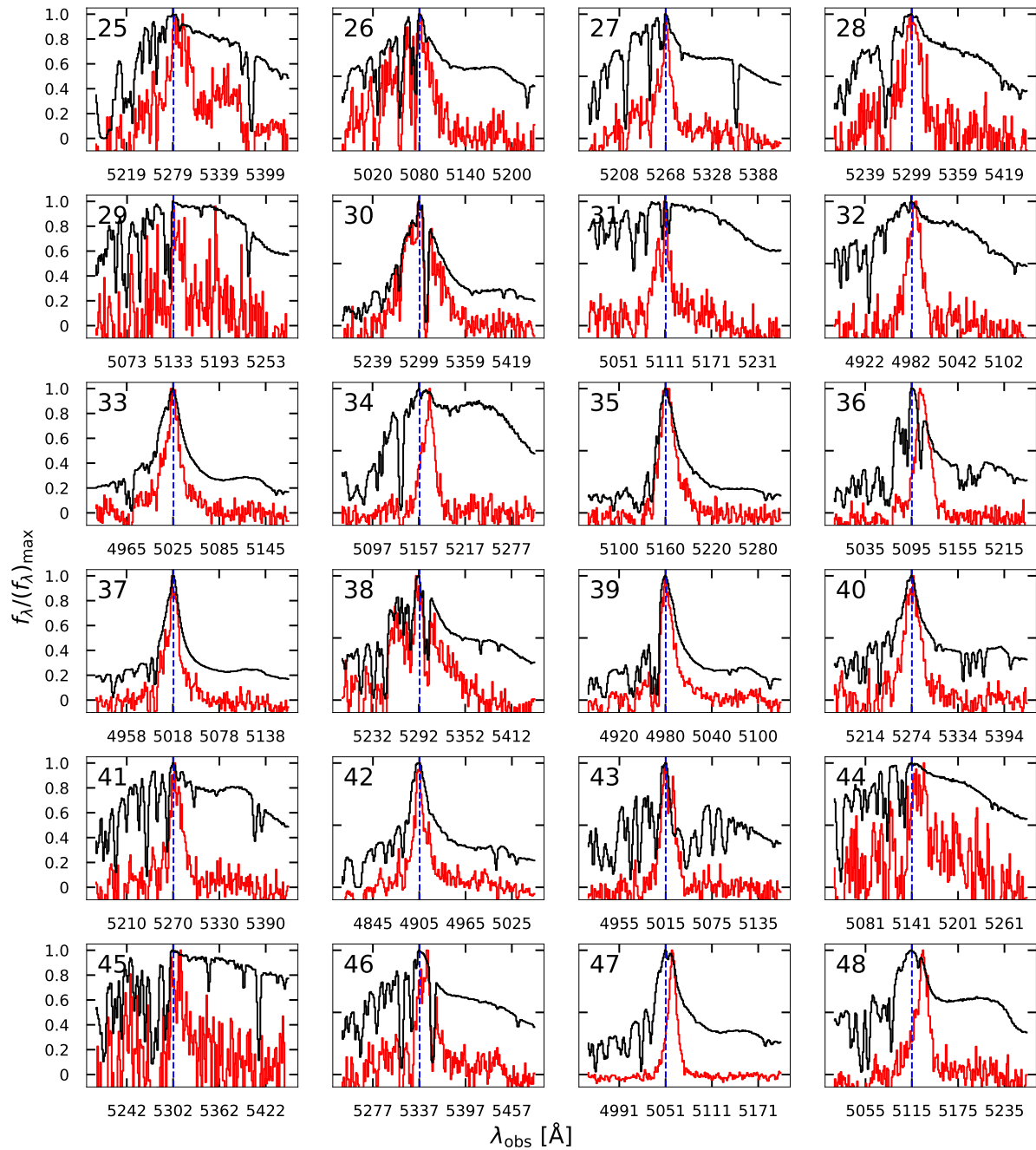
Figure 4.25: Same as Figure 4.24, but for ID 25-48.
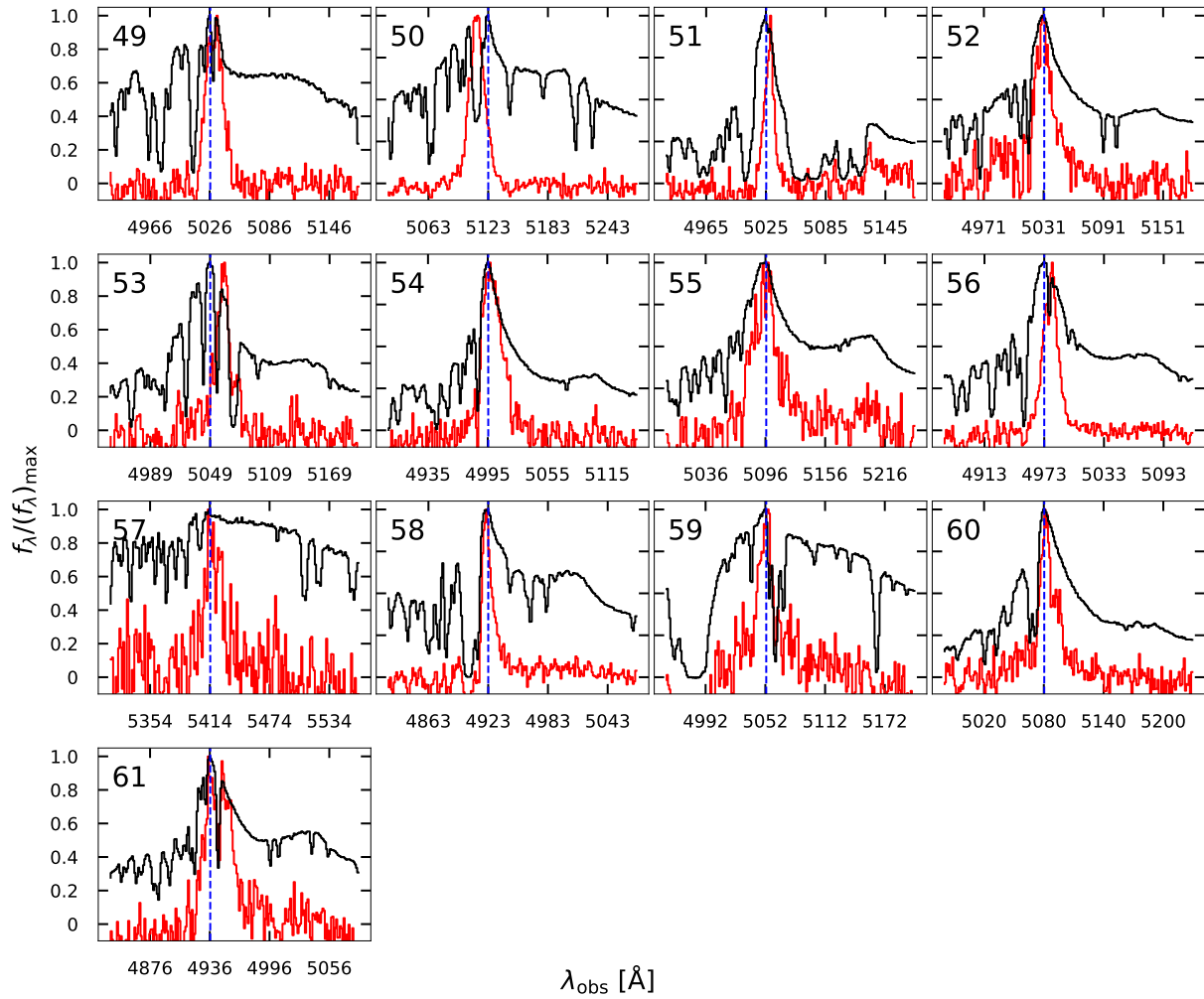
Figure 4.26: Same as Figure 4.24, but for ID 49-61.
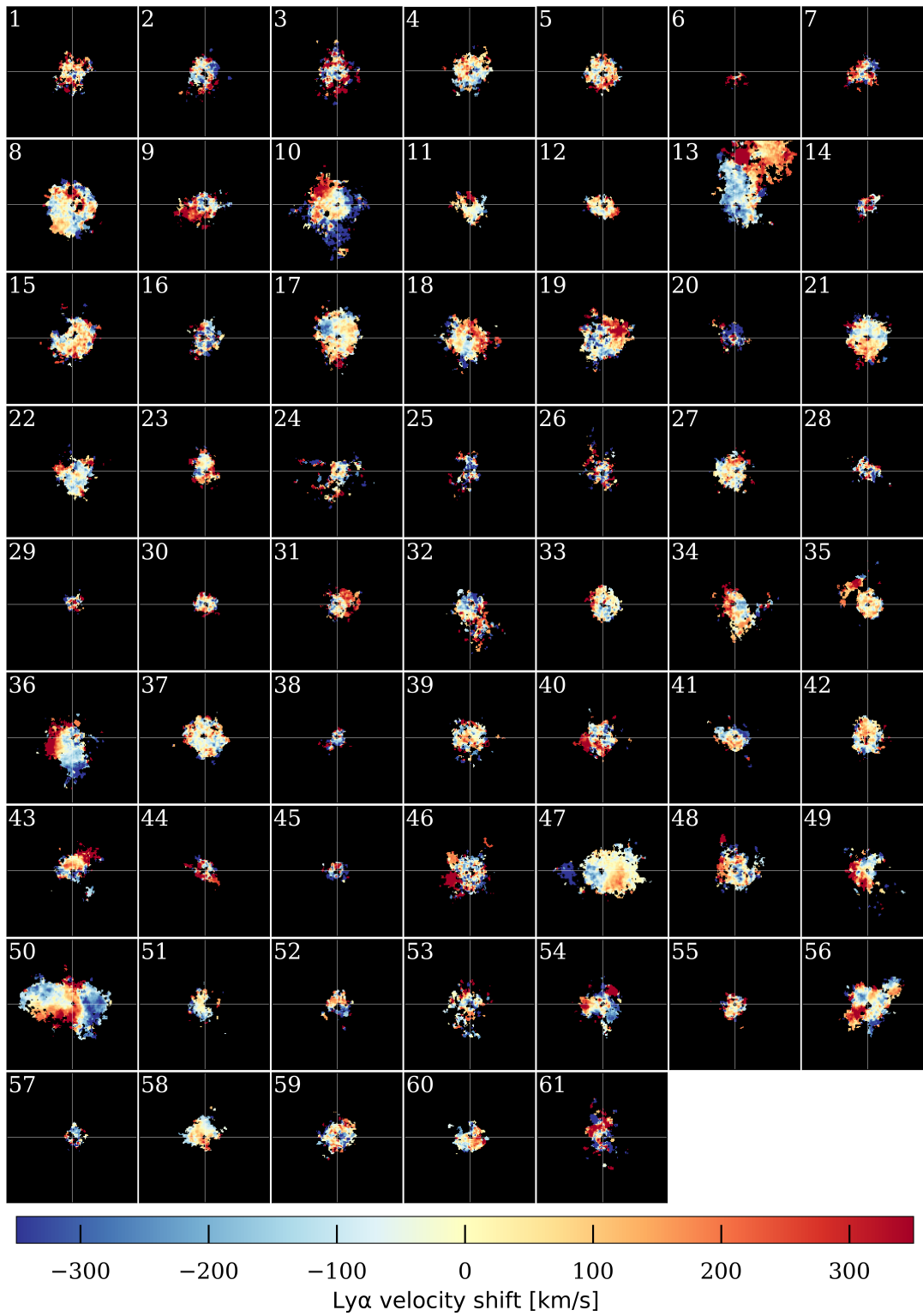
Figure 4.27: Same as Figure 4.8 but for the QSO MUSEUM bright sample.
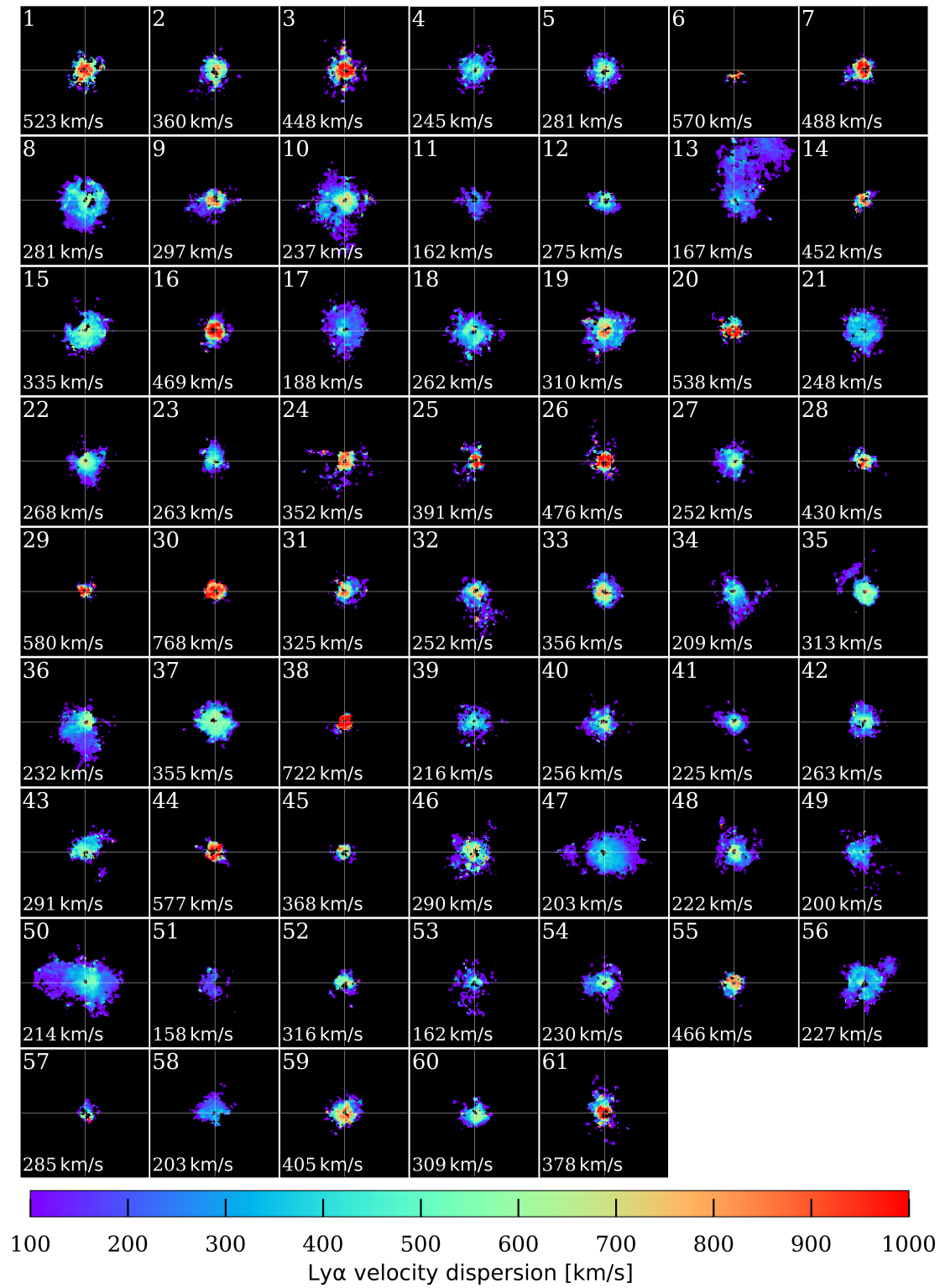
Figure 4.28: Similar to Figure 4.9 but for the QSO MUSEUM bright sample.

Chapter 5

Summary and future outlook

5.1 Summary and main results

In this thesis, I have studied the cool $T \sim 10^4$ K gas reservoir of the CGM around $z \sim 3$ massive galaxies with DM halo masses of $M_{\mathrm{DM}} \sim 10^{12}$ M$_\odot$ in Lyα emission. I characterized this emission and compared it with their host galaxy and AGN properties, providing a look into the different powering mechanisms of the extended emission. These studies help us understand the interplay between the physical mechanisms of the CGM with the observed quasars and link them with galaxy evolution and AGN feedback.

In Chapter 2 I have presented the analysis tools developed to reveal extended line emission around quasars, with a documentation on how these can be used for future studies. The Python scripts described in this chapter were written by me and will be made publicly available with a future publication (González Lobos et al. in prep.).

In Chapter 3 I carried out a VLT/MUSE pilot study to unveil the extended Lyα emission around five massive submillimeter galaxies (SMGs) with known systemic redshifts ($z \sim 3 - 4$) and increasing degrees of quasar radiation: two SMGs, two SMGs hosting a quasar, and one SMG hosting a quasar with an SMG companion (QSO+SMG). These systems are predicted to reside in similar dark matter halos $M_{\mathrm{DM}} \sim 10^{12}$ M$_\odot$, therefore expected to contain similar gas distributions. Additionally, I used ancillary observations to derive their host galaxy properties such as SFR and dust masses and link them to the mechanisms powering Lyα nebulae and their CGM, something that previous studies did not focus on. For this, I quantified the luminosities, extent and kinematics of the nebulae and discussed four possible Lyα powering mechanisms: photoionization from AGN or star formation followed by recombination, shocks due to galactic and/or AGN outflows, gravitational cooling radiation, and Lyα photon resonant scattering. The observations revealed a variety of Lyα luminosities and extents, with the QSO+SMG system displaying the brightest and largest nebula (~ 70 kpc size), followed by the two SMGs hosting quasars ~ 20 kpc and finally we report no detection of extended Lyα emission around the two SMGs. This diversity and the fact that these galaxies are expected to reside in similar halos suggest that gravitational cooling is unlikely to be the main powering mechanism of extended Lyα

nebulae, instead AGN presence is necessary to produce such emission. In that case, the AGN can illuminate the surrounding gas distribution producing Lyα emission due to photoionization followed by recombination in optically thin gas. I report that in order to produce the observed Lyα SB level in a photoionization scenario, it is required that the gas densities are of $> 0.5\,\mathrm{cm}^{-3}$. Additionally, I compared the SFR rates of the five systems with their Lyα emission and found that, assuming that all Lyα emission is produced by photoionization due to star formation, the SMGs should have enough star formation to power detectable nebulae. This finding suggests that UV photons from star formation in these SMGs are not able to escape to CGM scales, likely due to their high dust contents. Moreover, I found that the nebulae presented large Lyα linewidths (FWHM$\gtrsim$ 1200) and evidence of outflows in the QSO+SMG system, suggesting that shocks due to AGN winds/outflows also play a role in powering the nebulae. Finally, I present tentative evidence that the observed Lyα nebular luminosities scale with the quasar's budget of Lyα photons and could be modulated by the dust content of the host galaxy, highlighting that resonant scattering of Lyα photons could also contribute to power the observed nebulae. This study highlighted that AGN presence is essential to produce detectable extended Lyα nebulae and offered a discussion on the importance of linking the CGM properties of quasars with their hosts.

In Chapter 4 I presented the largest VLT/MUSE effort to date to unveil the extended CGM Lyα emission around 120 quasars at the peak of cosmic AGN activity ($z \sim 3$). Particularly, this study extends to fainter magnitudes than previously studied ($-27 < M_i(z = 2) < -24$) and covers the full luminosity range of $z \sim 3$ SDSS quasars. I report the detection of 110 Lyα nebulae and characterize their luminosities, spectra, spatial extent, morphologies and kinematics. Furthermore, I investigated the link between these and their quasar properties, such as peak Lyα luminosity density, bolometric luminosity, black hole mass and Eddington ratios. The nebulae display a variety of luminosities and extents with direct evidence that the nebulae Lyα SB scale with the quasar peak Lyα luminosity density and bolometric luminosity. Moreover, the non detections are all at the low bolometric luminosity end of our survey and their stacking revealed extended Lyα emission, which is below our individual detection limit. Additionally, the morphologies are varied and the nebulae tend to be round and asymmetrical, specifically low luminosity nebulae appear to be more lopsided. This finding could suggest that geometric effects of the systems can suppress the Lyα signal below our detection levels, such as quasar opening angle, viewing orientation, and dust or molecular content. Moreover, I construct velocity dispersion radial profiles and further reveal that brighter quasars show increased central velocity dispersions, suggesting that AGN activity and feedback modulate the detected Lyα emission. I discuss the aforementioned extended Lyα powering mechanisms and highlight that a combination of photionization followed by recombination, resonant scattering of Lyα photons and AGN outflows could contribute to produce the detected SB level. Particularly, I highlighted the possibility that faint nebulae reflect smaller quasar opening angles and their emission could be dominated from their inner CGM or ISM photoionization. In this case, the dimmer quasars display less efficient feedback, which in turn decreases the amount of Lyα photons to escape. Additionally, their small ionization cones do not significantly

enhance the photoionization of the surrounding gas distribution, which instead could be preferentially illuminated by the UVB. Moreover, we test whether the observed kinematics are a product of gravitational motions and show that these instead appear to be linked to AGN activity. I suggest that we require radiative transfer simulations of $z \sim 3$ halos hosting quasars in order to carefully interpret the observed kinematics of the nebula. Finally, further search for additional line emission in these systems (e.g., He II and C IV) could test the link between the observed Lyα nebulae and AGN feedback.

5.2 Future perspectives

This thesis identifies current open questions in the study of the CGM of quasars and its link to galaxy evolution and AGN feedback: at which scale does each powering mechanism participate in producing extended Lyα emission? How is Lyα emission linked to AGN feedback? Is it possible to detect the signal from gravitational cooling? What is the role of host galaxy properties and environment in shaping the observed CGM around quasars?

To address these questions I propose to exploit the sensitivities reached by the current dataset and to gather further observations of massive galaxies without AGN radiation.

5.2.1 Detecting the Lyα gravitational cooling radiation around massive galaxies

The results from this thesis highlighted that the observed CGM emission scales with the quasar radiation, therefore the depth of our observations is biased towards brighter systems. As mentioned in Chapter 1, not all massive halos contain an active galaxy at a given time, however if these trace high cosmic density peaks then they should contain similar massive gas reservoirs. In this case, their extended Lyα emission could be produced due to cooling flows expected at these halo spec and/or UV photons from their interstellar medium. Candidate systems that could test this scenario are SMGs (Smail et al., 1997; Blain et al., 1999), which are expected to reside in similar dark matter halos as quasars (Chapter 3). In the case of isolated SMGs, there is no quasar photoionization and their CGM emission could instead arise from gravitational cooling and the few UV photons that escape these dusty systems.

I have proposed MUSE observations of 24 SMGs at $3 < z < 4.8$ selected from recent spectroscopic [C II] and CO emission surveys (**?**Birkin et al., 2021; **?**). Together with the SMG observations presented in Chapter 3, these 26 systems are the smallest ensemble of SMGs that would allow to detect extended Lyα emission from gravitational cooling through stacking of the datacubes at their systemic redshifts. If detected, the Lyα signal from gravitational cooling at these high halo masses should scale linearly with the halo mass (Figure 3 in Dijkstra and Loeb 2009, see also Faucher-Giguère et al. 2010). In that framework, I expect the Lyα cooling signal to be at a SB$(1 + z)^4 = 9 \times 10^{-15}\,\mathrm{erg\,s^{-1}\,cm^{-2}\,arcsec^{-2}}$ at $100\,\mathrm{ckpc}$ (Figure 5.1). This should be detected at 5σ significance through averaging the pseudo-NBs and datacubes, such measurement can provide a novel estimate of the DM
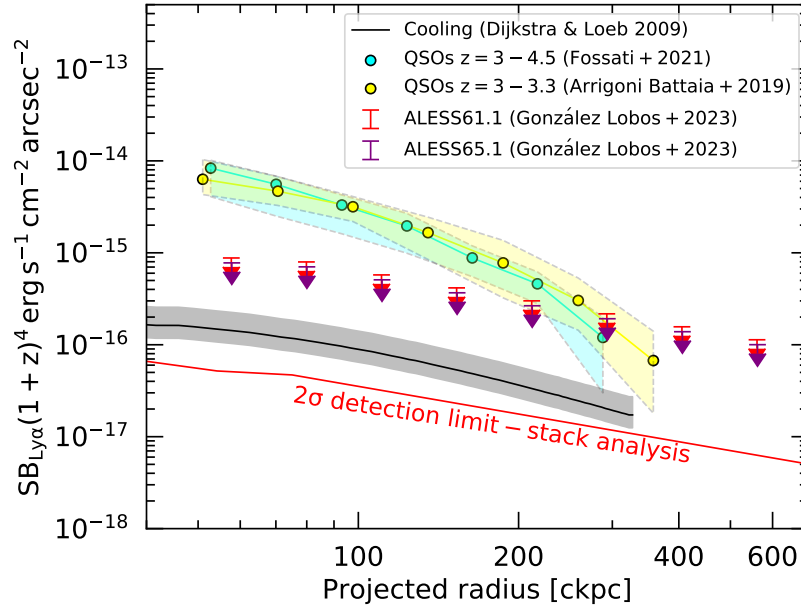
Figure 5.1: Upper limits of the Lyα SB corrected by cosmological dimming as a function of projected comoving distance of the two SMGs from González Lobos et al. (2023). For comparison, the median profiles of Lyα nebulae around quasars at similar redshift from Fossati et al. (2021) and Arrigoni Battaia et al. (2019a) are shown with cyan and yellow circles and shaded region indicating their 25th to 85th percentiles. The black line indicates the predicted Lyα SB signal from cooling radiation (Dijkstra and Loeb, 2009) computed assuming the redshifts and halo mass of the targeted SMGs, with the shaded region indicating the uncertainty of the halo mass estimate. The red line indicates the 2σ detection limit obtained from stacking the targeted SMGs.

halo masses of SMGs and the detection of their CGM cooling radiation. Additionally, the cool gas reservoirs of such massive systems is expected to trace gravitational motions, and therefore halo mass, which would produce an increase of the velocity dispersion of the gas towards the center of these systems (de Beer et al., 2023). Finally, this dataset would also allow to compare the host galaxy properties to the average gas reservoir and halo mass of SMGs.

5.2.2   Detection of additional line emissions in the CGM of $z \sim 3$ quasars

The statistical value of the QSO MUSEUM III survey (Chapter 4) allows me to reach SB limits within 30 Å pseudo-NBs of $2 \times 10^{-17}\,\mathrm{erg\,s^{-1}\,cm^{-2}\,arcsec^{-2}}$ by stacking the complete sample. Therefore, this should allow the detection of fainter line emissions such as He II and C IV expected in the CGM of quasars (see Chapter 1). Indeed,Guo et al. (2018) pre-
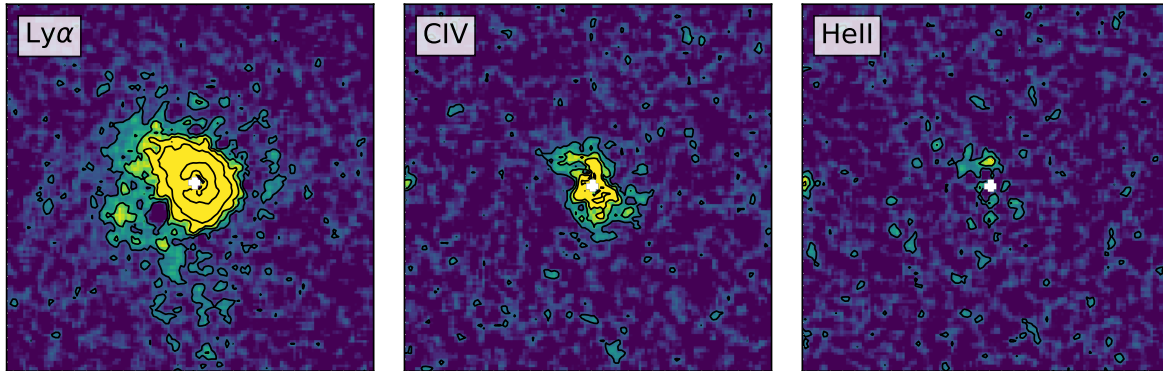
Figure 5.2: Signal to noise maps of Lyα, C IV and He II of ID 10 of the QSO MUSEUM III survey. The maps have sizes of about $20'' \times 20''$ and are constructed from pseudo-NB centered at the expected wavelength of the lines given the redshift of the nebular Lyα emission ($z = 3.245$). The black contours indicate S/N levels of 2, 4, 6, 10 and 30.

sented a compilation of $z \sim 3$ quasars observed with MUSE and revealed systems with individual detections of C IV and He II which have been already observed as part of the QSO MUSEUM survey (ID 10, 47 and 50). Moreover, Fossati et al. (2021) presented a deep MUSE survey of 27 bright quasars and detected extended C IV emission through stacking, indicating that the CGM of $z \sim 3$ quasars is enriched with metals. A similar case should be expected for the QSO MUSEUM III, therefore I plan to carry out such study and test the origin of the Lyα emission in the AGN outflow scenario discussed in Chapter 4. I expect that, if brighter nebulae are correlated with stronger AGN radiation and possibly feedback, then brighter quasars should display stronger emission from shocks and increased CGM metallicity. This measurement can be directly obtained by detecting these additional line emissions by stacking. Additionally, a detection of extended He II can provide information on the ionization cones of the quasars and constrain the photoionization scenario by comparing with the Lyα emission.

I have re-analyzed the QSO MUSEUM survey in Chapter 4 and now search for extended line emission such as the one reported in Guo et al. (2018). Figure **??** shows signal-to-noise (S/N) maps of pseudo-NBs constructed at the redshift of the nebular Lyα emission of ID 10 ($z = 3.245$) at the expected wavelengths of Lyα, C IV and He II. The narrow band widths are chosen to reflect the velocity range of the Lyα 30 Å pseudo-NB used for the analysis in Chapter 4. The black contours indicate S/N of 2, 4, 6, 10 and 30. This figure shows that the analysis and dataset presented in this thesis can be exploited to detect additional line emission which will help me further constrain the CGM of high redshift quasars.

Bibliography

Abdurro'uf, Katherine et al., Conny Aerts, et al. The Seventeenth Data Release of the Sloan Digital Sky Surveys: Complete Release of MaNGA, MaStar, and APOGEE-2 Data. *ApJS*, 259(2):35, April 2022. doi: 10.3847/1538-4365/ac4414.

Mark G. Allen, Brent A. Groves, Michael A. Dopita, et al. The MAPPINGS III Library of Fast Radiative Shock Models. *ApJS*, 178(1):20–55, September 2008. doi: 10.1086/589652.

Andrés Almeida, Scott F. Anderson, Maria Argudo-Fernández, et al. The Eighteenth Data Release of the Sloan Digital Sky Surveys: Targeting and First Spectra from SDSS-V. *ApJS*, 267(2):44, August 2023. doi: 10.3847/1538-4365/acda98.

Daniel Anglés-Alcázar, Claude-André Faucher-Giguère, Dušan Kereš, et al. The cosmic baryon cycle and galaxy mass assembly in the FIRE simulations. *MNRAS*, 470(4): 4698–4719, October 2017. doi: 10.1093/mnras/stx1517.

F. Arrigoni Battaia, A. Obreja, C. C. Chen, et al. JCMT/SCUBA-2 uncovers an excess of 850 μm counts on megaparsec scales around high-redshift quasars. Characterization of the overdensities and their alignment with the quasars' Lyα nebulae. *Astronomy & Astrophysics*, 676:A51, August 2023a. doi: 10.1051/0004-6361/202245520.

Fabrizio Arrigoni Battaia, Joseph F. Hennawi, J. Xavier Prochaska, and Sebastiano Cantalupo. Deep He II and C IV Spectroscopy of a Giant Lyα Nebula: Dense Compact Gas Clumps in the Circumgalactic Medium of a z ~2 Quasar. *ApJ*, 809(2):163, August 2015a. doi: 10.1088/0004-637X/809/2/163.

Fabrizio Arrigoni Battaia, Yujin Yang, Joseph F. Hennawi, et al. A Deep Narrowband Imaging Search for C IV and He II Emission from Lyα Blobs. *ApJ*, 804(1):26, May 2015b. doi: 10.1088/0004-637X/804/1/26.

Fabrizio Arrigoni Battaia, Joseph F. Hennawi, Sebastiano Cantalupo, and J. Xavier Prochaska. The Stacked LYα Emission Profile from the Circum-Galactic Medium of z $\sim$ 2 Quasars. *ApJ*, 829(1):3, September 2016. doi: 10.3847/0004-637X/829/1/3.

Fabrizio Arrigoni Battaia, J. Xavier Prochaska, Joseph F. Hennawi, et al. Inspiraling halo accretion mapped in Ly α emission around a z $\sim$ 3 quasar. *MNRAS*, 473(3):3907–3940, January 2018. doi: 10.1093/mnras/stx2465.

Fabrizio Arrigoni Battaia, Joseph F. Hennawi, J. Xavier Prochaska, et al. QSO MUSEUM I: a sample of 61 extended Ly α-emission nebulae surrounding z $\sim$ 3 quasars. *MNRAS*, 482(3):3162–3205, jan 2019a. doi: 10.1093/mnras/sty2827.

Fabrizio Arrigoni Battaia, A. Obreja, J. X. Prochaska, et al. Discovery of intergalactic bridges connecting two faint z $\sim$ 3 quasars. *A&A*, 631:A18, nov 2019b. doi: 10.1051/0004-6361/201936211.

Fabrizio Arrigoni Battaia, Chian-Chou Chen, Hau-Yu Baobab Liu, et al. A Multiwavelength Study of ELAN Environments (AMUSE^2). Mass Budget, Satellites Spin Alignment, and Gas Infall in a Massive z 3 Quasar Host Halo. *ApJ*, 930(1):72, May 2022. doi: 10.3847/1538-4357/ac5a4d.

Fabrizio Arrigoni Battaia, Aura Obreja, Tiago Costa, et al. The Luminosity-Area Relation of z ¿ 2 Quasars' Lyα Nebulae. *ApJ*, 952(1):L24, July 2023b. doi: 10.3847/2041-8213/ace42b.

Astropy Collaboration, T. P. Robitaille, E. J. Tollerud, et al. Astropy: A community Python package for astronomy. *A&A*, 558:A33, October 2013. doi: 10.1051/0004-6361/201322068.

Astropy Collaboration, A. M. Price-Whelan, B. M. Sipőcz, et al. The Astropy Project: Building an Open-science Project and Status of the v2.0 Core Package. *AJ*, 156(3):123, September 2018. doi: 10.3847/1538-3881/aabc4f.

Astropy Collaboration, Adrian M. Price-Whelan, Pey Lian Lim, et al. The Astropy Project: Sustaining and Growing a Community-oriented Open-source Project and the Latest Major Release (v5.0) of the Core Package. *ApJ*, 935(2):167, August 2022. doi: 10.3847/1538-4357/ac7c74.

R. Bacon, M. Accardo, L. Adjali, et al. The MUSE second-generation VLT instrument. In Ian S. McLean, Suzanne K. Ramsay, and Hideki Takami, editors, *Ground-based and Airborne Instrumentation for Astronomy III*, volume 7735 of *Society of Photo-Optical Instrumentation Engineers (SPIE) Conference Series*, page 773508, July 2010. doi: 10.1117/12.856027.

R. Bacon, J. Brinchmann, J. Richard, et al. The MUSE 3D view of the Hubble Deep Field South. *Astronomy & Astrophysics*, 575:A75, March 2015. doi: 10.1051/0004-6361/201425419.

R. Bacon, D. Mary, T. Garel, et al. The MUSE Extremely Deep Field: The cosmic web in emission at high redshift. *Astronomy & Astrophysics*, 647:A107, March 2021. doi: 10.1051/0004-6361/202039887.

Roland Bacon, Laure Piqueras, Simon Conseil, et al. MPDAF: MUSE Python Data Analysis Framework. Astrophysics Source Code Library, record ascl:1611.003, November 2016.

A. J. Benson, R. G. Bower, C. S. Frenk, et al. What Shapes the Luminosity Function of Galaxies? *ApJ*, 599(1):38–49, December 2003. doi: 10.1086/379160.

J. Bergeron and P. Boissé. A sample of galaxies giving rise to Mg II quasar absorption systems. *A&A*, 243:344, March 1991.

Serena Bertone and Joop Schaye. Rest-frame ultraviolet line emission from the intergalactic medium at $2 \leq z \leq 5$. *MNRAS*, 419(1):780–798, January 2012. doi: 10.1111/j.1365-2966.2011.19742.x.

James Binney. On the origin of the galaxy luminosity function. *MNRAS*, 347(4):1093–1096, February 2004. doi: 10.1111/j.1365-2966.2004.07277.x.

Jack E. Birkin, Axel Weiss, J. L. Wardlow, et al. An ALMA/NOEMA survey of the molecular gas properties of high-redshift star-forming galaxies. *MNRAS*, 501(3):3926–3950, March 2021. doi: 10.1093/mnras/staa3862.

M. Bischetti, C. Feruglio, E. Piconcelli, et al. The WISSH quasars project. IX. Cold gas content and environment of luminous QSOs at $z \sim 2.4$-4.7. *Astronomy & Astrophysics*, 645:A33, January 2021. doi: 10.1051/0004-6361/202039057.

A. W. Blain, Ian Smail, R. J. Ivison, and J. P. Kneib. The history of star formation in dusty galaxies. *MNRAS*, 302(4):632–648, February 1999. doi: 10.1046/j.1365-8711.1999.02178.x.

Jérémy Blaizot, Thibault Garel, Anne Verhamme, et al. Simulating the diversity of shapes of the Lyman-α line. *MNRAS*, 523(3):3749–3772, August 2023. doi: 10.1093/mnras/stad1523.

Michael R. Blanton and John Moustakas. Physical Properties and Environments of Nearby Galaxies. *ARA&A*, 47(1):159–210, September 2009. doi: 10.1146/annurev-astro-082708-101734.

Michael R. Blanton, David W. Hogg, Neta A. Bahcall, et al. The Galaxy Luminosity Function and Luminosity Density at Redshift $z = 0.1$. *ApJ*, 592(2):819–838, August 2003. doi: 10.1086/375776.

G. R. Blumenthal, H. Pagels, and J. R. Primack. Galaxy formation by dissipationless particles heavier than neutrinos. *Nature*, 299(5878):37–38, September 1982. doi: 10.1038/299037a0.

T. Böker, S. Arribas, N. Lützgendorf, et al. The Near-Infrared Spectrograph (NIRSpec) on the James Webb Space Telescope. III. Integral-field spectroscopy. *Astronomy & Astrophysics*, 661:A82, May 2022. doi: 10.1051/0004-6361/202142589.

Alberto D. Bolatto, Mark Wolfire, and Adam K. Leroy. The CO-to-H_2 Conversion Factor. *ARA&A*, 51(1):207–268, August 2013. doi: 10.1146/annurev-astro-082812-140944.

J. Richard Bond, Lev Kofman, and Dmitry Pogosyan. How filaments of galaxies are woven into the cosmic web. *Nature*, 380(6575):603–606, April 1996. doi: 10.1038/380603a0.

Elena Borisova, Sebastiano Cantalupo, Simon J. Lilly, et al. Ubiquitous Giant Lyα Nebulae around the Brightest Quasars at z $\sim$ 3.5 Revealed with MUSE. *ApJ*, 831(1):39, November 2016. doi: 10.3847/0004-637X/831/1/39.

N. Bouché, W. Hohensee, R. Vargas, et al. Physical properties of galactic winds using background quasars. *MNRAS*, 426(2):801–815, October 2012. doi: 10.1111/j.1365-2966. 2012.21114.x.

Robert W. Boyd. The wavelength dependence of seeing. *J. Opt. Soc. Am.*, 68(7):877–883, Jul 1978. doi: 10.1364/JOSA.68.000877. URL https://opg.optica.org/abstract. cfm?URI=josa-68-7-877.

Larry Bradley, Brigitta Sipőcz, Thomas Robitaille, et al. astropy/photutils: 1.12.0, April 2024. URL https://doi.org/10.5281/zenodo.10967176.

Zheng Cai, Erika Hamden, Matt Matuszewski, et al. Keck/Palomar Cosmic Web Imagers Reveal an Enormous Lyα Nebula in an Extremely Overdense Quasi-stellar Object Pair Field at z = 2.45. *ApJ*, 861(1):L3, July 2018. doi: 10.3847/2041-8213/aacce6.

Zheng Cai, Sebastiano Cantalupo, J. Xavier Prochaska, et al. Evolution of the Cool Gas in the Circumgalactic Medium of Massive Halos: A Keck Cosmic Web Imager Survey of Lyα Emission around QSOs at z $\approx$ 2. *ApJS*, 245(2):23, December 2019. doi: 10.3847/1538-4365/ab4796.

Sebastiano Cantalupo, Cristiano Porciani, Simon J. Lilly, and Francesco Miniati. Fluorescent Lyα Emission from the High-Redshift Intergalactic Medium. *ApJ*, 628(1):61–75, July 2005. doi: 10.1086/430758.

Sebastiano Cantalupo, Fabrizio Arrigoni-Battaia, J. Xavier Prochaska, et al. A cosmic web filament revealed in Lyman-α emission around a luminous high-redshift quasar. *Nature*, 506(7486):63–66, February 2014. doi: 10.1038/nature12898.

Sebastiano Cantalupo, Gabriele Pezzulli, Simon J. Lilly, et al. The large- and small-scale properties of the intergalactic gas in the Slug Ly α nebula revealed by MUSE He II emission observations. *MNRAS*, 483(4):5188–5204, March 2019. doi: 10.1093/mnras/ sty3481.

C. L. Carilli, D. Riechers, F. Walter, et al. The Anatomy of an Extreme Starburst within 1.3 Gyr of the Big Bang Revealed by ALMA. *ApJ*, 763(2):120, February 2013. doi: 10.1088/0004-637X/763/2/120.

Caitlin M. Casey, Desika Narayanan, and Asantha Cooray. Dusty star-forming galaxies at high redshift. *Phys. Rep.*, 541(2):45–161, August 2014. doi: 10.1016/j.physrep.2014.02. 009.

Renyue Cen and Zheng Zheng. The Nature of Lyα Blobs: Powered by Extreme Starbursts. *ApJ*, 775(2):112, October 2013. doi: 10.1088/0004-637X/775/2/112.

Gilles Chabrier. Galactic Stellar and Substellar Initial Mass Function. *PASP*, 115(809): 763–795, July 2003. doi: 10.1086/376392.

Seok-Jun Chang, Yujin Yang, Kwang-Il Seon, et al. Radiative Transfer in Lyα Nebulae. I. Modeling a Continuous or Clumpy Spherical Halo with a Central Source. *ApJ*, 945(2): 100, March 2023. doi: 10.3847/1538-4357/acac98.

Chian-Chou Chen, J. A. Hodge, Ian Smail, et al. A Spatially Resolved Study of Cold Dust, Molecular Gas, H II Regions, and Stars in the z = 2.12 Submillimeter Galaxy ALESS67.1. *ApJ*, 846(2):108, September 2017. doi: 10.3847/1538-4357/aa863a.

Chian-Chou Chen, Fabrizio Arrigoni Battaia, Bjorn H. C. Emonts, et al. A Multiwavelength Study of ELAN Environments (AMUSE^2). Detection of a Dusty Star-forming Galaxy within the Enormous Lyα Nebula at z=2.3 Sheds Light on its Origin. *ApJ*, 923 (2):200, December 2021. doi: 10.3847/1538-4357/ac2b9d.

Hsiao-Wen Chen, Jennifer E. Helsby, Jean-René Gauthier, et al. An Empirical Characterization of Extended Cool Gas Around Galaxies Using Mg II Absorption Features. *ApJ*, 714(2):1521–1541, May 2010. doi: 10.1088/0004-637X/714/2/1521.

L. Christensen, K. Jahnke, L. Wisotzki, and S. F. Sánchez. Extended Lyman-α emission around bright quasars. *Astronomy & Astrophysics*, 459(3):717–729, December 2006. doi: 10.1051/0004-6361:20065318.

Luca Ciotti and Jeremiah P. Ostriker. Cooling Flows and Quasars: Different Aspects of the Same Phenomenon? I. Concepts. *ApJ*, 487(2):L105–L108, October 1997. doi: 10.1086/310902.

M. Colless. First results from the 2dF Galaxy Redshift Survey. *Philosophical Transactions of the Royal Society of London Series A*, 357(1750):105, January 1999. doi: 10.1098/rsta.1999.0317.

Matthew Colless, Gavin Dalton, Steve Maddox, et al. The 2dF Galaxy Redshift Survey: spectra and redshifts. *MNRAS*, 328(4):1039–1063, December 2001. doi: 10.1046/j.1365-8711.2001.04902.x.

Tiago Costa. The host dark matter haloes of the first quasars. *MNRAS*, 531(1):930–944, June 2024. doi: 10.1093/mnras/stae1157.

Tiago Costa, Debora Sijacki, and Martin G. Haehnelt. Feedback from active galactic nuclei: energy- versus momentum-driving. *MNRAS*, 444(3):2355–2376, November 2014. doi: 10.1093/mnras/stu1632.

Tiago Costa, Joakim Rosdahl, Debora Sijacki, and Martin G. Haehnelt. Quenching star formation with quasar outflows launched by trapped IR radiation. *MNRAS*, 479(2): 2079–2111, September 2018. doi: 10.1093/mnras/sty1514.

Tiago Costa, Fabrizio Arrigoni Battaia, Emanuele P. Farina, et al. AGN-driven outflows and the formation of Lyα nebulae around high-z quasars. *MNRAS*, 517(2):1767–1790, December 2022. doi: 10.1093/mnras/stac2432.

Scott M. Croom, B. J. Boyle, T. Shanks, et al. The 2dF QSO Redshift Survey - XIV. Structure and evolution from the two-point correlation function. *MNRAS*, 356(2):415–438, January 2005. doi: 10.1111/j.1365-2966.2004.08379.x.

Darren J. Croton, Volker Springel, Simon D. M. White, et al. The many lives of active galactic nuclei: cooling flows, black holes and the luminosities and colours of galaxies. *MNRAS*, 365(1):11–28, January 2006. doi: 10.1111/j.1365-2966.2005.09675.x.

Rebecca L. Davies, Mischa Schirmer, and James E. H. Turner. The 'Green Bean' Galaxy SDSS J224024.1-092748: unravelling the emission signature of a quasar ionization echo. *MNRAS*, 449(2):1731–1752, May 2015. doi: 10.1093/mnras/stv343.

S. de Beer, S. Cantalupo, A. Travascio, et al. Resolving the physics of quasar Ly α nebulae (RePhyNe): I. Constraining quasar host halo masses through circumgalactic medium kinematics. *MNRAS*, 526(2):1850–1873, December 2023. doi: 10.1093/mnras/stad2682.

R. Decarli, F. Walter, B. P. Venemans, et al. Rapidly star-forming galaxies adjacent to quasars at redshifts exceeding 6. *Nature*, 545(7655):457–461, May 2017. doi: 10.1038/ nature22358.

Roberto Decarli, Massimo Dotti, Eduardo Bañados, et al. ALMA and HST Kiloparsec-scale Imaging of a Quasar-galaxy Merger at Z $\approx$ 6.2. *ApJ*, 880(2):157, August 2019. doi: 10.3847/1538-4357/ab297f.

Davide Decataldo, Sijing Shen, Lucio Mayer, et al. The origin of cold gas in the circumgalactic medium. *Astronomy & Astrophysics*, 685:A8, May 2024. doi: 10.1051/ 0004-6361/202346972.

A. Dekel and J. Silk. The Origin of Dwarf Galaxies, Cold Dark Matter, and Biased Galaxy Formation. *ApJ*, 303:39, April 1986. doi: 10.1086/164050.

Avishai Dekel and Yuval Birnboim. Galaxy bimodality due to cold flows and shock heating. *MNRAS*, 368(1):2–20, May 2006. doi: 10.1111/j.1365-2966.2006.10145.x.

Luca Di Mascolo, Alexandro Saro, Tony Mroczkowski, et al. Forming intracluster gas in a galaxy protocluster at a redshift of 2.16. *Nature*, 615(7954):809–812, March 2023. doi: 10.1038/s41586-023-05761-x.

Tiziana Di Matteo, Volker Springel, and Lars Hernquist. Energy input from quasars regulates the growth and activity of black holes and their host galaxies. *Nature*, 433(7026): 604–607, February 2005. doi: 10.1038/nature03335.

Mark Dijkstra. Physics of Lyα Radiative Transfer. *Saas-Fee Advanced Course*, 46:1, January 2019. doi: 10.1007/978-3-662-59623-4_1.

Mark Dijkstra and Abraham Loeb. Lyα-driven outflows around star-forming galaxies. *MNRAS*, 391(1):457–466, November 2008. doi: 10.1111/j.1365-2966.2008.13920.x.

Mark Dijkstra and Abraham Loeb. Lyα blobs as an observational signature of cold accretion streams into galaxies. *MNRAS*, 400(2):1109–1120, December 2009. doi: 10.1111/j.1365-2966.2009.15533.x.

Mark Dijkstra, Zoltán Haiman, and Marco Spaans. Lyα Radiation from Collapsing Protogalaxies. II. Observational Evidence for Gas Infall. *ApJ*, 649(1):37–47, September 2006. doi: 10.1086/506244.

Bruce T. Draine. *Physics of the Interstellar and Intergalactic Medium*. 2011.

A. B. Drake, F. Walter, M. Novak, et al. The Ionized- and Cool-gas Content of the BR1202-0725 System as Seen by MUSE and ALMA. *ApJ*, 902(1):37, October 2020. doi: 10.3847/1538-4357/aba832.

Alyssa B. Drake, Emanuele Paolo Farina, Marcel Neeleman, et al. Lyα Halos around z $\sim$ 6 Quasars. *ApJ*, 881(2):131, August 2019. doi: 10.3847/1538-4357/ab2984.

Aaron A. Dutton and Andrea V. Macciò. Cold dark matter haloes in the Planck era: evolution of structural parameters for Einasto and NFW profiles. *MNRAS*, 441(4):3359–3374, July 2014. doi: 10.1093/mnras/stu742.

A. S. Eddington. *The Internal Constitution of the Stars*. 1926.

Arthur Stanley Eddington and Heinrich Vogt. 46. the mass-luminosity relation for stars on the relation between the masses and luminosities of the stars. *Monthly Notices of the Royal Astronomical Society*, 84:308–332, 1924.

G. Efstathiou and M. J. Rees. High-redshift quasars in the Cold Dark Matter cosmogony. *MNRAS*, 230:5p–11p, February 1988. doi: 10.1093/mnras/230.1.5P.

Sarah Eftekharzadeh, Adam D. Myers, Martin White, et al. Clustering of intermediate redshift quasars using the final SDSS III-BOSS sample. *MNRAS*, 453(3):2779–2798, November 2015. doi: 10.1093/mnras/stv1763.

Anna-Christina Eilers, Frederick B. Davies, Joseph F. Hennawi, et al. Implications of z $\sim$ 6 Quasar Proximity Zones for the Epoch of Reionization and Quasar Lifetimes. *ApJ*, 840(1):24, May 2017. doi: 10.3847/1538-4357/aa6c60.

B. H. C. Emonts, M. D. Lehnert, M. Villar-Martín, et al. Molecular gas in the halo fuels the growth of a massive cluster galaxy at high redshift. *Science*, 354(6316):1128–1130, December 2016. doi: 10.1126/science.aag0512.

Bjorn H. C. Emonts, Matthew D. Lehnert, Ilsang Yoon, et al. A cosmic stream of atomic carbon gas connected to a massive radio galaxy at redshift 3.8. *Science*, 379(6639): 1323–1326, March 2023. doi: 10.1126/science.abh2150.

A. C. Fabian. Observational Evidence of Active Galactic Nuclei Feedback. *ARA&A*, 50: 455–489, September 2012. doi: 10.1146/annurev-astro-081811-125521.

Xiaohui Fan, Joseph F. Hennawi, Gordon T. Richards, et al. A Survey of z¿5.7 Quasars in the Sloan Digital Sky Survey. III. Discovery of Five Additional Quasars. *AJ*, 128(2): 515–522, August 2004. doi: 10.1086/422434.

E. P. Farina, R. Falomo, R. Decarli, et al. On the cool gaseous haloes of quasars. *MNRAS*, 429(2):1267–1277, February 2013. doi: 10.1093/mnras/sts410.

E. P. Farina, R. Falomo, R. Scarpa, et al. The extent of the Mg II absorbing circumgalactic medium of quasars. *MNRAS*, 441(1):886–899, June 2014. doi: 10.1093/mnras/stu585.

Emanuele P. Farina, Bram P. Venemans, Roberto Decarli, et al. Mapping the Lyα Emission around a z $\sim$ 6.6 QSO with MUSE: Extended Emission and a Companion at a Close Separation. *ApJ*, 848(2):78, October 2017. doi: 10.3847/1538-4357/aa8df4.

Emanuele Paolo Farina, Fabrizio Arrigoni-Battaia, Tiago Costa, et al. The REQUIEM Survey. I. A Search for Extended Lyα Nebular Emission Around 31 z ¿ 5.7 Quasars. *ApJ*, 887(2):196, December 2019. doi: 10.3847/1538-4357/ab5847.

Claude-André Faucher-Giguère and S. Peng Oh. Key Physical Processes in the Circumgalactic Medium. *ARA&A*, 61:131–195, August 2023a. doi: 10.1146/ annurev-astro-052920-125203.

Claude-André Faucher-Giguère and S. Peng Oh. Key Physical Processes in the Circumgalactic Medium. *ARA&A*, 61:131–195, August 2023b. doi: 10.1146/ annurev-astro-052920-125203.

Claude-André Faucher-Giguère, Dušan Kereš, Mark Dijkstra, et al. Lyα Cooling Emission from Galaxy Formation. *ApJ*, 725(1):633–657, December 2010. doi: 10.1088/0004-637X/ 725/1/633.

F. Fiore, C. Feruglio, F. Shankar, et al. AGN wind scaling relations and the co-evolution of black holes and galaxies. *Astronomy & Astrophysics*, 601:A143, May 2017. doi: 10.1051/0004-6361/201629478.

Daniel Foreman-Mackey, David W. Hogg, Dustin Lang, and Jonathan Goodman. emcee: The MCMC Hammer. *PASP*, 125(925):306, March 2013. doi: 10.1086/670067.

M. Fossati, M. Fumagalli, E. K. Lofthouse, et al. MUSE analysis of gas around galaxies (MAGG) - III. The gas and galaxy environment of z = 3-4.5 quasars. *MNRAS*, 503(2): 3044–3064, May 2021. doi: 10.1093/mnras/stab660.

Hai Fu, Jacob Isbell, Caitlin M. Casey, et al. The Circumgalactic Medium of Submillimeter Galaxies. II. Unobscured QSOs within Dusty Starbursts and QSO Sightlines with Impact Parameters below 100 kpc. *ApJ*, 844(2):123, August 2017. doi: 10.3847/1538-4357/aa7c63.

Steven R. Furlanetto, Joop Schaye, Volker Springel, and Lars Hernquist. Lyα Emission from Structure Formation. *ApJ*, 622(1):7–27, March 2005. doi: 10.1086/426808.

T. Fusco, R. Bacon, S. Kamann, et al. Reconstruction of the ground-layer adaptive-optics point spread function for MUSE wide field mode observations. *Astronomy & Astrophysics*, 635:A208, March 2020. doi: 10.1051/0004-6361/202037595.

Cristina García-Vergara, Jacqueline Hodge, Joseph F. Hennawi, et al. The Clustering of Submillimeter Galaxies Detected with ALMA. *ApJ*, 904(1):2, November 2020. doi: 10.3847/1538-4357/abbdfe.

Jonathan P. Gardner, John C. Mather, Mark Clampin, et al. The James Webb Space Telescope. *Space Sci. Rev.*, 123(4):485–606, April 2006. doi: 10.1007/s11214-006-8315-7.

Massimo Gaspari, D Eckert, STEFANO Ettori, et al. The x-ray halo scaling relations of supermassive black holes. *The Astrophysical Journal*, 884(2):169, 2019.

J. E. Geach, D. M. Alexander, B. D. Lehmer, et al. The Chandra Deep Protocluster Survey: Lyα Blobs are Powered by Heating, Not Cooling. *ApJ*, 700(1):1–9, July 2009. doi: 10.1088/0004-637X/700/1/1.

M. Ginolfi, R. Maiolino, S. Carniani, et al. Extended and broad Ly α emission around a BAL quasar at z $\sim$ 5. *MNRAS*, 476(2):2421–2431, May 2018. doi: 10.1093/mnras/sty364.

M. Ginolfi, G. C. Jones, M. Béthermin, et al. The ALPINE-ALMA [C II] survey: Star-formation-driven outflows and circumgalactic enrichment in the early Universe. *A&A*, 633:A90, January 2020. doi: 10.1051/0004-6361/201936872.

A. Ginsburg, T. Robitaille, C. Beaumont, et al. Radio Astronomy Tools in Python: Spectral-cube, pvextractor, and more. In D. Iono, K. Tatematsu, A. Wootten, and L. Testi, editors, *Revolution in Astronomy with ALMA: The Third Year*, volume 499 of *Astronomical Society of the Pacific Conference Series*, pages 363–364, December 2015.

Adam Ginsburg, Brigitta M. Sipőcz, C. E. Brasseur, et al. astroquery: An Astronomical Web-querying Package in Python. *AJ*, 157(3):98, March 2019. doi: 10.3847/1538-3881/aafc33.

Vale González Lobos, Fabrizio Arrigoni Battaia, Seok-Jun Chang, et al. Circumgalactic Lyα emission around submillimeter-bright galaxies with different quasar contributions. *Astronomy & Astrophysics*, 679:A41, November 2023. doi: 10.1051/0004-6361/202346879.

M. Gronke, P. Bull, and M. Dijkstra. A Systematic Study of Lyman-α Transfer through Outflowing Shells: Model Parameter Estimation. *ApJ*, 812(2):123, October 2015. doi: 10.1088/0004-637X/812/2/123.

Max Gronke and Simeon Bird. Giant Lyman-alpha Nebulae in the Illustris Simulation. *ApJ*, 835(2):207, February 2017. doi: 10.3847/1538-4357/835/2/207.

Hengxiao Guo, Yue Shen, and Shu Wang. PyQSOFit: Python code to fit the spectrum of quasars. Astrophysics Source Code Library, record ascl:1809.008, September 2018.

Yucheng Guo, Roberto Maiolino, Linhua Jiang, et al. Metal Enrichment in the Circumgalactic Medium and Lyα Halos around Quasars at z ∼ 3. *ApJ*, 898(1):26, July 2020. doi: 10.3847/1538-4357/ab9b7f.

A. H. Guth and P. J. Steinhardt. The inflationary universe. *Scientific American*, 250:116–128, May 1984. doi: 10.1038/scientificamerican0584-116.

Zoltán Haiman and Martin J. Rees. Extended Lyα Emission around Young Quasars: A Constraint on Galaxy Formation. *ApJ*, 556(1):87–92, July 2001a. doi: 10.1086/321567.

Zoltán Haiman and Martin J. Rees. Extended Lyα Emission around Young Quasars: A Constraint on Galaxy Formation. *ApJ*, 556(1):87–92, July 2001b. doi: 10.1086/321567.

Zoltán Haiman, Marco Spaans, and Eliot Quataert. Lyα Cooling Radiation from High-Redshift Halos. *ApJ*, 537(1):L5–L8, July 2000. doi: 10.1086/312754.

Kevin Hall and Hai Fu. H I Lyα Emission from a Metal-poor Cool Stream Fueling an Early Dusty Starburst. *ApJ*, 969(1):39, July 2024. doi: 10.3847/1538-4357/ad4601.

Matthew Hansen and S. Peng Oh. Lyman α radiative transfer in a multiphase medium. *MNRAS*, 367(3):979–1002, April 2006. doi: 10.1111/j.1365-2966.2005.09870.x.

Charles R. Harris, K. Jarrod Millman, Stéfan J. van der Walt, et al. Array programming with NumPy. *Nature*, 585(7825):357–362, September 2020. doi: 10.1038/s41586-020-2649-2. URL https://doi.org/10.1038/s41586-020-2649-2.

Chris M. Harrison and Cristina Ramos Almeida. Observational Tests of Active Galactic Nuclei Feedback: An Overview of Approaches and Interpretation. *Galaxies*, 12(2):17, April 2024a. doi: 10.3390/galaxies12020017.

Chris M. Harrison and Cristina Ramos Almeida. Observational Tests of Active Galactic Nuclei Feedback: An Overview of Approaches and Interpretation. *Galaxies*, 12(2):17, April 2024b. doi: 10.3390/galaxies12020017.

Matthew Hayes, Claudia Scarlata, and Brian Siana. Central powering of the largest Lyman-α nebula is revealed by polarized radiation. *Nature*, 476(7360):304–307, August 2011. doi: 10.1038/nature10320.

Matthew Hayes, Jens Melinder, Göran Östlin, et al. O vi emission imaging of a galaxy with the hubble space telescope: A warm gas halo surrounding the intense starburst sdss j115630.63+500822.1∗. *The Astrophysical Journal*, 828(1):49, August 2016. ISSN 1538-4357. doi: 10.3847/0004-637x/828/1/49. URL http://dx.doi.org/10.3847/0004-637X/828/1/49.

Timothy M. Heckman, Matthew D. Lehnert, George K. Miley, and Wil van Breugel. Spectroscopy of Spatially Extended Material around High-Redshift Radio-loud Quasars. *ApJ*, 381:373, November 1991a. doi: 10.1086/170660.

Timothy M. Heckman, Matthew D. Lehnert, Wil van Breugel, and George K. Miley. Spatially Resolved Optical Images of High-Redshift Quasi-stellar Objects. *ApJ*, 370:78, March 1991b. doi: 10.1086/169794.

Joseph F. Hennawi and J. Xavier Prochaska. Quasars Probing Quasars. IV. Joint Constraints on the Circumgalactic Medium from Absorption and Emission. *ApJ*, 766(1):58, March 2013. doi: 10.1088/0004-637X/766/1/58.

Joseph F. Hennawi and Jason X. Prochaska. Quasars Probing Quasars. II. The Anisotropic Clustering of Optically Thick Absorbers around Quasars. *ApJ*, 655(2):735–748, February 2007. doi: 10.1086/509770.

Joseph F. Hennawi, J. Xavier Prochaska, Sebastiano Cantalupo, and Fabrizio Arrigoni-Battaia. Quasar quartet embedded in giant nebula reveals rare massive structure in distant universe. *Science*, 348(6236):779–783, May 2015. doi: 10.1126/science.aaa5397.

Edmund Christian Herenz, Matthew Hayes, and Claudia Scarlata. Deciphering the Lyman α blob 1 with deep MUSE observations. *Astronomy & Astrophysics*, 642:A55, October 2020. doi: 10.1051/0004-6361/202037464.

César Hernández-Aguayo, Volker Springel, Rüdiger Pakmor, et al. The MillenniumTNG Project: high-precision predictions for matter clustering and halo statistics. *MNRAS*, 524(2):2556–2578, September 2023. doi: 10.1093/mnras/stad1657.

Eileen Herwig, Fabrizio Arrigoni Battaia, Jay González Lobos, et al. QSO MUSEUM II: Search for extended Lyα emission around 8 $z \sim 3$ quasar pairs. *arXiv e-prints*, art. arXiv:2408.16826, August 2024. doi: 10.48550/arXiv.2408.16826.

J. A. Hodge, D. Riechers, R. Decarli, et al. The Kiloparsec-scale Star Formation Law at Redshift 4: Widespread, Highly Efficient Star Formation in the Dust-obscured Starburst Galaxy GN20. *ApJ*, 798(1):L18, January 2015. doi: 10.1088/2041-8205/798/1/L18.

Philip F. Hopkins, Lars Hernquist, Thomas J. Cox, et al. A Unified, Merger-driven Model of the Origin of Starbursts, Quasars, the Cosmic X-Ray Background, Supermassive Black Holes, and Galaxy Spheroids. *ApJS*, 163(1):1–49, March 2006. doi: 10.1086/499298.

Esther M. Hu and Lennox L. Cowie. The Distribution of Gas and Galaxies around the Distant Quasar PKS 1614+051. *ApJ*, 317:L7, June 1987a. doi: 10.1086/184902.

Esther M. Hu and Lennox L. Cowie. The Distribution of Gas and Galaxies around the Distant Quasar PKS 1614+051. *ApJ*, 317:L7, June 1987b. doi: 10.1086/184902.

A. Humphrey, J. Vernet, M. Villar-Martín, et al. Polarized Extended Lyα Emission from a z = 2.3 Radio Galaxy. *ApJ*, 768(1):L3, May 2013. doi: 10.1088/2041-8205/768/1/L3.

J. D. Hunter. Matplotlib: A 2d graphics environment. *Computing in Science & Engineering*, 9(3):90–95, 2007. doi: 10.1109/MCSE.2007.55.

B. Husemann, G. Worseck, F. Arrigoni Battaia, and T. Shanks. Discovery of a dual AGN at z $\simeq$ 3.3 with 20 kpc separation. *Astronomy & Astrophysics*, 610:L7, February 2018. doi: 10.1051/0004-6361/201732457.

Daisuke Iono, Min S. Yun, Martin Elvis, et al. A Detection of [C II] Line Emission in the z = 4.7 QSO BR 1202-0725. *ApJ*, 645(2):L97–L100, July 2006. doi: 10.1086/506344.

P. Jakobsen, P. Ferruit, C. Alves de Oliveira, et al. The Near-Infrared Spectrograph (NIRSpec) on the James Webb Space Telescope. I. Overview of the instrument and its capabilities. *Astronomy & Astrophysics*, 661:A80, May 2022. doi: 10.1051/0004-6361/202142663.

Priyanka Jalan, Hum Chand, and Raghunathan Srianand. Probing the Environment of High-z Quasars Using the Proximity Effect in Projected Quasar Pairs. *ApJ*, 884(2):151, October 2019. doi: 10.3847/1538-4357/ab4191.

J. H. Jeans. The Stability of a Spherical Nebula. *Philosophical Transactions of the Royal Society of London Series A*, 199:1–53, January 1902. doi: 10.1098/rsta.1902.0012.

Guinevere Kauffmann and Martin Haehnelt. A unified model for the evolution of galaxies and quasars. *MNRAS*, 311(3):576–588, January 2000a. doi: 10.1046/j.1365-8711.2000.03077.x.

Guinevere Kauffmann and Martin Haehnelt. A unified model for the evolution of galaxies and quasars. *MNRAS*, 311(3):576–588, January 2000b. doi: 10.1046/j.1365-8711.2000.03077.x.

Jr. Kennicutt, Robert C. The Global Schmidt Law in Star-forming Galaxies. *ApJ*, 498(2):541–552, May 1998. doi: 10.1086/305588.

Robert C. Kennicutt and Neal J. Evans. Star Formation in the Milky Way and Nearby Galaxies. *ARA&A*, 50:531–608, September 2012. doi: 10.1146/annurev-astro-081811-125610.

Dušan Kereš, Neal Katz, David H. Weinberg, and Romeel Davé. How do galaxies get their gas? *MNRAS*, 363(1):2–28, October 2005. doi: 10.1111/j.1365-2966.2005.09451.x.

Eunchong Kim, Yujin Yang, Ann Zabludoff, et al. What Makes Lyα Nebulae Glow? Mapping the Polarization of LABd05. *ApJ*, 894(1):33, May 2020. doi: 10.3847/1538-4357/ab837f.

Andrew King and Ken Pounds. Powerful Outflows and Feedback from Active Galactic Nuclei. *ARA&A*, 53:115–154, August 2015. doi: 10.1146/annurev-astro-082214-122316.

Juna A. Kollmeier, Zheng Zheng, Romeel Davé, et al. Lyα Emission from Cosmic Structure. I. Fluorescence. *ApJ*, 708(2):1048–1075, January 2010. doi: 10.1088/0004-637X/708/2/1048.

John Kormendy and Douglas Richstone. Inward Bound—The Search For Supermassive Black Holes In Galactic Nuclei. *ARA&A*, 33:581, January 1995. doi: 10.1146/annurev.aa.33.090195.003053.

Charles J. Lada and Elizabeth A. Lada. Embedded Clusters in Molecular Clouds. *ARA&A*, 41:57–115, January 2003. doi: 10.1146/annurev.astro.41.011802.094844.

Marie Wingyee Lau, J. Xavier Prochaska, and Joseph F. Hennawi. Quasars Probing Quasars. VIII. The Physical Properties of the Cool Circumgalactic Medium Surrounding z ~2-3 Massive Galaxies Hosting Quasars. *ApJS*, 226(2):25, October 2016. doi: 10.3847/0067-0049/226/2/25.

Marie Wingyee Lau, Fred Hamann, Jarred Gillette, et al. Probing the inner circumgalactic medium and quasar illumination around the reddest 'extremely red quasar'. *MNRAS*, 515(2):1624–1643, September 2022. doi: 10.1093/mnras/stac1823.

Peter Laursen, Jesper Sommer-Larsen, and Anja C. Andersen. Lyα Radiative Transfer with Dust: Escape Fractions from Simulated High-Redshift Galaxies. *ApJ*, 704(2):1640–1656, October 2009. doi: 10.1088/0004-637X/704/2/1640.

C. Ledoux, P. Noterdaeme, P. Petitjean, and R. Srianand. Neutral atomic-carbon quasar absorption-line systems at z¿ 1.5. Sample selection, H i content, reddening, and 2175 Å extinction feature. *A&A*, 580:A8, August 2015. doi: 10.1051/0004-6361/201424122.

K. J. Leech, L. Metcalfe, and B. Altieri. ISO observations of the dusty quasar BR 1202-0725. *MNRAS*, 328(4):1125–1128, December 2001. doi: 10.1046/j.1365-8711.2001.04941.x.

Aigen Li and B. T. Draine. Infrared Emission from Interstellar Dust. II. The Diffuse Interstellar Medium. *ApJ*, 554(2):778–802, June 2001. doi: 10.1086/323147.

Jianrui Li, Bjorn H. C. Emonts, Zheng Cai, et al. The SUPERCOLD-CGM Survey. I. Probing the Extended CO(4-3) Emission of the Circumgalactic Medium in a Sample of 10 Enormous Lyα Nebulae at z $\sim$ 2. *ApJ*, 950(2):180, June 2023. doi: 10.3847/1538-4357/accbbd.

Qiong Li, Zheng Cai, J. Xavier Prochaska, et al. Discovery of a Lyα-emitting Dark Cloud within the z $\sim$ 2.8 SMM J02399-0136 System. *ApJ*, 875(2):130, April 2019. doi: 10.3847/1538-4357/ab0e6f.

Chen-Fatt Lim, Chian-Chou Chen, Ian Smail, et al. SCUBA-2 Ultra Deep Imaging EAO Survey (STUDIES). IV. Spatial Clustering and Halo Masses of Submillimeter Galaxies. *ApJ*, 895(2):104, June 2020. doi: 10.3847/1538-4357/ab8eaf.

Chris J. Lintott, Kevin Schawinski, William Keel, et al. Galaxy Zoo: 'Hanny's Voorwerp', a quasar light echo? *MNRAS*, 399(1):129–140, October 2009. doi: 10.1111/j.1365-2966.2009.15299.x.

E. Lusso, G. Worseck, J. F. Hennawi, et al. The first ultraviolet quasar-stacked spectrum at z $\simeq$ 2.4 from WFC3. *MNRAS*, 449(4):4204–4220, June 2015. doi: 10.1093/mnras/stv516.

Brad W. Lyke, Alexandra N. Higley, J. N. McLane, et al. The Sloan Digital Sky Survey Quasar Catalog: Sixteenth Data Release. *ApJS*, 250(1):8, September 2020. doi: 10.3847/1538-4365/aba623.

Ruari Mackenzie, Gabriele Pezzulli, Sebastiano Cantalupo, et al. Revealing the impact of quasar luminosity on giant Ly α nebulae. *MNRAS*, 502(1):494–509, March 2021a. doi: 10.1093/mnras/staa3277.

Ruari Mackenzie, Gabriele Pezzulli, Sebastiano Cantalupo, et al. Revealing the impact of quasar luminosity on giant Ly α nebulae. *MNRAS*, 502(1):494–509, March 2021b. doi: 10.1093/mnras/staa3277.

Chelsea L. MacLeod, Željko Ivezić, Branimir Sesar, et al. A Description of Quasar Variability Measured Using Repeated SDSS and POSS Imaging. *ApJ*, 753(2):106, July 2012. doi: 10.1088/0004-637X/753/2/106.

A. Marconi, G. Risaliti, R. Gilli, et al. Local supermassive black holes, relics of active galactic nuclei and the X-ray background. *MNRAS*, 351(1):169–185, June 2004. doi: 10.1111/j.1365-2966.2004.07765.x.

Paul Martini. QSO Lifetimes. In Luis C. Ho, editor, *Coevolution of Black Holes and Galaxies*, page 169, January 2004. doi: 10.48550/arXiv.astro-ph/0304009.

Paul Martini and David H. Weinberg. Quasar Clustering and the Lifetime of Quasars. *ApJ*, 547(1):12–26, January 2001. doi: 10.1086/318331.

Christopher F. McKee and Eve C. Ostriker. Theory of Star Formation. *ARA&A*, 45(1): 565–687, September 2007. doi: 10.1146/annurev.astro.45.051806.110602.

Peter D. Mitchell and Joop Schaye. Baryonic mass budgets for haloes in the EAGLE simulation, including ejected and prevented gas. *MNRAS*, 511(2):2600–2609, April 2022. doi: 10.1093/mnras/stab3686.

Houjun Mo, Frank C. van den Bosch, and Simon White. *Galaxy Formation and Evolution.* 2010.

Juan Molina, Luis C. Ho, Ran Wang, et al. Enhanced Star Formation Efficiency in the Central Regions of Nearby Quasar Hosts. *ApJ*, 944(1):30, February 2023. doi: 10.3847/ 1538-4357/acaa9b.

P. Møller. Spectral PSF subtraction I: the SPSF look-up-table method. *The Messenger*, 99:31–33, March 2000.

Masao Mori and Masayuki Umemura. Early metal enrichment and Lyman α emission. *New A Rev.*, 50(1-3):199–203, March 2006. doi: 10.1016/j.newar.2005.11.035.

Masao Mori, Masayuki Umemura, and Andrea Ferrara. The Nature of Lyα Blobs: Supernova-dominated Primordial Galaxies. *ApJ*, 613(2):L97–L100, October 2004. doi: 10.1086/425255.

Patrick Morrissey, Matuesz Matuszewski, D. Christopher Martin, et al. The Keck Cosmic Web Imager Integral Field Spectrograph. *ApJ*, 864(1):93, September 2018. doi: 10.3847/ 1538-4357/aad597.

Benjamin P. Moster, Thorsten Naab, and Simon D. M. White. EMERGE - an empirical model for the formation of galaxies since z $\sim$ 10. *MNRAS*, 477(2):1822–1852, June 2018. doi: 10.1093/mnras/sty655.

N. Muñoz-Elgueta, F. Arrigoni Battaia, G. Kauffmann, et al. APEX at the QSO MU-SEUM: molecular gas reservoirs associated with z 3 quasars and their link to the extended Ly α emission. *MNRAS*, 511(1):1462–1483, March 2022. doi: 10.1093/mnras/stac041.

Hasti Nateghi, Glenn G. Kacprzak, Nikole M. Nielsen, et al. Signatures of Gas Glows-I: Connecting the kinematics of the H I circumgalactic medium to galaxy rotation. *MN-RAS*, July 2024. doi: 10.1093/mnras/stae1843.

Julio F. Navarro, Carlos S. Frenk, and Simon D. M. White. A Universal Density Profile from Hierarchical Clustering. *ApJ*, 490(2):493–508, December 1997. doi: 10.1086/304888.

Dylan Nelson, Chris Byrohl, Celine Peroux, et al. The cold circumgalactic medium in emission: Mg II haloes in TNG50. *MNRAS*, 507(3):4445–4463, November 2021. doi: 10.1093/mnras/stab2177.

Hagai Netzer. Revisiting the Unified Model of Active Galactic Nuclei. *ARA&A*, 53:365–408, August 2015. doi: 10.1146/annurev-astro-082214-122302.

Marta Nowotka, Chian-Chou Chen, Fabrizio Arrigoni Battaia, et al. A MUltiwavelength Study of ELAN Environments (AMUSE^2). Ubiquitous dusty star-forming galaxies associated with enormous Lyα nebulae on megaparsec scales. *Astronomy & Astrophysics*, 658:A77, February 2022. doi: 10.1051/0004-6361/202040133.

Aura Obreja, Andrea V. Macciò, Benjamin Moster, et al. Local photoionization feedback effects on galaxies. *MNRAS*, 490(2):1518–1538, December 2019. doi: 10.1093/mnras/stz2639.

Aura Obreja, Fabrizio Arrigoni Battaia, Andrea V. Macciò, and Tobias Buck. AGN radiation imprints on the circumgalactic medium of massive galaxies. *MNRAS*, 527(3): 8078–8102, January 2024. doi: 10.1093/mnras/stad3410.

Youichi Ohyama, Yoshiaki Taniguchi, Koji S. Kawabata, et al. On the Origin of Lyα Blobs at High Redshift: Kinematic Evidence of a Hyperwind Galaxy at z = 3.1. *ApJ*, 591(1): L9–L12, July 2003. doi: 10.1086/376959.

A. Omont, R. G. McMahon, P. Cox, et al. Continuum millimetre observations of high-redshift radio-quiet QSOs II. Five new detections at z¿4. *Astronomy & Astrophysics*, 315:1–10, November 1996a.

Alain Omont, Patrick Petitjean, Stéphane Guilloteau, et al. Molecular gas and dust around a radio-quiet quasar at redshift 4.69. *Nature*, 382(6590):428–431, August 1996b. doi: 10.1038/382428a0.

Benjamin D. Oppenheimer, Romeel Davé, Neal Katz, et al. The intergalactic medium over the last 10 billion years - II. Metal-line absorption and physical conditions. *MNRAS*, 420(1):829–859, February 2012. doi: 10.1111/j.1365-2966.2011.20096.x.

Donal B. O'Sullivan, Christopher Martin, Mateusz Matuszewski, et al. The FLASHES Survey. I. Integral Field Spectroscopy of the CGM around 48 z $\simeq$ 2.3-3.1 QSOs. *ApJ*, 894(1):3, May 2020. doi: 10.3847/1538-4357/ab838c.

Rüdiger Pakmor, Volker Springel, Jonathan P. Coles, et al. The MillenniumTNG Project: the hydrodynamical full physics simulation and a first look at its galaxy clusters. *MNRAS*, 524(2):2539–2555, September 2023. doi: 10.1093/mnras/stac3620.

Isabelle Pâris, Patrick Petitjean, Éric Aubourg, et al. The Sloan Digital Sky Survey Quasar Catalog: Fourteenth data release. *Astronomy & Astrophysics*, 613:A51, May 2018. doi: 10.1051/0004-6361/201732445.

P. J. E. Peebles. Large-scale background temperature and mass fluctuations due to scale-invariant primeval perturbations. *ApJ*, 263:L1–L5, December 1982. doi: 10.1086/183911.

Céline Péroux and J. Christopher Howk. The Cosmic Baryon and Metal Cycles. *ARA&A*, 58:363–406, August 2020. doi: 10.1146/annurev-astro-021820-120014.

Matthew M. Pieri, Michael J. Mortonson, Stephan Frank, et al. Probing the circumgalactic medium at high-redshift using composite BOSS spectra of strong Lyman α forest absorbers. *MNRAS*, 441(2):1718–1740, June 2014. doi: 10.1093/mnras/stu577.

Laure Piqueras, Simon Conseil, Martin Shepherd, et al. MPDAF - A Python package for the analysis of VLT/MUSE data. *arXiv e-prints*, art. arXiv:1710.03554, October 2017. doi: 10.48550/arXiv.1710.03554.

L. K. Pitchford, E. Hatziminaoglou, A. Feltre, et al. Extreme star formation events in quasar hosts over 0.5 ¡ z ¡ 4. *MNRAS*, 462(4):4067–4077, November 2016. doi: 10.1093/mnras/stw1840.

Planck Collaboration, N. Aghanim, Y. Akrami, et al. Planck 2018 results. VI. Cosmological parameters. *A&A*, 641:A6, September 2020. doi: 10.1051/0004-6361/201833910.

Cristiano Porciani, Manuela Magliocchetti, and Peder Norberg. Cosmic evolution of quasar clustering: implications for the host haloes. *MNRAS*, 355(3):1010–1030, December 2004. doi: 10.1111/j.1365-2966.2004.08408.x.

P. Predehl, R. A. Sunyaev, W. Becker, et al. Detection of large-scale X-ray bubbles in the Milky Way halo. *Nature*, 588(7837):227–231, December 2020. doi: 10.1038/s41586-020-2979-0.

Moire K. M. Prescott, Crystal L. Martin, and Arjun Dey. Spatially Resolved Gas Kinematics within a Lyα Nebula: Evidence for Large-scale Rotation. *ApJ*, 799(1):62, January 2015. doi: 10.1088/0004-637X/799/1/62.

William H. Press and Paul Schechter. Formation of Galaxies and Clusters of Galaxies by Self-Similar Gravitational Condensation. *ApJ*, 187:425–438, February 1974. doi: 10.1086/152650.

J. Xavier Prochaska, Marie Wingyee Lau, and Joseph F. Hennawi. Quasars Probing Quasars. VII. The Pinnacle of the Cool Circumgalactic Medium Surrounds Massive z ~2 Galaxies. *ApJ*, 796(2):140, December 2014. doi: 10.1088/0004-637X/796/2/140.

Suvendu Rakshit, C. S. Stalin, and Jari Kotilainen. Spectral Properties of Quasars from Sloan Digital Sky Survey Data Release 14: The Catalog. *ApJS*, 249(1):17, July 2020. doi: 10.3847/1538-4365/ab99c5.

M. J. Rees and J. P. Ostriker. Cooling, dynamics and fragmentation of massive gas clouds: clues to the masses and radii of galaxies and clusters. *MNRAS*, 179:541–559, June 1977. doi: 10.1093/mnras/179.4.541.

Martin J. Rees. Quasars as probes of gas in extended protogalaxies. *MNRAS*, 231:91P–95, April 1988. doi: 10.1093/mnras/231.1.91P.

Gordon T. Richards, Mark Lacy, Lisa J. Storrie-Lombardi, et al. Spectral Energy Distributions and Multiwavelength Selection of Type 1 Quasars. *ApJS*, 166(2):470–497, October 2006. doi: 10.1086/506525.

Dominik A. Riechers, Fabian Walter, Christopher L. Carilli, et al. CO(1-0) in z ¿~4 Quasar Host Galaxies: No Evidence for Extended Molecular Gas Reservoirs. *ApJ*, 650(2):604–613, October 2006. doi: 10.1086/507014.

Dominik A. Riechers, C. M. Bradford, D. L. Clements, et al. A dust-obscured massive maximum-starburst galaxy at a redshift of 6.34. *Nature*, 496(7445):329–333, April 2013. doi: 10.1038/nature12050.

Adam G. Riess, Alexei V. Filippenko, Peter Challis, et al. Observational Evidence from Supernovae for an Accelerating Universe and a Cosmological Constant. *AJ*, 116(3): 1009–1038, September 1998. doi: 10.1086/300499.

Thomas Robitaille and Eli Bressert. APLpy: Astronomical Plotting Library in Python. Astrophysics Source Code Library, record ascl:1208.017, August 2012.

Thomas Robitaille, Adam Ginsburg, Chris Beaumont, et al. spectral-cube: Read and analyze astrophysical spectral data cubes. Astrophysics Source Code Library, record ascl:1609.017, September 2016.

J. Rosdahl and J. Blaizot. Extended Lyα emission from cold accretion streams. *MNRAS*, 423(1):344–366, June 2012a. doi: 10.1111/j.1365-2966.2012.20883.x.

J. Rosdahl and J. Blaizot. Extended Lyα emission from cold accretion streams. *MNRAS*, 423(1):344–366, June 2012b. doi: 10.1111/j.1365-2966.2012.20883.x.

Nicholas P. Ross, Ian D. McGreer, Martin White, et al. The SDSS-III Baryon Oscillation Spectroscopic Survey: The Quasar Luminosity Function from Data Release Nine. *ApJ*, 773(1):14, August 2013. doi: 10.1088/0004-637X/773/1/14.

Martin M. Roth, Andreas Kelz, Thomas Fechner, et al. PMAS: The Potsdam Multi-Aperture Spectrophotometer. I. Design, Manufacture, and Performance. *PASP*, 117 (832):620–642, June 2005. doi: 10.1086/429877.

Jessie C. Runnoe, Michael S. Brotherton, and Zhaohui Shang. Updating quasar bolometric luminosity corrections. *MNRAS*, 422(1):478–493, May 2012. doi: 10.1111/j.1365-2966. 2012.20620.x.

D. S. N. Rupke, M. Schweitzer, V. Viola, et al. QUESTFIT: Fitter for mid-infrared galaxy spectra, December 2021.

David S. N. Rupke. IFSFIT: Spectral Fitting for Integral Field Spectrographs, September 2014.

Sanchit Sabhlok, Shelley A. Wright, Andrey Vayner, et al. Circumgalactic Environments Around Distant Quasars 3C 9 and 4C 05.84. *ApJ*, 964(1):84, March 2024. doi: 10.3847/1538-4357/ad2350.

E. E. Salpeter. Accretion of Interstellar Matter by Massive Objects. *ApJ*, 140:796–800, August 1964. doi: 10.1086/147973.

Kevin Schawinski, Michael Koss, Simon Berney, and Lia F. Sartori. Active galactic nuclei flicker: an observational estimate of the duration of black hole growth phases of $\sim 10^5$ yr. *MNRAS*, 451(3):2517–2523, August 2015. doi: 10.1093/mnras/stv1136.

P. Schechter. An analytic expression for the luminosity function for galaxies. *ApJ*, 203: 297–306, January 1976. doi: 10.1086/154079.

M. Schirmer, R. Diaz, K. Holhjem, et al. A Sample of Seyfert-2 Galaxies with Ultraluminous Galaxy-wide Narrow-line Regions: Quasar Light Echoes? *ApJ*, 763(1):60, January 2013. doi: 10.1088/0004-637X/763/1/60.

M. Schmidt. 3C 273 : A Star-Like Object with Large Red-Shift. *Nature*, 197(4872):1040, March 1963. doi: 10.1038/1971040a0.

Xuejian Shen, Philip F. Hopkins, Claude-André Faucher-Giguère, et al. The bolometric quasar luminosity function at z = 0-7. *MNRAS*, 495(3):3252–3275, January 2020. doi: 10.1093/mnras/staa1381.

Yue Shen. Rest-frame Optical Properties of Luminous 1.5 ¡ Z ¡ 3.5 Quasars: The Hβ-[O III] Region. *ApJ*, 817(1):55, January 2016. doi: 10.3847/0004-637X/817/1/55.

Yue Shen, Michael A. Strauss, Nicholas P. Ross, et al. Quasar Clustering from SDSS DR5: Dependences on Physical Properties. *ApJ*, 697(2):1656–1673, June 2009. doi: 10.1088/0004-637X/697/2/1656.

Yue Shen, Gordon T. Richards, Michael A. Strauss, et al. A Catalog of Quasar Properties from Sloan Digital Sky Survey Data Release 7. *ApJS*, 194(2):45, June 2011. doi: 10.1088/0067-0049/194/2/45.

Yue Shen, Jin Wu, Linhua Jiang, et al. Gemini GNIRS Near-infrared Spectroscopy of 50 Quasars at z $\gtrsim$ 5.7. *ApJ*, 873(1):35, March 2019. doi: 10.3847/1538-4357/ab03d9.

Joseph Silk and Martin J. Rees. Quasars and galaxy formation. *A&A*, 331:L1–L4, March 1998. doi: 10.48550/arXiv.astro-ph/9801013.

Ian Smail, R. J. Ivison, and A. W. Blain. A Deep Sub-millimeter Survey of Lensing Clusters: A New Window on Galaxy Formation and Evolution. *ApJl*, 490(1):L5–L8, November 1997. doi: 10.1086/311017.

D. J. B. Smith, M. J. Jarvis, C. Simpson, and A. Martínez-Sansigre. An 80-kpc Lyα halo around a high-redshift type-2 quasi-stellar object. *MNRAS*, 393(1):309–316, February 2009. doi: 10.1111/j.1365-2966.2008.14232.x.

Kurt T. Soto, Simon J. Lilly, Roland Bacon, et al. ZAP - enhanced PCA sky subtraction for integral field spectroscopy. *MNRAS*, 458(3):3210–3220, May 2016. doi: 10.1093/mnras/stw474.

Volker Springel, Tiziana Di Matteo, and Lars Hernquist. Modelling feedback from stars and black holes in galaxy mergers. *MNRAS*, 361(3):776–794, August 2005. doi: 10.1111/j.1365-2966.2005.09238.x.

Charles C. Steidel, Milan Bogosavljević, Alice E. Shapley, et al. Diffuse Lyα Emitting Halos: A Generic Property of High-redshift Star-forming Galaxies. *ApJ*, 736(2):160, August 2011. doi: 10.1088/0004-637X/736/2/160.

Greg Stinson, Anil Seth, Neal Katz, et al. Star formation and feedback in smoothed particle hydrodynamic simulations - I. Isolated galaxies. *MNRAS*, 373(3):1074–1090, December 2006. doi: 10.1111/j.1365-2966.2006.11097.x.

Chris Stoughton, Robert H. Lupton, Mariangela Bernardi, et al. Sloan Digital Sky Survey: Early Data Release. *AJ*, 123(1):485–548, January 2002. doi: 10.1086/324741.

A. M. Swinbank, A. Karim, Ian Smail, et al. An ALMA survey of submillimetre galaxies in the Extended Chandra Deep Field-South: detection of [C II] at z = 4.4. *MNRAS*, 427(2):1066–1074, December 2012. doi: 10.1111/j.1365-2966.2012.22048.x.

Linda J. Tacconi, Reinhard Genzel, and Amiel Sternberg. The Evolution of the Star-Forming Interstellar Medium Across Cosmic Time. *ARA&A*, 58:157–203, August 2020. doi: 10.1146/annurev-astro-082812-141034.

Yoshiaki Taniguchi and Yasuhiro Shioya. Superwind Model of Extended Lyα Emitters at High Redshift. *ApJ*, 532(1):L13–L16, March 2000. doi: 10.1086/312557.

Yoshiaki Taniguchi, Yasuhiro Shioya, and Yuko Kakazu. On the Origin of Lyα Blobs at High Redshift: Submillimetric Evidence for a Hyperwind Galaxy at z = 3.1. *ApJ*, 562(1):L15–L17, November 2001. doi: 10.1086/338101.

John D. Timlin, Nicholas P. Ross, Gordon T. Richards, et al. The Clustering of High-redshift (2.9 ≤ z ≤ 5.1) Quasars in SDSS Stripe 82. *ApJ*, 859(1):20, May 2018. doi: 10.3847/1538-4357/aab9ac.

Davide Tornotti, Michele Fumagalli, Matteo Fossati, et al. High-definition imaging of an extended filament connecting active quasars at cosmic noon. *arXiv e-prints*, art. arXiv:2406.17035, June 2024. doi: 10.48550/arXiv.2406.17035.

A. Travascio, L. Zappacosta, S. Cantalupo, et al. The WISSH quasars project. VIII. Outflows and metals in the circum-galactic medium around the hyper-luminous z ∼ 3.6 quasar J1538+08. *Astronomy & Astrophysics*, 635:A157, March 2020. doi: 10.1051/0004-6361/201936197.

Maxime Trebitsch, Anne Verhamme, Jérémy Blaizot, and Joakim Rosdahl. Lyman-α blobs: polarization arising from cold accretion. *Astronomy & Astrophysics*, 593:A122, October 2016. doi: 10.1051/0004-6361/201527024.

Ezequiel Treister, Julian H. Krolik, and Cornelis Dullemond. Measuring the Fraction of Obscured Quasars by the Infrared Luminosity of Unobscured Quasars. *ApJ*, 679(1):140–148, May 2008. doi: 10.1086/586698.

Nhut Truong, Annalisa Pillepich, Dylan Nelson, et al. X-ray metal line emission from the hot circumgalactic medium: probing the effects of supermassive black hole feedback. *MNRAS*, 525(2):1976–1997, October 2023. doi: 10.1093/mnras/stad2216.

Jason Tumlinson, Molly S. Peeples, and Jessica K. Werk. The Circumgalactic Medium. *ARA&A*, 55(1):389–432, August 2017. doi: 10.1146/annurev-astro-091916-055240.

H. Umehata, M. Fumagalli, I. Smail, et al. Gas filaments of the cosmic web located around active galaxies in a protocluster. *Science*, 366(6461):97–100, October 2019. doi: 10.1126/science.aaw5949.

R. van Ojik, H. J. A. Roettgering, G. K. Miley, and R. W. Hunstead. The gaseous environments of radio galaxies in the early Universe: kinematics of the Lyman α emission and spatially resolved H I absorption. *Astronomy & Astrophysics*, 317:358–384, January 1997.

Daniel E. Vanden Berk, Gordon T. Richards, Amanda Bauer, et al. Composite Quasar Spectra from the Sloan Digital Sky Survey. *AJ*, 122(2):549–564, August 2001. doi: 10.1086/321167.

Marianne Vestergaard and Bradley M. Peterson. Determining Central Black Hole Masses in Distant Active Galaxies and Quasars. II. Improved Optical and UV Scaling Relationships. *ApJ*, 641(2):689–709, April 2006. doi: 10.1086/500572.

A. Vidal-García, E. Falgarone, F. Arrigoni Battaia, et al. Where infall meets outflows: turbulent dissipation probed by CH^+ and Lyα in the starburst/AGN galaxy group SMM J02399-0136 at z 2.8. *MNRAS*, 506(2):2551–2573, September 2021. doi: 10.1093/mnras/stab1503.

Pauli Virtanen, Ralf Gommers, Travis E. Oliphant, et al. SciPy 1.0: Fundamental Algorithms for Scientific Computing in Python. *Nature Methods*, 17:261–272, 2020. doi: 10.1038/s41592-019-0686-2.

J. Wagg, T. Wiklind, C. L. Carilli, et al. [C II] Line Emission in Massive Star-forming Galaxies at z = 4.7. *ApJ*, 752(2):L30, June 2012. doi: 10.1088/2041-8205/752/2/L30.

Fabian Walter, Dominik Riechers, Pierre Cox, et al. A kiloparsec-scale hyper-starburst in a quasar host less than 1gigayear after the Big Bang. *Nature*, 457(7230):699–701, February 2009. doi: 10.1038/nature07681.

Feige Wang, Jinyi Yang, Xiaohui Fan, et al. A Luminous Quasar at Redshift 7.642. *ApJ*, 907(1):L1, January 2021. doi: 10.3847/2041-8213/abd8c6.

M. Weidinger, P. Møller, J. P. U. Fynbo, and B. Thomsen. The extended Lyman-α emission surrounding the z = 3.04 radio-quiet QSO1205-30: Primordial infalling gas illuminated by the quasar? *Astronomy & Astrophysics*, 436(3):825–835, June 2005. doi: 10.1051/0004-6361:20042304.

Michael Weidinger, Palle Møller, and Johan Peter Uldall Fynbo. The Lyman-α glow of gas falling into the dark matter halo of a z = 3 galaxy. *Nature*, 430(7003):999–1001, August 2004. doi: 10.1038/nature02793.

P. M. Weilbacher, O. Streicher, T. Urrutia, et al. The MUSE Data Reduction Pipeline: Status after Preliminary Acceptance Europe. In N. Manset and P. Forshay, editors, *Astronomical Data Analysis Software and Systems XXIII*, volume 485 of *Astronomical Society of the Pacific Conference Series*, page 451, May 2014.

Peter M. Weilbacher, Ole Streicher, Tanya Urrutia, et al. Design and capabilities of the MUSE data reduction software and pipeline. In Nicole M. Radziwill and Gian-luca Chiozzi, editors, *Software and Cyberinfrastructure for Astronomy II*, volume 8451 of *Society of Photo-Optical Instrumentation Engineers (SPIE) Conference Series*, page 84510B, September 2012. doi: 10.1117/12.925114.

Peter M. Weilbacher, Ralf Palsa, Ole Streicher, et al. The data processing pipeline for the MUSE instrument. *Astronomy & Astrophysics*, 641:A28, September 2020. doi: 10.1051/0004-6361/202037855.

Jessica K. Werk, J. Xavier Prochaska, Jason Tumlinson, et al. The COS-Halos Survey: Physical Conditions and Baryonic Mass in the Low-redshift Circumgalactic Medium. *ApJ*, 792(1):8, September 2014. doi: 10.1088/0004-637X/792/1/8.

Martin White, Adam D. Myers, Nicholas P. Ross, et al. The clustering of intermediate-redshift quasars as measured by the Baryon Oscillation Spectroscopic Survey. *MNRAS*, 424(2):933–950, August 2012. doi: 10.1111/j.1365-2966.2012.21251.x.

S. D. M. White and M. J. Rees. Core condensation in heavy halos: a two-stage theory for galaxy formation and clustering. *MNRAS*, 183:341–358, May 1978. doi: 10.1093/mnras/183.3.341.

Aaron Wilkinson, Omar Almaini, Chian-Chou Chen, et al. The SCUBA-2 Cosmology Legacy Survey: the clustering of submillimetre galaxies in the UKIDSS UDS field. *MN-RAS*, 464(2):1380–1392, January 2017. doi: 10.1093/mnras/stw2405.

R. J. Wilman, J. Gerssen, R. G. Bower, et al. The discovery of a galaxy-wide superwind from a young massive galaxy at redshift z ~3. *Nature*, 436(7048):227–229, July 2005. doi: 10.1038/nature03718.

L. Wisotzki, R. Bacon, J. Blaizot, et al. Extended Lyman α haloes around individual high-redshift galaxies revealed by MUSE. *Astronomy & Astrophysics*, 587:A98, March 2016. doi: 10.1051/0004-6361/201527384.

L. Wisotzki, R. Bacon, J. Brinchmann, et al. Nearly all the sky is covered by Lyman-α emission around high-redshift galaxies. *Nature*, 562(7726):229–232, October 2018. doi: 10.1038/s41586-018-0564-6.

Ruby J. Wright, Rachel S. Somerville, Claudia del P. Lagos, et al. The baryon cycle in modern cosmological hydrodynamical simulations. *MNRAS*, 532(3):3417–3440, August 2024. doi: 10.1093/mnras/stae1688.

Yi Zhang, Johan Comparat, Gabriele Ponti, et al. The Hot Circum-Galactic Medium in the eROSITA All Sky Survey I. X-ray Surface Brightness Profiles. *arXiv e-prints*, art. arXiv:2401.17308, January 2024. doi: 10.48550/arXiv.2401.17308.

Acknowledgements

I would like to thank the people who helped the development and finalization of this thesis.

I am very grateful to Guinevere, Fabrizio and Eiichiro who supported me at difficult times during my PhD.

Also to Guinevere for the commitment to this thesis and useful advice, both in scientific and academic career subjects.

I am very thankful to Fabrizio for the guidance and bringing opportunities for me to develop my skills as a researcher, also for listening to my ideas and helping realize them.

Those who accompanied me from the beginning and those who joined afterwards, mom, dad, Lita, Nico, Camila, Cona, Odette, Rocío, Carlos, Pachi, Luan, Vanesa, Rubén, Pipe, Feña, Simón, Joaquin, Yru, Vivian, Nahir, Daniel, Alejandra, Lazaros, Stavroula, Davide, Fran, Juanjo, Silvia, Bea. And of course Gin Tonic.